From inner structural arrangements in elastic materials to tailored overall behavior

Thesis

for the degree of

doctor rerum naturalium (Dr. rer. nat.)

approved by the Faculty of Natural Sciences of
Otto von Guericke University Magdeburg

by M. Sc. Lukas Fischer

born on June 12, 1996 in Krefeld

Examiners: Prof. Dr. Andreas M. Menzel

Prof. Dr.-Ing. Thomas Wallmersperger

submitted on: November 20, 2024

defended on: April 30, 2025

Abstract

In this dissertation, the main focus is on magnetic gels and elastomers, fascinating composite materials that consist of magnetic or magnetizable inclusions embedded in a soft, usually polymeric, elastic matrix material. These inclusions cause the materials to be responsive to external magnetic fields. The two most noticeable and well-studied effects are changes in the rheological behavior (magnetorheological effect) and overall deformations (magnetostriction) in response to the applied external magnetic fields. We mostly concentrate on the latter effect. More precisely, we investigate what the influence of the arrangement of magnetizable inclusions within the elastic matrix on the magnetostrictive response is.

So far, mostly randomized or chain-like configurations have been investigated. However, with modern technologies such as 3D printing, manufacturing magnetic gels and elastomers with targeted placements of the inclusions is within reach.

For the model system of a homogeneous, isotropic, and linearly elastic sphere with embedded magnetizable inclusions, we managed to calculate overall magnetically induced deformations from the arrangement of magnetizable inclusions directly. First, we investigate the consequences of various regular lattice arrangements for the magnetostrictive response, which even leads to qualitative differences. Additionally, the deformational response depends on the employed elastic matrix material as well. Next, we show that specific arrangements of magnetizable inclusions can induce twist-type deformations of the whole material. Moreover, we investigate samples with a polydisperse, binary distribution of the inclusion sizes. Targeted placements of bigger and smaller inclusions allows to further tailor the magnetostrictive effects. Next, we investigate several other configurations, regarding higher-order modes of deformation and relate them to the underlying configuration. As a major contribution, we then identify arrangements of magnetizable inclusions that lead to the largest magnetostrictive effects, which is often desirable in applications, by combining analytical theory with a computational optimization scheme. Furthermore, we study magnetically induced changes in the transport properties and the thermal conductivity of these materials, which is related to chain formation in the arrangement of the inclusions. As an addition, we investigate spherical, linearly elastic core-shell systems for their response to an applied isotropic line force in the equatorial plane, which is relevant, e.g., for functionalized microgels adsorbed to a liquid-liquid interface.

In summary, we wish to support the path towards tailored applications of this exciting class of materials. This dissertation is intended to provide a fundamental theoretical framework for this ambition.

Kurzzusammenfassung

Thema dieser Dissertation sind magnetische Gele und Elastomere, faszinierende Komposit-Materialien, bestehend aus magnetischen oder magnetisierbaren Einschlüssen in einer weichen, typischerweise polymerartigen, elastischen Matrix. Durch diese Einschlüsse sind die Materialien durch externe Magnetfelder ansprechbar. Die zwei deutlichsten und am besten untersuchten Effekte sind die Änderungen des rheologischen Verhaltens (magnetorheologischer Effekt) und globale Deformationen (Magnetostriktion) durch die Anwendung externer Magnetfelder. Wir konzentrieren uns überwiegend auf Zweiteres. Insbesondere untersuchen wir, welchen Einfluss die Anordnung der magnetisierbaren Einschlüsse innerhalb der elastischen Matrix auf das magnetostriktive Verhalten hat.

Bisher wurden hauptsächlich zufällige oder kettenartige Strukturen untersucht. Allerdings ist durch moderne Techniken wie den 3D-Druck die Herstellung magnetischer Gele und Elastomere mit gezielter Platzierung der Einschlüsse in greifbarer Nähe.

Für das Modell-System einer homogenen, isotropen und linear elastischen Kugel mit eingebetteten magnetisierbaren Einschlüsse konnten wir die magnetisch induzierten Deformationen direkt aus der Anordnung der magnetisierbaren Einschlüsse berechnen. Zuerst untersuchen wir die Auswirkungen verschiedener Gitterstrukturen auf das magnetostriktive Verhalten, was sogar zu qualitativen Unterschieden führt. Weiterhin hängt die Deformationsantwort ebenfalls vom elastischen Material ab. Als Nächstes zeigen wir, dass spezifische Anordnungen zu einer Verdrillung des gesamten Materials führen können. Anschließend betrachten wir Systeme mit einer polydispersen, binären Größenverteilung der Einschlüsse. Gezielte Platzierungen der größeren und kleineren Einschlüsse ermöglichen ebenfalls die Anpassung magnetostriktiver Effekte. Hiernach untersuchen wir weitere Anordnungen bezüglich ihrer höheren Deformationsmoden und führen diese auf die verwendete Konfiguration zurück. Als wichtigen Beitrag identifizieren wir danach solche Anordnungen der magnetisierbaren Einschlüsse, die zu den größten magnetostriktiven Effekten führen, was oft in Anwendungen gewünscht ist. Hierzu verbinden wir analytische Theorie mit numerischer Optimierung. Weiterhin untersuchen wir magnetisch induzierte Änderungen in den Transporteigenschaften und der thermischen Leitfähigkeit dieser Materialien, was von einer Kettenbildung herrührt. Zusätzlich betrachten wir kugelförmige, linear elastische Kern-Schalen-Systeme bezüglich deren Antwort auf isotrope Linienkraftdichten in der Äquatorialebene, was beispielsweise relevant ist für funktionalisierte Mikrogele, die an einer Flüssig-Flüssig-Grenzfläche adsorbiert sind.

Zusammenfassend möchten wir die Entwicklung zu maßgeschneiderten Anwendungen dieser spannenden Materialklasse fördern. Diese Dissertation soll dazu einen fundierten theoretischen Rahmen liefern.

Preface

The main contents of this cumulative dissertation is based on jointly published articles (my name is highlighted by an underscore in the following list), and that have been published in or submitted to peer-reviewed scientific journals. The work for all publications has been supervised by Prof. Dr. Andreas M. Menzel. These articles are reproduced in Chapter 2 and are listed according to their topical order:

- **P1** L. Fischer and A. M. Menzel, *Magnetostriction in magnetic gels and elastomers as a function of the internal structure and particle distribution*, J. Chem. Phys. **151**, 114906 (2019).
- **P2** L. Fischer and A. M. Menzel, *Towards a soft magnetoelastic twist actuator*, Phys. Rev. Research **2**, 023383 (2020).
- **P3** L. Fischer and A. M. Menzel, *Magnetically induced elastic deformations in model systems of magnetic gels and elastomers containing particles of mixed size*, Smart Mater. Struct. **30**, 014003 (2021).
- **P4** L. Fischer and A. M. Menzel, *Magnetic elastomers as specific soft actuators – predicting particular modes of deformation from selected configurations of magnetizable inclusions*, J. Magn. Magn. Mater. **591**, 171695 (2024).
- **P5** L. Fischer and A. M. Menzel, *Maximized response by structural optimization of soft elastic composite systems*, PNAS Nexus **3**, pgae353 (2024).
- **P6** L. Fischer and A. M. Menzel, *Analytical expressions for the two basic modes of surface displacement and overall deformation of a free-standing or elastically embedded sphere*, arXiv:2407.09291 (2024).
- **P7** G. J. L. Jäger, L. Fischer, T. Lutz, and A. M. Menzel, *Variations in the thermal conductivity of magnetosensitive elastomers by magnetically induced internal restructuring*, J. Phys.: Condens. Matter **34**, 485101 (2022).
- **P8** J. Kolker, L. Fischer, A. M. Menzel, and H. Löwen, *Elastic deformations of loaded core-shell systems*, J. Elasticity **150**, 77 (2022).

My contributions to each of these scientific articles are specified in detail in Chapter 2.

Contents

Chapter 1

Introduction

In this chapter, we start by introducing the publications and their general background and common themes in Sec. 1.1. Afterward, we expand on the theoretical background of this dissertation and corresponding experimental realizations. The background is split into two parts: First, we introduce linear elasticity theory, describing deformations of low amplitudes in Sec. 1.2. We then continue by discussing magnetic or magnetizable inclusions concerning their phenomenology and most important characteristics in Sec. 1.3. A combination of elastic and magnetic properties is then provided by magnetic gels and elastomers, which belong to the class of magnetic hybrid materials that we discuss in Sec. 1.4.

1.1 Overview

The present dissertation roots in the area of *soft matter physics*. This field concerns materials or systems showing strong responses to applied forces and that are easily driven out of equilibrium or even permanently in a non-equilibrium state [1]. More specifically, my studies concern the subject of *magnetic gels and elastomers* [2–8]. While a more detailed definition is given later in Sec. 1.4.2, in short, they consist of a soft, usually polymeric, matrix with embedded magnetic or magnetizable particles. One prominent feature of these materials are strong responses to external magnetic fields which drive them out of their initial equilibrium configuration (and often into a new equilibrium state). Therefore, they present prime examples of soft matter systems.

One of those responses is the so-called *magnetostriction*, i.e. shape changes of materials in homogeneous external magnetic fields [9–21]. In our works, we use a *mesoscopic* model to describe these effects: We do not resolve the elastic matrix material itself, for instance, by taking into account the discrete nature of individual polymer chains, as has been done in some previous studies. This is what we term the *microscopic* level of description. Instead, we treat it as a fully homogeneous and isotropic continuous medium. Nevertheless, the arrangement of the magnetic or magnetizable inclusions inside of the elastic matrix is resolved by respecting their discrete character. This is in contrast to the *macroscopic* level, where the whole

system is described by macroscopic continuous fields. Corresponding equations are derived, amongst others, based on conservation laws and symmetry properties. For a more detailed discussion, we refer to Sec. 1.4.4.

Naturally, each level features its own set of advantages and disadvantages. For the microscopic level, the main advantage is naturally that it is the most basic one, resolving many individual degrees of freedom of the material (albeit not on a quantum level). The disadvantage of these models is their high computational cost, which often limits them to rather small systems with a low number of magnetic or magnetizable particles. On the macroscopic level, the description is naturally quite general and some purely analytical calculations are possible. The description does not resolve the magnetizable inclusions explicitly, so it works even for huge numbers of them. Yet, details of individual interactions between the discrete inclusions and their consequences on the material behavior remain unresolved. The mesoscopic level that we choose is naturally somewhere in between the microscopic and macroscopic model. This level is ideal for the question that we aim to answer in this thesis: What is the effect of different structural arrangements of the magnetic or magnetizable inclusions on the overall, macroscopic material behavior? As we show later, the answer is that the arrangement is a very important ingredient concerning which type of magnetostrictive deformation or also magnetorheological effect results, even qualitatively.

It is important to note that this question is not a purely hypothetical one. While some improvements are still needed to allow for an easy manufacturing of these materials with precisely controlled arrangements of magnetizable inclusions within the elastic matrix, recently developed technology allows to control these arrangements more and more [22–33]. Thus, we can expect them to become increasingly common in the future, see Sec. 1.4. This opens another means to tune magnetic gels and elastomers for their desired applications. By predicting what the effect of these targeted placements is, we determine which types of placements should be investigated experimentally and what the important requirements for these new manufacturing methods are, such that they are useful for potential applications.

Firstly, in **P1**, we present results for irregular randomized arrangements of magnetizable inclusions, representing the type most commonly found in experiments to date. They are placed in a soft, homogeneous and isotropic as well as linearly elastic sphere, which allows us to treat the deformational response analytically, based on earlier work by Walpole [34]. We previously extended it to a free-standing sphere [35], which is further worked out in the present work. Here, vanishing overall forces and torques are required to avoid non-static situations that cause diverging displacements.

Concerning the magnetizable inclusions, we describe them as magnetic dipoles, which is reasonable, provided the inclusions are sufficiently far apart from each other. This is guaranteed in our work because we only consider well-separated

inclusions. From these magnetically induced dipole–dipole forces, we calculate the overall deformation of the initial sphere by calculating the displacement field at 49152 approximately evenly spread positions on the spherical surface. In that evaluation, we iteratively calculate the influence of the deformations on the magnetic interactions and the resulting magnetic forces to find the new equilibrium positions of the magnetizable inclusions. Finally, to analyze the resulting displacement field in more detail, we expand the displacement field into spherical harmonics to quantify the dominant modes of deformation.

From there, we obtain qualitatively the same results as in the experiments for the randomized arrangements [20, 21], namely an elongation along the external field direction. Additionally, we investigate multiple regular lattice-type arrangements of magnetizable inclusions. Different types of responses result, not only as a function of the arrangement, but also depending on the parameters describing the elastic matrix material (specifically the Poisson ratio, see Sec. 1.2) for the same configuration of magnetizable inclusions.

Next, in **P2**, we show that with specific arrangements of magnetizable inclusions, a twist-type or torsional magnetostrictive deformation can result in spherical magnetic gels and elastomers (quantified by a specific mode of deformation). We also discuss which of the proposed arrangements lead to the strongest effect. In detail, we compare globally twisted structures on the one hand to different helical arrangements on the other hand, where many helices are placed next to each other and the central axis of the globally twisted structures or of the helices coincides with the magnetization direction. We vary the radius as well as the pitch of the helices or the degree of initial structural twist for helical and globally twisted arrangements, respectively. Finally, the results are rationalized in terms of a minimal analytical model. Afterward, another group has observed corresponding effects experimentally [36] and a scale-bridging description that allows to calculate macroscopic material parameters as a function of the mesoscopic arrangement has been proposed [37].

Third, we move on to magnetic gels and elastomers that feature a set of magnetizable inclusions showing polydispersity, as is inherent to any experimental system. As the simplest model, we investigate a binary size distribution **P3**. In this publication, we conclude on the one hand that a randomized usage of polydisperse magnetizable inclusions does not majorly influence the resulting magnetostrictive effects. This is quite helpful for experimentalists because it means that a certain degree of polydispersity does not change the observed effects significantly. On the other hand, however, if the polydisperse magnetizable inclusions are placed in a strategic manner in the elastic matrix, even qualitative changes of the magnetostrictive effects can result for positionally identical but size-controlled arrangements of magnetizable inclusions.

Moreover, we investigate additional regular arrangements, similar to **P1**, but now focusing on the higher modes of deformation in **P4**. The main arrangements that

we investigate are chain-like arrangements (with different lateral configurations of the chains), inspired by experimental configurations, as well as three-dimensional spherical or star-shaped arrangements and arrangements that induce twist-type magnetostrictive deformations, similar to those from **P2**. We find that these higher modes of deformation can be seen in some cases as a fingerprint of the underlying arrangement of magnetizable inclusions.

As a final publication that investigates magnetostrictive effects, we managed to derive analytical formulae for the two most basic relevant modes of overall deformation: One of these characterizes overall changes in volume, while the other characterizes elongation along the external magnetic field direction relative to lateral contraction or vice versa (depending on the sign of this mode). A (lengthy) derivation of these analytical formulae is provided in **P6**. With these formulae at hand, we proceed to optimize the arrangements of magnetizable inclusions for the largest magnitudes of these two modes of deformation **P5**. For this purpose and due to the many degrees of freedom, we employ a numerical optimization technique based on *simulated annealing* (SA) [38–41]. In this manner, we manage to find the configurations of magnetizable inclusions that lead to the largest deformations, distinguishing maximized elongation or contraction along the field direction as well as maximized increases or decreases in volume. For applications, large magnetostrictive deformations are usually desirable. Consequently, this represents an important step forward. As in the previous publications, we evaluate the influence of different elastic matrix materials on these effects.

Moreover, **P5** likewise presents results for optimizing the so-called *magnetorheological (MR) effect*. This term refers to another type of response of these materials to applied external magnetic fields, namely, changes in their rheological behavior. Commonly, these materials show hardening upon magnetization [2, 27, 42–46]. Much more rarely, also the opposite behavior of magnetically induced softening is considered, the so-called negative MR effect [47, 48]. In this work, we consider both of them in view of their static elastic moduli. We find optimized structures for maximized amplitude of the positive as well as the negative MR effect, here considering systems of overall cubical shape. We distinguish MR effects under uniaxial elongation conserving the overall volume and simple shear deformations. Additionally, we compare all optimized configurations to regular lattice arrangements, identifying as far as possible those regular arrangements that can lead to similar magnetostrictive or MR effects.

The optimized configurations as well as the resulting magnitude of these effects depend on the number of magnetizable inclusions, as we show here. Our method should apply for other soft elastic systems as well. Immediately, electrorheological elastomers [49–51] or thermally actuated systems [52] come to mind. More generally, whenever one can connect the overall macroscopic response of soft elastic composite materials to some internal degrees of freedom, one can optimize the former for the latter. In this manner, **P5** represents an example how a so-called *inverse problem*

might be solved, which is a current research topic that has received much attention lately [53].

P7 was the result of supporting and working together with a bachelor student of physics, G. J. L. Jäger. Here, we continue to study magnetic gels and elastomers, but now investigate the effect of magnetically induced deformations on the transport properties, particularly thermal conductivity. We use a dipole-spring model to investigate two-dimensional model systems of magnetic gels and elastomers, representing thin films or membranes. The magnetically induced restructuring of these materials is linked to a change in the thermal conductivity. We discuss the influence of several parameters on these changes, such as the strength of magnetization, the particle number, their area fraction, and the aspect ratio of the system.

Finally, we return to spherical, linearly elastic systems, but now consider materials consisting of an elastic core and an elastic shell in the collaborative work **P8**. We calculate how these systems deform in response to a radially applied force line density of constant strength in the equatorial plane. This situation is relevant on various scales and for different example systems, but a motivating example are microgels adsorbed to a fluid-fluid interface, where the surface line tension at the interface provides the force density. We discuss how the deformational behavior depends on the different elastic properties of the core and the shell and their relative sizes.

Having provided an overview of our own works that form the basis of this dissertation, we next briefly review fundamental relations of linear elasticity. They form the quantitative theory that constitutes the backbone of our calculations.

1.2 Elements from linear elasticity theory

The continuum theory of linear elasticity is reviewed briefly in this section to overview the relevant aspects for our work. Other aspects are at least partially omitted, specifically concerning more general nonlinear elastic descriptions. Throughout this section, our presentation mainly follows Ref. 54.

First, we recall that we use a mesoscopic description for the materials, which means that we do not resolve the discrete nature of the constituents of the elastic matrix. Instead, we treat it as a continuous elastic material – a material that can perform *reversible* deformations under applied forces (excluding effects related to plasticity). For simplicity, we further assume the elastic matrix to be fully homogeneous and isotropic. Furthermore, we do not resolve the time-dependence of the deformations. Instead, we calculate which final state is reached when forces are acting inside the elastic matrix, not resolving the time-dependent deformations that happen in the time period from the undeformed to the final deformed state. This would require a viscoelastic description, which is much more involved. For example, Ref. 55 presents a possible approach. Throughout this section, we always assume the elastic materials to be three-dimensional.

The central quantity of linear elasticity theory is the so-called displacement field $\mathbf{u}(\mathbf{r})$, describing how much the material elements are displaced from their initial positions $\mathbf{r}$. In formulae, if we denote the positions in the deformed final state by $\mathbf{r}'(\mathbf{r})$, then we can define

$$\mathbf{u}(\mathbf{r}) := \mathbf{r}'(\mathbf{r}) - \mathbf{r}. \tag{1.1}$$

Obviously, since this is a field description, displacements $\mathbf{u}$ and positions in the deformed state $\mathbf{r}'$ depend on the initial positions $\mathbf{r}$. Furthermore, we assume that $\mathbf{r}'(\mathbf{r})$ is one-to-one, because material elements are neither created nor destroyed during the process of deformation.

1.2.1 Changes in length and the strain tensor

Next, we are interested in how much distances change during the deformation. This is relevant because, for example, the interactions of the magnetizable inclusions depend on their mutual distance. Using Einstein's summation convention (summation over repeated indices, with each index $i, j, \ldots = 1, 2, 3$ indicating the Cartesian components of a vector/tensor), we calculate the difference of the squares of an infinitesimal initial distance $\mathrm{d}r$ between two material elements and the distance

between the same material elements in the deformed state $\mathrm{d}r'$:

$$\begin{aligned}
\mathrm{d}r'^2 - \mathrm{d}r^2 &= \mathrm{d}r'_i \mathrm{d}r'_i - \mathrm{d}r_i \mathrm{d}r_i && (1.2)\\
&= \mathrm{d}\left(r_i + u_i\right) \mathrm{d}\left(r_i + u_i\right) - \mathrm{d}r_i \mathrm{d}r_i && (1.3)\\
&= 2\mathrm{d}u_i \mathrm{d}r_i + \mathrm{d}u_i \mathrm{d}u_i && (1.4)\\
&= \frac{\partial u_i}{\partial r_j} \mathrm{d}r_i \mathrm{d}r_j + \frac{\partial u_j}{\partial r_i} \mathrm{d}r_i \mathrm{d}r_j + \frac{\partial u_i}{\partial r_j} \mathrm{d}r_j \frac{\partial u_i}{\partial r_k} \mathrm{d}r_k && (1.5)\\
&= \mathrm{d}r_i 2\varepsilon_{ij} \mathrm{d}r_j. && (1.6)
\end{aligned}$$

From the first to the second line, we have used Eq. (1.1). In the last line, we have renamed summation indices and introduced the so-called strain tensor (the factor 2 is added by convention), the components of which read:

$$\varepsilon_{ij} = \frac{1}{2}\left[\frac{\partial u_i}{\partial r_j} + \frac{\partial u_j}{\partial r_i} + \frac{\partial u_k}{\partial r_i}\frac{\partial u_k}{\partial r_j}\right]. \tag{1.7}$$

As we can deduce from this line, the strain tensor is dimensionless. In linear elasticity theory, we assume the magnitudes of deformation to be small. Therefore, we linearize Eq. (1.7) as

$$\varepsilon_{ij} \approx \frac{1}{2}\left[\frac{\partial u_i}{\partial r_j} + \frac{\partial u_j}{\partial r_i}\right]. \tag{1.8}$$

Consequently, the strain tensor $\underline{\boldsymbol{\varepsilon}}$ in linear elasticity theory is simply given as the symmetrized gradient of the displacement field.

1.2.2 Changes in volume and incompressibility

In addition to how lengths change in the deformed state, we can also calculate how the change of an infinitesimal volume element (at a position $\mathbf{r}$) can be expressed in the coordinates of the deformed state:

$$\begin{aligned}
\mathrm{d}V' - \mathrm{d}V &= \left(\det \frac{\partial \mathbf{r}'}{\partial \mathbf{r}} - 1\right) \mathrm{d}V && (1.9)\\
&= \left[\det\left(\frac{\partial \mathbf{u}}{\partial \mathbf{r}} + \mathbb{1}\right) - 1\right] \mathrm{d}V. && (1.10)
\end{aligned}$$

Here, we introduced the unit matrix $\mathbb{1}$, the determinant det, and we used the definition of the displacement field $\mathbf{u}(\mathbf{r})$ in the last line. Continuing the calculation,

we obtain

$$\mathrm{d}V' - \mathrm{d}V = \left[\det\begin{pmatrix} 1+\frac{\partial u_1}{\partial r_1} & \frac{\partial u_1}{\partial r_2} & \frac{\partial u_1}{\partial r_3} \\ \frac{\partial u_2}{\partial r_1} & 1+\frac{\partial u_2}{\partial r_2} & \frac{\partial u_2}{\partial r_3} \\ \frac{\partial u_3}{\partial r_1} & \frac{\partial u_3}{\partial r_2} & 1+\frac{\partial u_3}{\partial r_3} \end{pmatrix} - 1\right]\mathrm{d}V \tag{1.11}$$

$$= \left[1 + \frac{\partial u_1}{\partial r_1} + \frac{\partial u_2}{\partial r_2} + \frac{\partial u_3}{\partial r_3} - 1 + \mathcal{O}\left(\left(\frac{\partial u_i}{\partial r_j}\right)^2\right)\right]\mathrm{d}V \tag{1.12}$$

$$= \left[\frac{\partial u_i}{\partial r_i} + \mathcal{O}\left(\left(\frac{\partial u_i}{\partial r_j}\right)^2\right)\right]\mathrm{d}V \tag{1.13}$$

$$\approx \varepsilon_{ii}\mathrm{d}V. \tag{1.14}$$

In linear elasticity theory, we omit quadratic terms in the derivative of the displacement field in these expressions. In this case, the last line shows that the trace (written as Tr in the following) of the strain tensor is related to changes in the volume at a certain position. If we require all volumes to be the same in the undeformed and in the deformed state, we formulate the condition of *incompressibility*. We can write this condition within the framework of linear elasticity theory as

$$\varepsilon_{ii} = \mathrm{Tr}\,\underline{\boldsymbol{\varepsilon}} \stackrel{!}{=} 0. \tag{1.15}$$

This is often a reasonable assumption for rubber-like materials [56] and is commonly assumed for hydrogels [57,58]. Still, it should be verified experimentally, for example using the method proposed in Ref. 58, because it may depend on the situation at hand.

1.2.3 The stress tensor

In (linear) elasticity theory, deformations cost energy. Therefore, restoring forces emerge upon deformation that try to return the elastic body to its initial undeformed shape. These forces are counteracted by the forces applied in the material. Considering a volume element V at position $\mathbf{r}$, two possibilities exist for forces to be applied to this volume element: The forces can either attack the bulk of the material directly as bulk force densities $\mathbf{f}_b(\mathbf{r})$ or act on the surface of a volume element. In the latter case, they are called stresses, the corresponding surface force density is given by $\hat{\mathbf{n}}(\mathbf{r}) \cdot \underline{\boldsymbol{\sigma}}(\mathbf{r})$. Here, we introduced the stress tensor $\underline{\boldsymbol{\sigma}}$ and the surface normal (pointing towards the outside) $\hat{\mathbf{n}}$ at position $\mathbf{r}$.
Therefore, the k-th component of the total force acting on this volume element is

given by the sum of those two terms:

$$\int_V f_{b,k}(\mathbf{r})\mathrm{d}V + \oint_{\partial V} \left[\hat{\mathbf{n}}(\mathbf{r}) \cdot \underline{\boldsymbol{\sigma}}(\mathbf{r})\right]_k \mathrm{d}f \tag{1.16}$$

$$= \int_V f_{b,k}(\mathbf{r})\mathrm{d}V + \oint_{\partial V} \sigma_{lk}(\mathbf{r})\, \mathrm{d}\vec{f}_l(\mathbf{r}) \tag{1.17}$$

$$\overset{\text{Gauss}}{=} \int_V \left[f_{b,k}(\mathbf{r}) + \nabla_l \sigma_{lk}(\mathbf{r})\right] \mathrm{d}V \tag{1.18}$$

$$=: \int_V f_k(\mathbf{r})\mathrm{d}V. \tag{1.19}$$

Here, $\mathrm{d}f$ marks the infinitesimal surface element with $\mathrm{d}\vec{f}(\mathbf{r}) \coloneqq \hat{\mathbf{n}}(\mathbf{r})\,\mathrm{d}f$, "Gauss" refers to Gauss's divergence theorem with the nabla operator $\boldsymbol{\nabla}$, and $\mathbf{f}(\mathbf{r})$ denotes the net force density at position $\mathbf{r}$. Here and in the following, integrals are formulated in the undeformed state over the volume V.
In static equilibrium, no net forces act on any volume V. Therefore, we can set the expression in Eq. (1.19) to zero. Since the volume of integration is arbitrary, we can conclude that the integrand is vanishing identically, i.e. in index notation

$$f_{b,k}(\mathbf{r}) + \nabla_l \sigma_{lk}(\mathbf{r}) = 0 \tag{1.20}$$

or in vector notation

$$\mathbf{f}_b(\mathbf{r}) + \boldsymbol{\nabla} \cdot \underline{\boldsymbol{\sigma}}(\mathbf{r}) = \mathbf{0}. \tag{1.21}$$

As can be seen from this formula, the units of the stress tensor $\underline{\boldsymbol{\sigma}}$ are those of a force density times a length, or in other words, those of a pressure (measured in Pa). In the following, we will connect the stress tensor to the deformations via the energy that is required to induce these deformations. Illustratively, the stress tensor $\sigma_{ij}(\mathbf{r})$ measures the j-th component of the force applied at that surface of the considered volume element with normal vector in i-direction per surface direction.

Before we continue with the elastic energy, we will also consider the total torque density $\mathbf{M}$ acting on a given volume V (again considering the k-th component):

$$\int_V M_k(\mathbf{r})\mathrm{d}V = \int_V \epsilon_{klm}\, f_l(\mathbf{r})\, r_m \mathrm{d}V \tag{1.22}$$

$$= \int_V \epsilon_{klm}\, f_{b,l}(\mathbf{r})\, r_m \mathrm{d}V + \oint_{\partial V} \epsilon_{klm}\, \sigma_{nl}(\mathbf{r})\, r_m \mathrm{d}\vec{f}_n(\mathbf{r}) \tag{1.23}$$

$$\overset{\text{Gauss}}{=} \int_V \epsilon_{klm} \left[f_{b,l}(\mathbf{r})\, r_m + \nabla_n \left(\sigma_{nl}(\mathbf{r})\, r_m\right)\right] \mathrm{d}V \tag{1.24}$$

$$= \int_V \epsilon_{klm} \left[f_{b,l}(\mathbf{r}) + \nabla_n \left(\sigma_{nl}(\mathbf{r})\right)\right] r_m \mathrm{d}V + \int_V \epsilon_{klm}\, \sigma_{ml}(\mathbf{r})\mathrm{d}V. \tag{1.25}$$

Here, we introduced the Levi-Civita symbol ϵ_{klm}. Assuming static equilibrium, i.e. vanishing total torque, and using Eq. (1.20) to eliminate the term in the square bracket in Eq. (1.25), we can conclude due to the integration over an arbitrary volume:

$$\epsilon_{klm}\,\sigma_{ml}(\mathbf{r}) = 0 = \epsilon_{klm}\,\sigma_{lm}(\mathbf{r}) \qquad \forall k \in \{1,2,3\}. \tag{1.26}$$

Thus, we conclude that symmetry of the stress tensor is required to avoid global rotations. Consequently, we can also rewrite Eq. (1.20) as

$$f_{b,k}(\mathbf{r}) + \nabla_l \sigma_{kl}(\mathbf{r}) = 0. \tag{1.27}$$

As a remark, a uniform compressing pressure p that acts on the material from all sides equally can be written as the stress $\underline{\boldsymbol{\sigma}} = -p\,\mathbb{1}$ for $\mathbf{f}_b = \mathbf{0}$.

1.2.4 Relation to the thermodynamic energy

For a purely elastic material, the deformation is assumed to be independent of its deformational history. Instead, we can deduce the deformational state of the elastic body by minimizing an (appropriate) energy, as detailed in the following. This allows us to connect the stress and strain tensors, as defined in Secs. 1.2.1 and 1.2.3, respectively.
We assume that the material is in a deformed state with displacement field $\mathbf{u}(\mathbf{r})$. Then, we change the displacement field by an infinitesimal amount $\delta\mathbf{u}(\mathbf{r})$. The (infinitesimal) work $\delta\mathcal{W}$ needed for this change in a volume V can be calculated by summing up the contributions from the bulk and the surface, as in Eq. (1.16). We use the convention $\delta\mathcal{W} > 0$ for an increasing internal energy density of the system. As in classical mechanics, the work is given as the product of the forces and displacements, which results (in index notation) in

$$\delta\mathcal{W} = \int_V f_{b,i}(\mathbf{r})\delta u_i(\mathbf{r})\mathrm{d}V + \oint_{\partial V} \sigma_{ji}(\mathbf{r})\delta u_i(\mathbf{r})\mathrm{d}\vec{f}_j \tag{1.28}$$

$$\overset{\text{Eq. (1.20)}}{=} \int_V \left[-\nabla_j \sigma_{ji}(\mathbf{r})\right] \delta u_i(\mathbf{r})\mathrm{d}V + \oint_{\partial V} \sigma_{ji}(\mathbf{r})\delta u_i(\mathbf{r})\mathrm{d}\vec{f}_j \tag{1.29}$$

$$= -\int_V \nabla_j \left[\sigma_{ji}(\mathbf{r})\delta u_i(\mathbf{r})\right] \mathrm{d}V + \int_V \sigma_{ji}(\mathbf{r})\nabla_j \delta u_i(\mathbf{r})\mathrm{d}V + \oint_{\partial V} \sigma_{ji}(\mathbf{r})\delta u_i(\mathbf{r})\mathrm{d}\vec{f}_j \tag{1.30}$$

$$\overset{\text{Gauss}}{=} -\oint_{\partial V} \sigma_{ji}(\mathbf{r})\delta u_i(\mathbf{r})\mathrm{d}\vec{f}_j + \int_V \sigma_{ji}(\mathbf{r})\nabla_j \delta u_i(\mathbf{r})\mathrm{d}V + \oint_{\partial V} \sigma_{ji}(\mathbf{r})\delta u_i(\mathbf{r})\mathrm{d}\vec{f}_j. \tag{1.31}$$

Here, obviously the first and the third terms cancel each other. Therefore, only the second term remains, which can be rewritten using the symmetry of the stress

tensor and linearity of the derivative as

$$\delta\mathcal{W} = \frac{1}{2}\int_V \sigma_{ij}(\mathbf{r})\ \delta\nabla_j u_i(\mathbf{r})\mathrm{d}V + \frac{1}{2}\int_V \sigma_{ij}(\mathbf{r})\ \delta\nabla_i u_j(\mathbf{r})\mathrm{d}V \tag{1.32}$$

$$= \int_V \sigma_{ij}(\mathbf{r})\frac{1}{2}\ \delta\left[\nabla_j u_i(\mathbf{r}) + \nabla_i u_j(\mathbf{r})\right]\mathrm{d}V \tag{1.33}$$

$$= \int_V \sigma_{ij}(\mathbf{r})\delta\varepsilon_{ij}(\mathbf{r})\mathrm{d}V. \tag{1.34}$$

As the integration volume V is arbitrary, we can conclude that the integrand is vanishing identically. It follows for the work density by taking the limit of the change in the displacement field $\delta\mathbf{u}(\mathbf{r})$ to zero, then writing d instead of δ:

$$\mathrm{d}W(\mathbf{r}) = \sigma_{ij}(\mathbf{r})\mathrm{d}\varepsilon_{ij}(\mathbf{r}). \tag{1.35}$$

For the systems that we consider, it is usually appropriate to work in the *canonical* thermodynamic ensemble, because the temperature T is usually fixed overall by the room/environmental temperature and no material is added or taken away. Therefore, we consider the free-energy density F of the materials. Its thermodynamic relation to the work density W, chemical potential μ and entropy density S is given as

$$\mathrm{d}F = -S\mathrm{d}T + \mathrm{d}W + \mu\mathrm{d}N \tag{1.36}$$

$$= -S\mathrm{d}T + \sigma_{ij}\mathrm{d}\varepsilon_{ij} + \mu\mathrm{d}N. \tag{1.37}$$

Therefore, we can conclude

$$\sigma_{ij} = \left(\frac{\partial F}{\partial\varepsilon_{ij}}\right)_{T,N}, \tag{1.38}$$

i.e., we can calculate the stress tensor in linear elasticity theory by calculating the derivative of the free energy density with respect to the strain tensor at fixed temperature T and particle number N.

1.2.5 Free-energy density

Next, we present an ansatz for the free-energy density that can then be used to calculate the stress-strain relation via Eq. (1.38). Obviously, the free-energy density is a function of the deformations, which we describe by the strain tensor. In particular, the derivatives of the displacements enter the free-energy density because homogeneous displacements do not cost energy (they correspond to rigid translations of the whole elastic body). First, we set the free energy of the undeformed ground state ($\underline{\boldsymbol{\sigma}} = \underline{\mathbf{0}} = \underline{\boldsymbol{\varepsilon}}$) to zero, fixing the zero of the free energy. Next, linear terms in the strain tensor of the free energy are forbidden because they would lead to

stresses without deformations of the material via Eq. (1.38). Therefore, we focus on the quadratic terms in the strain tensor. Cubic and higher-order terms of the energy in the strain tensor are neglected due to the assumption of small strains in linear elasticity theory. For more general nonlinear descriptions, they can become important – they are incorporated in so-called hyperelastic models, which are beyond the scope of this dissertation.

To get a scalar quantity from quadratic terms of the symmetric strain tensor ε_{ij} (as is required for a scalar energy function), there are only two possibilities that respect the condition of isotropy: The squared trace of the strain tensor and the squared *Frobenius norm*, i.e., the sum of the squares of each element of the strain tensor. Therefore, we can write the most general form of the isotropic free-energy density that only contains quadratic terms in the strain tensor as

$$F = \frac{\lambda}{2}\,\varepsilon_{ii}^2 + \mu\,\varepsilon_{ij}\varepsilon_{ij}. \tag{1.39}$$

Here, we introduced the so-called Lamé parameters λ and μ. The 2 is added by convention. Since the strain tensor is dimensionless [see its definition in Eq. (1.8)], the Lamé parameters are both measured in the units of an energy density of $\mathrm{J\,m^{-3}}$ or equivalently $\mathrm{N\,m^{-2}} = \mathrm{Pa}$. Their exact numerical values always depend on the material that is to be described by our theory.

From Eq. (1.38), we calculate the stress tensor from the free-energy density as

$$\sigma_{ij} = \frac{\lambda}{2}\,2\delta_{il}\delta_{jl}\varepsilon_{kk} + 2\mu\,\varepsilon_{ij} \tag{1.40}$$

$$= \lambda\,\delta_{ij}\varepsilon_{kk} + 2\mu\,\varepsilon_{ij}. \tag{1.41}$$

In this equation, we introduced the Kronecker delta δ_{ij}, which represents the i,j-component of the unit matrix $\mathbb{1}$.

One issue with the form of the free-energy density in Eq. (1.39) is that both components are not independent: The second term is related to the squared Frobenius norm, which is a norm and therefore only nonzero for nonzero strain tensors. Therefore, if it is larger than zero, also the first term is always larger than zero. Consequently, it makes sense to split the strain tensor into a trace-free part, the so-called pure *shear* part, and the remaining pure *compression/dilation* part, related to changes in volume [see Eq. (1.14)]:

$$\varepsilon_{ij} = \underbrace{\varepsilon_{ij} - \frac{1}{3}\delta_{ij}\varepsilon_{kk}}_{\text{trace-free}} + \frac{1}{3}\delta_{ij}\varepsilon_{kk}. \tag{1.42}$$

Next, we split Eq. (1.39) in the same manner:

$$F = \frac{\lambda}{2}\varepsilon_{kk}^2 + \mu\left[\left(\varepsilon_{ij} - \frac{1}{3}\delta_{ij}\varepsilon_{kk}\right) + \frac{1}{3}\delta_{ij}\varepsilon_{kk}\right]^2 \tag{1.43}$$

$$= \frac{\lambda}{2}\varepsilon_{kk}^2 + \mu\left(\varepsilon_{ij} - \frac{1}{3}\delta_{ij}\varepsilon_{kk}\right)^2 + \frac{2\mu}{3}\delta_{ij}\varepsilon_{kk}\left(\varepsilon_{ij} - \frac{1}{3}\delta_{ij}\varepsilon_{ll}\right) + \frac{\mu}{9}\varepsilon_{kk}^2\underbrace{\delta_{ij}\delta_{ij}}_{\delta_{ii}=3} \tag{1.44}$$

$$= \mu\left(\varepsilon_{ij} - \frac{1}{3}\delta_{ij}\varepsilon_{kk}\right)^2 + \frac{1}{2}\varepsilon_{kk}^2\left(\lambda + \frac{4\mu}{3} - \frac{4\mu}{9}3 + \frac{2\mu}{9}3\right) \tag{1.45}$$

$$= \mu\left(\varepsilon_{ij} - \frac{1}{3}\delta_{ij}\varepsilon_{kk}\right)^2 + \frac{1}{2}\varepsilon_{kk}^2\underbrace{\left(\lambda + \frac{2\mu}{3}\right)}_{=:K} \tag{1.46}$$

$$= \mu\left(\varepsilon_{ij} - \frac{1}{3}\delta_{ij}\varepsilon_{kk}\right)^2 + \frac{K}{2}\varepsilon_{kk}^2. \tag{1.47}$$

The parameters μ and K are called shear and bulk modulus, respectively. (The naming is consistent: μ is related to the pure shear part of the strain tensor.)
We can vary the two parts of the strain tensor in Eq. (1.42), related to the two contributions to the energy density, independently. Thus, to guarantee thermodynamic stability of the system, i.e., for the undeformed state to be the global minimum of F, we equivalently require positivity of the two moduli,

$$\mu > 0, \quad K > 0. \tag{1.48}$$

Another possible choice to express the two parameters in the free-energy density is to use only the shear modulus as a dimensional quantity and another dimensionless parameter, the so-called Poisson ratio ν, which is defined as

$$\nu := \frac{1}{2}\frac{3K - 2\mu}{3K + \mu} \tag{1.49}$$

or equivalently when using the two Lamé parameters as

$$\nu := \frac{1}{2}\frac{\lambda}{\lambda + \mu}. \tag{1.50}$$

From Eq. (1.49), we deduce that the Poisson ratio is bounded by -1 from below (for $K \to 0$ or $\mu \to \infty$) and by $1/2$ from above (for $\mu \to 0$ or $K \to \infty$). The latter is called the limit of incompressibility: As Eq. (1.47) shows, $K \to \infty$ implies that non-zero values of the trace cost an infinite amount of energy, which therefore implies that Eq. (1.15) must be fulfilled for a finite energy. Moreover, materials with a negative Poisson ratio, i.e. $\nu < 0$, are called auxetic [59–64]. They have the unusual property that uniaxial elongation of these materials leads to a perpendicular

elongation (instead of the contraction for "normal" materials, i.e., those with a positive Poisson ratio).

In the following, we always describe linearly elastic materials by the shear modulus and Poisson ratio. This combination of parameters leads to the free-energy density [from Eq. (1.39)]:

$$\lambda = \frac{2\mu\nu}{1-2\nu} \tag{1.51}$$

$$\Rightarrow F = \frac{\mu\nu}{1-2\nu}\,\varepsilon_{ii}^2 + \mu\,\varepsilon_{ij}\varepsilon_{ij}. \tag{1.52}$$

Inserting these parameters into Eq. (1.41) leads to

$$\sigma_{ij} = \frac{2\mu\nu}{1-2\nu}\delta_{ij}\varepsilon_{kk} + 2\mu\,\varepsilon_{ij} \tag{1.53}$$

$$= \frac{2\mu\nu}{1-2\nu}\delta_{ij}\boldsymbol{\nabla}\cdot\mathbf{u} + \mu\left(\nabla_j u_i + \nabla_i u_j\right). \tag{1.54}$$

In the last equation, we have used the definition of the strain tensor from Eq. (1.8).

1.2.6 Navier–Cauchy equations

The final step is to insert Eq. (1.54) into the equilibrium condition Eq. (1.27):

$$0 = f_{b,i}(\mathbf{r}) + \nabla_j\left[\frac{2\mu\nu}{1-2\nu}\delta_{ij}\boldsymbol{\nabla}\cdot\mathbf{u}(\mathbf{r}) + \mu\left(\nabla_j u_i(\mathbf{r}) + \nabla_i u_j(\mathbf{r})\right)\right] \tag{1.55}$$

$$= f_{b,i}(\mathbf{r}) + \frac{2\mu\nu}{1-2\nu}\nabla_i\boldsymbol{\nabla}\cdot\mathbf{u}(\mathbf{r}) + \mu\nabla_j\nabla_j u_i(\mathbf{r}) + \mu\nabla_i\nabla_j u_j(\mathbf{r}) \tag{1.56}$$

$$= f_{b,i}(\mathbf{r}) + \mu\left(\frac{2\nu}{1-2\nu}+1\right)\nabla_i\boldsymbol{\nabla}\cdot\mathbf{u}(\mathbf{r}) + \mu\Delta u_i(\mathbf{r}) \tag{1.57}$$

In the last line, we have introduced the *Laplace operator* $\Delta \coloneqq \boldsymbol{\nabla}\cdot\boldsymbol{\nabla}$. Finally, combining the terms in the bracket, reordering terms, and switching to vector notation leads to

$$\boxed{\mu\Delta\mathbf{u}(\mathbf{r}) + \frac{\mu}{1-2\nu}\boldsymbol{\nabla}\boldsymbol{\nabla}\cdot\mathbf{u}(\mathbf{r}) + \mathbf{f}_b(\mathbf{r}) = \mathbf{0}}. \tag{1.58}$$

These are the so-called Navier–Cauchy equations [65] that are the central equations of linear elasticity theory. Mathematically, they represent second-order partial differential equations for the displacement field for a given bulk force density.

For an infinitely extended linearly elastic medium, the solution for an arbitrary force density is straightforward. It can be calculated using the Green's function approach. Along these lines, we search for the solution of the Navier–Cauchy

equations with a delta-distributed force distribution $\mathbf{f}_b(\mathbf{r}) = \mathbf{F}\delta(\mathbf{r} - \bar{\mathbf{r}})$, where $\delta(\mathbf{r})$ is the Dirac delta distribution, $\bar{\mathbf{r}}$ marks the position where the force is concentrated, and $\mathbf{F}$ denotes the force that acts there. Since the Navier–Cauchy equations are linear in the forces and displacements, we write the solution in the form of a Matrix-vector product:

$$\mathbf{u}(\mathbf{r}) = \underline{\mathbf{G}}(\mathbf{r}, \bar{\mathbf{r}}) \cdot \mathbf{F}, \tag{1.59}$$

where $\underline{\mathbf{G}}(\mathbf{r}, \bar{\mathbf{r}})$ is the so-called Kelvin tensor, the searched-for Green's function for the Navier–Cauchy equations, which assumes vanishing displacements at infinity. Its name derives from Lord Kelvin, who presented the solution in Ref. 66. A derivation is given for example in Ref. 67, Appendix A. The components of the Kelvin tensor read

$$G_{ij}(\mathbf{r}, \bar{\mathbf{r}}) = G_{ij}(\mathbf{r} - \bar{\mathbf{r}}) = \frac{1}{16\pi\mu(1-\nu)} \left(\frac{(3-4\nu)\delta_{ij}}{|\mathbf{r} - \bar{\mathbf{r}}|} + \frac{(r_i - \bar{r}_i)(r_j - \bar{r}_j)}{|\mathbf{r} - \bar{\mathbf{r}}|^3} \right). \tag{1.60}$$

The first equality follows from the homogeneity of the material. Returning to general bulk force densities, the resulting displacement field is calculated by a convolution (via the superposition principle):

$$\mathbf{u}(\mathbf{r}) = \int_V \underline{\mathbf{G}}(\mathbf{r} - \bar{\mathbf{r}}) \cdot \mathbf{f}_b(\bar{\mathbf{r}}) \mathrm{d}^3\bar{r}. \tag{1.61}$$

As a final remark, we add that, for perfectly incompressible materials, i.e. for $\nu = 1/2$, the Kelvin tensor formally coincides with the Oseen tensor of low-Reynolds-number hydrodynamics [68], replacing the displacement field $\mathbf{u}(\mathbf{r})$ and the shear modulus μ by the velocity field $\mathbf{v}(\mathbf{r})$ and the hydrodynamic (shear) viscosity, respectively.

Furthermore, for rather incompressible materials of $\nu = 1/2$, a scale–separation occurs in the Navier–Cauchy equations. As a consequence, Eq. (1.58) is split into the following set of two equations for incompressible materials:

$$\boldsymbol{\nabla} \cdot \mathbf{u}(\mathbf{r}) = 0, \tag{1.62}$$

$$\mu \Delta \mathbf{u}(\mathbf{r}) + \mathbf{f}_b(\mathbf{r}) = \mathbf{0}. \tag{1.63}$$

1.2.7 Summary of this section

To summarize, the methods in Sec. 1.2 are used throughout to describe the deformations of linearly elastic materials. More precisely, we assume that the elastic matrix materials are fully homogeneous and isotropic, which means that their elastic properties can be described by two parameters: their shear modulus μ and the nondimensional Poisson ratio ν. Particularly the latter value is extensively discussed in **P1**–**P6** and **P8**. To calculate the deformations, we use the Navier–Cauchy equations as formulated in Eq. (1.58).

These equations can be solved by a Green's function method, with the Green's function given by the Kelvin tensor in Eq. (1.60) for bulk systems. However, real experiments complicate matters in a few different ways: The deformations are not infinitesimally small and real samples are never infinitely extended. For the former issue, we note that linear elasticity is still often a very good approximation, even for finite deformations, as comparisons with nonlinear finite-element simulations show [69]. To address the second issue of finite extension, we explicitly included the boundaries of the systems into our investigations: Walpole [34] has developed a Green's function for a linearly elastic sphere embedded in an infinitely extended elastic background medium. We have adapted this Green's function to the case of a free-standing elastic sphere [35, 70]. This function is used to study magnetostrictive effects in **P1**–**P5**. Earlier work considered the interactions of magnetizable inclusions in linearly elastic media in the presence of a rigid wall, for which a corresponding Green's function is also available [71].
Moreover, in **P8**, we also study the deformational behavior of a finite-sized sphere, but here, the sphere is composed of a core and a shell. Additionally, forces are applied from the outer surface as a force line density at the equator, acting radially outward or inward. For this case, we calculate the displacement field analytically, based on linear elasticity, see **P8**.

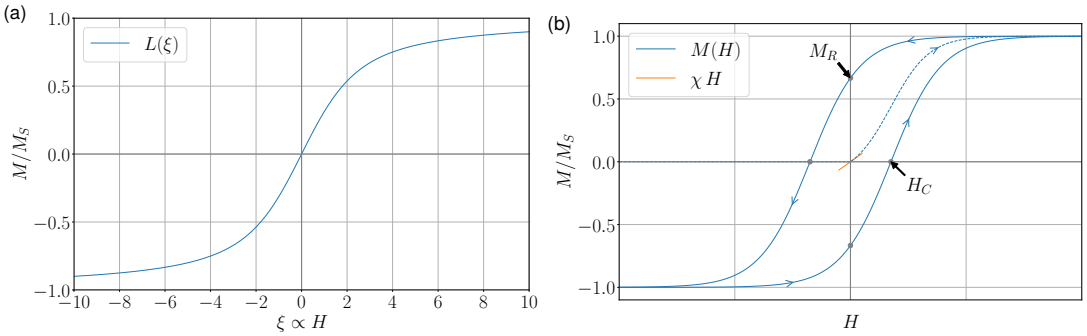

Figure 1.1: (a) Magnetization M, divided by its saturation value M_S, for paramagnetic materials as a function of the applied magnetic field H. We here plot the so-called *Langevin function*, which is a common model for the magnetization behavior, see Sec. 1.3.2. Its argument is the nondimensional parameter ξ which is proportional to H. (b) Qualitative sketch of a hysteresis curve of $M(H)$ for ferro- or ferrimagnetic materials in blue. The initial magnetization behavior, drawn as the dashed line, can be approximated for small values of H by the linear function χH, indicated as the orange line. The order of the hysteresis loop is illustrated by small arrows. Furthermore, we mark characteristic points on the curve with gray dots with corresponding labels, namely the remanence magnetization M_r and the coercivity field magnitude H_C.

1.3 Magnetic or magnetizable inclusions

1.3.1 Overview and phenomenology from experiments

In order to control the properties of the soft elastic materials by external magnetic fields, they require magnetic or magnetizable inclusions. These inclusions are discussed in this section for the situation of magnetic gels and elastomers. They are of particulate character, therefore often also called magnetic or magnetizable particles. However, we mainly refer to them as inclusions throughout, to stress the fact that they are included in the elastic matrix material. In this section, we give an overview of the commonly used inclusions from an application point of view, not discussing the quantum mechanical origin of magnetic phenomena.

Generally, two typical magnetization curves are shown in Fig. 1.1. It describes the magnetization $\mathbf{M}$ of a given material in response to an external magnetic field $\mathbf{H}$. In the absence of any other preferred directions, these two vectors have to point to the same or opposite directions. Therefore they are only depicted in a one-dimensional plot. In general, these curves contain the precise information needed to calculate the magnetization behavior of a material, at least if they

cover the full range of the external field magnitude of interest. The resulting total magnetic field **B** (magnetic flux density field) is then given as the sum of these values, multiplied by the vacuum permeability μ_0.

In practice, one often simplifies these curves by discussing specific characteristic properties of the curve. Firstly, the response to an initial magnetization in the still linear regime is characterized by the magnetic susceptibility χ, which is given by the initial slope of the magnetization curve, see Fig. 1.1(b). The susceptibility allows to distinguish two types of materials:

- diamagnetic materials for $\chi < 0$,
- paramagnetic materials for $\chi > 0$ [see Fig. 1.1(a)].

In this context, it should be noted that the elastic or liquid matrix material is often diamagnetic [72]. However, its magnetization is usually comparatively small and not sufficient for the desired significant changes in response to external magnetic fields. Therefore, magnetic or magnetizable inclusions dominate the magnetic behavior in view of their much more pronounced responses to external magnetic fields. Consequently, the magnetic properties of the matrix materials can typically be safely neglected in the characterization of magnetic hybrid materials.

Continuing the discussion of the magnetization curve, the next important aspect is the saturation magnetization, commonly denoted as M_S. It describes the magnitude of the magnetization for very strong (in theory: infinitely strong) external magnetic fields of magnitude H, in a formula:

$$\lim_{H\to\infty} M(H) =: M_S. \tag{1.64}$$

We use the value of M_S to rescale the magnetization in Figs. 1.1(a) and (b). Some magnetic materials also show hysteretic behavior: When the magnetic field is reduced from an elevated magnitude, the magnetization does not (necessarily) return along the same curve. Instead, at least for so-called ferromagnetic and ferrimagnetic materials, for which the magnetization generally aligns with applied external fields, the magnetization is higher than the value when initially magnetizing the materials. Even at zero external field, the so-called remanence magnetization M_r remains, see Fig. 1.1(b). The external magnetic field must then be reoriented into the opposite direction to remove the effect of the previous saturation magnetization. In Fig. 1.1(b), we also display the so-called coercivity field magnitude H_C, the value at which the magnetization M reaches zero again.

In contrast to ferromagnetic and ferrimagnetic materials, a paramagnetic material does not show hysteresis, see Fig. 1.1(a). Similarly, many ferromagnetic and ferrimagnetic materials show a hysteresis loop with relatively small width, allowing to neglect their hysteretic behavior. These materials are denoted as magnetically soft materials. In contrast to that, ferromagnetic and ferrimagnetic materials with significant hysteresis are denoted as magnetically hard.

Returning to the nature of the magnetizable or magnetic inclusions (magnetically soft or hard), the most important factor is thus obviously the material that they consist of. However, other features are important as well, for example their size, shape [73], and temperature [74].

One important aspect of the size-dependent properties is the fact that below a threshold size of typically 100 nm [73, 75], ferro- or ferrimagnetic particles become *single-domain*, i.e. they can be viewed as featuring only one magnetic moment that can be reoriented by an external magnetic field. However, there is often a so-called magnetic *easy axis*, depending on the shape or crystalline structure, anchoring the direction of magnetization [75]. Changing the direction of magnetization is therefore unfavorable energetically. Consequently, these materials are also denoted as *magnetically blocked*. Still, this threshold size depends strongly on the material and can range from 20–800 nm [75].

When changing the magnetization direction, in principle two mechanisms are possible. One is the so-called *Brownian mechanism*, which means that the particle as a whole rotates. Another possibility is the *Néel mechanism*, which indicates internal rotation of the magnetic moment against the "easy axis" [4, 76]. Which of those two dominates depends on the particle size: The smaller the particle, the more important is the latter mechanism [76].

For even smaller particles of about 10–15 nm, their magnetic behavior is changed further. In that case, the Néel mechanism dominates and the magnetic moment can easily rotate internally. These particles can change their magnetization direction quickly, as the thermal energy is now sufficient to rotate it against an easy axis. Therefore, the time average over typical measurement times of their magnetization amounts to zero in the absence of an external magnetic field, as in bulk paramagnetic materials. Still, a collection of many of such particles usually maintains stronger saturation magnetization compared to bulk paramagnetic materials [77]. Consequently, a collection of these particles, termed *superparamagnetic*, is often used in applications if reversible changes in properties combined with a strong response to applied external magnetic fields is desirable, such as in magnetic hybrid materials. Still, if the particles become even smaller, surface effects dominate and their magnetic behavior can change again [75].

1.3.2 Theoretical description

To describe the role of the magnetic or magnetizable inclusions theoretically, the simplest option is to consider their magnetic effect in terms of point-like magnetic dipoles – the first term of a multipole expansion (the zero-order term vanishes because there are no magnetic monopoles [78]): Each inclusion i features an associated dipole moment $\mathbf{m}_i$ at position $\mathbf{r}_i$, the center position of the inclusion. This is a simple but common approach, see Sec. 1.4.4. Furthermore, if the magnetization is caused by a sufficiently strong external magnetic field, mutual magnetization effects can be neglected. The external field magnetizes the inclusions to saturation, and all magnetic dipole moments are oriented in the same direction: $\hat{\mathbf{m}}_i = \hat{\mathbf{m}}\ \forall i = 1, \ldots, N$. Here, we defined the orientation of the magnetic moment $\hat{\mathbf{m}}_i \coloneqq \mathbf{m}_i/m_i$ with the magnitude of the dipole moment $m_i \coloneqq \|\mathbf{m}_i\|$. For this description, we recapitulate some known equations from classical electrodynamics [78].
The magnetic field generated by a magnetic dipole $\mathbf{m}$, located at the origin, reads [78, Eq. (5.56)]:

$$\mathbf{B}(\mathbf{r}) = \frac{\mu_0}{4\pi\, r^3}\left[3\hat{\mathbf{r}}\,(\mathbf{m}\cdot\hat{\mathbf{r}}) - \mathbf{m}\right] \tag{1.65}$$

where $\hat{\mathbf{r}} \coloneqq \mathbf{r}/r$ and $r \coloneqq \|\mathbf{r}\|$. μ_0 denotes the vacuum permeability. If we now return to the set of N magnetic dipoles $\mathbf{m}_i$ at positions $\mathbf{r}_i$, $i = 1, \ldots, N$, which are all oriented in the $\hat{\mathbf{m}}$-direction, we calculate the resulting potential energy [78, Eq. (5.72)] using the superposition principle as

$$U = -\sum_{\substack{i,j=1\\ i<j}}^{N} \mathbf{m}_i \cdot \mathbf{B}_j(\mathbf{r}_{ij}) \tag{1.66}$$

$$\overset{\text{Eq. (1.65)}}{=} -\frac{\mu_0}{4\pi}\sum_{\substack{i,j=1\\ i<j}}^{N} \frac{m_i\, m_j}{r_{ij}^3}\left[3\left(\hat{\mathbf{m}}\cdot\hat{\mathbf{r}}_{ij}\right)^2 - 1\right]. \tag{1.67}$$

Here, we introduced the magnetic field generated by dipole j as $\mathbf{B}_j$, the distance vector between two dipoles $\mathbf{r}_{ij} \coloneqq \mathbf{r}_i - \mathbf{r}_j$, $\hat{\mathbf{r}}_{ij} \coloneqq \mathbf{r}_{ij}/r_{ij}$, and $r_{ij} = \|\mathbf{r}_{ij}\|$.
Finally, we calculate the force acting on dipole i as

$$\mathbf{F}_i = -\nabla_{\mathbf{r}_i} U \tag{1.68}$$

$$= \frac{\mu_0}{4\pi}\sum_{\substack{j=1\\ j\neq i}}^{N} \nabla_{\mathbf{r}_{ij}}\left(\frac{m_i\, m_j}{r_{ij}^3}\left[3\left(\hat{\mathbf{m}}\cdot\hat{\mathbf{r}}_{ij}\right)^2 - 1\right]\right) \tag{1.69}$$

$$= -\frac{3\mu_0}{4\pi}\sum_{\substack{j=1\\ j\neq i}}^{N} \frac{m_i\, m_j}{r_{ij}^4}\left[5\hat{\mathbf{r}}_{ij}\left(\hat{\mathbf{m}}\cdot\hat{\mathbf{r}}_{ij}\right)^2 - \hat{\mathbf{r}}_{ij} - 2\hat{\mathbf{m}}\left(\hat{\mathbf{m}}\cdot\hat{\mathbf{r}}_{ij}\right)\right]. \tag{1.70}$$

It should be noted that one generally needs to add the external magnetic field to the one generated by the other inclusions in Eq. (1.66). However, if we assume homogeneous external fields (as in the case of magnetostrictive deformations), the gradient of the external field vanishes and it therefore does not enter the resulting forces.

As a side note, calculating the dipolar interactions directly as in Eq. (1.70) requires an order of N^2 evaluations for a number N of magnetizable inclusions. This scaling can be reduced to $N \log N$ by a recently introduced method based on a fast Fourier transform [79], but this reduction only becomes more efficient for $N \gtrsim 10000$ [79], which is beyond the number of magnetizable inclusions used in our evaluations. We typically use values for N of the order 1000.

As we deduce from Eq. (1.70), the magnetic dipole–dipole interactions are quite sensitive to the distance of each pair of dipoles and the relative orientation of their distance vectors to the magnetic field direction. More in detail, we can investigate the character of the interaction by projecting the dipole–dipole interaction force of dipole i and j onto the orientation of their distance vector $\hat{\mathbf{r}}_{ij}$ (ignoring the effects of other dipoles $k \neq i, j$ here):

$$\mathbf{F}_i \cdot \hat{\mathbf{r}}_{ij} = -\frac{3\mu_0}{4\pi} \frac{m_i\, m_j}{r_{ij}^4} \left[5\,(\hat{\mathbf{m}} \cdot \hat{\mathbf{r}}_{ij})^2 - 1 - 2\,(\hat{\mathbf{m}} \cdot \hat{\mathbf{r}}_{ij})^2\right] \tag{1.71}$$

$$= -\frac{3\mu_0}{4\pi} \frac{m_i\, m_j}{r_{ij}^4} \left[3\cos^2\theta - 1\right], \tag{1.72}$$

where θ marks the angle between the distance vector of the positions and the magnetization direction, i.e. $\cos\theta \coloneqq \hat{\mathbf{m}} \cdot \hat{\mathbf{r}}_{ij}$. Therefore, we distinguish angles $\theta < \theta_m$ where the interaction is attractive, characterized by a negative sign of the force projected onto the distance vector, i.e., a positive term in the square brackets. Repulsion occurs for $\theta > \theta_m$. θ_m is the so-called magic angle [80], the angle for which the interaction flips from attractive to repulsive:

$$\theta_m \coloneqq \arccos\left(\sqrt{\frac{1}{3}}\right) \approx 54.74^\circ. \tag{1.73}$$

As a side remark, the term in the square bracket in Eq. (1.72) is identical to twice the second Legendre polynomial $P_2(\cos\theta)$ [81].

In many cases, we further simplify Eq. (1.70) by assuming that all magnetizable inclusions are identical, setting $m_i = m$, see **P1**, **P2**, **P4**, **P5**, and **P7**. Still, we also discuss explicitly what happens when this is not the case: We instead assumed a binary size distribution of the magnetizable inclusions, therefore distinguishing two possible values of m_i for each inclusion i in **P3**, see chapter 2 for details.

In the dipole approximation under saturating external magnetic fields and for identical magnetizable inclusions, only one parameter remains that needs

to be adjusted based on the experimental system that we model, namely, the magnitude of the magnetic dipole moment m_i or m. To find realistic values for it, we compare to values of corresponding possible experimental realizations. We assume that the magnetizable inclusions only consist of one material, for example pure magnetite (Fe_3O_4), which is a ferrimagnetic, magnetically soft material. For it, we find values for the volume saturation magnetization of approximately $100\,\mathrm{J\,T^{-1}\,kg^{-1}}$ [82], corresponding via a density of approximately $5.18\,\mathrm{g\,cm^{-3}}$ [82] to $M_S \approx 518\,\mathrm{kJ\,T^{-1}\,m^{-3}} (= 518\,\mathrm{kA\,m^{-1}})$. The magnetic moment of a magnetizable inclusion in a saturating external magnetic field can be calculated simply as the product of its volume with the volume saturation magnetization.

Interestingly, magnetite is even found naturally in the human brain [83]. A more detailed account of magnetite nanoparticles, including their experimental synthesis as well as biological and other applications, is given in Ref. 73.

Restricting ourselves to reversibly magnetizable inclusions implies that all evaluated effects are completely reversible. Still, magnetically hard materials might open new avenues for applications, see Sec. 1.4.2. They represent a possible extension of our work in the future.

In general, a dipole approximation of the magnetizable inclusions might not always suffice, especially for smaller distances between two inclusions. In that case, one option is to also include higher-order moments of magnetization [84]. Another issue that is discussed in the literature is mutual magnetization of the magnetizable inclusions, in cases where the external magnetic field is not strong enough for saturation [69]. In Ref. 69, two examples are presented of taking into account effects of mutual magnetization between the inclusions. A simpler approach still restricts itself to magnetic dipole moments, but calculates the dipole moments in an iterative loop to account for the mutual magnetization effects. A more involved approach uses finite-element simulations to resolve the inhomogeneous magnetization profiles within each inclusion. The dipole approximation is reasonable for many purposes, if the distance between the inclusions is at least $1.5d$, where d is the diameter of the inclusions [84–86].

For the full magnetization curve, a common model for paramagnetic materials (and approximately also for magnetically soft materials) is given by the Langevin function [75, 87–89], which we plot in Fig. 1.1(a):

$$L(\xi) = M_S \left(\coth \xi - 1/\xi\right), \tag{1.74}$$

$$\text{with } \xi = \frac{\mu_0 m H}{k_B T}. \tag{1.75}$$

Here, we introduced the the magnetic moment of a monodomain ferromagnetic particle m, the Boltzmann constant k_B, and temperature T. For example, it was proven to be a very good fit for Nickel particles with a diameter of $280\,\mu\mathrm{m}$ [90, 91]. For magnetically hard materials, different models are used to model the magnetization behavior [92–94].

1.4 Magnetic hybrid materials

The class of magnetic hybrid materials consists of magnetic or magnetizable particles inside a matrix material [3]. Usually, two prominent types of materials are distinguished: Those with a liquid and those with a solid, elastic matrix. Naturally, there can also be intermediate materials with a viscoelastic matrix. More exotic types of matrices exist, such as foams or plastomers, see Refs. [95, 96] and the references therein. The more exotic ones are not discussed here. Historically, those with a liquid carrier matrix were addressed first, so we will start by discussing them.

1.4.1 Magnetorheological fluids and ferrofluids

In 1948, Rabinov patented what is now known as a *magnetorheological fluid* (MRF): Micron-sized magnetic particles ("finely divided iron", i.e. carbonyl iron) in an appropriate carrier fluid, here light machine oil [97]. In this paper, not only is the material presented, but the author already points towards applications in clutches that can be controlled magnetically. The trend of emphasis on applications continues in the magnetic hybrid materials community until today. In turn, this causes the community to be very broad, with theoretical research (as in this dissertation) often going hand in hand with experimental research and engineering or even further outreaching (e.g. biological or medical) applications.

Interestingly, these MRFs show quite strong responses to applied external magnetic fields in their rheology, hence their name. Because of the liquid matrix, it is quite easy for the magnetic particles to rearrange under the presence of magnetic fields, mainly forming chain-like aggregates along the field direction. While these materials can be regarded as conventional suspensions in the absence of the fields, the chain-formation means that they are almost solid-like under applications of magnetic fields [98], at least in the so-called *pre-yield regime*. This is in contrast to the so-called *post-yield regime*: These chains can break under the application of sufficiently strong static or dynamic shear stresses (the critical value is the *yield stress*), particularly when induced by hydrodynamic shear flows. It is often the goal to generate materials of a yield stress as high as possible, maximizing the magnetorheological (MR) effect [98].

MRFs have found successful commercial applications in the meantime, see Ref. 98, Sec. 2.7, and references therein. In particular, they are used in damping applications, brakes, sound propagation, and thermal transport applications.

Still, many challenges or problems have been identified over the years [98, 99]. Besides questions of chemical stability and durability, the main one is the sedimentation problem: Because of the much higher density of the magnetic particles compared to the carrier fluid, the particles will sediment to the bottom of a container over time. After a few hours, almost all of the particles will sediment [99].

The development of *ferrofluids* is one approach to reduce the impact of this problem. These materials are quite similar to magnetorheological fluids, but instead they use nanometer-sized magnetic particles (typically about 10 nm in size [100]). Commonly, magnetite or maghemite are used [77, 101]. While the density mismatch is obviously still unchanged, the smaller size reduces the sedimentation as Brownian motion becomes more important [102]. These smaller magnetic particles are usually superparamagnetic collectively [77] (see also Sec. 1.3). Still, the magnetically induced solid-like properties of MRFs cannot be found in ferrofluids. They remain fluid also under application of external magnetic fields, but with a huge increase in viscosity [100]. One interesting aspect of ferrofluids is that they show a surface instability, featuring a spike formation when magnetized. This is the so-called *Rosensweig instability* [103].

Historically, ferrofluids were developed by NASA in 1963 to develop a rocket fuel that can be pumped and controlled even under zero-gravity conditions [104]. Nowadays, they can be found more commonly in a share of commercial applications, such as sealing (e.g. in mass spectrometers, clean room robots, and in spinning hard disk drives in computers), damping (e.g. for stepper motors), heat transfer, bearing and sensing/detection [77, 101]. Additionally, many loudspeakers contain ferrofluids, combining their damping and heat transfer properties, see Refs. 77, 101 and references therein.

Still, any liquid such as MRF or ferrofluid faces issues such as the need for a container/storage device and potential leakage [95]. Therefore, it is helpful for some applications to use a soft solid matrix instead, which is the topic of the next section.

1.4.2 Magnetic gels and elastomers

The goal for these materials is to combine the field-dependent properties of MRFs or ferrofluids with the benefits of a soft, polymeric matrix material. Depending on the employed matrix material as well as the magnetizable inclusions, different names are used in the literature, such as magnetic gels, magnetic elastomers, magnetorheological elastomers, magnetosensitive elastomers, or ferrogels. In the following, we will denote them as magnetic gels and elastomers.

Concerning the matrix material, on the one hand, the term "gels" usually refers to soft polymeric matrices that are swollen by a solvent such as water (in that case, the gels are called hydrogels) [3, 4, 20, 87, 105, 106]. On the other hand, the term "elastomers" refers to polymers not explicitly swollen by a solvent, similar to natural rubbers [3, 4, 10, 17, 105, 107, 108].

Another distinction is provided by the employed magnetic or magnetizable particles: These can be nanometer-sized ones as in ferrofluids, therefore the similar name "ferrogels" was chosen. It is also possible to use larger, typically micrometer-sized inclusions, which can be either magnetically hard or soft [2]. In **P1**–**P5**, **P7**, we always assume superparamagnetic or magnetically soft inclusions, which naturally cause reversible magnetic effects by externally applied magnetic fields. In contrast, when permanent changes should be induced that persist upon removal of the external magnetic fields, magnetically hard inclusions should be used instead [44, 109–112]. In recent years, there is even interest in combining magnetically hard and soft inclusions in a single sample [113–115]. An interesting recent variation is given by magnetically hard inclusions with a very low Curie temperature (the temperature above which the material looses its permanent magnetization), such that laser radiation is sufficient to remove the magnetization of these materials. This allows for targeted reprogramming of the magnetization and thereby the overall material behavior for different purposes [116].

According to a recent review [95], the most common matrix material is silicone rubber (such as PDMS) in 56% of the investigated cases. For the magnetic particles, the most common choice is a carbonyl iron powder (CIP, 88% of the studies), representing a magnetically soft particle. For magnetically hard particles, the most common choice is NdFeB. Besides the elastic matrix and the magnetic particles, many studies also use additives, such as plasticizers that increase the softness of the matrix. Typically, all three ingredients are mixed in the liquid state and then cured/vulcanized in a mold. Two cases should be distinguished here: On the one hand, these are materials cured without applied external magnetic fields, commonly denoted as possessing an isotropic or random microstructure (arrangement of magnetizable inclusions) [2, 6, 17, 117, 118]. On the other hand, materials cured in the presence of external magnetic fields are denoted anisotropic, usually exhibiting chain-like aggregates along the field direction [6, 107, 117, 119, 120]. Still, the precise amount and length of the chains depends on the strength of the

applied field and particle concentration [121].

Moreover, other means are available for a more targeted placement of the magnetizable inclusions, which is a main topic of our research. As experimental techniques that could be utilized for this purpose, we are thinking mainly of 3D printing [22–24, 24–27]. Other options are structuring by magnetic fields [28], sequential photopolymerization [29], acoustic holography [30], layerwise polymerization combined with particle placement by molds or by hand [31, 32], and wax-cast molding [33].

After the fabrication of magnetic gels and elastomers with a controlled arrangement of magnetizable inclusions, it is possible to analyze the arrangement of magnetizable inclusions after the fabrication has been completed. An important technique for this purpose is given by X-ray microtomography [119, 122–126].

Another way is to tie the inclusions into the elastic matrix in a more literal way: In so-called *particle-crosslinked gels* [106, 127–131], the particles themselves, after appropriate surface functionalization, act as the crosslinkers of the elastic polymer network. Besides the obvious coupling of the displacement of the inclusions to the deformations of the gels, these particle-crosslinked gels also affect the rotation of the inclusions. When the inclusions rotate, for example due to changes in the magnetization (see Sec. 1.3), they transmit the magnetic torques to the polymeric network, which leads to elastic deformation and therefore energetic costs. This effect is not present in the usual magnetic gels and elastomers without particle crosslinking, if the polymeric network is not sufficiently adsorbed to the surfaces of the inclusions.

Naturally, a first area of study in magnetic gels and elastomers is the magnetorheological (MR) effect, i.e., changes in the rheological or mechanical properties of these materials induced by external magnetic fields. This continues the research previously performed for MRFs and ferrofluids, see Sec. 1.4.1. One of the early works addressing magnetic gels and elastomers is given by Rigbi and Jilkén in 1983 [132]. However, the topic only gained increasing interest later in 1996 [87, 107, 133]. In Refs. [107, 133], the change in shear modulus for these new materials was already measured and the dependence on the volume concentration of particles was examined. A maximal MR effect of 39 %, i.e. an increase of the shear modulus by 39 % relative to the shear modulus without field, was reported for samples with a volume concentration of 20 % [107]. Additionally, the viscoelastic properties were probed, observing an increase in the loss factor (the ratio of the imaginary part of the complex shear modulus divided by its real part) with increasing strain when an external magnetic field is applied [133].

Experimentally, it is quite straightforward to determine the MR effect: One uses a rheometer for the samples without applied external magnetic field and compares it to the values with applied field. Here, the rheometer measures, e.g., the force needed to obtain a certain amount of shear deformation of the whole sample. A number of experiments have determined associated changes in the

static elastic moduli [2, 27, 42–46] as well as in the dynamic storage and loss moduli [107, 108, 134–141].

The second major effect in magnetic gels and elastomers are macroscopic deformations induced by applied external magnetic fields. Here, one typically distinguishes those deformations induced by homogeneous and those by inhomogeneous fields. The former is called *magnetostriction*, while the latter is known as magnetodeformation [142]. (Still, this nomenclature is not always used uniformly across the literature, for example, the term "magnetodeformation" is sometimes used in the case of homogeneous fields as well [143].) Already in 1996, a magnetodeformation of about 10 % was observed [87].

As mentioned in Sec. 1.3, inhomogeneous magnetic fields directly apply forces to inclusions carrying magnetic dipoles. Since this inhomogeneity stems from the outside, the whole sample can in this way be set into motion, which means that the sample needs to be fixed to avoid net displacement [144]. In our investigations, this effect does not emerge, because we only describe magnetostrictive effects (those induced by homogeneous external magnetic fields) in **P1**–**P5**, **P7**.

More in detail, the effect that is now known as magnetostriction dates back to observations by Joule in 1842 [145], who quotes a previous observation by Arstall in 1841. At that time, solid iron bars were observed to change their length in response to magnetic fields. However, the associated relative length changes are rather small, quoted as 1/720000. Nowadays, magnetic materials of much higher magnetostrictive amplitude have been found, such as rare-earth-Fe_2 alloys showing effects of relative magnitude 1/500 [146]. Still, these effects are rather small, because they are induced by changes in the crystal lattice structure on the atomic scale.

For magnetic gels and elastomers, the mechanism is different, rendering magnetostriction of the individual embedded particles as no longer relevant. Important are the magnetic forces that act on these inclusions. Since the inclusions are typically much bigger compared to the mesh size of the polymer network that makes up the elastic matrix, so that they cannot easily move through it, or the particles themselves are used as crosslinkers for the polymers, the magnetic forces on these particles make them push or tear on and deform the elastic matrix [31, 67, 147, 148]. This can lead to overall deformations of the material up to a couple of percent, which is much larger compared to the amplitudes of magnetostriction in metals.

These magnetostrictive effects have been extensively studied experimentally, often in cylindrical specimen [9–19]. In early investigations [9], a magnetostrictive length change of about 1 % was observed in very high fields (up to 8 T). This magnitude was significantly increased in later works, e.g. Ref. [18] reports respective values of about 16 % in fields of only 0.8 T and Ref. 19 even 21 % for anisotropic samples or 14.6 % for isotropic samples in fields of only 0.5 T. One major contribution to this increase is the usage of softer matrices: While Ref. 9 used an elastic matrix of a Young's modulus of about 0.25 MPa, the matrix material in Ref. 19 is much

softer, that is, of a shear modulus of about 30 kPa. (In the case of incompressible media, the Young's modulus is three times the shear modulus, which is a reasonable approximation to compare these two values.) It is even possible to measure the spatially resolved surface displacement field within the surface plane using a light speckle method, at least for a planar surface [149].

In particular, two experimental works have studied samples of spherical shape [20,21], which is the most relevant case for our considerations in Ch. 2. Still, Ref. 20 only addressed isotropic arrangements of the magnetizable inclusions. In contrast to that, Ref. 21 also studied anisotropic distributions, albeit not observing any significant magnetostrictive effect in the latter case with the external magnetic field applied along the axis of anisotropy. In the isotropic case, both studies found elongation along the field direction, in qualitative agreement with our results in **P1**.

Another effect, which we study in **P7**, relates to magnetically induced restructuring [123, 150]. Not only are the samples magnetically deformed, also the magnetizable particles in the samples are shifted in position upon the application of an external magnetic field. This affects, amongst others, the transport properties such as the electric conductivity [151–153] and thermal conductivity [154, 155] of the whole material, which has only been rarely investigated previously. A magnetically tunable thermal conductivity is also observed for MRFs [156, 157].

1.4.3 Current and future applications of magnetic gels and elastomers

For (potential) applications, magnetic gels and elastomers combine a variety of desirable properties. Naturally, applying magnetic fields to these materials is contactless [144, 158] and silent [87]. Additionally, these materials are inexpensive in general [4, 95, 159, 160]. Furthermore, biological tissues are usually transparent for magnetic fields [4, 160–163], which opens the path towards possible internal medical applications. Especially for specific matrix materials of magnetic gels and elastomers, biocompatibility has been confirmed [45, 164, 165].

Concerning possible applications, we refer to corresponding reviews [6, 96, 166]. In summary, the two main responses of magnetic gels and elastomers, implying magnetostrictive and magnetorheological effects, allow for various possible applications. On the one hand, the MR effect qualifies these materials for the use as vibrational absorbers/isolators or damping devices with magnetically tunable behavior [167–171]. On the other hand, magnetostrictive properties facilitate applications such as artificial muscles [172, 173], valves [174, 175], microfluidic pumps [160, 176], or soft actuators more generally [2, 49, 87, 106, 177–181]. Associated deformations are typically reversible [123]. Dynamically varying the magnetic field, even locomotion can be realized [182–184]. Additionally, the use of magnetic gels and elastomers for grippers [158, 183] or sensors [46, 185] was pointed out.

Another important area of potential applications is found in the medical context. One particular realization has been suggested in terms of targeted drug delivery, where the drugs could be placed in magnetic gels as carrier materials that transport drugs to their target and then are released by magnetically induced deformations [186–188].

1.4.4 Theoretical description of magnetic gels and elastomers

A theoretical treatment of magnetic gels and elastomers is quite difficult because effects on different length scales influence the overall, macroscopic material behavior. Therefore, some simplifying assumptions are unavoidable. (Theoretical descriptions of MRFs and ferrofluids are not discussed here.) For a recent review of the employed theoretical approaches, we refer to Ref. 142.

Starting on the smallest scale, microscopic approaches resolve the elastic polymer matrix as an ensemble of discrete polymer chains in a coarse-grained manner [144,189–191], instead of treating it as a continuous elastic matrix. These approaches are based on molecular dynamics, i.e. computer simulations of the movement of magnetic or magnetizable particles as well as the polymer chains. Consequently, when the interactions of the magnetic or magnetizable particles with individual polymer chains should be resolved, this level of description is the right one. For example, to study the differences of particle-crosslinked elastomers and the usual magnetic elastomers with the magnetic particles dispersed in the medium, a microscopic picture is needed [189, 190, 192]. A scale-bridging description for a particle-crosslinked gel is also available [193], however, evaluations are based on pairwise interactions between two particles. In other words, this approach allows to treat pairwise interactions between inclusions, but not the long-range interactions between all magnetic or magnetizable particles.

On the other end of the modeling spectrum, macroscopic theories aim to directly describe overall properties, representing the polymer matrix as well as the arrangement of magnetic or magnetizable inclusions only by continuum fields. Instead, conservation laws and symmetry arguments are used as a basis. For ferrogels with isotropic distributions of magnetizable inclusions, a macroscopic theory is presented in Ref. 194. It couples the macroscopic strain to the macroscopic magnetization, based on a hydrodynamic and thermodynamic description. Additionally, it considers how an oscillating temperature gradient and gradient of the magnetic field can induce shear deformations. It also discusses the effect of the magnetic field on sound propagation. For anisotropic magnetic gels, a related macroscopic theory has likewise been developed [195]. There, shear flow is predicted to induce rotations of the magnetization. Moreover, oscillating magnetic fields perpendicular to the magnetization direction can induce shear strains of the material. Later, this approach has been extended to anisotropic magnetic gels with tetrahedral order and permanent magnetization [196]. Additionally, shear stresses can again be induced by temperature gradients.

Besides, magnetostrictive effects were predicted from macroscopic models, using an analytical continuum approach. Spherical two-dimensional samples were studied in Ref. 197 and three-dimensional cylindrical samples in Ref. 198. Apart from that, for spherical isotropic samples, which we also study in **P1**, elongation along the field direction was predicted, assuming linear magnetization and Hookean elasticity by

Raikher and Stolbov [143]. This description was extended to hollow spheres [199] as well as to ellipsoidal samples [200]. A similar model for the magnetostriction of spheroidal samples was provdided [201]. Ref. 201 predicts an elongation for $a/b < 1.35$ (including the case of spherical samples) and contraction otherwise (and no deformation for $a/b \approx 1.35$), where a and b are the semi-minor and minor semi-major axis of the spheroid, respectively (b is the length of two perpendicular axes of the corresponding ellipsoid).

By construction, these macroscopic approaches cannot resolve dependencies of the overall properties on the arrangement of magnetic or magnetizable inclusions in detail. Therefore, mesoscopic models are useful, located in between microscopic and macroscopic models. They explicitly resolve the discrete arrangement of magnetizable inclusions, while usually treating the elastic matrix as a homogeneous and isotropic carrier medium.

With the rise of computational power, it is quite logical to use finite-element (FE) simulations for modeling magnetic gels and elastomers on the mesoscopic scale [17, 47, 84, 202]. In these approaches, the volume of the material is discretized into finite elements (hence the name). With these methods, (almost) arbitrary non-linear elastic models can be used and can even be combined with a spatially resolved magnetization of the particles. Typically, the magnetic inclusions in these approaches are also treated as elastic, but with a much higher shear or Young modulus, such that their deformations are negligible. Still, these approaches remain very demanding computationally and therefore cannot treat overly large numbers of magnetizable inclusions.

Another common method is dipole-spring modeling. In that case, the elastic matrix is represented by a network of discrete elastic springs, while the presence of magnetizable particles is simply represented by magnetic dipoles. Therefore, it constitutes one of the least computationally demanding approaches, allowing to treat comparatively large numbers of magnetizable inclusions. **P7** is based on such a model. Additionally, many other groups have also used this type of approach previously [42, 139, 203–209]. However, these springs are obviously just a very reduced representation of the elastic matrix. Additionally, it is more difficult to adjust the Poisson ratio of corresponding dipole-spring models [210, 211], e.g. for modeling incompressible elastic matrices.

Moreover, a simple way to describe magnetic gels and elastomers is to assume that the magnetically induced deformations are affine, i.e. that the macroscopic deformations are identically mapped to all scales of the material [212–214]. Obviously, this is quite a strong simplification that might not always be reasonable [42]. From this assumption, some works calculated magnetostrictive effects for different arrangements of magnetizable inclusions [213–215]. This assumption is also used in **P5** to calculate the resulting MR effects.

A recent work studied the effect of the particle rearrangements on the magne-

tostrictive and MR effect in a mesoscopic model for an ellipsoidal sample. The evolution of the particle arrangement due to the applied external magnetic field was resolved in a coarse-grained manner via the field-dependent fraction of particles in columnar structures [89].

A statistical description for magnetic gels and elastomers is available in terms of density functional theory (DFT): This theory in principle describes equilibrium thermodynamics of many-particle systems in an exact way. In DFT, the arrangement of magnetizable inclusions is represented by (statistically averaged) density profiles, hence the name. Still, to adapt this theory to magnetic gels and elastomers, the fact that the permanent elastic locking in the polymeric matrix renders the particles distinguishable complicates the description. Each particle has its own unique positional state that it returns to in the undeformed ground state. Based on DFT, macroscopic properties of the systems can be calculated. First, a corresponding theory was developed (due to the technical difficulties) for one-dimensional models of magnetic gels and elastomers in Ref. 216. Subsequently, it was extended to two-dimensional [217] and three-dimensional systems [218]. For the one-dimensional and two-dimensional case, the DFT was tested against Monte Carlo (MC) simulations. It was used to calculate magnetostrictive [217, 218] as well as MR effects [216–218].

Concerning continuous linearly elastic representations of the elastic matrix material in a mesoscopic description, previously infinitely extended media were considered, for which the solution of the Kelvin tensor is available, see Sec. 1.2. However, due to the presence of the other magnetizable inclusions in the vicinity of each other and their finite size, the resulting solution is altered. To allow for analytical progress, the inclusions are modeled as fully rigid. Nevertheless, the problem can only be solved in an expansion in the inverse inter-inclusion distances [31, 67, 147]. When the inclusions are positioned far from any the boundary, the results agree well with experiments and can even be used to determine elastic moduli from experimental measurements [31]. A related description has investigated viscoelastic carrier media [55], allowing to describe overdamped dynamic effects. Afterward, a similar description was used to study particles subject to an externally imposed torque in viscoelastic environments, e.g., torques induced by external magnetic fields [219]. Additionally, the corresponding expressions for two-dimensional elastic sheets or membranes, including matrix-mediated interactions between the inclusions, have been derived [220]. Geometries of membranes of finite thickness [221] and boundary effects [222] have been addressed as well. A modification of the three-dimensional Kelvin tensor is available for inclusions in bulk elastic media near a no-slip or free-slip wall [71].

Some works combine or compare different approaches for the theoretical modeling of magnetic gels and elastomers. As mentioned previously,Ref. [69] compares FE simulations to analytical descriptions in the framework of linear elasticity theory.

Additionally, both theoretical descriptions are compared to experiments and the linearly elastic description is even mapped to a simple dipole-spring model. Raikher and Stolbov also compared an analytical model based on the assumption of affine deformations, using two different elastic models (neo-Hookean and Peng-Landel energy), to FE simulations in Ref. 223. Another work that compares dipole-spring and FE models to calculate the MR effect is given by Ref. 47.

A fruitful combination is given by FE simulations, which are very accurate, but limited to lower numbers of magnetizable inclusions, with a homogenization approach. In that way, the whole material does not need to be represented in full by FE simulations, but the accuracy of the FE approach enters the construction of a material model on the macroscopic level. First, the continuum equations are analyzed for a small volume that still contains a sufficient number of particles using FE simulations. These small volumes are labeled representative volume elements (RVEs) or statistical volume elements (SVEs). Then, by an appropriate scale transition scheme, the overall, macroscopic material behavior can be obtained, while ensuring that some averaged quantities coincide in the meso- and macroscopic representation [224]. This strategy was used to calculate magnetostrictive effects in two-dimensional [225] and three-dimensional [148, 226–228] samples. Additionally, these descriptions that combine FE simulations with homogenization have been compared to a dipolar mean-field approach (magnetization field instead of individual dipoles) that calculates the magnetization in a self-consistent manner with the assumption of affine deformations. Those comparisons were performed in the two-dimensional case [229]. In a later work, the three-dimensional case was addressed [85], now using a linearly elastic description for the deformations based on Ref. [67]. Nowadays, the computational homogenization can be performed by neural networks for magnetic gels and elastomers, at least when the neural networks are restricted by physical constraints such as polyconvexity [230].

Concerning comparisons between experiment and theory, we already mentioned Ref. 31 that includes experiments and analytical theory. A similar work, but now for two-, three-, and four-particle systems with comparatively lower interparticle distances relates experiments to FE simulations [231]. Another strategy determines experimentally arrangements of particles, e.g. via X-ray microtomography, as input for numerical evaluations [42, 124, 139, 232].

In the next chapter (see chapter 2), my own contributions are presented. As discussed in the introduction (see chapter 1), they mainly focus on the dependence of magnetostrictive effects on the arrangement of the magnetizable inclusions as well as on the elastic matrix of magnetic gels and elastomers. This approach is based on linear elasticity of the elastic matrix material (see Sec. 1.2), explicitly accounting for boundary effects and nonaffine deformations, but restricted to systems of overall spherical shape. Furthermore, we restrict ourselves to a dipolar approximation for the magnetic interactions. This combination is presented in detail in **P1**–**P5**.

The analytical background of **P5** is provided in **P6**. Additionally, we analyze magnetically induced changes in the thermal conductivity in **P7** and finally close with a linearly elastic description of core-shell particles in **P8**.

Chapter 2

Scientific publications

In the following, the publications that form the basis of this dissertation are reproduced, numbered by **P1**–**P8**. For each publication, I summarize my contributions and present a notice on copyright and licensing.

P1 Magnetostriction in magnetic gels and elastomers as a function of the internal structure and particle distribution

Reprinted from

L. Fischer and A. M. Menzel,
Magnetostriction in magnetic gels and elastomers as a function of the internal structure and particle distribution,
J. Chem. Phys. **151**, 114906 (2019),
with the permission of AIP Publishing.

Digital Object Identifier (DOI): `https://doi.org/10.1063/1.5118875`

Statement of contribution

Both authors contributed to the work. During my PhD, we particularly added the investigation into the nonlinear effect that arises because of particle relocations under the mutual magnetic interactions between the inclusions lead to changed magnetic interactions between them. Furthermore, the investigations into the randomized configurations were significantly altered and expanded. I performed all calculations. The main text was drafted by AMM, with some parts added and revisions performed by me. I prepared all figures in the manuscript and drafted the first version of the supplemental material. I estimate my contribution to this work during my PhD as 45 %.

Copyright and license notice

The Journal of Chemical Physics ARTICLE scitation.org/journal/jcp

Magnetostriction in magnetic gels and elastomers as a function of the internal structure and particle distribution

Cite as: J. Chem. Phys. 151, 114906 (2019); doi: 10.1063/1.5118875
Submitted: 5 July 2019 • Accepted: 20 August 2019 •
Published Online: 19 September 2019

Lukas Fischer[a] and Andreas M. Menzel[b]

AFFILIATIONS

Institut für Theoretische Physik II: Weiche Materie, Heinrich-Heine-Universität Düsseldorf, Universitätsstraße 1, D-40225 Düsseldorf, Germany

[a]lfischer@thphy.uni-duesseldorf.de
[b]menzel@thphy.uni-duesseldorf.de

ABSTRACT

Magnetic gels and elastomers are promising candidates to construct reversibly excitable soft actuators, triggered from outside by magnetic fields. These magnetic fields induce or alter the magnetic interactions between discrete rigid particles embedded in a soft elastic polymeric matrix, leading to overall deformations. It is a major challenge in theory to correctly predict from the discrete particle configuration the type of deformation resulting for a finite-sized system. Considering an elastic sphere, we here present such an approach. The method is in principle exact, at least within the framework of linear elasticity theory and for large enough interparticle distances. Different particle arrangements are considered. We find, for instance, that regular simple cubic configurations show elongation of the sphere along the magnetization if oriented along a face or space diagonal of the cubic unit cell. Contrariwise, with the magnetization along the edge of the cubic unit cell, they contract. The opposite is true in this geometry for body- and face-centered configurations. Remarkably, for the latter configurations but the magnetization along a face or space diagonal of the unit cell, contraction was observed to revert to expansion with decreasing Poisson ratio of the elastic material. Randomized configurations were considered as well. They show a tendency of elongating the sphere along the magnetization, which is more pronounced for compressible systems. Our results can be tested against actual experiments for spherical samples. Moreover, our approach shall support the search of optimal particle distributions for a maximized effect of actuation.

I. INTRODUCTION

Magnetic gels and elastomers, also referred to as magnetorheological elastomers, magnetosensitive elastomers, ferrogels, or differently, are magnetoelastic hybrid composite materials of magnetic or magnetizable colloidal particles embedded in a soft polymer-based elastic matrix.[1–5] Many of their outstanding properties arise because they can be addressed by external magnetic fields. Through these fields, the magnetic interactions between the particles are affected, which presses or rotates the embedded particles against the surrounding elastic environment. As a consequence, the overall properties of the material are altered. For instance, in this way, the mechanical stiffness can be tuned and adjusted to a certain amount as requested.[1,2,6–24] Such induced switching, because of the involved restoring elastic forces, is typically reversible.[25]

Here, we concentrate on a different magnetically induced effect, namely, on overall shape changes resulting from the modified particle interactions. Corresponding externally and reversibly induced magnetostrictive behavior can be exploited to construct, for example, soft actuation devices.[1,26–35] Naturally, in this context, it becomes crucial to know whether the employed system or sample will contract or elongate along an applied magnetic field (usually involving opposite behavior along the transverse directions because of the typical quasi-incompressibility of the materials). Our central focus in the present work is on the question of the kind of overall resulting shape changes.

In experiments, commonly an elongation of the investigated materials along the axis of the applied magnetic field is observed.[36–45] Yet, as has been revealed by many theoretical studies, the type of expected deformation strongly depends on the internal structural

The Journal of Chemical Physics ARTICLE scitation.org/journal/jcp

particle arrangement of the investigated systems. For instance, simple regular rectangular lattice structures with magnetic moments induced along the edges of the rectangular unit cells were found to contract along these edges.[13,46,47] An extreme example of this kind is given by just a pair of magnetic particles that are driven toward each other by induced magnetic attraction.[48–50] In contrast to that, regular body-centered cubic (bcc) lattices are found to extend along the induced axis of magnetization when oriented along the edges of the cubic lattice cells,[13] as are two-dimensional systems containing hexagonal or initially wiggled chainlike structures.[47] Likewise, the rotation of embedded clusters can lead to an extension along the applied magnetic field.[51,52]

One significant problem in theoretical treatments is that simplifications and approximations are mostly unavoidable when characterizing complex materials of the considered kind. Consequently, the results need to be treated with special care. Studies based on assumptions of affine (homogeneous) deformations suppress internal degrees of freedom that may become important.[12,13,46] Basic dipole-spring models may serve to include such internal degrees of freedom to a certain amount;[18,20,23,53–56] however, it is difficult to fully comply with quasi-incompressibility in such approaches. The same applies to more microscopic simulation approaches resolving in a coarse-grained manner individual polymer chains.[57–59] Finite-element simulations, although quantitatively very reliable,[15,47,48,52,60] may be limited at some point concerning the number of considered embedded particles. So far, the majority of these simulation works seems to have been carried out for bulk systems. Moreover, statistical and scale-bridging procedures likewise and naturally contain certain types of approximations.[61–65]

To avoid many of the problems involved in the approaches just summarized, we adhere to the following strategy. We consider elastic spherical systems, as realized in some experiments,[44,45] to explicitly include the role of the system boundaries. Moreover, we confine ourselves to linear elasticity, that is, only distortions of low amplitude are addressed.[66–69] For elastic spheres embedded under no-slip surface conditions in a homogeneous and infinitely extended elastic background, an analytical expression for the linearly elastic Green's function is available.[70] It describes the static elastic displacements that result in response to a constant force acting onto the elastic material at one pointlike force center. We adapt this expression to pairwise forces acting inside a free-standing elastic sphere without any additional elastic background medium. Elastic distortions of the sphere, particularly along its surface, are then evaluated when many such force centers are present. Consequently, the force centers are identified with the embedded magnetic particles, subject to pairwise magnetic interaction forces between them. In this way, we analyze the resulting overall deformation of the whole free-standing sphere upon induced magnetization of various different contained regular and randomized particle distributions.

II. SYSTEM UNDER INVESTIGATION

As already indicated above, we confine ourselves to spherical elastic systems, strongly relying on previous work by Walpole.[70] In his study, a system as sketched in Fig. 1(a) was investigated. An elastic sphere of modulus μ and Poisson ratio ν is embedded in an infinitely extended elastic background of modulus $\tilde{\mu}$ and Poisson ratio $\tilde{\nu}$. The sphere of radius R is centered around the origin. Both parts, the sphere and the surrounding elastic background, are linearly elastic, spatially homogeneous, and locally isotropic in their undeformed states. At the interface between the two parts, perfect bonding prevails, implying continuity of the corresponding displacement fields and traction vectors.

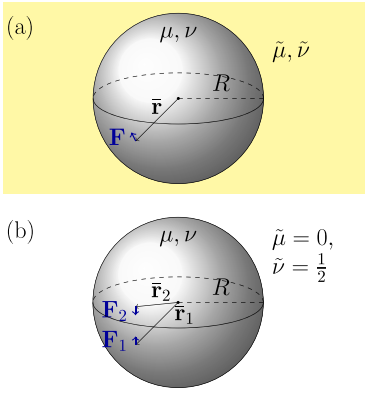

FIG. 1. Illustration of the system under investigation. (a) Walpole considered a deformable elastic sphere of elastic shear modulus μ and Poisson ratio ν embedded under no-slip surface conditions in an infinitely extended elastic background medium of shear modulus $\tilde{\mu}$ and Poisson ratio $\tilde{\nu}$. He determined the corresponding Green's function, which quantifies the displacement field $\mathbf{u}(\mathbf{r})$ inside and outside the sphere resulting from a pointlike force center acting on the inside.[70] (b) On this basis, we investigate the deformation of a free-standing sphere (for $\tilde{\mu} \to 0$ and $\tilde{\nu} \to 1/2$) that contains many pointlike force centers exerting pairwise magnetic forces of vanishing global force on the sphere. In this case, terms in the original solution[70] that would diverge, connected to a net translation of the sphere, balance each other. Then, Walpole's solution can be adapted accordingly. Similar reasoning applies to net rotations of the sphere in response to net torques acting on it.

In an impressive treatment of this problem, Walpole managed to derive the associated Green's function.[70] It solves the corresponding Navier–Cauchy equations[71]

$$\mu\Delta\mathbf{u}(\mathbf{r}) + \frac{\mu}{1-2\nu}\nabla\nabla\cdot\mathbf{u}(\mathbf{r}) = -\mathbf{f}(\mathbf{r}) \tag{1}$$

inside the sphere ($r = |\mathbf{r}| < R$) and with the replacements $\mu \to \tilde{\mu}$ and $\nu \to \tilde{\nu}$ outside the sphere ($r > R$), respecting the described boundary conditions at the interface ($r = R$). In these equations, $\mathbf{u}(\mathbf{r})$ represents the displacement field and the force density $\mathbf{f}(\mathbf{r})$ is specified as $\mathbf{f}(\mathbf{r}) = \mathbf{F}\delta(\mathbf{r} - \bar{\mathbf{r}})$. That is, the Green's function $\underline{\mathbf{G}}(\mathbf{r}, \bar{\mathbf{r}})$ provides the solution for the resulting displacement field $\mathbf{u}(\mathbf{r})$ in response to a static force $\mathbf{F}$. The force $\mathbf{F}$ acts on one pointlike force center located at position $\bar{\mathbf{r}}$. It leads to the displacement field $\mathbf{u}(\mathbf{r}) = \underline{\mathbf{G}}(\mathbf{r}, \bar{\mathbf{r}}) \cdot \mathbf{F}$. To evaluate $\underline{\mathbf{G}}(\mathbf{r}, \bar{\mathbf{r}})$, we have implemented it numerically following the presentation in Ref. 70.

All force centers are located on the inside of the sphere ($\bar{r} = |\bar{\mathbf{r}}| < R$). It was already mentioned in Ref. 70 that the limit $\tilde{\mu} \to 0$ leads to a divergence of $\mathbf{u}(\mathbf{r})$. From a physical point of view,

The Journal of Chemical Physics ARTICLE scitation.org/journal/jcp

this can be understood as follows: The limit $\tilde{\mu} \to 0$ (and simultaneously $\tilde{\nu} \to 1/2$) implies the absence of an elastic background. Thus, a free-standing sphere is considered [see Fig. 1(b)]. If a net force **F** acts on the sphere, there is no surrounding elastic background that would hold the sphere back from displacing. Thus, an arbitrarily small but finite magnitude of the force **F** can displace the sphere by an infinite amount.

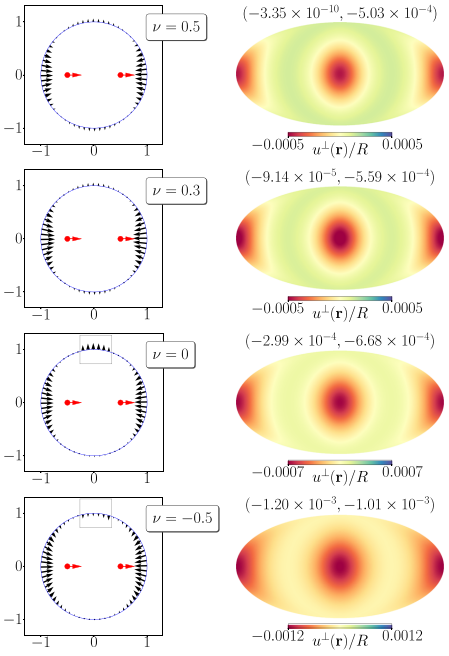

FIG. 2. Deformation of a sphere with two mutually attracting magnetic dipoles aligned along the horizontal symmetry axis, each at a distance of $0.5R$ from the center, and for $3\mu_0 m^2/4\pi\mu R^6 = 0.001$. The left column shows cross-sectional cuts through the sphere containing the symmetry axis. We mark the initial positions of the inclusions by red dots and the direction of the magnetic moments by red arrows. The surface displacements, indicated by black arrows, are enhanced by a factor of 500 for $\nu > 0$, 350 for $\nu = 0$, and 200 for $\nu < 0$. Inside the gray frames, we enhanced the displacement arrows by an additional factor of 4. On the right-hand side, we illustrate the induced displacements on the surface of the sphere by so-called Mollweide projection plots. Outward displacements are marked in green/blue, inward displacements in orange/red, with the numbers on the scale bars encoding the radial displacements. All Mollweide plots were arranged so that the magnetic moments point outwards toward the reader from the centers of the plots and inwards on the left and right ends. Furthermore, all plots indicate a contraction of the sphere along the symmetry axis. For positive Poisson ratio ν, the sphere expands along the lateral directions. In contrast to that, for the auxetic case of $\nu = -0.5$, a contraction along all directions is observed. The plots on the right-hand side were generated using the HEALPix package.[81] Moreover, the pairs of numbers on each plot indicate the coefficients $(u_{00}^{\perp}, u_{20}^{\perp})$ of an expansion into spherical harmonics of the radial outward displacement in units of R, associated with the overall change in volume and relative elongation along the axis of magnetization, respectively.

Physical intuition then implies that the corresponding divergence for $\tilde{\mu} \to 0$ should be lifted when pairwise reciprocal forces are considered. In this case, there are zero remaining net forces acting on the sphere. The sole effect of the forces is then to deform (or rotate) the sphere.

We could demonstrate by analytical considerations that, in fact, the terms that lead to the described divergence lift each other for pairwise reciprocal forces. The necessary condition for the forces is indeed satisfied for the pairwise magnetic forces considered in our present study. We thus drop the corresponding terms from the expressions listed in Ref. 70.

A similar divergence results if the applied forces lead to a net torque on the sphere. Analogously, this situation leads to a divergence of the displacement field for $\tilde{\mu} \to 0$. A free-standing sphere can be rotated by an infinite amount, if an arbitrarily small but finite net torque is applied to it. Again, if the net torque vanishes, terms that would lead to the divergence lift each other, and we thus drop them from the solution in Ref. 70.

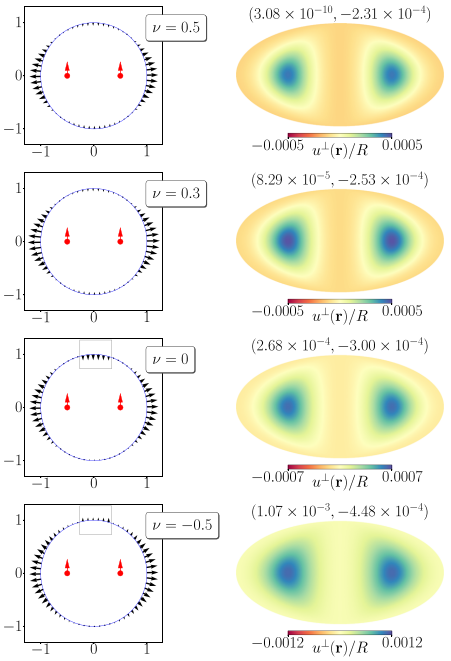

FIG. 3. Same as in Fig. 2, but now with the magnetic dipole moments located in a mutually repulsive configuration on the horizontal axis running through the center of the sphere and for $3\mu_0 m^2/4\pi\mu R^6 = 0.002$. The corresponding plots on the right-hand side were generated using the HEALPix package.[81] As in all our plots using the Mollweide projection, the magnetization vector points toward the reader at the center of each plot. The horizontal extension in the plots on the left-hand side due to the repulsion between the two dipoles is clearly visible by the dark blue spot in the Mollweide projections on the right-hand side. In the auxetic case of $\nu = -0.5$, an expansion along all directions is observed.

The Journal of Chemical Physics ARTICLE scitation.org/journal/jcp

We numerically implemented the corresponding expressions and confirmed their validity by comparison with extrapolated results obtained from the numerical implementation of Walpole's expressions[70] for decreasing $\tilde{\mu}$. To confirm the correctness of the latter, we tested that our implementation satisfies Eq. (1) and the boundary conditions on the surface of the sphere. Moreover, we have tested that our numerical implementation of the Green's function reduces to the results from the well-known bulk Green's function[72] when we set $\mu = \tilde{\mu}$ and $\nu = \tilde{\nu}$. Apart from that, for $\mu \neq 0$ and $\tilde{\mu} \to \infty$, we considered force centers located close to the boundary of the sphere. In this case, the boundary can be approximated as a flat rigid wall. Our numerical results in this limit agree well with those of the Green's function calculated for a half-space filling elastic material bordered by a rigid no-slip boundary.[73,74] A similar solution exists for a half-space in the case of $\mu \neq 0$ and $\tilde{\mu} \to 0$ with $\tilde{\nu} \to 1/2$, i.e., a semi-infinite solid with a free boundary.[75] Again, in the considered limit, the results of our numerical implementation match the results obtained from these analytical expressions.

As a result, the deformations induced by magnetic interactions of inclusions within a free-standing elastic sphere can be calculated. For simplicity, we concentrate on magnetic dipolar interactions between the inclusions.[57,76] All inclusions are assumed to be identical and to carry the same magnetic dipole moment $\mathbf{m} = m\hat{\mathbf{m}}$, with $m = |\mathbf{m}|$. Such a situation arises, for example, if a strong external magnetic field magnetizes all small identical spherical inclusions to saturation. Then, the induced magnetic force acting on the ith inclusion, exerted by all other inclusions, reads[77]

$$\mathbf{F}_i = -\frac{3\mu_0 m^2}{4\pi} \sum_{\substack{j=1 \\ j\neq i}}^{N} \frac{5\hat{\mathbf{r}}_{ij}\left(\hat{\mathbf{m}}\cdot\hat{\mathbf{r}}_{ij}\right)^2 - \hat{\mathbf{r}}_{ij} - 2\hat{\mathbf{m}}\left(\hat{\mathbf{m}}\cdot\hat{\mathbf{r}}_{ij}\right)}{\tilde{r}_{ij}^4}, \tag{2}$$

where μ_0 denotes the magnetic vacuum permeability, $\tilde{\mathbf{r}}_i$ sets the position of the ith inclusion, $\tilde{\mathbf{r}}_{ij} = \tilde{\mathbf{r}}_i - \tilde{\mathbf{r}}_j = \tilde{r}_{ij}\hat{\mathbf{r}}_{ij}$ with $\tilde{r}_{ij} = |\tilde{\mathbf{r}}_{ij}|$, $i = 1, \ldots, N$, and N fixes the number of inclusions.

In all that follows, we rescale lengths by the radius R of the elastic sphere and measure forces in units of μR^2. Thermodynamic stability requires $\mu > 0$ for the shear modulus of the sphere and $-1 < \nu < 1/2$ for the Poisson ratio,[66] while the limit $\nu \to 1/2$ characterizes an incompressible material. Negative Poisson ratios refer to so-called auxetic materials that, if stretched along one axis, expand to the lateral directions instead of contracting.

Summarizing, the free-standing elastic sphere is distorted in response to the magnetic forces acting on the embedded magnetic inclusions. These inclusions are assumed to be spherical and of radius $a = 0.02R$. To find the steady distorted state, we adhere to the following iterative numerical scheme.

First, we estimate how a rigid sphere of radius a embedded inside the free-standing elastic sphere is displaced in response to

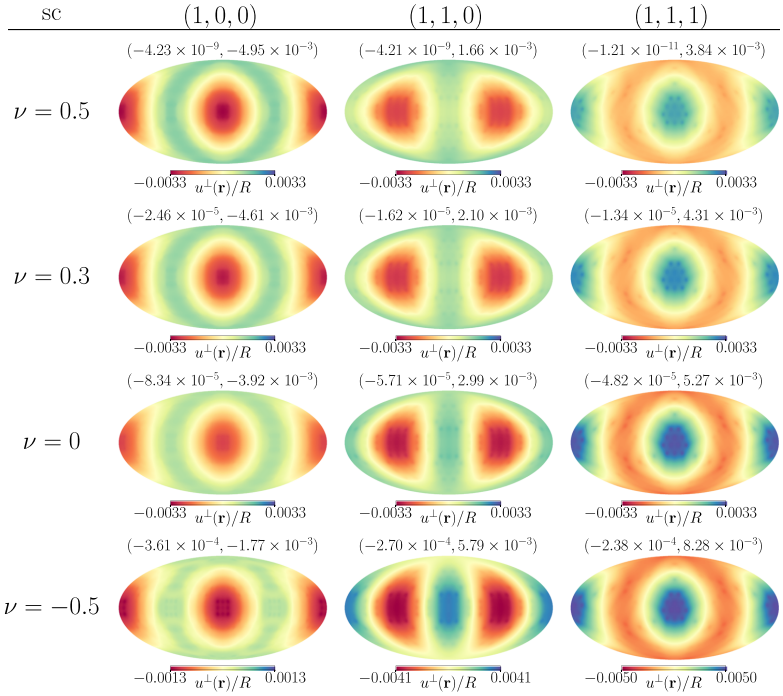

FIG. 4. Mollweide projections and expansion coefficients $(u_{00}^{\perp}, u_{20}^{\perp})$ in units of R[81] for a simple cubic (sc) lattice structure of the embedded particle configuration for $3\mu_0 m^2/4\pi\mu R^6 = 5.4 \times 10^{-8}$. Again, the magnetization points toward the reader at the center of each plot.

The Journal of Chemical Physics ARTICLE scitation.org/journal/jcp

a force acting on it (see the supplementary material). Analytical expressions fitted to the numerical estimates are obtained for these displacements (see again the supplementary material). Next, the forces on all other inclusions induce elastic distortions within the elastic sphere that add to the displacement of the considered inclusion. These additional contributions to the displacement are calculated from our modified version of Walpole's solution. To evaluate this mutual interaction, mediated by the elastic environment, the inclusions are treated as pointlike, assuming them to be sufficiently far apart from each other. Then, after having calculated the new positions of all inclusions, we can evaluate the magnetic interactions between them anew. This in turn leads to different displacements, which again leads to adjusted forces, and so on. After multiple of these steps of iteration, we reach a steady state. Our goal is the final steady magnetic force distribution that can then be used in conjunction with our modified solution by Walpole to calculate the deformation on the surface of the elastic sphere within the framework of linear elasticity theory, once more treating the inclusions as pointlike.

III. SETTING THE REMAINING SYSTEM PARAMETERS

Upon the mentioned rescaling, we obtain in Eq. (2) a dimensionless force coefficient of $3\mu_0 m^2/4\pi\mu R^6$. To set its value in our subsequent evaluations in agreement with possible experimental realizations, we consider nickel or iron oxide (Fe_3O_4) as the material for the magnetic inclusions. For nickel, the literature, for instance, lists a saturation magnetization of approximately 55.1 J T^{-1} kg^{-1}[178] or, by using the density of nickel of approximately 8.908 g cm^{-3},[79] $M_S \approx 490.8$ kJ T^{-1} m^{-3}(= 490.8 kA m^{-1}). For iron oxide, we use a saturation magnetization of approximately 100 J T^{-1} kg^{-1},[80] corresponding via a density of approximately 5.18 g cm^{-3}[80] to $M_S \approx 518$ kJ T^{-1} m^{-3} (= 518 kA m^{-1}). In both cases, we assume a shear modulus of 1.67 kPa. A further parameter is the radius of the magnetic inclusions a which we choose as $a = 0.02R$. Furthermore, we assume that the elastic material does not influence the magnetic interactions. These choices lead to a dimensionless force coefficient $3\mu_0 m^2/4\pi\mu R^6$ of approximately 4.9×10^{-8} for nickel or 5.4×10^{-8} for iron oxide, respectively. The latter value is used in all our evaluations unless otherwise noted.

IV. BASIC ILLUSTRATIVE EXAMPLES

As a first step, we illustrate the formalism using two basic example situations as depicted in Figs. 2 and 3. Since here only two magnetic inclusions are considered, we use much higher dimensionless force coefficients than introduced in Sec. III to still produce visible displacements. First, in Fig. 2, two mutually attractive magnetic dipole moments are induced on the horizontal symmetry axis running through the center of the sphere. As expected, the sphere in response to these induced forces contracts along the horizontal axis. For positive Poisson ratio, $\nu > 0$, this contraction leads to an expansion in the lateral directions. This effect is most pronounced for an incompressible elastic sphere, i.e., for $\nu = 0.5$ (see the first row in Fig. 2). In contrast to that, the negative Poisson ratio $\nu = -0.5$ reverses this secondary response (see the bottom row in Fig. 2).

A repulsive magnetic interaction between two inclusions is considered in Fig. 3. Again, the magnetized particles are located on a horizontal axis running through the center of the sphere. In this case, the magnetic dipoles point into the vertical direction. As expected, the sphere now expands along the horizontal axis. Moreover, the sphere contracts along the vertical axis, except for the depicted case of $\nu = -0.5$, in which it expands along all directions.

The right columns in both Figs. 2 and 3 show how we illustrate our results in the following. To display the surface deformation, the resulting displacement field is evaluated on 49 152 surface points. Then, the surface of the sphere is slit open and bent into the plane in a so-called Mollweide projection.[82] By the color code, we mark whether the surface is pushed toward the outside (green/blue) or pulled toward the inside (orange/red) of the sphere. Furthermore, the spheres are always rotated so that the magnetic moments point toward the reader in the center of the plots. We used the HEALPix package (http://healpix.sourceforge.net)[81] to generate these plots.

To obtain a more quantitative measure for the overall elongation or contraction of the sphere as well as for the overall change of volume, we proceed along the following lines. We determine for each of the 49 152 surface points the radial outward component

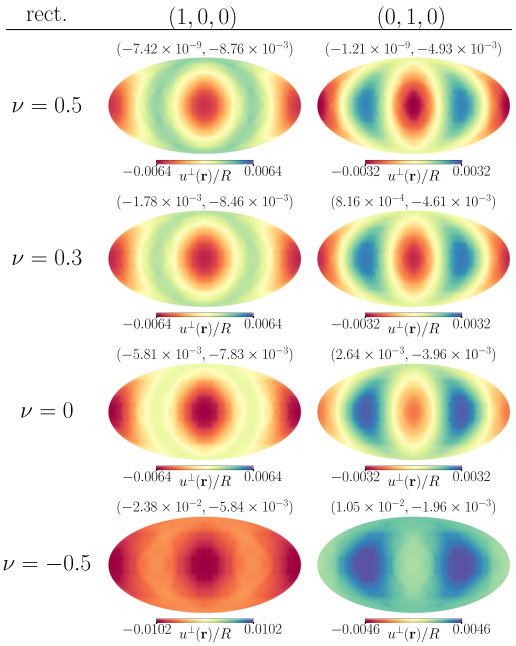

FIG. 5. Same as in Fig. 4, but for a rectangular (rect.) lattice structure featuring two identical edge lengths of the unit cell and the third edge length of 0.7 of that value, for $3\mu_0 m^2/4\pi\mu R^6 = 5.4 \times 10^{-8}$. In the plots on the left-hand side, the magnetization is directed along the edge of smaller lattice constant, while it points along one of the edges of the larger lattice constant in the right-hand plots.

The Journal of Chemical Physics ARTICLE scitation.org/journal/jcp

$u^{\perp}(\mathbf{r}) = \mathbf{u}(\mathbf{r}) \cdot \hat{\mathbf{r}}$ of the resulting displacement field $\mathbf{u}(\mathbf{r})$. Then, again using the HEALPix package,[81] we expand $u^{\perp}(\mathbf{r})$ into spherical harmonics.[77] The coefficient $u^{\perp}_{00}$ of the spherical harmonic $Y_{00} = \sqrt{1/4\pi}$ indicates an overall expansion of the sphere (increased volume) for $u^{\perp}_{00} > 0$ and an overall contraction (decreased volume) for $u^{\perp}_{00} < 0$. Similarly, we determine the expansion coefficient $u^{\perp}_{20}$ for the spherical harmonic $Y_{20} = \sqrt{5/16\pi}\left(3\cos^2\theta - 1\right)$, with θ denoting the angle of the center-to-surface vector on the sphere with respect to the magnetization direction. This coefficient, for $u^{\perp}_{20} > 0$, indicates an elongation of the sphere along the axis of magnetization, relative to its transverse deformation. For $u^{\perp}_{20} < 0$, contraction along the axis of magnetization, relative to the transverse deformation, occurs.

Values of the corresponding pairs $(u^{\perp}_{00}, u^{\perp}_{20})$ are indicated on the plots of Figs. 2 and 3. As expected, $u^{\perp}_{20} < 0$ in Fig. 2 as well as in Fig. 3 due to the relative contraction along the direction of magnetization in both cases. Moreover, $u^{\perp}_{00} < 0$ in Fig. 2 and $u^{\perp}_{00} > 0$ in Fig. 3 (except for $\nu = 0.5$) due to the mutual attraction and repulsion, respectively. The absolute values of $u^{\perp}_{00}$ strongly increase for decreasing ν as the sphere gets more compressible. Not shown are the displacements of the inclusions obtained from our iterative numerical procedure. These displacements are in each situation pointing into the directions of the forces, i.e., toward and away from the center in the attractive and repulsive case, respectively.

V. MANY-PARTICLE CONFIGURATIONS

To now turn toward the situation in small model systems of magnetic gels and elastomers, we address the structures of approximately $N = 1000$ magnetic force centers distributed throughout the sphere. First, the effects of regular lattice configurations are analyzed for different orientations of the magnetization with respect to the corresponding unit cells. To position the force centers ("particles") inside the sphere, we cut from a bulk-filling lattice structure all particles that are located on the inside of the sphere with a minimal distance of $3a = 0.06R$ from the surface. Afterward, we also briefly illustrate situations of randomized particle distributions. As outlined at the end of Sec. III, we from now on set $3\mu_0 m^2/4\pi\mu R^6 = 5.4 \times 10^{-8}$ throughout.

A. Simple cubic lattice structure

We started with a configuration cut from a regular simple cubic (sc) lattice. As a lattice constant, we chose $0.15R$, which yields 1021 particles inside the elastic sphere. Three different orientations of the magnetization direction were probed, namely, along the (1, 0, 0) direction (edge of the unit cell), (1, 1, 0) direction (face diagonal of the unit cell), and (1, 1, 1) direction (space diagonal of the unit cell). See the left, center, and right column of plots in Fig. 4, respectively.

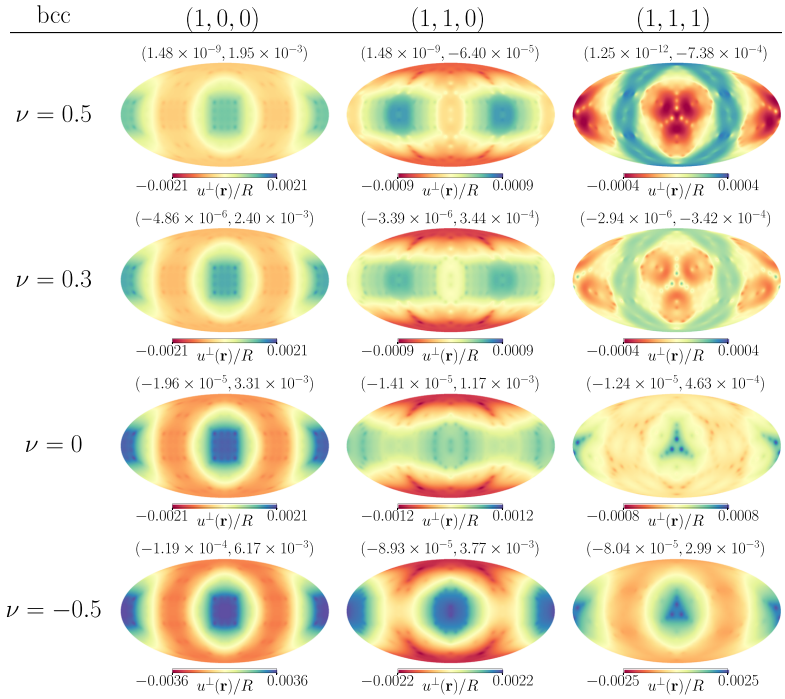

FIG. 6. Same as in Fig. 4, but for a body-centered cubic (bcc) lattice configuration, again setting $3\mu_0 m^2/4\pi\mu R^6 = 5.4 \times 10^{-8}$.

The Journal of Chemical Physics ARTICLE scitation.org/journal/jcp

First, we observe a contraction of the sphere along the magnetization axis when it is directed along the edge of the unit cell (left column of plots) in qualitative agreement with Ref. 13. This can be understood already by considering the interactions within a pair of nearest neighbors. The corresponding dipole–dipole interactions are attractive along the magnetization direction and repulsive perpendicular to it. Second, in both other cases of orienting the magnetization, we find an expansion along the direction of the magnetization, which is more pronounced and uniaxial for the magnetization along the space diagonal of the unit cell (right column of plots). For the magnetization along the face diagonal (center column of plots), we observe contraction along the perpendicular face diagonal in the xy-plane, i.e., in the (1, −1, 0) or (−1, 1, 0) direction. Indicated by $u_{00}^{\perp}$, we find that the volume of the sphere is shrinking in every case.

B. Rectangular lattice structure

Next, we broke the cubic symmetry along one direction by turning to a rectangular lattice configuration. For this purpose, we considered a unit cell within which the lattice constant along one direction is 70% of the lattice constants along the perpendicular directions. The latter lattice spacings were chosen as $0.171R$, leading to 999 inclusions. We imposed the magnetization along the axis of smaller lattice constant as well as along one of the other axes. These cases are referred to by (1, 0, 0) and (0, 1, 0), respectively.

Figure 5 reveals a contraction of the sphere along the magnetization axis in both cases (except for $\nu = -0.5$). A relative contraction along this axis is observed in the spherical harmonic coefficients as $u_{20}^{\perp} < 0$ in every case. In the auxetic situation ($\nu = -0.5$), a global contraction or expansion of the sphere is observed, respectively. We can understand this behavior from the interactions between the closest neighbors (along the axis of shorter lattice constant) which attract each other in the left-hand plots and repel each other in the right-hand plots in analogy to Sec. IV. Furthermore, we observe a fourfold symmetric deformation on the left-hand side due to the fourfold symmetry around the axis of magnetization, which is no longer present on the right-hand side. In the latter case, the symmetry axis parallel to the edges of shorter lattice constant runs through the center of the dark blue spots. Our results for the situation (1, 0, 0) and $\nu > 0$ can be compared to those of Ref. 46 obtained for spatially homogeneous deformations of the elastic environment, showing qualitative agreement.

C. Body-centered cubic lattice structure

Next, we address magnetostriction for body-centered cubic (bcc) lattice configurations. We probed the same magnetization directions (1, 0, 0), (1, 1, 0), and (1, 1, 1) as for the sc lattice

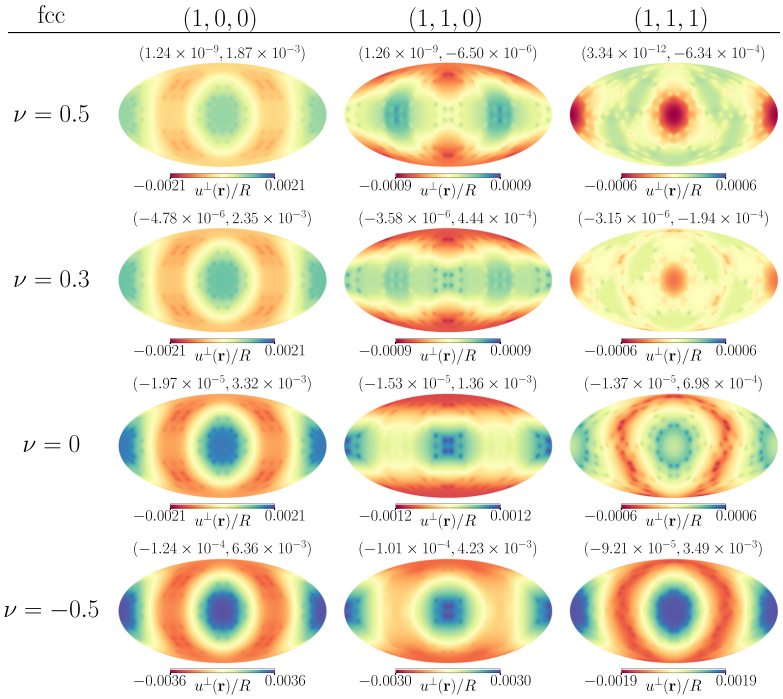

FIG. 7. Same as in Fig. 4, but for a face-centered cubic (fcc) lattice configuration, again setting $3\mu_0 m^2/4\pi\mu R^6 = 5.4 \times 10^{-8}$.

The Journal of Chemical Physics ARTICLE scitation.org/journal/jcp

(see Sec. V A). For comparison, these directions again refer to the cubic unit cell. A lattice constant for the cubic cell of $0.1885R$ was used, which implies 1037 inclusions. As a result, we observe a relative expansion along the magnetization axis for the (1, 0, 0)-case (see Fig. 6). For the other two orientations of the magnetization, the opposite is true for $\nu = 0.5$. Yet, for the auxetic spheres in the bottom row of Fig. 6, an expansion along the magnetization direction can be observed in all cases. Thus, for the (1, 1, 0) and (1, 1, 1) orientations, the response switches from contraction to expansion along the magnetization with decreasing ν.

D. Face-centered cubic lattice structure

Likewise, for face-centered cubic (fcc) lattice configurations, we label the orientations of the magnetization direction (1, 0, 0), (1, 1, 0), and (1, 1, 1). We used a lattice constant for the cubic cell of $0.236R$, which implies 1055 inclusions.

In the case of this lattice structure, we find a strong resemblance to the previous situation of a bcc lattice (see Sec. V C) for all three magnetization directions that were probed. The corresponding results are summarized in Fig. 7.

E. Randomized configurations

Finally, we also considered the response of less ordered particle configurations. For this purpose, the pointlike particles were inserted at random into the sphere. During the process, we impose a minimum distance of $6a = 0.12R$ of the particles from each other.

When aligned magnetic dipoles are generated on the particles, mutual magnetic interactions between them lead to deformations of the elastic sphere also for these more irregular configurations. Due to the disordered particle arrangement underneath the surface of the sphere, by eye the surface deformation appears quite irregular in most cases (see Fig. 8). Generally, the observed irregularities in the shape of the deformed surface are in line with previous experimental observations and simulations.[51,52]

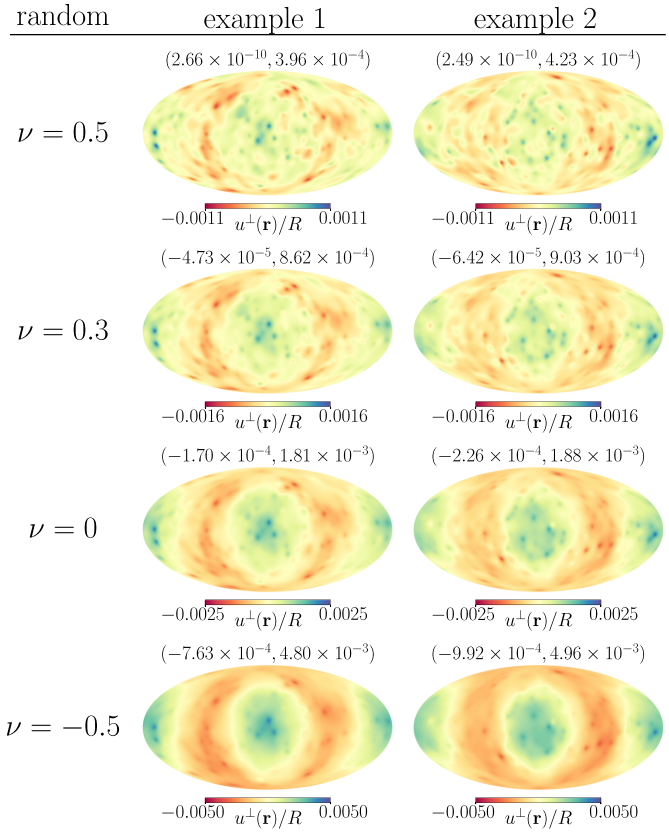

FIG. 8. Same as in Fig. 4, but for two randomized configurations, again setting $3\mu_0 m^2/4\pi\mu R^6 = 5.4 \times 10^{-8}$.

The Journal of Chemical Physics ARTICLE scitation.org/journal/jcp

To obtain a definite measure for the overall volume changes and elongation or contraction along the axis of magnetization, we again determined the coefficients $u_{00}^{\perp}$ and $u_{20}^{\perp}$, respectively. As demonstrated for two randomly selected example realizations in Fig. 8, the displacements generally tend to become more pronounced for decreasing ν. Our plots indicate an elongation along the magnetization axis, similarly to the situation for the fcc lattice magnetized along the (1, 0, 0) axis (see Fig. 7). To search for more general trends in the behavior of the values $u_{00}^{\perp}$ and $u_{20}^{\perp}$, in total 50 different realizations of randomized configurations were generated and evaluated.

The averaged results are summarized in Fig. 9. A trend of overall contraction of the whole sphere is identified for smaller Poisson ratios [see the darker data points for $u_{00}^{\perp}$ in Fig. 9(a)]. For an incompressible elastic sphere, i.e., for $\nu = 0.5$, the volume remains unchanged, as expected. In fact, we observe a trend of relative elongation of the sphere along the direction of magnetization ($u_{20}^{\perp} > 0$) [see the darker data points in Fig. 9(b)]. The absolute values quantifying the degree of deformation increase with decreasing Poisson ratio ν. For clarity, we also summarize the averaged values in Table I. Comparing with the related experimental results,[44,45] we find qualitative agreement.

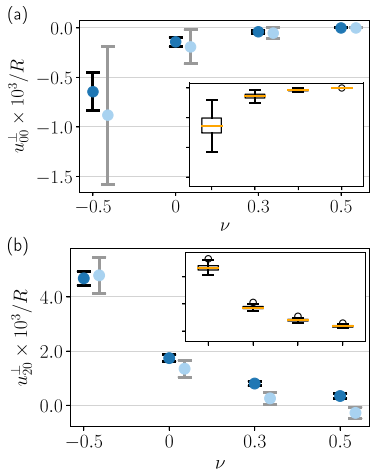

FIG. 9. (a) Volume expansion ($u_{00}^{\perp}$) and (b) relative elongation along the magnetization axis ($u_{20}^{\perp}$) of the elastic sphere when randomized particle configurations within the sphere are magnetized as $3\mu_0 m^2/4\pi\mu R^6 = 5.4 \times 10^{-8}$. We depict the corresponding mean values by darker (blue) dots and standard deviations by dark error bars obtained from 50 realizations of the particle distributions for the four studied values of the Poisson ratio (as marked on a nonlinear scale on the abscissae). Insets show the corresponding boxplots using the same scaling of the axes. The medians are plotted as (orange) horizontal lines. Boxes indicate the middle 50% of obtained values, while the whiskers mark the highest and lowest values except for outliers that are shown as circles. Outliers are defined as points for which the distance to the end of the box is larger than 1.5 times the box height. Lighter symbols in the main plots were obtained for comparison for the same values of the Poisson ratio from threefold mirror symmetric but otherwise randomized configurations.

TABLE I. Rounded averaged values of the expansion coefficients $u_{00}^{\perp}$ and $u_{20}^{\perp}$, averaged over 50 randomized configurations.

ν	−0.5	0	0.3	0.5
$u_{00}^{\perp}$	-6×10^{-4}	-1×10^{-4}	-4×10^{-5}	3×10^{-10}
$u_{20}^{\perp}$	5×10^{-3}	2×10^{-3}	8×10^{-4}	3×10^{-4}

We remark that, in general, the randomized particle configurations exposed to an external magnetic field will experience a net torque that would induce a macroscopic rotation. Still, we were able to perform our calculations. In our approach, as explained before, we have excluded corresponding contributions. For comparison, to generate systems of vanishing overall torque, we changed our procedure of initialization. The particles were now inserted at random into that eighth of the sphere of Cartesian coordinates of $x, y, z > 0$. Afterward, the configuration was mirrored at the planes $x = 0$, $y = 0$, and $z = 0$ so that the whole sphere is filled. The resulting data points for the same values of the Poisson ratio ν are included in lighter color in Fig. 9 and confirm the previously inferred trends. As one significant deviation, for incompressible systems ($\nu = 0.5$), we now observe a weak tendency of relative contraction instead of elongation along the axis of magnetization. We can understand this deviation illustratively. The procedure of mirroring introduces pairs of nearby particles that mutually attract each other along or repel each other perpendicularly to the axis of magnetization, supporting an overall relative contraction of the sphere. We have checked that the associated change in the overall behavior for $\nu = 0.5$ is related to the finite size of the sphere. When we double the radius R of the elastic sphere, keeping the concentration of contained particles constant, we found the mean value in Fig. 9(b) for $\nu = 0.5$ and for the threefold mirror-symmetric configuration (lighter data point) to move toward positive numbers. It would be interesting to know whether global rotations were observed in the macroscopic experiments.[44,45]

VI. CONCLUSIONS

In summary, we have adapted the Green's function derived by Walpole for an elastic sphere embedded in an infinitely extended elastic environment[70] to the case of a free-standing elastic sphere. As a result, we can, in the linear regime of elasticity, calculate the small-amplitude deformations of the sphere if ensembles of point-like inclusions exert forces in the absence of global translations and rotations.

Our approach has the advantage of explicitly including the boundaries of the system, incompressibility or auxetic behavior if required, and all internal degrees of freedom of the elastic matrix. It treats the matrix as an elastic continuum. In principle, the formalism becomes exact for linear small-amplitude distortions and low volume fractions of the inserted particles, that is, large interparticle distances when compared to the particle diameters. At the same time, the action of many force centers can be conveniently superimposed in this way. We stress that this formalism naturally takes into account the spatial inhomogeneities of deformation that occur within the elastic material.

The Journal of Chemical Physics ARTICLE scitation.org/journal/jcp

Along these lines, we have addressed the deformation of spherical elastic example systems that contain different spatial arrangements of magnetized pointlike inclusions. We started from the illustrative examples of two mutually attracting or repelling dipoles. Next, we addressed several different types of configurations of approximately 1000 inclusions. Interestingly, for simple cubic configurations, we observed contraction or extension along the magnetization direction, depending on whether the magnetization was along the edge or face/space diagonal of the unit cells. Body- and face-centered cubic configurations, in contrast to that, led to expansion along the magnetization direction when oriented along the edges of the unit cells. Remarkably, for magnetizations along the face and space diagonals of the latter two lattice types, the behavior switched from relative contraction to relative expansion along the magnetization direction with decreasing Poisson ratio. Moreover, simple rectangular and randomized configurations were addressed.

Out of these examples, spheres containing randomized particle configurations probably represent the most relevant considered systems concerning actual experimental realizations using presently available tools of fabrication. These spheres tend to elongate along the axis of magnetization, which becomes more pronounced with decreasing Poisson ratio. Moreover, with decreasing Poisson ratio, they tend to decrease their volume upon magnetization. By construction, our approach is restricted to the linear regime of deformation. This means that only small-scale deformations of the elastic spheres can be described.

In reality, it is possible to generate spherical samples of magnetic gels and elastomers by curing the material in a spherical compartment.[44,45] Afterward, the internal structure and overall magnetostriction induced by an external magnetic field can be reconstructed, for example, using x-ray microtomographic analyses.[83,84] Small-scale spherical samples could likewise be generated using different methods such as solvent evaporation[85] or microfluidic methods.[86] Another type of complex polymeric material, spherical samples of which were produced in the latter way successfully, are liquid-crystalline elastomers. They can likewise show induced deformations and actuation.[87,88] Magnetic gels and liquid-crystalline elastomers share several similarities in their overall stress-strain properties.[89,90] Potentially, also the induced distortions of spherical samples of magnetic gels generated by microfluidic production techniques[91,92] reveal such related behavior. Possibly, our approach may further be helpful in characterizing the deformational response of biological cells containing embedded magnetic particles.[93]

SUPPLEMENTARY MATERIAL

See supplementary material for further details on how we obtain approximate analytical expressions for the displacement of a finite-sized inclusion in our free-standing elastic sphere when the inclusion is subject to an applied net force.

ACKNOWLEDGMENTS

Some of the results in this paper have been derived using the HEALPix package.[81] The authors thank the Deutsche Forschungsgemeinschaft for support of this work through the priority program SPP 1681 (Grant No. ME 3571/3).

REFERENCES

[1]G. Filipcsei, I. Csetneki, A. Szilágyi, and M. Zrínyi, Adv. Polym. Sci. **206**, 137 (2007).
[2]A. M. Menzel, Phys. Rep. **554**, 1 (2015).
[3]S. Odenbach, Arch. Appl. Mech. **86**, 269 (2016).
[4]M. T. Lopez-Lopez, J. D. G. Durán, L. Y. Iskakova, and A. Y. Zubarev, J. Nanofluids **5**, 479 (2016).
[5]R. Weeber, M. Hermes, A. M. Schmidt, and C. Holm, J. Phys.: Condens. Matter **30**, 063002 (2018).
[6]M. R. Jolly, J. D. Carlson, B. C. Muñoz, and T. A. Bullions, J. Intell. Mater. Syst. Struct. **7**, 613 (1996).
[7]M. R. Jolly, J. D. Carlson, and B. C. Muñoz, Smart Mater. Struct. **5**, 607 (1996).
[8]E. Jarkova, H. Pleiner, H.-W. Müller, and H. R. Brand, Phys. Rev. E **68**, 041706 (2003).
[9]G. V. Stepanov, S. S. Abramchuk, D. A. Grishin, L. V. Nikitin, E. Y. Kramarenko, and A. R. Khokhlov, Polymer **48**, 488 (2007).
[10]H. Böse and R. Röder, J. Phys.: Conf. Ser. **149**, 012090 (2009).
[11]A. V. Chertovich, G. V. Stepanov, E. Y. Kramarenko, and A. R. Khokhlov, Macromol. Mater. Eng. **295**, 336 (2010).
[12]D. S. Wood and P. J. Camp, Phys. Rev. E **83**, 011402 (2011).
[13]D. Ivaneyko, V. Toshchevikov, M. Saphiannikova, and G. Heinrich, Condens. Matter Phys. **15**, 33601 (2012).
[14]B. A. Evans, B. L. Fiser, W. J. Prins, D. J. Rapp, A. R. Shields, D. R. Glass, and R. Superfine, J. Magn. Magn. Mater. **324**, 501 (2012).
[15]Y. Han, W. Hong, and L. E. Faidley, Int. J. Solids Struct. **50**, 2281 (2013).
[16]D. Y. Borin, G. V. Stepanov, and S. Odenbach, J. Phys.: Conf. Ser. **412**, 012040 (2013).
[17]N. Chiba, K. Yamamoto, T. Hojo, M. Kawai, and T. Mitsumata, Chem. Lett. **42**, 253 (2013).
[18]G. Pessot, P. Cremer, D. Y. Borin, S. Odenbach, H. Löwen, and A. M. Menzel, J. Chem. Phys. **141**, 124904 (2014).
[19]V. V. Sorokin, G. V. Stepanov, M. Shamonin, G. J. Monkman, A. R. Khokhlov, and E. Y. Kramarenko, Polymer **76**, 191 (2015).
[20]G. Pessot, H. Löwen, and A. M. Menzel, J. Chem. Phys. **145**, 104904 (2016).
[21]T. I. Volkova, V. Böhm, T. Kaufhold, J. Popp, F. Becker, D. Y. Borin, G. V. Stepanov, and K. Zimmermann, J. Magn. Magn. Mater. **431**, 262 (2017).
[22]T. Oguro, H. Endo, T. Kikuchi, M. Kawai, and T. Mitsumata, React. Funct. Polym. **117**, 25 (2017).
[23]G. Pessot, M. Schümann, T. Gundermann, S. Odenbach, H. Löwen, and A. M. Menzel, J. Phys.: Condens. Matter **30**, 125101 (2018).
[24]M. Watanabe, J. Ikeda, Y. Takeda, M. Kawai, and T. Mitsumata, Gels **4**, 49 (2018).
[25]M. Schümann and S. Odenbach, J. Magn. Magn. Mater. **441**, 88 (2017).
[26]M. Zrínyi, L. Barsi, and A. Büki, J. Chem. Phys. **104**, 8750 (1996).
[27]D. Collin, G. K. Auernhammer, O. Gavat, P. Martinoty, and H. R. Brand, Macromol. Rapid Commun. **24**, 737 (2003).
[28]Y. An and M. T. Shaw, Smart Mater. Struct. **12**, 157 (2003).
[29]K. Zimmermann, V. A. Naletova, I. Zeidis, V. A. Turkov, E. Kolev, M. V. Lukashevich, and G. V. Stepanov, J. Magn. Magn. Mater. **311**, 450 (2007).
[30]Y. L. Raikher, O. V. Stolbov, and G. V. Stepanov, J. Phys. D: Appl. Phys. **41**, 152002 (2008).
[31]R. Fuhrer, E. K. Athanassiou, N. A. Luechinger, and W. J. Stark, Small **5**, 383 (2009).
[32]H. Böse, R. Rabindranath, and J. Ehrlich, J. Intell. Mater. Syst. Struct. **23**, 989 (2012).
[33]P. Ilg, Soft Matter **9**, 3465 (2013).
[34]M. M. Schmauch, S. R. Mishra, B. A. Evans, O. D. Velev, and J. B. Tracy, ACS Appl. Mater. Interfaces **9**, 11895 (2017).
[35]L. Hines, K. Petersen, G. Z. Lum, and M. Sitti, Adv. Mater. **29**, 1603483 (2017).
[36]S. Bednarek, Appl. Phys. A **68**, 63 (1999).
[37]J. M. Ginder, S. M. Clark, W. F. Schlotter, and M. E. Nichols, Int. J. Mod. Phys. B **16**, 2412 (2002).

The Journal of Chemical Physics ARTICLE scitation.org/journal/jcp

[38]X. Guan, X. Dong, and J. Ou, J. Magn. Magn. Mater. **320**, 158 (2008).
[39]G. Diguet, E. Beaugnon, and J.-Y. Cavaillé, J. Magn. Magn. Mater. **321**, 396 (2009).
[40]G. Diguet, E. Beaugnon, and J. Y. Cavaillé, J. Magn. Magn. Mater. **322**, 3337 (2010).
[41]J. Maas and D. Uhlenbusch, Smart Mater. Struct. **25**, 104002 (2016).
[42]Y. Han, A. Mohla, X. Huang, W. Hong, and L. E. Faidley, Int. J. Appl. Mech. **7**, 1550001 (2015).
[43]D. Y. Borin, S. Odenbach, and G. V. Stepanov, J. Magn. Magn. Mater. **470**, 85 (2019).
[44]C. Gollwitzer, A. Turanov, M. Krekhova, G. Lattermann, I. Rehberg, and R. Richter, J. Chem. Phys. **128**, 164709 (2008).
[45]G. Filipcsei and M. Zrínyi, J. Phys.: Condens. Matter **22**, 276001 (2010).
[46]D. Ivaneyko, V. P. Toshchevikov, M. Saphiannikova, and G. Heinrich, Macromol. Theory Simul. **20**, 411 (2011).
[47]P. Metsch, K. A. Kalina, C. Spieler, and M. Kästner, Comput. Mater. Sci. **124**, 364 (2016).
[48]A. M. Biller, O. V. Stolbov, and Y. L. Raikher, J. Appl. Phys. **116**, 114904 (2014).
[49]A. M. Biller, O. V. Stolbov, and Y. L. Raikher, Phys. Rev. E **92**, 023202 (2015).
[50]M. Puljiz, S. Huang, K. A. Kalina, J. Nowak, S. Odenbach, M. Kästner, G. K. Auernhammer, and A. M. Menzel, Soft Matter **14**, 6809 (2018).
[51]O. V. Stolbov, Y. L. Raikher, and M. Balasoiu, Soft Matter **7**, 8484 (2011).
[52]X. Gong, G. Liao, and S. Xuan, Appl. Phys. Lett. **100**, 211909 (2012).
[53]M. A. Annunziata, A. M. Menzel, and H. Löwen, J. Chem. Phys. **138**, 204906 (2013).
[54]R. Weeber and C. Holm, preprint arXiv:1704.06578 (2017).
[55]D. Ivaneyko, V. Toshchevikov, and M. Saphiannikova, Polymer **147**, 95 (2018).
[56]S. Goh, A. M. Menzel, and H. Löwen, Phys. Chem. Chem. Phys. **20**, 15037 (2018).
[57]R. Weeber, S. Kantorovich, and C. Holm, Soft Matter **8**, 9923 (2012).
[58]R. Weeber, S. Kantorovich, and C. Holm, J. Chem. Phys. **143**, 154901 (2015).
[59]R. Weeber, P. Kreissl, and C. Holm, Arch. Appl. Mech. **89**, 3 (2019).
[60]K. A. Kalina, P. Metsch, and M. Kästner, Int. J. Solids Struct. **102**, 286 (2016).
[61]A. Y. Zubarev, Soft Matter **8**, 3174 (2012).
[62]D. Ivaneyko, V. Toshchevikov, M. Saphiannikova, and G. Heinrich, Soft Matter **10**, 2213 (2014).
[63]A. M. Menzel, J. Chem. Phys. **141**, 194907 (2014).
[64]A. Y. Zubarev and D. Y. Borin, J. Magn. Magn. Mater. **377**, 373 (2015).
[65]D. Romeis, V. Toshchevikov, and M. Saphiannikova, Soft Matter **12**, 9364 (2016).
[66]L. D. Landau and E. M. Lifshitz, *Theory of Elasticity* (Elsevier, Oxford, 1986).
[67]M. Puljiz, S. Huang, G. K. Auernhammer, and A. M. Menzel, Phys. Rev. Lett. **117**, 238003 (2016).
[68]M. Puljiz and A. M. Menzel, Phys. Rev. E **95**, 053002 (2017).
[69]M. Puljiz and A. M. Menzel, Phys. Rev. E **99**, 053002 (2019).
[70]L. J. Walpole, Proc. R. Soc. London, Ser. A **458**, 705 (2002).
[71]A.-L. Cauchy, *Exercices de Mathématiques* (Bure Frères, Paris, 1828), Vol. 3, pp. 160–187.
[72]C. Teodosiu, *The Elastic Field of Point Defects* (Springer, Berlin, Heidelberg, 1982).
[73]N. Phan-Thien, J. Elasticity **13**, 231 (1983).
[74]A. M. Menzel, Soft Matter **13**, 3373 (2017).
[75]R. D. Mindlin, Physics **7**, 195 (1936).
[76]S. H. L. Klapp, J. Phys.: Condens. Matter **17**, R525 (2005).
[77]J. D. Jackson, *Classical Electrodynamics* (Wiley, New York, 1999).
[78]J. Crangle and G. Goodman, Proc. R. Soc. London, Ser. A **321**, 477 (1971).
[79]N. N. Greenwood and A. Earnshaw, *Chemistry of the Elements* (Pergamon Press, Oxford, 1984).
[80]R. Cornell and U. Schwertmann, *The Iron Oxides: Structure, Properties, Reactions, Occurrences and Uses* (John Wiley & Sons, Weinheim, 2003).
[81]K. M. Górski, E. Hivon, A. J. Banday, B. D. Wandelt, F. K. Hansen, M. Reinecke, and M. Bartelmann, Astrophys. J. **622**, 759 (2005).
[82]E. W. Grafarend, R. You, and R. Syffus, *Map Projections: Cartographic Information Systems* (Springer, Berlin, Heidelberg, 2014).
[83]T. Gundermann, P. Cremer, H. Löwen, A. M. Menzel, and S. Odenbach, Smart Mater. Struct. **26**, 045012 (2017).
[84]M. Schümann, D. Y. Borin, S. Huang, G. K. Auernhammer, R. Müller, and S. Odenbach, Smart Mater. Struct. **26**, 095018 (2017).
[85]N. H. Hai, N. H. Luong, N. Chau, and N. Q. Tai, J. Phys.: Conf. Ser. **187**, 012009 (2009).
[86]C.-H. Chen, A. R. Abate, D. Lee, E. M. Terentjev, and D. A. Weitz, Adv. Mater. **21**, 3201 (2009).
[87]C. Ohm, C. Serra, and R. Zentel, Adv. Mater. **21**, 4859 (2009).
[88]E.-K. Fleischmann, H.-L. Liang, N. Kapernaum, F. Giesselmann, J. Lagerwall, and R. Zentel, Nat. Commun. **3**, 1178 (2012).
[89]A. M. Menzel, H. Pleiner, and H. R. Brand, J. Appl. Phys. **105**, 013503 (2009).
[90]P. Cremer, H. Löwen, and A. M. Menzel, Phys. Chem. Chem. Phys. **18**, 26670 (2016).
[91]J.-W. Kim, A. S. Utada, A. Fernández-Nieves, Z. Hu, and D. A. Weitz, Angew. Chem. **119**, 1851 (2007).
[92]D. K. Hwang, D. Dendukuri, and P. S. Doyle, Lab Chip **8**, 1640 (2008).
[93]H. Huang, C. Y. Dong, H.-S. Kwon, J. D. Sutin, R. D. Kamm, and P. T. C. So, Biophys. J. **82**, 2211 (2002).

Supplemental material to "Magnetostriction in magnetic gels and elastomers as a function of the internal structure and particle distribution"

Lukas Fischer[1] and Andreas M. Menzel[1]

[1] *Institut für Theoretische Physik II: Weiche Materie, Heinrich-Heine-Universität Düsseldorf, D-40225 Düsseldorf, Germany*

(Dated: July 5, 2019)

In this supplemental file, we describe how we calculate in our free-standing elastic sphere the displacement of each finite-sized inclusion when it is subject to a non-vanishing but sufficiently small force.

In our iterative numerical scheme, it is necessary to know during each step how much each magnetic inclusion is displaced directly in response to the force acting on it. This force, in our situation, results from the magnetic interactions with all other inclusions. Here, we assume the inclusions to be of rigid spherical shape of radius $a = 0.02R$, where R is the radius of the free-standing embedding elastic sphere.

We note that because of the spherical geometry of the overall elastic body in combination with the linearity of the underlying equations, we only need to consider two complementary situations: First, the force may act parallel to the positional vector of the inclusion within the sphere, that is along a radial axis. Second, the force may act perpendicular to this axis. In general, we can split any force into these two orthogonal components.

To take into account the finite size of the spherical inclusion, we distribute about 3×10^6 point-like force centers approximately evenly on a spherical shell around the center of the inclusion (again using the HEALPix package [1]). Then, we let a force of unit magnitude, divided by the number of force centers, act on each of these force centers. The resulting displacement field is evaluated on the spherical shell at 192 different positions, again distributed approximately evenly.

We calculate this displacement field using our modified version of Walpole's solution. At the end, we determine from the 192 positions of evaluation the average displacement. The latter is assigned as the displacement of the whole inclusion. (Corresponding standard deviations over the shell are calculated as well.)

In principle, we need to repeat this procedure for all positions along one (arbitrary) radial axis. Obviously, this is only possible for a finite number of center positions of the inclusion. Therefore, we interpolate our results for intermediate positions. To achieve this, we use a fitting function for the resulting displacements of the form

$$u^d(\bar{r}) = \sum_{i=0}^{6} \frac{\alpha_i^d}{(1-\bar{r})^i} \,, \tag{1}$$

where $d \in \{\|, \perp\}$ marks displacement components in response to forces parallel or perpendicular to the radial axis, $\bar{r}$ sets the distance of the center of the inclusion from the center of the elastic sphere, and α_i^d are fit parameters.

Figure S1 demonstrates very good agreement between our fits using the functional form of Eq. (1) and our calculated data. Thus, we used the fitted functions to calculate the displacements of the inclusions during the iterative numerical loop as described in the main article. Naturally, the curves for the cases of displacement parallel and perpendicular to the radial axis coincide for $\bar{r} = 0$ for all considered values of the Poisson ratio ν. This is expected for symmetry reasons. In the limit $\bar{r}/R \to 1$, we compare the resulting displacements to corresponding displacements calculated via the solution by Mindlin [2]. The latter refers to a homogeneous elastic half-space bounded by a free surface. We find good agreement for all four values of the Poisson ratio ν and both force directions (data not shown). We note the increased standard deviation in Fig. S1 of the displacements on the shell of evaluation around the center of the inclusion for positions closer to the elastic surface. The points on that side located closer to the surface of the elastic sphere get displaced more than on the opposite side because there is less elastic material in the closer vicinity that needs to be dragged along (the elastic sphere ends within a finite distance). In our numerical evaluations associated with the results in the main article, we only used values $\bar{r} < \bar{r}_{max}$, see Fig. S1, for which these deviations are reasonably small.

[1] K. M. Górski, E. Hivon, A. J. Banday, B. D. Wandelt, F. K. Hansen, M. Reinecke, and M. Bartelmann, Astrophys. J. **622**, 759 (2005).

[2] R. D. Mindlin, Physics **7**, 195 (1936).

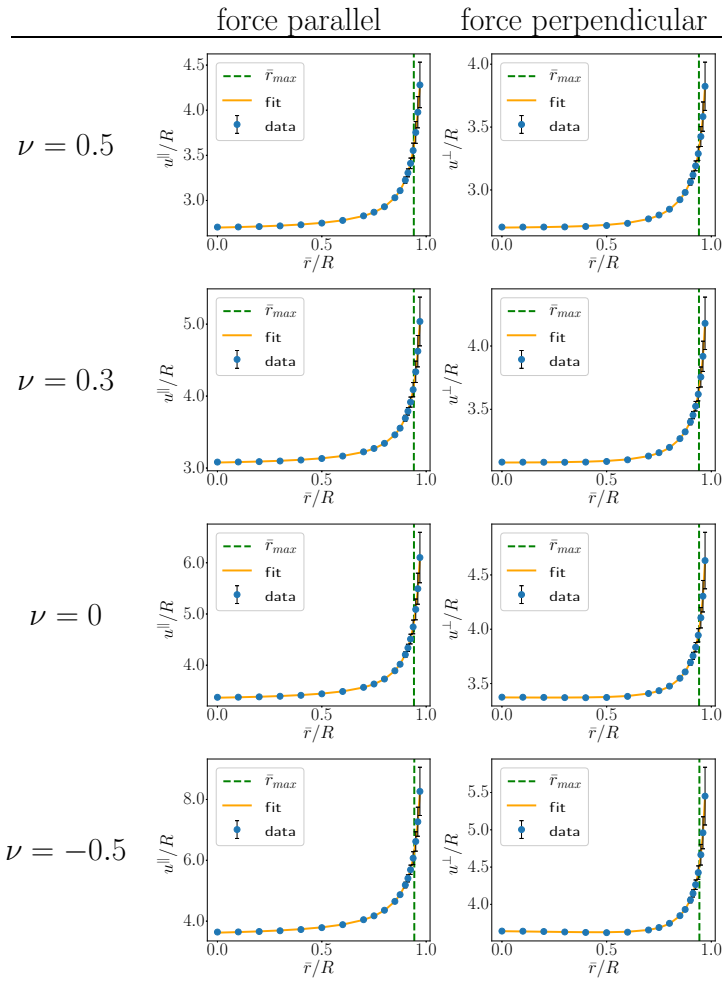

FIG. S1. A spherical shell of radius $a = 0.02R$ is located at a distance $\bar{r}$ from the center of a free-standing elastic sphere of radius R centered around the origin. As a measure for the induced displacements of a spherical inclusion of radius a, we distribute point-like force centers on the shell. Each force center exerts a force of identical magnitude on the elastic body. Resulting displacements are evaluated at probe positions also located on the shell. We distinguish cases in which the force is applied parallel to the positional vector, i.e., along a radial axis (on the left-hand side), and cases in which the force is applied perpendicular to the positional vector (on the right-hand side). The (blue) dots represent mean values calculated from 192 probe positions distributed over each shell, together with corresponding standard deviations. Results for the fitting functions in Eq. (1) are indicated by solid (orange) lines. The vertical dashed (green) lines mark the maximal value of $\bar{r}$ used in the evaluations reported in the main article. As in the main article, we distinguish four values of the Poisson ratio ν.

P2 Towards a soft magnetoelastic twist actuator

Reproduced from

L. Fischer and A. M. Menzel,
Towards a soft magnetoelastic twist actuator,
Phys. Rev. Research **2**, 023383 (2020).

Digital Object Identifier (DOI):
`https://doi.org/10.1103/PhysRevResearch.2.023383`

Statement of contribution

Both authors contributed to this work. I performed all calculations and amended the theory, based on ideas and discussions with AMM. Moreover, I drafted most of the first version of the manuscript, including all figures, and the supplemental material. I estimate my contribution to this work during my PhD as 90 %.

Copyright and license notice

PHYSICAL REVIEW RESEARCH **2**, 023383 (2020)

Towards a soft magnetoelastic twist actuator

Lukas Fischer* and Andreas M. Menzel†
Institut für Theoretische Physik II: Weiche Materie, Heinrich-Heine-Universität Düsseldorf, Universitätsstraße 1, D-40225 Düsseldorf, Germany

(Received 9 March 2020; accepted 29 May 2020; published 23 June 2020)

Soft actuators allow external stimuli to transform into mechanical deformations. Because of their deformational response to external magnetic fields, magnetic gels and elastomers are ideal candidates for such tasks. Mostly, linear magnetostrictive deformations, that is, elongations or contractions along straight axes, are discussed in this context. In contrast to that, here we propose the concept of a twist actuator that responds by torsional deformations around the axis of an applied magnetic field. For this purpose, we theoretically investigate the overall mechanical response of a basic model system containing discrete magnetizable particles in a soft elastic matrix. Two different types of discrete particle arrangements are used as starting conditions in the nonmagnetized state. These contain globally twisted anisotropic particle arrangements on the one hand, and groups of discrete helical-like particle structures positioned side by side on the other hand. Besides the resulting twist upon magnetization, we also evaluate other modes of deformation. Our analysis supports the construction of magnetically orientable and actuatable torsional mixing devices in fluidic applications or other types of soft actuators that initiate relative rotations between different components.

DOI: 10.1103/PhysRevResearch.2.023383

I. INTRODUCTION

Torsional actuators respond by a twist-type deformation to external stimuli. Most studies are concerned with linear actuators that contract or elongate along a certain axis upon actuation. However, there are several important prospective applications of twist actuators, for example, microfluidic mixing, microscopic surgery tools, and prosthetics [1]. Depending on the application, a certain degree of softness of the actuator in combination with a certain degree of biocompatibility may be beneficial or even mandatory, particularly when it comes to medical applications. This is one of the reasons why so-called magnetic gels and elastomers (also commonly referred to as magnetorheological elastomers or ferrogels) [2–11] were introduced as important candidates for the construction of soft actuators [2,12–24]. These materials usually consist of magnetic or magnetizable colloidal particles embedded in an elastic, typically polymeric matrix. Such magnetic gels have the advantage that their distortions can be induced by external magnetic fields, and the resulting deformation is typically reversible [25].

To now generate magnetoelastic twist actuators in the form of magnetic gels or elastomers (see Fig. 1), we suggest to build on the following previously explored insights. When the materials are fabricated in the presence of strong homogeneous external magnetic fields, chainlike structures of the inserted particles may form before the surrounding polymeric matrix is permanently established through corresponding chemical processes. Once the elastic matrix has reached its elastic (solid) state, these particle structures remain locked in the material, as can be seen in many experimental realizations [13,26–33]. One possible route to generate torsional actuators may be to additionally twist these chainlike aggregates, before the particle positions are fixed in the material by the final chemical crosslinking and establishing of the elastic polymeric matrix. This leads to self-supported torsional actuators. Such a concept is different from materials that are clamped at one end, contain anisotropic nonchiral structures, and are twisted by external magnetic fields that exert torques on the contained anisotropic aggregates [34,35]. Naturally, the situation that we consider is also different from studying how magnetic fields modify the stiffness of magnetic gels and elastomers when distorted by externally imposed torsional deformations [36–42].

To realize soft torsional actuators, in our case, on the one hand, one may think of a globally, collectively twisted state of the whole set of embedded chainlike aggregates in the initial, cured state of the materials. On the other hand, one may assume each individual chainlike aggregate to show an initially twisted structure.

We start by considering globally twisted particle arrangements as initial states. To generate corresponding samples, a procedure of the following kind could be realistic. The approach is inspired by a protocol of synthesizing monodomain nematic liquid-crystalline elastomers [43–45] consisting of liquid-crystal molecules that are chemically attached to or part of crosslinked polymeric networks [45–47]. Its scheme follows a two-step crosslinking process [43–45], employing two crosslinkers of different speed of chemical reaction. The

*lfischer@thphy.uni-duesseldorf.de
†menzel@thphy.uni-duesseldorf.de

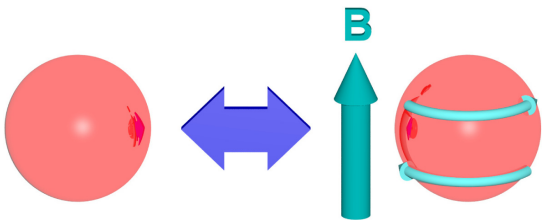

FIG. 1. Illustration of the general idea and setup. The considered soft magnetoelastic composite system is spherical in overall shape. Upon application of a homogeneous external magnetic field **B**, it shows a reversible torsional twist deformation, as indicated by the bent arrows on the right-hand side.

action of the first crosslinker generates a weakly crosslinked elastomeric sample that is stiff enough to already be uniaxially stretched. Maintaining this stretched state in which the liquid-crystal molecules are on average uniaxially oriented in response to the imposed strain, the second crosslinker reacts and locks in this configuration. Along these lines, monodomain nematic samples, featuring an average uniaxial molecular liquid-crystalline alignment, are obtained. Such materials show pronounced nonlinear stress-strain properties when stretched perpendicular to the direction of nematic alignment [43,44,48,49].

In our case of magnetic gels and elastomers, the two-step crosslinking process may be performed accordingly. First, under the presence of strong homogeneous external magnetic fields, uniaxially ordered chainlike aggregates of the magnetized particles form. They get locked into the sample by the generated surrounding elastic environment resulting from the quick action of the first crosslinker [26–28,31–33,50,51]. Finite gaps between the particles as considered below may result from previous coating of the particles or by using surface-functionalized particles themselves as crosslinkers [19,52–55]. In a next step, this precrosslinked system is twisted around the anisotropy axis. This leads to a global twist of the contained chainlike particle aggregates. The sample is maintained in this state while the second, slower crosslinker is reacting chemically and establishing the final elastic matrix. In this way, the twisted structure gets permanently locked in.

Another, possibly more academic procedure to generate example systems for investigations of the effects that we predict here might be to deposit the particles in a controlled way, maybe even by hand, at prescribed positions while generating the elastic environment layer by layer [56,57]. Even macroscopic spherical particles could be used for such proofs of concept [58]. In this case, besides implementing globally twisted structures, one could also arrange the magnetizable particles in individual helices, positioned in an aligned way side by side. Maybe, in the future, such a deposition process can be automated, as has recently been achieved for the production of magnetic microhelices [59,60].

In the present work, we use such twisted discrete particle configurations as an input to calculate the resulting magnetically induced overall deformations of corresponding elastic composite systems. Our theoretical approach is analytical, based on linear elasticity theory, and then evaluated numerically. To achieve such an analytical approach, we concentrate on elastic systems of overall spherical shape. The degree of initial twist is varied and the consequences of such variations are analyzed, both by numerical evaluations and by simplified analytical considerations. Both the globally twisted structures as well as several individual helical-like aggregates arranged side by side are addressed.

We give a brief overview of our theoretical approach in Sec. II, together with a motivation of our chosen parameter values. After that, in Sec. III the torsional actuation of systems containing globally twisted particle configurations is addressed. In Sec. IV, we consider particle arrangements of helical aggregates positioned side by side. To further facilitate the understanding, we compare the resulting twisting deformation to a minimal analytical consideration in Sec. V. We conclude in Sec. VI.

II. THEORETICAL FRAMEWORK

To perform the following evaluations, we build on our methods developed in Ref. [61]. We assume that the elastic material used for the magnetorheological elastomer and containing the magnetizable particles is spatially isotropic as well as homogeneous. Moreover, we confine ourselves to small deformations (up to a couple of percent) so that we can use linear elasticity theory. This allows us to superimpose the deformations resulting from each internal force center.

Consequently, we describe this material via only two elastic coefficients, namely, the shear modulus μ and the Poisson ratio ν. They quantify the stiffness and compressibility of the material, respectively. A Poisson ratio ν of $1/2$, representing an upper bound [62], describes incompressible materials. However, the Poisson ratio can reach negative values as well, down to -1 [62]. In these cases, the corresponding material is called auxetic, implying that when stretched along one axis it will show expansion to the lateral directions instead of contraction.

Generally, the response of the elastic material to an applied force density $\mathbf{f}(\mathbf{r})$ inside it is then quantified by the so-called Navier-Cauchy equations [63],

$$\mu\Delta\mathbf{u}(\mathbf{r}) + \frac{\mu}{1-2\nu}\nabla\nabla\cdot\mathbf{u}(\mathbf{r}) = -\mathbf{f}(\mathbf{r}), \tag{1}$$

where $\mathbf{u}(\mathbf{r})$ denotes the displacement field at position $\mathbf{r}$. In our case, the elastic material forms a freestanding elastic sphere of radius R. Fortunately, an analytical solution for Eq. (1) in this case is available in terms of the corresponding Green's function. $\mathbf{f}(\mathbf{r})$ then specifies the effect of a pointlike force center inside the elastic sphere. We were able to transfer this solution to the case of a freestanding sphere of free surface [61], starting from previous work that considered the sphere embedded in an elastic background material [64]. This analytical solution for the elastic part of the problem was afterwards implemented numerically.

Next, to include the magnetic effects of magnetorheological gels and elastomers, we distributed magnetic inclusions at prescribed positions inside the elastic material, see Secs. III and IV. We always assume the magnetic inclusions to be sufficiently far apart from each other so that we can describe their magnetic signature as magnetic dipoles. As a further

simplification, we assume that the magnetic dipole moment $\mathbf{m} = m\hat{\mathbf{m}}$, where $m = |\mathbf{m}|$, is identical for all inclusions. In experiments, such a situation could be realized by applying a strong external magnetic field that magnetizes all (identical) inclusions to saturation.

In this case, the magnetic dipole-dipole forces are given by [65]

$$\mathbf{F}_i = -\frac{3\mu_0 m^2}{4\pi} \sum_{\substack{j=1 \\ j\neq i}}^{N} \frac{5\hat{\bar{\mathbf{r}}}_{ij}(\hat{\mathbf{m}}\cdot\hat{\bar{\mathbf{r}}}_{ij})^2 - \hat{\bar{\mathbf{r}}}_{ij} - 2\hat{\mathbf{m}}(\hat{\mathbf{m}}\cdot\hat{\bar{\mathbf{r}}}_{ij})}{\bar{r}_{ij}^4}, \quad (2)$$

where $\mathbf{F}_i$ is the force exerted by all other inclusions on the ith inclusion. Moreover, μ_0 denotes the magnetic vacuum permeability, $\bar{\mathbf{r}}_i$ marks the position of the ith inclusion, the difference vector of positions is given by $\bar{\mathbf{r}}_{ij} = \bar{\mathbf{r}}_i - \bar{\mathbf{r}}_j = \bar{r}_{ij}\hat{\bar{\mathbf{r}}}_{ij}$ with $\bar{r}_{ij} = |\bar{\mathbf{r}}_{ij}|$ $(i, j = 1, ..., N)$, and N sets the number of magnetized inclusions. The resulting force density inserted into Eq. (1) based on Eq. (2) is

$$\mathbf{f}(\mathbf{r}) = \sum_{i=1}^{N} \mathbf{F}_i\, \delta(\mathbf{r} - \bar{\mathbf{r}}_i), \quad (3)$$

where $\delta(\mathbf{r})$ represents the Dirac delta function, and we thus assume pointlike magnetic force centers.

After rescaling lengths by R and forces by μR^2, the strength of the magnetic forces relative to the elastic restoring forces is characterized by a dimensionless force coefficient $3\mu_0 m^2/4\pi\mu R^6$. Its value is set to 5.4×10^{-8} for all that follows, as inspired by realistic experimental parameters [61]. The inclusions are assumed to be of spherical shape as well, with their radius set to $a = 0.02R$.

To include the effect of the induced elastic distortions on the positions of the magnetized inclusions and thus on the resulting magnetic forces and vice versa, an iterative scheme had been developed, see Ref. [61]. Finally, to characterize the induced overall deformations and capabilities of actuation, we evaluate the resulting displacement field on 49 152 surface points of the elastic sphere. These points are approximately evenly distributed with positions generated by the HEALPix package [66].

For the problem at hand, we choose the z axis to always coincide with the magnetization direction of the magnetic inclusions, i.e., $\hat{\mathbf{m}} = \hat{\mathbf{z}}$. Moreover, we express the displacement of each surface point using spherical coordinates as

$$\mathbf{u}(\mathbf{r}(\theta,\varphi)) = u^{\perp}(\theta,\varphi)\begin{pmatrix}\sin\theta\cos\varphi\\ \sin\theta\sin\varphi\\ \cos\theta\end{pmatrix} + u^{\theta}(\theta,\varphi)\begin{pmatrix}\cos\theta\cos\varphi\\ \cos\theta\sin\varphi\\ -\sin\theta\end{pmatrix} + u^{\varphi}(\theta,\varphi)\begin{pmatrix}-\sin\varphi\\ \cos\varphi\\ 0\end{pmatrix}, \quad (4)$$

with

$$\mathbf{r}(\theta,\varphi) = R\begin{pmatrix}\sin\theta\cos\varphi\\ \sin\theta\sin\varphi\\ \cos\theta\end{pmatrix}. \quad (5)$$

Thus, the components $u^{\perp}$, u^{θ}, and u^{φ} describe displacements inwards or outwards of the elastic surface, tangential deformations along the polar direction, and tangential deformations along the azimuthal direction, respectively. Below, the component u^{φ} will become particularly important to quantify the overall twisting deformation.

To associate the resulting displacement field with different modes of overall deformation, we perform spherical harmonic expansions of $u^{\perp}$, u^{θ}, and u^{φ}. We use the same definitions for spherical harmonics, especially concerning the Condon-Shortley phase, as in Ref. [65]. The most relevant spherical harmonics for our analysis are given by $Y_{00} = \sqrt{1/4\pi}$, $Y_{10} = \sqrt{3/4\pi}\cos\theta$, and $Y_{20} = \sqrt{5/16\pi}(3\cos^2\theta - 1)$.

As announced above, we then focus on the resulting overall torsional deformations for two types of spatial arrangements of the magnetizable inclusions: globally twisted and side-by-side aligned helical structures, see Secs. III and IV, respectively. The degree of initial structural twist in the nonmagnetized state is quantified by a parameter γ; see below for its definition. In both cases we confine the initial positions of the inclusions by requiring a minimal distance of $3a = 0.06R$ to the elastic spherical surface.

III. GLOBALLY TWISTED STRUCTURES

To numerically generate the globally twisted structures, we start from layers of hexagonally arranged magnetic inclusions [51,67–69]. These layers are all oriented parallel to the xy plane and spaced equally from each other in their normal direction by a distance $d_{\text{layer}} = 0.11R$. The center layer is located in the plane $z = 0$. In the initial, nonmagnetized situation, the hexagonal particle arrangements within each layer are in a state rotated by an angle of $\gamma z/d_{\text{layer}}$ relative to the arrangement in the plane $z = 0$. This corresponds to a globally twisted configuration of the inclusions when compared to straight chainlike aggregates aligned parallel to the z axis. Here we consider small angles $\gamma \lesssim 0.159\pi$ to preserve the chainlike structure, see Fig. 2. The lattice constant within each plane, which equals the lateral distance between the chains, is set to $d_{\text{chain}} = 0.25R$. Overall, this leads to 623 magnetizable inclusions in 55 chains. An illustration of an initial structure is presented in Fig. 3, where we have, however, increased d_{chain} to $0.5R$ for clarity. In the numerical evaluation, we consider the range $0 \lesssim \gamma \lesssim 0.159\pi$ in steps of approximately 0.0016π. We distinguish four possible values of the Poisson ratio: $\nu = 0.5$ (incompressible), $\nu = 0.3$, $\nu = 0$, and $\nu = -0.5$ (auxetic).

As a first step, we focus on the following spherical harmonic expansion parameters for the resulting overall surface distortions: $u_{00}^{\perp}$, $u_{20}^{\perp}$, and u_{10}^{φ}. The coefficient $u_{00}^{\perp}$ quantifies overall changes in volume of the composite material. Positive values correspond to an increase in volume, while negative values correspond to a decrease in volume. Next, the coefficient $u_{20}^{\perp}$ describes a relative elongation ($u_{20}^{\perp} > 0$) or contraction ($u_{20}^{\perp} < 0$) along the direction of magnetization, here along the z axis. Most important for our investigation in the present context is the parameter u_{10}^{φ}. This coefficient is set by the lowest mode of a twist-type deformation around the z axis. For a counterclockwise rotation of the upper hemisphere against

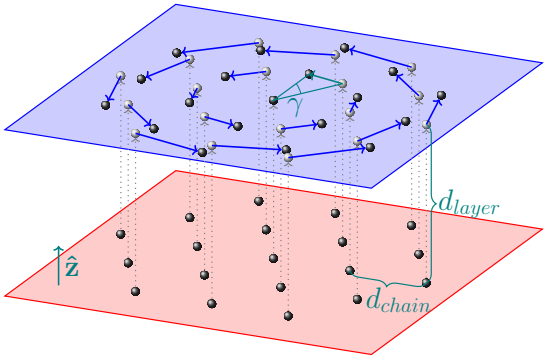

FIG. 2. Illustration of two layers of hexagonally arranged magnetizable inclusions inside the elastic material. d_{layer} sets the vertical distance between two layers, d_{chain} the in-plane particle distance. We set $d_{\text{chain}} = 0.25R > d_{\text{layer}} = 0.11R$, which implies vertically aligned, chainlike aggregates. Here, for illustration, d_{layer} is exaggerated. The upper arrangement shows a rotation by an angle γ relative to the lower arrangement, where we chose $\gamma = \pi/6$ for reasons of visibility. To emphasize the twist from layer to layer, we plot the positions corresponding to the lower layer in the upper layer as gray spheres, together with a dotted arrow that shows their vertical identification. Having applied a rotation by γ to the structure from the lower layer, the positions marked by dark spheres result. We indicate this in-plane rotational displacement by blue in-plane arrows. In the teal triangle, we illustrate the definition of the angle γ.

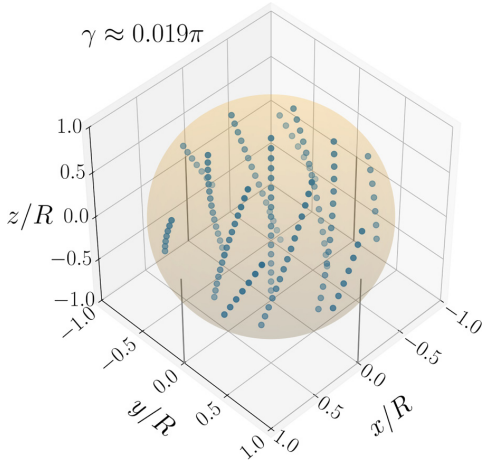

FIG. 3. Illustration of an example for the initial structure of the magnetizable inclusions, indicated as small (blue) spheres, inside the larger elastic sphere. This structure is generated from hexagonally arranged parallel chainlike aggregates of particles, where each horizontal layer of particles is rotated relative to the next particle layer underneath by an angle γ, see Fig. 2. In this illustration, we chose $\gamma \approx 0.019\pi$. Moreover, for better visibility, we here set $d_{\text{chain}} = 0.5R$. Instead, for our actual numerical evaluation, we used a value of $d_{\text{chain}} = 0.25R$.

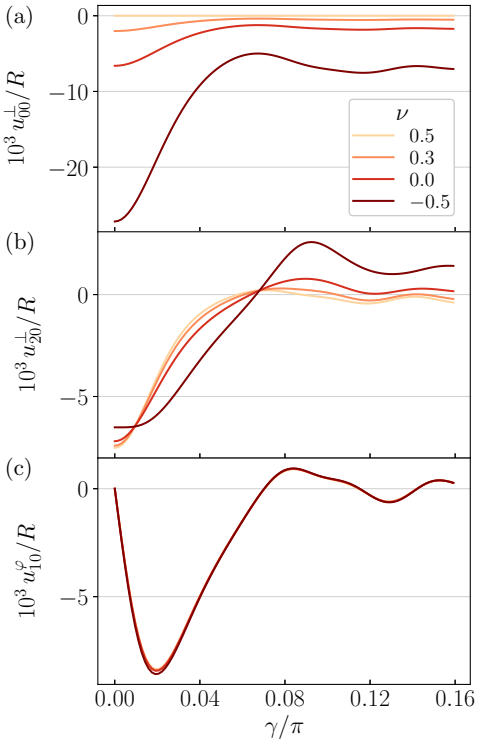

FIG. 4. Resulting overall surface displacement field of the spherical magnetoelastic composite upon magnetization for an initially globally twisted configuration of the magnetizable inclusions. To quantify perpendicular surface displacements, we plot the two coefficients (a) $u_{00}^{\perp}$ and (b) $u_{20}^{\perp}$, indicating overall volume changes and overall elongation along the magnetization direction relative to lateral contraction, respectively. To quantify the lowest mode of an overall twist deformation around the magnetization axis, we plot the coefficient (c) u_{10}^{φ}. In all three cases, we display the behavior with increasing angle γ, characterizing the global twist of the initial nonmagnetized structure of inclusions (see Fig. 2 for the definition of γ). Moreover, we show graphs for the four different values of the Poisson ratio, namely, $\nu = 0.5$, $\nu = 0.3$, $\nu = 0$, and $\nu = -0.5$.

the lower hemisphere it becomes $u_{10}^{\varphi} > 0$. For a reversed mutual sense of rotation, one obtains $u_{10}^{\varphi} < 0$.

The three coefficients $u_{00}^{\perp}$, $u_{20}^{\perp}$, and u_{10}^{φ} are shown in Fig. 4 when the aforementioned particle structures are magnetized. We have not included the data for negative values of γ because the curves in Figs. 4(a) and 4(b) are mirror symmetric with respect to the line $\gamma = 0$, while the curve in Fig. 4(c) features a point symmetry with respect to the origin.

As a first result, we infer from Fig. 4(a) that the overall volume is constant ($u_{00}^{\perp} \approx 0$) for $\nu = 0.5$, as expected for an incompressible material. With decreasing Poisson ratio, we find that the elastic sphere shrinks more and more upon magnetization. Naturally, this volume decrease is maximal for $\gamma = 0$, i.e., straight chains of magnetizable inclusions. In this case, the induced attraction between the particles along each

chain is strongest. When increasing γ, the volume decrease becomes smaller and oscillates for higher values of γ.

Similarly, we infer from Fig. 4(b) that the overall contraction along the magnetization direction relative to a lateral expansion, as quantified by $u^{\perp}_{20}$, is strongest for $\gamma = 0$ for the same reason as above. This effect is most pronounced for incompressible materials because the contraction along the field implies lateral expansions for reasons of volume conservation. In contrast to that, the auxetic nature for $\nu = -0.5$ counteracts the lateral expansion for $\gamma = 0$. The oscillations for increasing values of γ can be found in this coefficient as well.

When we focus on the behavior of u^{φ}_{10} in Fig. 4(c), we observe that it is almost independent of the Poisson ratio. This is expected because a pure twist-type deformation leaves the total volume unchanged. A small effect of the Poisson ratio is still present and can most likely be attributed to nonlinear effects revealed by our iterative scheme, i.e., to the effects of the resulting displacements of the magnetic inclusions, which are larger for more compressible materials. Furthermore, we do not observe any torsional deformation for $\gamma = 0$ because our initial configuration is not twisted in this case. Increasing γ from zero, we see that the corresponding values of u^{φ}_{10} first become more and more negative. The sign here represents the sense of the induced torsional deformation of the composite, which is opposing the sense of initial twist of the initial structure. We reach a maximum magnitude of this twist deformation at $\gamma \approx 0.019\pi$. For larger values of γ, the magnitude of u^{φ}_{10} again decreases. This effect results from the increasing distance between the inclusions with increasing γ, implying a decreasing magnetic interaction. At even larger values of γ, u^{φ}_{10} oscillates around zero. We return to this feature in Sec. V.

In practice, one would typically be interested in the situation of maximum observed effect. We therefore concentrate on the system for $\gamma \approx 0.019\pi$. First, we checked how the magnitude of the induced torsion around the z axis varies with the height z above or below the horizontal center plane (the xy plane). For this purpose, we calculated the average azimuthal angular displacement of the horizontal plane parallel to the xy plane at height z as

$$\Delta\varphi(z) = \left\langle \arctan\left(\frac{u^{\varphi}}{\sqrt{R^2 - z^2}}\right)\right\rangle_z, \tag{6}$$

where $\langle \ldots \rangle_z$ denotes an average over all surface points at which u^{φ} was evaluated at a given height z. We found that this quantity is approximately proportional to z. Furthermore, we find that it is nearly independent of the Poisson ratio, in agreement with the behavior of u^{φ}_{10} in Fig. 4(c).

As a further visualization of the magnetically induced deformation of the spherical elastic systems, again for angles of initial global twist of $\gamma \approx 0.019\pi$ and for the four values of the Poisson ratio as in Fig. 4, we illustrate in Fig. 5 the types and magnitudes of deformation associated with the three main modes that we have focused on, namely, $u^{\perp}_{00}$, $u^{\perp}_{20}$, and u^{φ}_{10}. For this purpose, we show in each case the elastic sphere in the undeformed state in blue. The sphere in the deformed state is shown in ocher. Only the modes with expansion coefficients $u^{\perp}_{00}$ and $u^{\perp}_{20}$, associated with the overall change in volume and the relative elongation along the axis of the magnetic field,

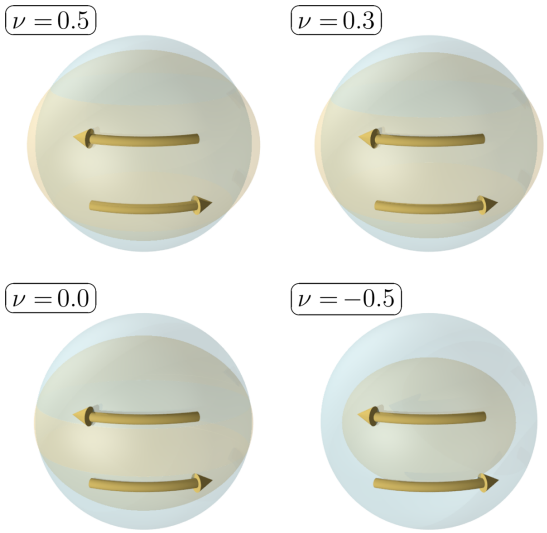

FIG. 5. Illustrations of the differences between the undeformed spherical state of each system (blue) and its deformed state (ocher) upon magnetization for elastic spheres containing globally twisted structures of the magnetic inclusions. The structures initially feature the same value of γ as in Fig. 3. Only the effects of the modes $u^{\perp}_{00}$ and $u^{\perp}_{20}$ are included to draw the deformed spheres. These deformations are represented (approximately) quantitatively; however, we have increased their magnitudes by a factor of 50 for illustration. Moreover, the deformation associated with the mode u^{φ}_{10}, representing the magnitude as well as the direction of the magnetically induced torsional deformation, is encoded by the lengths (increased by a common global factor for illustration) and directions of the bent (ocher) arrows. Results are displayed for the same four values of the Poisson ratio ν as in Fig. 4.

respectively, are used to determine the shape of the deformed sphere in these illustrations. We multiply the values of $u^{\perp}_{00}$ and $u^{\perp}_{20}$ by a factor of 50 for visualization. Furthermore, the lengths of the bent arrows encode the magnitude of u^{φ}_{10} and the sense of the associated torsional deformation.

Considering the results, Fig. 5 confirms the aforementioned trends of the overall shrinking volume for compressible materials and the additional relative contraction along the axis of the magnetic field. The latter process is linked to an expansion/contraction along the lateral directions for the positive/negative value(s) of the Poisson ratio. Furthermore, we see that the magnitude of the induced twist-type deformation is approximately independent of the Poisson ratio.

Next, in Fig. 6 we provide additional information on the importance of different modes involved in the overall surface displacement, obtained by our expansion of the perpendicular and tangential components of the surface displacement field into spherical harmonics. Again, we concentrate on the value of $\gamma \approx 0.019\pi$, and we use the same four values of the Poisson ratio as in Fig. 4. We select the expansion coefficients a_{lm} of ten representative spherical harmonic modes for each component of the displacement field according to the following scheme. First, for each mode the value of

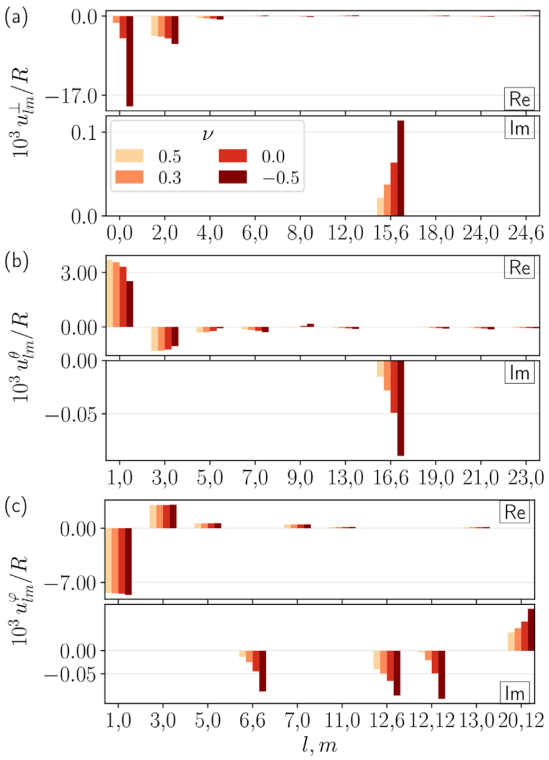

FIG. 6. For the same systems considered in Fig. 4, we depict for $\gamma \approx 0.019\pi$ the values of the expansion coefficients into spherical harmonics for the three components (a) $u^{\perp}$, (b) u^{θ}, and (c) u^{φ} of the overall surface displacement field. The value of γ is the same as in Fig. 3. The real part is always plotted along the upper line, while the lower line illustrates the imaginary part of the corresponding spherical harmonic expansion coefficient. We use bar plots with the four colors corresponding to the four selected values of the Poisson ratio $\nu = 0.5$, $\nu = 0.3$, $\nu = 0$, and $\nu = -0.5$. In this way, the values of the expansion coefficients for ten representative modes are displayed for the three components of the surface displacement field. Particularly, we note the dominating character of the mode $(l, m) = (1, 0)$ for u^{φ}, which is associated with the type of twist actuation upon magnetization that we here focus on. Additionally, we include matrix plots to illustrate the magnitudes of the expansion coefficients associated with these and additional modes in the Supplemental Material [70].

a_{lm} of highest magnitude is identified from the four values associated with the different Poisson ratios ν. These a_{lm} are then ordered according to their absolute values, and we find the labels l, m for the ten largest ones. Due to the high degree of symmetry of our configurations, the most dominant modes are those of $m = 0$. However, we observe nonvanishing modes that depend on φ as well, characterized by $m \neq 0$. This leads to complex expansion coefficients. Since $u^{\perp}$, u^{θ}, and u^{φ} are real, we can find values for negative m via the relation $a_{l(-m)} = (-1)^m a^*_{lm}$, where the star denotes complex conjugation. Consequently, for real a_{lm} the corresponding spherical harmonics result together with $a_{l(-m)}$ in a $\cos(m\varphi)$ mode, while purely imaginary a_{lm} result in a $-\sin(m\varphi)$ mode. The real and the imaginary parts of a_{lm} are shown separately in the plots. (For an illustration of the values of the coefficients a_{lm} in a different way, namely, matrix plots, together with values for additional modes and for modes of negative m, we refer to the Supplemental Material [70].)

Figure 6 confirms that those coefficients that we have been concentrating on so far indeed dominate the spectrum. For $u^{\perp}$, see Fig. 6(a), these correspond to an overall volume change ($l = m = 0$), especially for auxetic materials and except for $\nu = 0.5$, and to an overall contraction along the magnetization direction relative to a lateral expansion ($l = 2$, $m = 0$), with small higher-order corrections. All coefficients odd in l for $m = 0$ are approximately zero here. We observe some very small contributions related to the sixfold symmetry about the z axis in the modes of $l = 15$, $m = 6$ and $l = 24$, $m = 6$.

Turning to u^{θ} in Fig. 6(b), significantly smaller absolute values of the expansion coefficients are obtained. Here, as for u^{φ} in Fig. 6(c), the coefficients even in l vanish approximately for $m = 0$, in contrast to the case for $u^{\perp}$. The most important contribution to u^{θ} in the mode $l = 1$, $m = 0$ corresponds to an overall surface displacement towards the equator on both the upper hemisphere and the lower hemisphere upon magnetization. In the incompressible case this effect is most pronounced, as we then have the strongest expansion of the sphere in the lateral directions. Again, higher-order contributions emerge which strengthen the aforementioned effect in the vicinity of the equatorial plane.

Considering u^{φ} in Fig. 6(c) reveals the most important mode in the present context, associated with the twist deformation through magnetization. As noted already above, the mode $l = 1$, $m = 0$ is associated with a rotation around the magnetization direction of the upper hemisphere relative to the lower hemisphere. This mode dominates the overall behavior by its absolute value [only exceeded by the mode corresponding to overall volume expansion for the auxetic case $\nu = -0.5$ in Fig. 6(a)]. Near the equatorial plane, higher-order modes in combination still support the effect of the upper hemisphere being rotated relatively to the lower hemisphere.

IV. HELICAL STRUCTURES

As a next step we address helical structures of the magnetizable particles embedded in the same elastic spheres as before, arranged side by side. In contrast to the globally twisted structure of parallel chainlike aggregates investigated in Sec. III, we now consider each chainlike element by itself to feature an initial helical shape. To set up our numerical systems, we again start from hexagonal arrangements of aligned chainlike aggregates as before, this time for $d_{\text{chain}} = 0.5R$, i.e., for double the distance to each other. As above, the vertical distance of the horizontal layers of particles is set to $d_{\text{layer}} = 0.11R$. However, instead of initiating each layer rigidly rotated relatively to its upper and lower neighboring one, we now rigidly displace each layer laterally by adding a

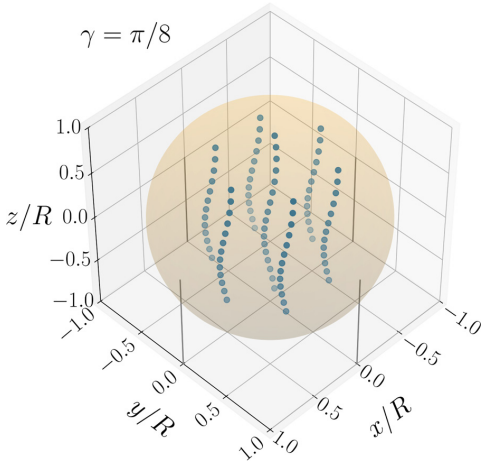

FIG. 7. Illustration of initially nonmagnetized particle structures composed of helical elements of magnetizable inclusions, arranged side by side. Within each layer parallel to the xy plane, the particles form a hexagonal lattice of lattice constant $d_{\text{chain}} = 0.5R$. The layers have a vertical spacing of $d_{\text{layer}} = 0.11R$. Furthermore, we here chose the radius of each helix to be $r_{\text{helix}} = 0.05R$. In the depicted case, we set $\gamma = \pi/8$.

vector

$$\mathbf{r}_{\text{helix}}(z) = r_{\text{helix}} \begin{pmatrix} \cos(\gamma z/d_{\text{layer}}) \\ \sin(\gamma z/d_{\text{layer}}) \\ 0 \end{pmatrix}. \tag{7}$$

This lateral shift introduces an additional parameter, namely, r_{helix}. Here we show results for structures corresponding to two different values $r_{\text{helix}} = 0.05R$ and $r_{\text{helix}} = 0.1R$, see Figs. 7 and 8, respectively. In both cases, we fit 95 magnetizable inclusions into our elastic sphere, avoiding inclusions

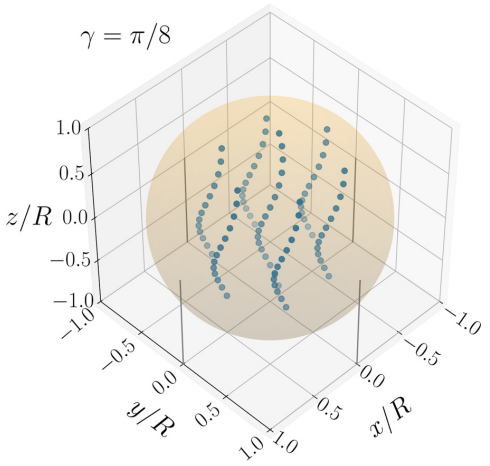

FIG. 8. Same as in Fig. 7, but for $r_{\text{helix}} = 0.1R$.

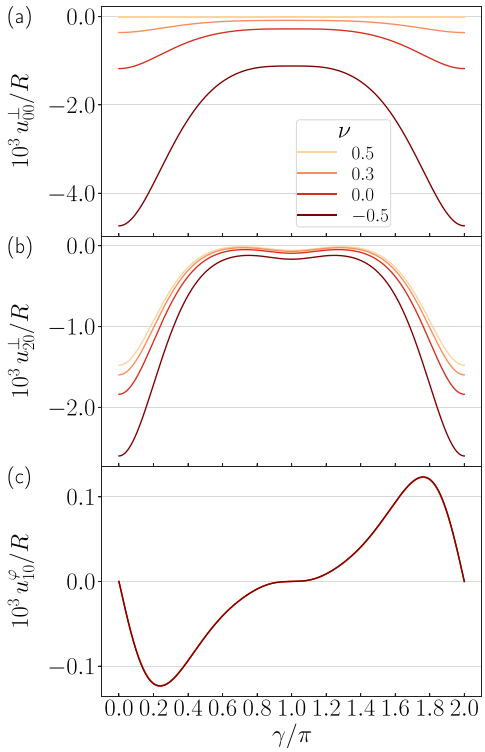

FIG. 9. Same as in Fig. 4 but for the systems composed of helical structure elements of magnetizable inclusions arranged side by side instead of a globally twisted structure. Here, $r_{\text{helix}} = 0.05R$, as in Fig. 7.

that would need to be deleted for particular values of γ. Importantly, the overall structure in each case is no longer sixfold rotationally symmetric about the z axis nor globally screw-symmetric within the spherical boundaries. In the center layer for $z = 0$, all helices start with a particle deflection in the x direction, $\mathbf{r}_{\text{helix}}(0) = r_{\text{helix}}\hat{\mathbf{x}}$, according to Eq. (7). The resulting structures composed of helical aggregates are depicted in Figs. 7 and 8. Using our numerical approach, we evaluate the full range $0 \leqslant \gamma \leqslant 2\pi$ in steps of $\pi/360$.

As in Sec. III, we first address the expansion coefficients $u_{00}^{\perp}$, $u_{20}^{\perp}$, and u_{10}^{φ} for the overall displacements upon magnetization as functions of γ. The curves in Figs. 9(a), 9(b), 10(a), and 10(b) show a mirror symmetry with respect to the vertical line $\gamma = \pi$, while those in Figs. 9(c) and 10(c) feature a point symmetry with respect to the point $(\gamma, u_{10}^{\varphi}) = (\pi, 0)$. This is expected because Y_{00} and Y_{20} are even in z, while Y_{10} is odd. Obviously, the results for helices of an initial twist $\pi < \gamma < 2\pi$ can be mapped onto those for a corresponding initial twist of $2\pi - \gamma$. Illustratively, this corresponds to helices that differ only by their sense of twist. The resulting displacements are of much smaller magnitude when compared to the results for the globally twisted arrangements in Fig. 4, which can already be expected from the lower total number of inclusions for the helical structures (95 here versus 623 inclusions in Fig. 4).

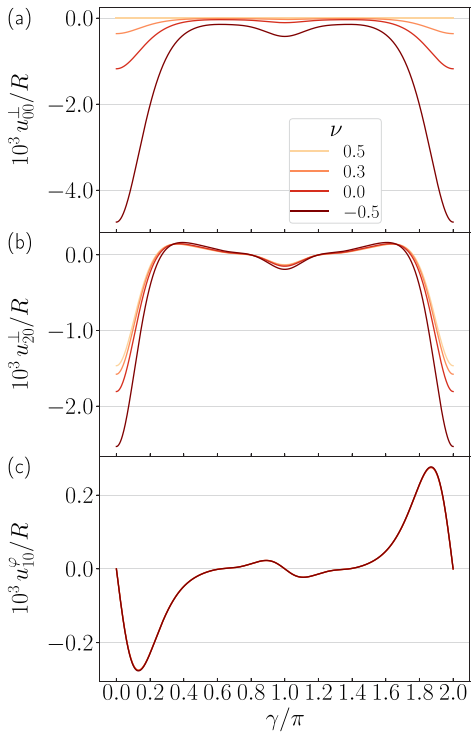

FIG. 10. Same as in Fig. 9 but for setups with $r_{\text{helix}} = 0.1R$.

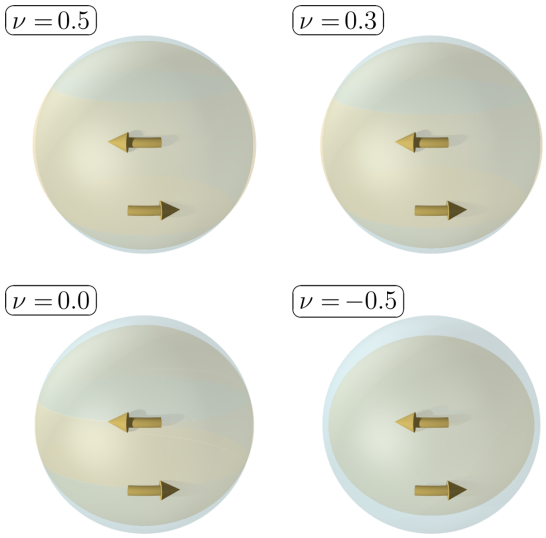

FIG. 11. Same as in Fig. 5, but here for a system containing helical structures of radius $r_{\text{helix}} = 0.05R$ arranged side by side, see Fig. 7, for $\gamma \approx 0.24\pi$. This value of γ corresponds to the minimum of the curves in Fig. 9(c) and thus to the maximal magnitude of induced twist actuation. Here the rescaling factor for illustrating the overall changes in volume and the relative elongation along the direction of the imposed magnetic field is two times bigger than in Fig. 5 for the case of the initially globally twisted structures. Moreover, we rescale the lengths of the bent arrows by an additional factor of 20 when compared to Fig. 5.

We start by considering the configurations of $r_{\text{helix}} = 0.05R$. In Fig. 9(a), we again find that the elastic sphere, except for $\nu = 0.5$, shrinks as a whole, specifically for the smallest and largest values of γ. For these values, the chains are straightest and therefore show the maximal internal longitudinal attractive forces. Furthermore, the absolute magnitude of overall contraction strongly increases with decreasing Poisson ratio, i.e., for more compressible spheres.

Next we address in Fig. 9(b) the elongation along the magnetization relative to the lateral contraction. Qualitatively, we infer a similar behavior as in Fig. 9(a). Here we observe a further, much smaller minimum for $\gamma = \pi$ because we have effectively generated two chains of distance $2r_{\text{helix}} = 0.1R$ out of each helix. Apart from that, auxetic materials show stronger relative contractions along the magnetization axis.

Concerning the magnitude of the twist actuation quantified by Fig. 9(c), we again find a pronounced minimum, here around $\gamma \approx 0.24\pi$. In line with the point symmetry of the curve mentioned above, the corresponding maximum is located at $\gamma \approx 1.76\pi$. As in Sec. III, u^{φ}_{10} as a measure for the twist actuation is approximately independent of the Poisson ratio. This behavior will also be discussed in Sec. V.

Figure 10 shows corresponding results for $r_{\text{helix}} = 0.1R$. The qualitative picture is similar to Fig. 9, with the same symmetries of the curves. We notice that the aforementioned minimum at $\gamma = \pi$ [Fig. 10(b)] is more pronounced and can be found in $u^{\perp}_{00}$ [Fig. 10(a)] as well. Concerning the coefficient u^{φ}_{10} quantifying the twist actuation, we see that the minimum is shifted to smaller values of γ, namely, to $\gamma \approx 0.13\pi$, and is increased in magnitude by a factor of approximately 2.23. Moreover, some oscillations together with positive values of u^{φ}_{10} occur at higher values of $\gamma < \pi$. Again, we will return to this topic in Sec. V.

To further visualize these deformations, we again add in Figs. 11 and 12 corresponding illustrations in analogy to Fig. 5. The values of γ are chosen as those identified for maximized amplitudes of magnetically induced torsional deformations, represented by the minima in the curves of Figs. 9(c) and 10(c). For $r_{\text{helix}} = 0.05R$ and $r_{\text{helix}} = 0.1R$, we show the results in Figs. 11 and 12, respectively. Here $u^{\perp}_{00}$ and $u^{\perp}_{20}$ are multiplied by a factor of 100 for illustration. The lengths of the bent arrows are rescaled by an additional factor of 20 when compared to Fig. 5 in Sec. III.

These different factors already indicate that the overall induced deformations are much smaller in the present cases of included helical structural elements when compared to the investigated globally twisted structures in Sec. III. Specifically, this remark concerns the twist deformation. Comparing the results for the two types of helical structures, we observe that in the case of $r_{\text{helix}} = 0.05R$ the amount of torsional deformation is much smaller (less than half the magnitude) than in the case of $r_{\text{helix}} = 0.1R$. However, the reduction in overall volume and the relative contraction along the axis of

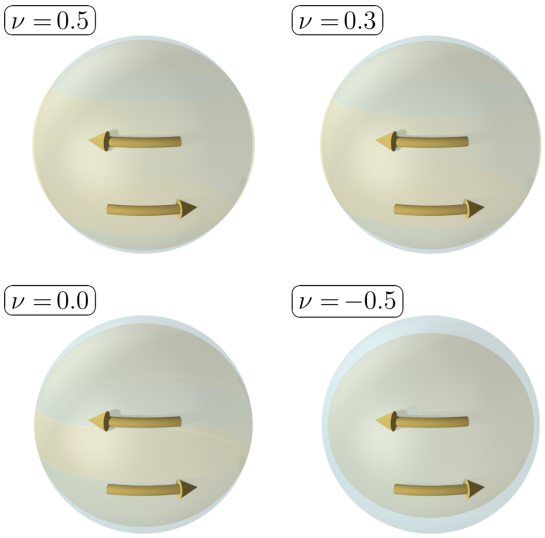

FIG. 12. Same as in Fig. 11 but for a system of the included helical structures of radius $r_{\text{helix}} = 0.1R$, as illustrated in Fig. 8, here for $\gamma \approx 0.13\pi$. The latter value identifies the minimum on the curves in Fig. 10(c).

the magnetic field are both very similar in magnitude, albeit slightly bigger in the former case.

We continue with a discussion on the coefficients obtained from an expansion of the surface displacement fields into spherical harmonics for the same two configurations. Corresponding values are displayed in Figs. 13 and 14 for the configurations of $r_{\text{helix}} = 0.05R$ and $r_{\text{helix}} = 0.1R$, respectively. Again, we plot ten relevant modes for each of the three components of the surface displacement field identified according to the same scheme as in Sec. III. (As before, additional illustrations in terms of matrix plots can be found in the Supplemental Material [70].)

Figure 13(a) shows that $u^{\perp}_{00}$ and $u^{\perp}_{20}$ dominate the overall behavior (for $\nu = 0.5$ we correctly find $u^{\perp}_{00} \approx 0$). Some higher-order contributions to $u^{\perp}$ are observed, however, of a relative magnitude of less than 15% of the dominant mode, given by either $u^{\perp}_{00}$ or $u^{\perp}_{20}$. The configurations are less symmetric than those in Sec. III, and we observe a stronger influence of the modes of $m \neq 0$, particularly for $m = 1$, which characterizes the lowest-order nontrivial dependence on φ.

Next, Fig. 13(b) identifies u^{θ}_{10} as a dominating mode of u^{θ} for $\nu \gtrsim 0$. The same was observed in Fig. 6(b). In general, higher-order modes enter as well, especially for auxetic materials. As before, the maximal magnitude of the modes described by u^{θ} is smaller than the magnitude of the dominating mode for $u^{\perp}$.

The modes relevant to torsional deformations of the elastic material are addressed in Fig. 13(c). We observe again the most dominant mode to be the lowest one, i.e., u^{φ}_{10}. However, we also find another mode to be almost equally as strong, namely, u^{φ}_{41}. This is most likely an effect related to the

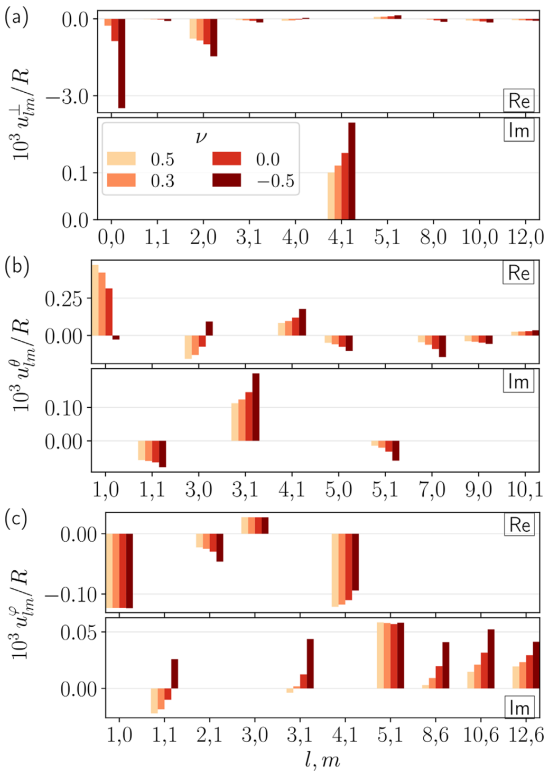

FIG. 13. Same as in Fig. 6 but for the configuration underlying Fig. 9 for $\gamma \approx 0.24\pi$. See also the Supplemental Material for corresponding matrix plots [70].

specific helical structure that was used in our investigation. Nevertheless, both modes are of smaller magnitude when compared to the modes of u^{θ} and even smaller when compared to $u^{\perp}$. Thus, the twisting actuation for this structure is only of secondary importance when compared, for instance, to the global volume change or relative elongation along the magnetization direction.

In addressing the results for the structures of $r_{\text{helix}} = 0.1R$ in Fig. 14, we mainly focus on the differences when compared to the situation in Fig. 13. Due to the larger magnitude of r_{helix}, the asymmetry of the configurations with respect to rotations around the z axis by $\pi/3$ is still more pronounced, and we thus observe even more relevant modes for $m \neq 0$. This trend concerns all three components of the surface displacement field in Figs. 14(a), 14(b), and 14(c). Differences between Figs. 13 and 14, especially in the mode numbers for $m \neq 0$, can to some extent be traced back to the different value of γ of the investigated structure, according to the different locations of the minima in Figs. 9(c) and 10(c).

Particularly when focusing on the torsional deformation addressed in Fig. 14(c), we observe that the mode u^{φ}_{10} identifying a global twist deformation is not even the strongest one here. Instead, the strongest mode is u^{φ}_{31}. This mode is symmetric for $z \to -z$, implying that it cannot describe an

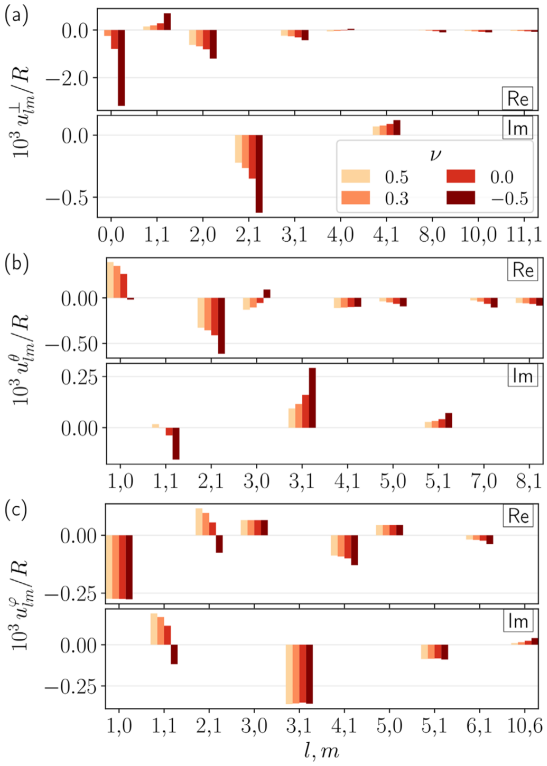

FIG. 14. Same as in Fig. 6 but for the configuration underlying Fig. 10 for $\gamma \approx 0.13\pi$. See also the Supplemental Material for corresponding matrix plots [70].

overall twist deformation corresponding to a relative rotation of the top hemisphere with respect to the bottom hemisphere. However, the lowest mode of twist actuation u^{φ}_{10} has a much higher absolute magnitude when compared to the structures of $r_{\text{helix}} = 0.05R$ in Fig. 13(c). Apparently, the radius of the helical elements can have a pronounced effect, partly of antagonistic consequences. If such systems are transferred to actual applications, it is therefore important to adjust the radius of the helical elements to the desired behavior.

Overall, we observe a significantly more pronounced influence of higher-order modes and particularly modes depending on φ for the displacement fields in Figs. 13 and 14 when compared to the results in Fig. 6. Importantly, the ratio of the magnitudes of u^{φ}_{10} to the magnitudes of $u^{\perp}_{00}$ (except for $\nu = 0.5$) or $u^{\perp}_{20}$ is much smaller. Thus, the twist actuation is not as pure for the investigated structures composed of helical elements, and we conclude that the globally twisted structures of Sec. III are in general more promising candidates to construct a magnetoelastic twist actuator.

V. MINIMAL ANALYTICAL MODEL

Having presented our numerical results for the functions $u^{\varphi}_{10}(\gamma)$ in Secs. III and IV, shown in Fig. 4(c) as well as in Figs. 9(c) and 10(c), respectively, we here discuss how we can understand the behavior qualitatively in simpler terms. To this end, we propose a minimal analytic model based on the dipole-dipole force between the inclusions, see Eq. (2). If we only concentrate on the magnetic interactions between two nearest neighbors on a single chain, the geometry can be parameterized as depicted in Fig. 15.

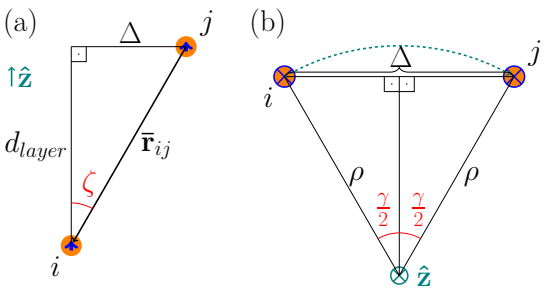

FIG. 15. In a simplified discussion, we consider the interactions between the magnetized nearest-neighboring particles i and j on an initially twisted chainlike aggregate. Their dipole moments, aligned with the center axis $\hat{\mathbf{z}}$, are depicted by small arrows. We denote the vector from the position of j to the position of i by $\bar{\mathbf{r}}_{ij}$. In (a), their distance along the z axis is given by d_{layer}, and their lateral distance is denoted as Δ. ζ quantifies the angle between the z axis and $\bar{\mathbf{r}}_{ij}$ at the site of particle i. In (b) we show a bottom view of the configuration. We introduce two right-angled triangles to relate the lateral distance Δ between the particles to the radial distance ρ of the particles from the center axis, around which the initial twist of the structure was set. The angle γ was defined previously for both the globally twisted structures and the helically twisted structural elements arranged side by side; see Fig. 2 and Eq. (7), respectively.

Obviously, the situation in reality is more complex as magnetic dipole interactions are long-ranged, leading to magnetic interactions between all particles. Furthermore, due to the magnetically induced deformations, the particle positions are affected as well, which in turn changes the magnetic interactions, see Sec. II. Nevertheless, considering pairwise nearest-neighbor interactions along one chain will allow for a basic qualitative description, see below.

Since we are interested in the magnetically induced overall twist deformation, we here focus on the magnetic force components perpendicular to the magnetization direction, i.e., in the xy plane. These in-plane force components are the source of torsional deformations around the z axis. Instead, the z components of the magnetic forces are associated with axial contractions. For initially twisted particle configurations and not-too-large values of γ, the in-plane force components aim to straighten the chains. Defining ζ as the angle between $\hat{\mathbf{m}}$ and the connecting vector $\bar{\mathbf{r}}_{ij}$ between two nearest-neighboring particles i and j, see Fig. 15(a), the magnitude F_{xy} of the in-plane force component on particle i, exerted by particle j, see Eq. (2), is given by

$$F_{xy}(\zeta) = \frac{3\mu_0 m^2}{4\pi} \frac{\cos^4\zeta}{d^4_{\text{layer}}} |5\sin\zeta\cos^2\zeta - \sin\zeta|. \qquad (8)$$

Here we have inserted $\hat{\mathbf{m}} \cdot \hat{\bar{\mathbf{r}}}_{ij} = \cos\zeta$, $\bar{r}_{ij} = d_{\text{layer}}/\cos\zeta$, and $\sin\zeta$ for the component of $\hat{\bar{\mathbf{r}}}_{ij}$ in the xy plane.

Next, we maximize $F_{xy}(\zeta)$ with respect to ζ to find an optimal configuration of particles i and j that supports a maximized twist actuation. The maximum is found for

$$\cos^2\zeta_{\max} = \frac{1}{2} + \frac{1}{2}\sqrt{\frac{19}{35}}. \tag{9}$$

If we now restrict the solutions to the range $0 < \zeta < \pi/2$, we find the unique solution

$$\zeta_{\max} = \arccos\left(\sqrt{\frac{1}{2} + \frac{1}{2}\sqrt{\frac{19}{35}}}\right) \approx 0.118\pi. \tag{10}$$

When we compare to our previous results, we can use the relations deduced from Fig. 15(a),

$$\tan\zeta = \frac{\Delta}{d_{\text{layer}}}, \tag{11}$$

and Fig. 15(b),

$$\sin\left(\frac{\gamma}{2}\right) = \frac{\Delta}{2\rho}, \tag{12}$$

where we have introduced ρ as the distance of the inclusions i and j from the axis of the initial twist of the corresponding structure. To relate the result of this analytical consideration to our numerical evaluation, we find from Eqs. (11) and (12)

$$\gamma_{\max} = 2\arcsin\left(\frac{d_{\text{layer}}}{2\rho}\tan\zeta_{\max}\right), \tag{13}$$

where $\gamma_{\max}$ implies a maximized in-plane torsional force component, based on this simplified analytical consideration. For the systems addressed in Sec. IV, to compare these analytical and the numerical results, we can simply set $\rho = r_{\text{helix}}$. For the globally twisted configurations in Sec. III, the situation is more complex, as there is not a single value of ρ that is equal for all chainlike aggregates, but the value of ρ depends on which chain we consider.

To illustrate this more complex dependence for the globally twisted structures on the angle γ, quantified by $u_{10}^{\varphi}(\gamma)$, we have generated additional globally twisted configurations while removing from the systems considered in Sec. III those chainlike elements that have a value of ρ smaller than a certain threshold. Illustratively, this corresponds to only considering those chains that are located outside a coaxial cylinder of diameter 2ρ. In Fig. 16 we present results for cutoff values for ρ of $R/2$, $2R/3$, and $\sqrt{13}\,d_{\text{chain}} \approx 0.901R$, where the latter value marks the outermost chains. For comparison, we have added in Fig. 16 the results for the configurations of Sec. III as well. For this evaluation, we restrict ourselves to incompressible elastic materials ($\nu = 0.5$) for clarity.

The main result of Fig. 16 is that as we increase the lower threshold value of ρ, the global minimum is shifted towards lower values of γ. For all chains considered, see Sec. III, the value of γ corresponding to a maximized twist deformation is $\gamma \approx 0.019\pi$. Introducing a cutoff for ρ of $R/2$, this value is reduced to $\gamma \approx 0.018\pi$. Moving on to a cutoff for ρ of $2R/3$, it is further reduced to $\gamma \approx 0.016\pi$. When keeping only the outermost chains, we obtain $\gamma \approx 0.014\pi$ for the location of the maximized twist deformation. Moreover, we observe a decrease in magnitude of the minimum of u_{10}^{φ}. This contains, however, a trivial effect, as we decrease the number of inclusions for increasing cutoff values for ρ. More precisely, we find 623, 324, 168, and 60 inclusions for the four different systems addressed in Fig. 16.

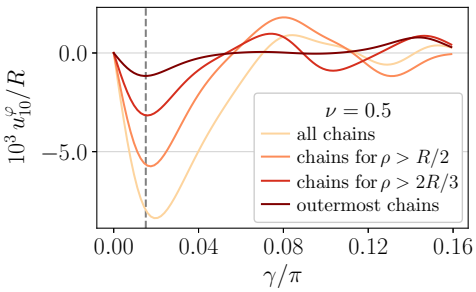

FIG. 16. Same as in Fig. 4(c) but for configurations for which we only consider those chains that have a minimal distance ρ from the axis of twist of the initial nonmagnetized structure. We show a comparison between the results of Fig. 4(c), here labeled as "all chains," and corresponding configurations that include only those chains for which $\rho > R/2$ and $\rho > 2R/3$. Furthermore, we show results for only keeping the outermost chains, i.e., chains of $\rho = \sqrt{13}\,d_{\text{chain}} \approx 0.901R$. In all cases, we only display the results for incompressible systems, i.e., for $\nu = 0.5$, for clarity. Particularly, we note how the position of the global minimum is slightly shifted towards smaller values of γ for configurations of larger average values of ρ for the chains. The vertical gray dashed line marks the value $\gamma_{\max} \approx 0.015\pi$ as obtained from Eqs. (10) and (13) for the outermost chains.

When we now compare our numerical results to the minimal analytical model according to Eqs. (10) and (13), we consider the configurations of only keeping the outermost chains. In this case, inserting $\rho \approx 0.901R$ into Eq. (13), we obtain a value of $\gamma_{\max} \approx 0.015\pi$; see the vertical dashed line in Fig. 16. This is only slightly bigger than the numerical value of $\gamma \approx 0.014\pi$. It shows a fair agreement, considering, for instance, the assumptions of including only nearest-neighbor particle interactions and rigid particle positions in the analytical model.

Next, we compare the numerical and analytical results for the structures composed of helical elements as considered in Sec. IV. Setting $\rho = r_{\text{helix}}$, we find from the analytical consideration $\gamma_{\max} \approx 0.28\pi$ and $\gamma_{\max} \approx 0.14\pi$ for $r_{\text{helix}} = 0.05R$ and $r_{\text{helix}} = 0.1R$, respectively. The results of our numerical investigation for u_{10}^{φ} were $\gamma \approx 0.24\pi$ and $\gamma \approx 0.13\pi$, respectively, see Sec. IV. While showing fair agreement concerning the involved approximations, our analytical model again shows a tendency of overestimating the numerical results, see above.

Within our minimal analytical model, we may equally well estimate analytically the lowest value of $\gamma > 0$ for which u_{10}^{φ} becomes zero. Again, we require a fixed value of ρ. From Eq. (8), we find that $F_{xy} = 0$ for a value $\zeta_0 > 0$ of

$$\zeta_0 = \arccos\left(\frac{1}{\sqrt{5}}\right) \approx 0.352\pi, \tag{14}$$

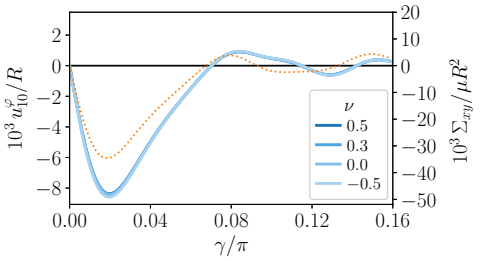

FIG. 17. Sum Σ_{xy} over the appropriately signed azimuthal magnetic force components acting on all particles as defined in the main text (dotted line) for the systems containing the globally twisted structures. The shape of the curve for Σ_{xy} qualitatively agrees with the shape of the curves for u_{10}^{φ} reproduced from Fig. 4(c) (solid lines) that quantify the induced overall torsional deformation.

corresponding to

$$\gamma_0 = 2\arcsin\left(\frac{d_{\text{layer}}}{2\rho}\tan\zeta_0\right) = 2\arcsin\left(\frac{d_{\text{layer}}}{\rho}\right). \qquad (15)$$

Inserting the value of ρ for the outermost chains in Fig. 16 implies $\gamma_0 \approx 0.078\pi$, while the numerical result for u_{10}^{φ} suggests $\gamma \approx 0.057\pi$. As before, we observe that the analytically determined value of γ exceeds that determined numerically. For the systems containing the helical structural elements, our analytical estimate does not imply any value of $0 < \gamma < \pi$ at which $F_{xy} = 0$, because $d_{\text{layer}} > r_{\text{helix}}$ in both cases. This is in line with our numerical results for $r_{\text{helix}} = 0.05R$, for which $u_{10}^{\varphi} < 0$ for all $0 < \gamma < \pi$. However, our numerical investigation reveals a value of $\gamma \approx 0.62\pi$, at which $u_{10}^{\varphi} = 0$ for $r_{\text{helix}} = 0.1R$.

As had become obvious above and from Fig. 16, comparing the simple analytical model approach to the numerical results for the complete globally twisted structures of Sec. III is less direct. The different chainlike aggregates in the system are located at different radial distances ρ from the center axis. These varying distances need to be taken into account.

To find a reasonable measure, we start from the magnetic forces $\mathbf{F}_i$ according to Eq. (2) on each particle i. We denote by $\hat{\boldsymbol{\varphi}}_i$ the local azimuthal unit vector in the spherical coordinate system at the position of particle i. To identify those force components that supposedly directly support the overall twist deformation, we project $\mathbf{F}_i$ onto $\hat{\boldsymbol{\varphi}}_i$ on the upper hemisphere and onto $-\hat{\boldsymbol{\varphi}}_i$ on the lower hemisphere. Particles i located on the center axis and on the equatorial plane are not taken into account. Finally, the sum over all force components obtained in this way is denoted as Σ_{xy}. It is plotted as the dotted line in Fig. 17, together with the results for u_{10}^{φ} as displayed in Fig. 4(c). Since the initial positions of the particles are used for this basic analytical evaluation, the curves for Σ_{xy} are independent of the value of the Poisson ratio ν.

Comparing these graphs, we notice that the force component Σ_{xy} as well as the curves for u_{10}^{φ} have a pronounced minimum at approximately the same value of $\gamma \approx 0.019\pi$. Moreover, for the lowest value of $\gamma > 0$ at which $\Sigma_{xy} = 0$ and $u_{10}^{\varphi} = 0$, we find $\gamma \approx 0.068\pi$ and $\gamma \approx 0.072\pi$, respectively.

In summary, we can estimate certain characteristic points on the curves of $u_{10}^{\varphi}(\gamma)$ by simple analytical model considerations. Often, it is sufficient to focus on the interactions between neighboring dipoles only. For the globally twisted structures, see Sec. III, the different distances of the chainlike aggregates from the center axis of the elastic sphere need to be taken into account for more quantitative evaluations. Nonaffine elastic deformations have not been included in the simple analytical model. Furthermore, our simplified analytical approach does not account for the change in magnetized particle positions during deformations included in our numerical description.

VI. CONCLUSIONS

To conclude, we have suggested a way to construct soft torsional actuators using magnetic gels and elastomers. For this purpose, we have addressed two different structural arrangements of the magnetizable inclusions in the elastic material: globally twisted structures and side-by-side arrangements of helical elements. Both are generated from initially hexagonally arranged parallel chainlike elements. For both configurations, we have explicitly calculated the resulting magnetostrictive distortion of the overall system upon magnetization. In this context, for reasons of analytical accessibility, we have here concentrated on systems of overall spherical shape. Particularly, we have focused on the degree of induced twist actuation, which we quantified using a spherical harmonic mode expansion of the surface displacement field.

Among the systems that we investigated, we found the globally twisted structures to show a significantly larger torsional actuation when compared to the systems containing helical elements arranged side by side. For the studied globally twisted structures, the overall deformational response is indeed dominated by a twist-type distortion. Instead, the overall twist response in the case of the embedded helical elements arranged side by side was less pure. Thus, it appears that the considered globally twisted structures are better suited to construct a soft torsional actuator. In the near future, these might also be the ones requiring less additional effort for actual fabrication.

Furthermore, we have quantified which degree of initial structural twist in the nonmagnetized state leads to a maximized torsional actuation. Such an optimized value arises from two antagonistic tendencies. If the internal structure is not twisted at all, then an overall torsional deformation cannot be induced. However, if the initial structure is twisted too much, then the interactions between the inclusions upon magnetization may even become repulsive for a too large lateral separation. We find an optimized value in between. In fact, these properties can be understood already on a qualitative basis by addressing the magnetic interactions between two neighboring particles on one initially deformed chainlike structural aggregate.

Concerning actual applications, soft magnetic actuators have the advantage that they can be addressed in a contactless way from outside by an external magnetic field and may respond relatively quickly on timescales of tens of milliseconds. This qualifies them, for instance, as candidates for microrobotic and microsurgical use [23,71]. Frequently, one is

interested in realizing maximized amplitudes of deformations or stresses. Here we have deliberately concentrated on comparatively small amplitudes of deformation. We emphasize that this is predominantly a necessary requirement by the employed method of calculation in the framework of linear elasticity theory, which then allows for a quantitative evaluation. Yet, in reality, various types of modification could increase and maximize the presented effects. For instance, the system size, particle size, and volume fraction could be increased, the mutual distances between the particles may be decreased, or a softer elastic matrix material could be used. By our work, we wish to stimulate investigations on such possible ways of optimization.

Overall, we hope that our study will inspire experimental realizations of corresponding soft magnetoelastic torsional actuators in the future. Such devices may find further possible applications, for instance, as microfluidic mixing actuators. Not only can twist deformations and thus torsional flows around such an element be induced upon request from outside by alternating magnetic fields, but also, due to the existence of an overall structural anisotropy axis associated with the axis of global twist, the mixing element can simultaneously be oriented by the direction of the external magnetic field. Moreover, as long as dynamic effects like leaking electrical currents do not play an important role, our results equally apply to the construction of corresponding devices from electrorheological gels and elastomers [14,72,73] using external electric fields for actuation.

ACKNOWLEDGMENTS

Some of the results in this paper have been derived using the HEALPix package [66]. The authors thank the Deutsche Forschungsgemeinschaft for support of this work through the priority program SPP 1681, Grant No. ME 3571/3.

[1] S. Aziz and G. M. Spinks, Mater. Horiz. **7**, 667 (2020).
[2] G. Filipcsei, I. Csetneki, A. Szilágyi, and M. Zrínyi, Adv. Polym. Sci. **206**, 137 (2007).
[3] M. R. Jolly, J. D. Carlson, B. C. Muñoz, and T. A. Bullions, J. Intel. Mater. Syst. Struct. **7**, 613 (1996).
[4] S. Odenbach, Arch. Appl. Mech. **86**, 269 (2016).
[5] A. M. Menzel, Phys. Rep. **554**, 1 (2015).
[6] M. M. Schmauch, S. R. Mishra, B. A. Evans, O. D. Velev, and J. B. Tracy, ACS Appl. Mater. Int. **9**, 11895 (2017).
[7] R. Weeber, M. Hermes, A. M. Schmidt, and C. Holm, J. Phys.: Condens. Matter **30**, 063002 (2018).
[8] R. Weeber, P. Kreissl, and C. Holm, Arch. Appl. Mech. **89**, 3 (2019).
[9] O. V. Stolbov and Y. L. Raikher, Arch. Appl. Mech. **89**, 63 (2019).
[10] A. M. Menzel, Arch. Appl. Mech. **89**, 17 (2019).
[11] M. Schümann, T. Gundermann, and S. Odenbach, Arch. Appl. Mech. **89**, 77 (2019).
[12] M. Zrínyi, L. Barsi, and A. Büki, J. Chem. Phys. **104**, 8750 (1996).
[13] D. Collin, G. K. Auernhammer, O. Gavat, P. Martinoty, and H. R. Brand, Macromol. Rapid Commun. **24**, 737 (2003).
[14] Y. An and M. T. Shaw, Smart Mater. Struct. **12**, 157 (2003).
[15] K. Zimmermann, V. A. Naletova, I. Zeidis, V. A. Turkov, E. Kolev, M. V. Lukashevich, and G. V. Stepanov, J. Magn. Magn. Mater. **311**, 450 (2007).
[16] Y. L. Raikher, O. V. Stolbov, and G. V. Stepanov, J. Phys. D: Appl. Phys. **41**, 152002 (2008).
[17] R. Fuhrer, E. K. Athanassiou, N. A. Luechinger, and W. J. Stark, Small **5**, 383 (2009).
[18] H. Böse, R. Rabindranath, and J. Ehrlich, J. Intell. Mater. Syst. Struct. **23**, 989 (2012).
[19] P. Ilg, Soft Matter **9**, 3465 (2013).
[20] Y. Li, J. Li, W. Li, and H. Du, Smart Mater. Struct. **23**, 123001 (2014).
[21] J. Maas and D. Uhlenbusch, Smart Mater. Struct. **25**, 104002 (2016).
[22] G. Z. Lum, Z. Ye, X. Dong, H. Marvi, O. Erin, W. Hu, and M. Sitti, Proc. Natl. Acad. Sci. USA **113**, E6007 (2016).
[23] L. Hines, K. Petersen, G. Z. Lum, and M. Sitti, Adv. Mater. **29**, 1603483 (2017).
[24] T. I. Becker, V. Böhm, J. C. Vega, S. Odenbach, Y. L. Raikher, and K. Zimmermann, Arch. Appl. Mech. **89**, 133 (2019).
[25] M. Schümann and S. Odenbach, J. Magn. Magn. Mater. **441**, 88 (2017).
[26] E. Coquelle and G. Bossis, J. Adv. Sci. **17**, 132 (2005).
[27] S. Abramchuk, E. Kramarenko, G. Stepanov, L. Nikitin, G. Filipcsei, A. Khokhlov, and M. Zrinyi, Polym. Adv. Technol. **18**, 883 (2007).
[28] H. Böse, Int. J. Mod. Phys. B **21**, 4790 (2007).
[29] L. Chen, X. Gong, and W. Li, Smart Mater. Struct. **16**, 2645 (2007).
[30] G. Filipcsei and M. Zrínyi, J. Phys.: Condens. Matter **22**, 276001 (2010).
[31] D. Günther, D. Y. Borin, S. Günther, and S. Odenbach, Smart Mater. Struct. **21**, 015005 (2011).
[32] T. Borbáth, S. Günther, D. Y. Borin, T. Gundermann, and S. Odenbach, Smart Mater. Struct. **21**, 105018 (2012).
[33] K. Danas, S. V. Kankanala, and N. Triantafyllidis, J. Mech. Phys. Solids **60**, 120 (2012).
[34] S. Monz, A. Tschöpe, and R. Birringer, Phys. Rev. E **78**, 021404 (2008).
[35] D. C. Stanier, J. Ciambella, and S. S. Rahatekar, Composites, Part A **91**, 168 (2016).
[36] S. Abramchuk, E. Kramarenko, D. Grishin, G. Stepanov, L. Nikitin, G. Filipcsei, A. Khokhlov, and M. Zrínyi, Polym. Adv. Technol. **18**, 513 (2007).
[37] P. Blom and L. Kari, Int. J. Mech. Sci. **60**, 54 (2012).
[38] H. A. Hashi, A. G. A. Muthalif, and N. H. D. Nordin, Iran. J. Sci. Technol., Trans. Mech. Eng. **40**, 181 (2016).
[39] N. Hoang, N. Zhang, W. Li, and H. Du, J. Intell. Mater. Syst. Struct. **24**, 2036 (2013).
[40] K.-H. Lee, J.-E. Park, and Y.-K. Kim, J. Intell. Mater. Syst. Struct. **30**, 2212 (2019).
[41] D. I. Merkulov, A. V. Muravlev, E. D. Martynova, D. A. Pelevina, V. A. Turkov, and V. A. Naletova, J. Magn. Magn. Mater. **470**, 81 (2019).

[42] V. V. Sorokin, G. V. Stepanov, M. Shamonin, G. J. Monkman, A. R. Khokhlov, and E. Y. Kramarenko, Polymer **76**, 191 (2015).
[43] J. Küpfer and H. Finkelmann, Makromol. Chem. Rapid Commun. **12**, 717 (1991).
[44] J. Küpfer and H. Finkelmann, Macromol. Chem. Phys. **195**, 1353 (1994).
[45] C. Ohm, M. Brehmer, and R. Zentel, Adv. Mater. **22**, 3366 (2010).
[46] K. Urayama, Macromolecules **40**, 2277 (2007).
[47] S. Krause, F. Zander, G. Bergmann, H. Brandt, H. Wertmer, and H. Finkelmann, C. R. Chimie **12**, 85 (2009).
[48] K. Urayama, R. Mashita, I. Kobayashi, and T. Takigawa, Macromolecules **40**, 7665 (2007).
[49] A. M. Menzel, H. Pleiner, and H. R. Brand, Eur. Phys. J. E **30**, 371 (2009).
[50] A. Y. Zubarev, Soft Matter **9**, 4985 (2013).
[51] G. V. Stepanov, D. Y. Borin, Y. L. Raikher, P. V. Melenev, and N. S. Perov, J. Phys.: Condens. Matter **20**, 204121 (2008).
[52] R. Messing, N. Frickel, L. Belkoura, R. Strey, H. Rahn, S. Odenbach, and A. M. Schmidt, Macromolecules **44**, 2990 (2011).
[53] R. Barbucci, D. Pasqui, G. Giani, M. De Cagna, M. Fini, R. Giardino, and A. Atrei, Soft Matter **7**, 5558 (2011).
[54] N. Frickel, R. Messing, and A. M. Schmidt, J. Mater. Chem. **21**, 8466 (2011).
[55] R. Weeber, S. Kantorovich, and C. Holm, J. Magn. Magn. Mater. **383**, 262 (2015).
[56] M. Puljiz, S. Huang, G. K. Auernhammer, and A. M. Menzel, Phys. Rev. Lett. **117**, 238003 (2016).
[57] M. Puljiz, S. Huang, K. A. Kalina, J. Nowak, S. Odenbach, M. Kästner, G. K. Auernhammer, and A. M. Menzel, Soft Matter **14**, 6809 (2018).
[58] W. Chen, L. Sun, X. Li, and D. Wang, Smart Mater. Struct. **22**, 105012 (2013).
[59] A. Ghosh and P. Fischer, Nano Lett. **9**, 2243 (2009).
[60] K. E. Peyer, S. Tottori, F. Qiu, L. Zhang, and B. J. Nelson, Chem. Eur. J. **19**, 28 (2013).
[61] L. Fischer and A. M. Menzel, J. Chem. Phys. **151**, 114906 (2019).
[62] L. D. Landau and E. M. Lifshitz, *Theory of Elasticity* (Elsevier, Oxford, 1986).
[63] A.-L. Cauchy, *Exercices de Mathématiques* (Bure Frères, Paris, 1828), Vol. 3, pp. 160–187.
[64] L. J. Walpole, Proc. R. Soc. London, Ser. A **458**, 705 (2002).
[65] J. D. Jackson, *Classical Electrodynamics* (Wiley, New York, 1999).
[66] K. M. Górski, E. Hivon, A. J. Banday, B. D. Wandelt, F. K. Hansen, M. Reinecke, and M. Bartelmann, Astrophys. J. **622**, 759 (2005); HEALPix, http://healpix.sourceforge.net.
[67] D. Ivaneyko, V. Toshchevikov, M. Saphiannikova, and G. Heinrich, Condens. Matter Phys. **15**, 33601 (2012).
[68] P. Metsch, K. A. Kalina, C. Spieler, and M. Kästner, Comput. Mater. Sci. **124**, 364 (2016).
[69] K. Zahn, R. Lenke, and G. Maret, Phys. Rev. Lett. **82**, 2721 (1999).
[70] See Supplemental Material at http://link.aps.org/supplemental/10.1103/PhysRevResearch.2.023383 for matrix plots to visualize the values of the expansion coefficients associated with those modes referred to in Figs. 6, 13, and 14 as well as with some additional modes.
[71] J. J. Abbott, E. Diller, and A. J. Petruska, Annu. Rev. Control Robot. Auton. Syst. **3**, 57 (2020).
[72] E. Allahyarov, H. Löwen, and L. Zhu, Phys. Chem. Chem. Phys. **17**, 32479 (2015).
[73] B. Liu and M. T. Shaw, J. Rheol. **45**, 641 (2001).

Supplemental material "Towards a soft magnetoelastic twist actuator"

Lukas Fischer[1] and Andreas M. Menzel[1]

[1] *Institut für Theoretische Physik II: Weiche Materie, Heinrich-Heine-Universität Düsseldorf, D-40225 Düsseldorf, Germany*

(Dated: May 26, 2020)

In this supplemental material, we add alternative illustrations for the values of the expansion coefficients of the displacement field shown in Figs. 6, 13, and 14 of the main body of the article. Corresponding matrix plots are included on the following pages.

During our investigations in the main body of the article, we focused on elastic spheres enclosing three different types of particle arrangements. First, the elastic sphere embedded an initially globally twisted structure of chain-like aggregates of particles. Next, we addressed two types of systems containing helical particle aggregates arranged side by side. These two types of systems differed by the radius of the helices.

In all situations, the degree of initial global twist or initial helical twist was quantified by a parameter γ. We determined that value of γ associated with the maximal amplitude of the magnetically induced overall torsional deformation. It was found by identifying the maximal value of $|u_{10}^{\varphi}|$. For the corresponding systems, Figs. 6, 13, and 14 in the main article depict in each case the values of the expansion coefficients associated with ten representative modes of the three components of the displacement field. Here, for further illustration, we include an alternative representation of the relative importance and values of the expansion coefficients of these ten and additional modes. For this purpose, we choose an illustration via matrix plots. One axis refers to the mode number l, one axis to the mode number m. We color-code the value of the expansion coefficient associated with each corresponding mode of the displacement field, connected to the spherical harmonic Y_{lm}. The resulting illustrations follow in Figs. S1–S3. Again, we used the HEALPix package for our evaluations [1]. More precisely, the values of the expansion coefficients into spherical harmonics are depicted for the three components (a) $u^{\perp}$, (b) u^{θ}, and (c) u^{φ} of the overall surface displacement field in each case. We color-code the related expansion coefficients in a nonlinear (symmetric linear-logarithmic) way. Yellow indicates a vanishing contribution of the related mode, while blue colors imply a positive and red colors a negative value of the expansion coefficient. Furthermore, we separate the real (Re) and imaginary (Im) parts, which are shown on the left- and right-hand sides, respectively.

[1] K. M. Górski, E. Hivon, A. J. Banday, B. D. Wandelt, F. K. Hansen, M. Reinecke, and M. Bartelmann, Astrophys. J. **622**, 759 (2005).

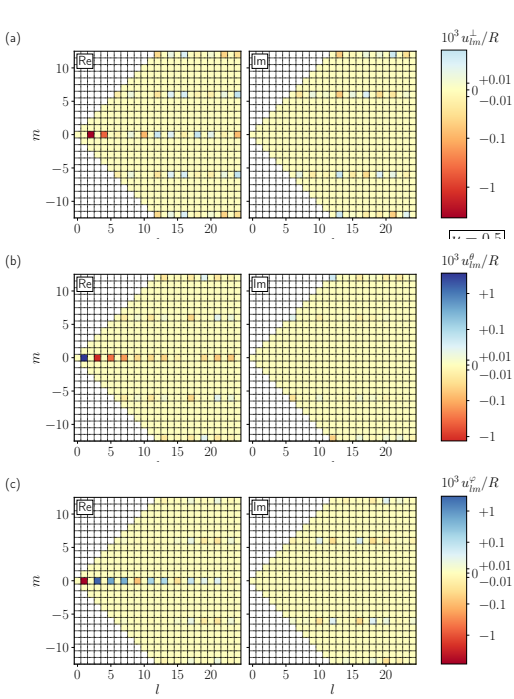

Results for a Poisson ratio of $\nu = 0.5$.

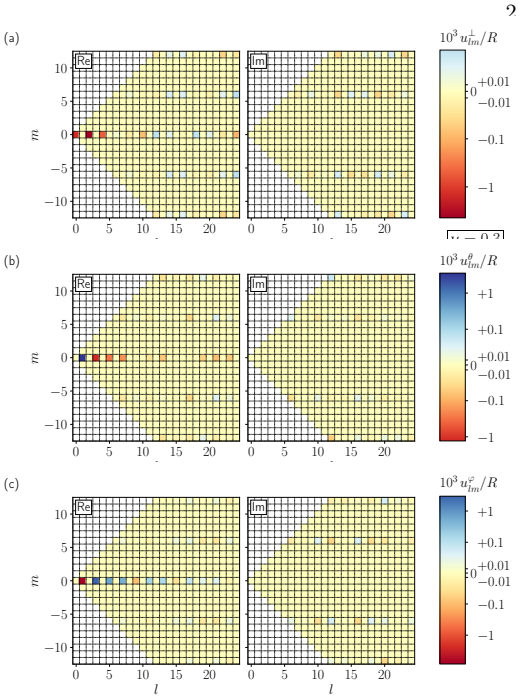

Results for a Poisson ratio of $\nu = 0.3$.

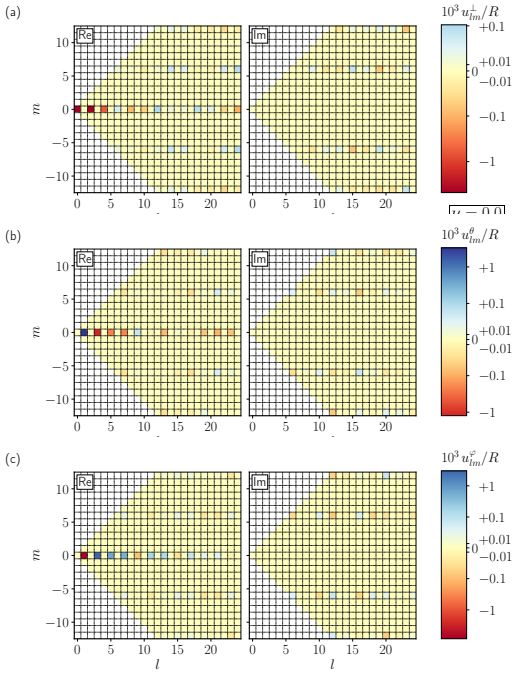

Results for a Poisson ratio of $\nu = 0.0$.

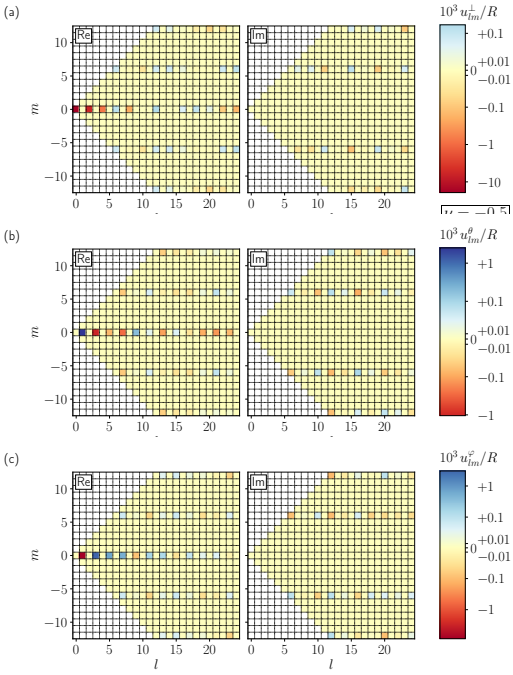

Results for a Poisson ratio of $\nu = -0.5$.

FIG. S1. Illustration of the values of the expansion coefficients of the magnetically induced surface displacement field for an initially globally twisted configuration of the magnetic inclusions ($\gamma \approx 0.019\pi$). Here, we consider at most $l = 24$ and $m = \pm 12$, so as to include all modes of the related Fig. 6 of the main body of the article.

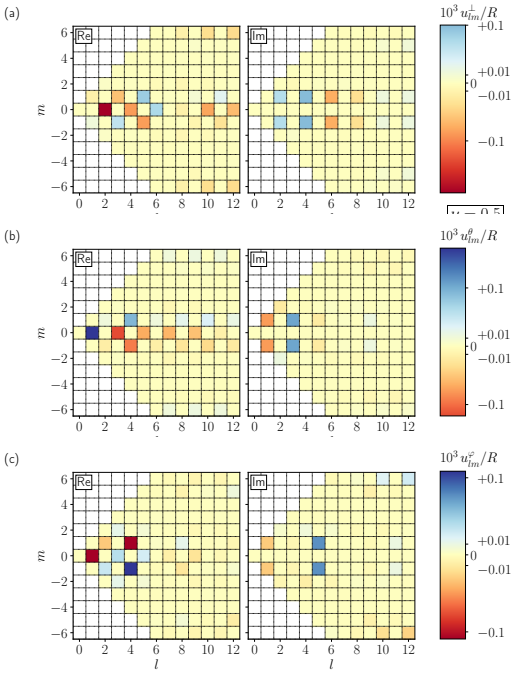

Results for a Poisson ratio of $\nu = 0.5$.

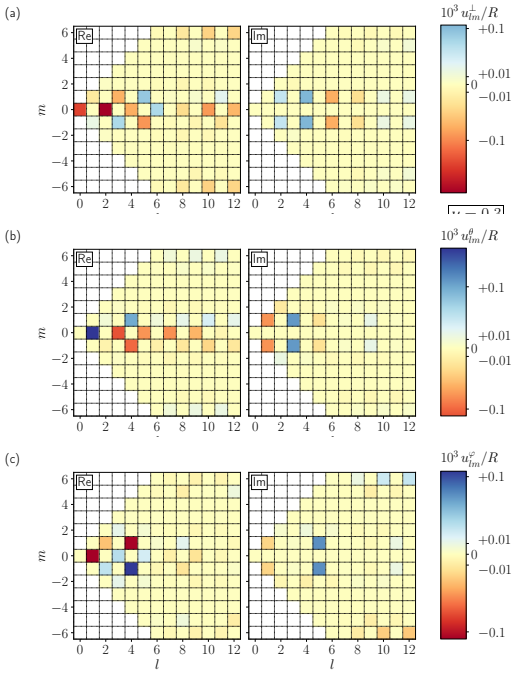

Results for a Poisson ratio of $\nu = 0.3$.

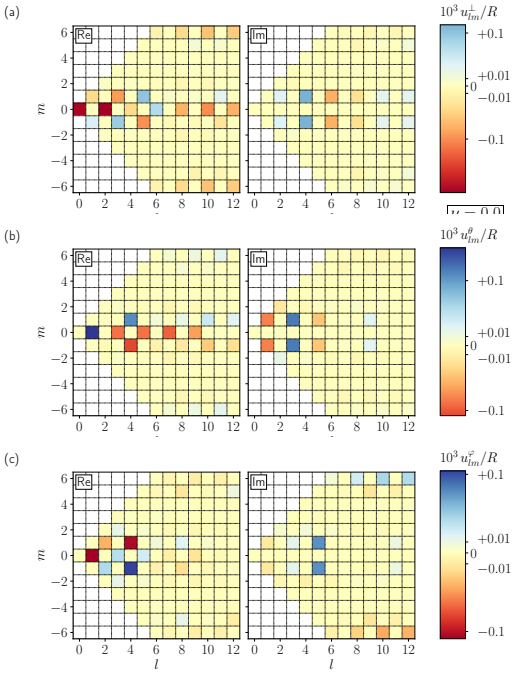

Results for a Poisson ratio of $\nu = 0.0$.

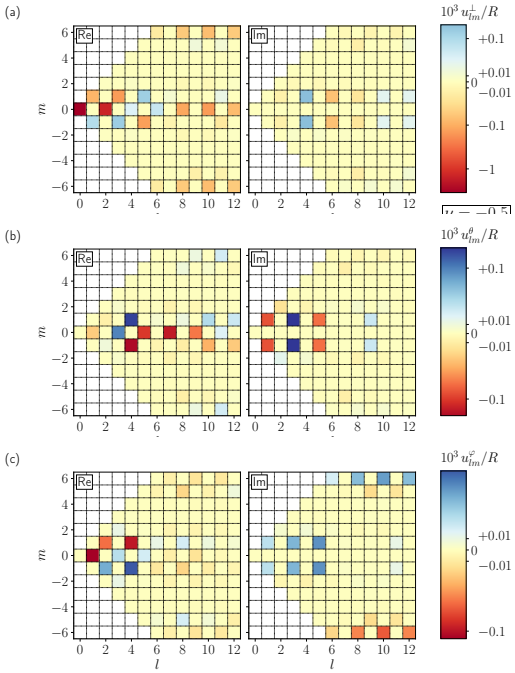

Results for a Poisson ratio of $\nu = -0.5$.

FIG. S2. Same as in Fig. S1, but for a system containing helical elements of inclusions, arranged side-by-side. The radius of all helices is set to $r_{helix} = 0.05R$. We here show expansion coefficients up to $l = 12$ and $m = \pm 6$, in analogy to the corresponding Fig. 13 of the main article.

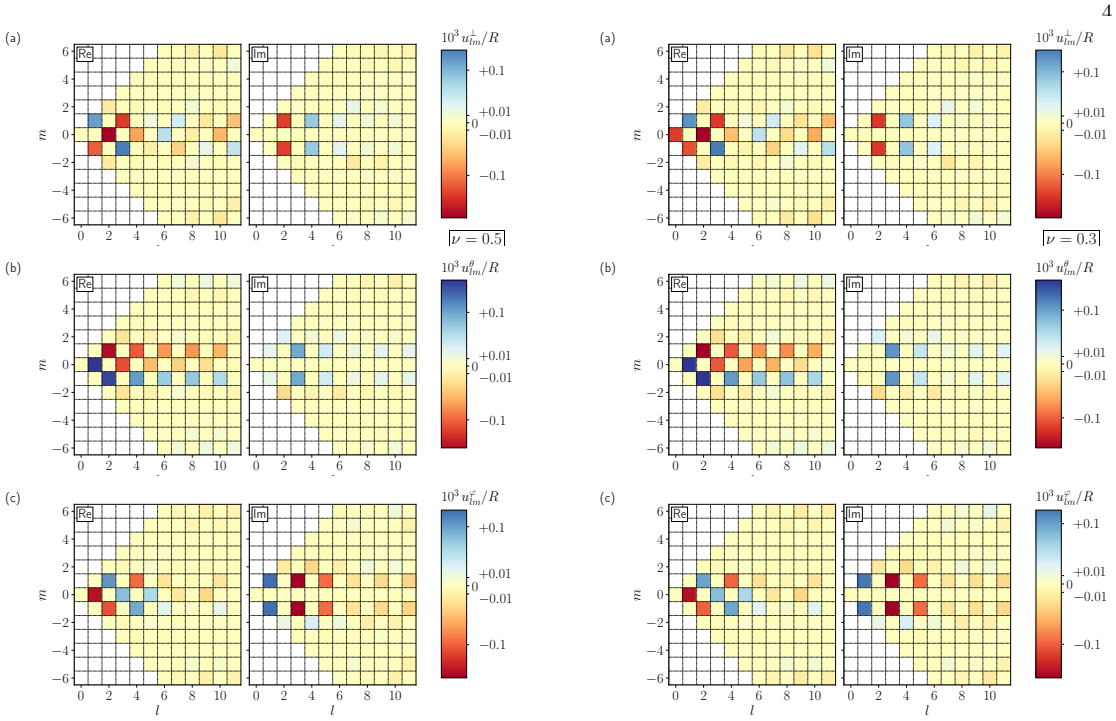

Results for a Poisson ratio of $\nu = 0.5$.

Results for a Poisson ratio of $\nu = 0.3$.

Results for a Poisson ratio of $\nu = 0.0$.

Results for a Poisson ratio of $\nu = -0.5$.

FIG. S3. Same as in Fig. S2, but for $r_{helix} = 0.1R$. In this case, expansion coefficients up to $l = 11$ and $m = \pm 6$ are considered, in analogy to the corresponding Fig. 14 of the main article.

P3 Magnetically induced elastic deformations in model systems of magnetic gels and elastomers containing particles of mixed size

Reproduced from

L. Fischer and A. M. Menzel,
Magnetically induced elastic deformations in model systems of magnetic gels and elastomers containing particles of mixed size,
Smart Mater. Struct. **30**, 014003 (2021),
published by IOP Publishing Ltd.

Digital Object Identifier (DOI): `https://doi.org/10.1088/1361-665X/abc148`

Statement of contribution

Both authors contributed to this work. The idea was proposed by AMM, with modifications added by me. I performed all calculations and prepared all figures except for Figs. 1 and 2. I estimate my contribution to this work during my PhD as 75 %.

Copyright and license notice

Focus on ERMR 2019

Magnetically induced elastic deformations in model systems of magnetic gels and elastomers containing particles of mixed size

Lukas Fischer and Andreas M. Menzel

Institut für Theoretische Physik II: Weiche Materie, Heinrich-Heine-Universität Düsseldorf, Universitätsstraße 1, D-40225 Düsseldorf, Germany

E-mail: lfischer@thphy.uni-duesseldorf.de, menzel@thphy.uni-duesseldorf.de

Abstract. Soft elastic composite materials can serve as actuators when they transform changes in external fields into mechanical deformation. Here, we theoretically address the corresponding deformational behavior in model systems of magnetic gels and elastomers exposed to external magnetic fields. In reality, such materials consist of magnetizable colloidal particles in a soft polymeric matrix. Since many practical realizations of such materials involve particulate inclusions of polydisperse size distributions, we concentrate on the effect that mixed particle sizes have on the overall deformational response. To perform a systematic study, our focus is on binary size distributions. We systematically vary the fraction of larger particles relative to smaller ones and characterize the resulting magnetostrictive behavior. The consequences for systems of various different spatial particle arrangements and different degrees of compressibility of the elastic matrix are evaluated. In parts, we observe a qualitative change in the overall response for selected systems of mixed particle sizes. Specifically, overall changes in volume and relative elongations or contractions in response to an induced magnetization can be reversed into the opposite types of behavior. Our results should apply to the characteristics of other soft elastic composite materials like electrorheological gels and elastomers when exposed to external electric fields as well. Overall, we hope to stimulate corresponding experimental realizations and the further investigation on the purposeful use of mixed particle sizes as a means to design tailored requested material behavior.

Keywords magnetorheological elastomers, magnetic gels, magnetostriction, binary particle size distribution, elasticity theory, particle arrangement, soft magnetic actuator

Submitted to: *Smart Mater. Struct.*

1. Introduction

Magnetic gels and elastomers consist of magnetic or magnetizable colloidal particles locked into a soft, elastic, permanently crosslinked polymeric body [1–13]. Representing a class of stimuli-responsive materials, at least two types of reaction to external magnetic fields are standing out. First, the overall mechanical properties and stiffness are affected by sufficiently strong external magnetic fields, a scenario that was termed magnetorheological effect [1, 2, 6, 14–31]. Second, the materials tend to respond by significant elastic deformations, which allows for the construction of soft actuators and is often referred to as magnetostrictive behavior [2,32–41], particularly when the external magnetic fields are homogeneous. We here concentrate on the latter effect.

Corresponding experiments on the magnetostrictive behavior based on spherical samples of ferrogels [33, 42] featuring rather random spatial arrangements of the inclusions suggest an overall elongation of the samples along the axis of an applied external magnetic field. This is confirmed by finite-element simulations [39]. However, several previous studies have revealed that the type of deformation, i.e., whether an elongation or contraction along the axis of the magnetic field occurs, strongly depends on the spatial arrangement of the magnetizable inclusions [20,35,40]. The consequences of nonuniform particle sizes are still to be further addressed in such theoretical works.

It is already known from the study of magnetic fluids, consisting of magnetic or magnetizable colloidal particles suspended in a carrier liquid [43–47], that the particle size is a key parameter. For example, it has been demonstrated that the magnetoviscous effect, that is, the change in the macroscopic fluid viscosity induced by external magnetic fields, is dominated mainly by the response of the larger suspended particles [48]. For magnetic gels and elastomers, the dependence of the material behavior on the particle size has been analyzed as well. Changes on the type of behavior with varying particle size were partially attributed to the higher rotational mobility of smaller particles in the elastic environment [49]. Similarly, the particle size can affect the formation of structural elements when the samples are cured under an external magnetic field [50]. A stronger magnetorheological effect was observed for samples containing particles of larger size [16, 17, 26, 51].

Actual samples are frequently based on particles of polydisperse size distribution. Nevertheless, theoretical approaches frequently assume a uniform particle size. Examples for exceptions are finite-element simulations [52] or dipole-spring models [30]. Moreover, hybrid models investigate the behavior of discrete large particles in an elastic environment containing a lot of magnetizable small particles by approximating the latter as a magnetizable elastic continuum [53]. In contrast to that, genuine macroscopic continuum theories often consider the whole system as a continuous magnetic or magnetizable medium, therefore they do not resolve any actual particle sizes explicitly, but represent the resulting effects by the values of the involved material parameters [15, 54, 55].

To be able to perform a systematic study of the consequences of the presence of

particles of different sizes in the system, we here concentrate on particles of binary size distribution in a mesoscopic description. It is well known that in general this reduced binary type of deviation from a uniform particle size can already have strong and qualitative effects on the overall behavior. To understand the often quite complex overall system properties, turning to binary size distributions, for instance, in model systems of hard spheres or rod-like particles of colloidal size, thus often marks the first step towards understanding the effects of polydispersity [56–58]. Accordingly, several previous experimental studies and associated strategies of modeling on magnetic gels and elastomers concentrate on materials of a relatively bimodal size distribution of the contained inclusions [16, 18, 26, 59–63]. It was found, for example, that bimodal size distributions can enhance the magnetorheological effect [64].

In the present study, our focus is on the influence of mixed particle sizes on the overall magnetostrictive response of the system. For this purpose, in model systems featuring binary particle size distributions, we systematically increase the number of smaller particles at the cost of the number of larger particles, keeping the overall particle number constant. We evaluate how the magnetostrictive behavior, appropriately rescaled to take into account the different particle sizes, changes during these variations of the size distribution. Different discrete spatial arrangements of the particles are considered. We rescale all lengths by the dimension of the system. Therefore, absolute lengths are not decisive. Instead, we set the relative sizes of the magnetizable inclusions to 1 % and 2 % of the overall system size.

As a benefit of our theoretical work, we are able to selectively concentrate on isolated properties related to the particle size and to study their impact on the overall behavior, excluding other aspects that may play a role in real samples as well. This helps us to understand the relative importance of specific aspects. In the present case, we concentrate on the roles of the magnitude of the magnetic moment and of the displaceability against the elastic matrix as related to the particle size. Other effects, for instance variations of the magnetization behavior with the particle size, are not taken into account.

We continue in the following way. In section 2, we provide a brief overview on the mesoscopic model system that we use to perform our evaluations, together with our protocol of introducing and modifying the binary size distribution of the magnetizable particles. Results for various different spatial particle arrangements and compressibilities of the elastic matrix are then presented in section 3. We conclude in section 4.

2. Mesoscopic model systems containing discrete spatial particle arrangements of binary size distributions

To perform our investigations, we utilize a recently developed discrete mesoscopic model system [40, 41]. It allows to calculate overall mechanical deformations of a soft elastic spherical body in response to the magnetization of a discrete set of embedded spherical

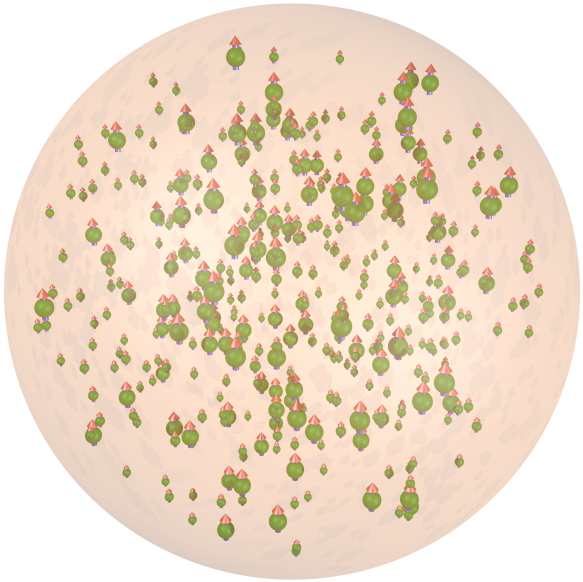

Figure 1. The system considered in the present study consists of a soft spherical elastic body that contains a discrete set of magnetizable spherical particles. These particles feature a binary size distribution, implying that the diameter of the larger particles is twice the diameter of the smaller particles. Upon exposure to a strong homogeneous external magnetic field, here vertically oriented, the particles are assumed to be magnetized to saturation. We indicate the induced magnetic particle moments by the small arrows on the inclusions. In our investigation, we analyze and quantify the types of overall deformation of the enclosing elastic sphere induced by this magnetization for different spatial arrangements of the particles, different number fractions x of the smaller particles, and different Poisson ratios ν of the soft elastic sphere.

particles, see figure 1.

The radius of the elastic spherical body is denoted as R. Only elastic deformations of small amplitude are addressed, so that linear elasticity theory can be used for our evaluations [65]. Our analysis assumes a homogeneous isotropic elastic material forming the soft spherical body. Its elastic properties are specified by the shear modulus μ and the Poisson ratio $-1 \leq \nu \leq 1/2$, the latter being connected to the compressibility of the elastic matrix material [65].

As a major benefit of the spherical shape of the elastic matrix body, a corresponding Green's function is available to quantify its elastic deformations. This function specifies the displacements of all volume elements of the elastic body in response to a mechanical force applied at an arbitrary point within the sphere. Building on the derivation of the Green's function for an elastic sphere embedded in an infinitely extended surrounding elastic medium [66], we determined this function for a free-standing elastic sphere [40]. The explicit analytical expression is very lengthy and thus we do not reproduce it here. Due to the linearly elastic characterization, the overall response of the elastic sphere to the action of many internal force centers is obtained by simple superposition.

In our case, it is the embedded magnetizable spherical particles that correspond

to the force centers. We here include smaller particles of radius $0.01R$ and larger particles of radius $0.02R$. The number fraction of smaller particles is denoted as x. All particles are at least separated by a center-to-center distance of $0.11R$ from each other and by a distance of $0.06R$ of their centers from the surface of the surrounding elastic sphere. Moreover, we assume strong homogeneous saturating external magnetic fields that magnetize the systems. Thus all induced magnetic particle moments point into the same direction and only differ by their magnitudes for different particle sizes. Assuming identical material and identical internal structure of the magnetic particles, this implies an eightfold magnetic moment for the larger inclusions.

Together, the induced magnetic interactions between the embedded particles are approximated using magnetic dipole forces. The magnetic force on particle i resulting from the magnetic interaction with particle j thus reads [67]

$$\mathbf{F}_i = \frac{3\mu_0}{4\pi r_{ij}^4}\Big[\mathbf{m}_i\,(\mathbf{m}_j\cdot\hat{\mathbf{r}}_{ij}) + \mathbf{m}_j\,(\mathbf{m}_i\cdot\hat{\mathbf{r}}_{ij}) + (\mathbf{m}_i\cdot\mathbf{m}_j)\,\hat{\mathbf{r}}_{ij} - 5\hat{\mathbf{r}}_{ij}\,(\mathbf{m}_i\cdot\hat{\mathbf{r}}_{ij})\,(\mathbf{m}_j\cdot\hat{\mathbf{r}}_{ij})\Big]. \tag{1}$$

Here, $\mathbf{m}_i$ and $\mathbf{m}_j$ are the magnetic dipole moments of particles i and j, respectively, μ_0 denotes the magnetic vacuum permeability, and $\mathbf{r}_{ij} = r_{ij}\hat{\mathbf{r}}_{ij}$ is the distance vector pointing from the center position of particle j to the center position of particle i, with $r_{ij} = |\mathbf{r}_{ij}|$. In our implementation, we measure lengths in units of R and forces in units of μR^2.

The magnetizable particles are assumed to be enclosed by the surrounding elastic body but not to be able to move through it. Therefore, when upon magnetization the particles are subject to the induced magnetic forces, they are pressed against their elastic surroundings. Thus, the particles transmit the forces to the elastic environment. This induces local and possibly global elastic distortions of the surrounding elastic medium [68–70]. The resulting long-ranged distortions are calculated from the Green's function as mentioned above [40, 41].

As a consequence of the distortions in response to the magnetic forces, the embedded magnetic particles are displaced. In turn, this couples back to the induced magnetic forces that depend on the distance vectors between the particles, see (1). This problem is solved by an iterative loop to determine the final particle positions and thus the final set of magnetic forces [40, 68]. Along that way, we need to know the displacement of a single particle within the elastic sphere when a force is applied to it, as a function of the particle position and the orientation of the force. We determined corresponding fit functions as approximations for spherical particles of the two different radii [40]. To take into account the mutual particle interactions mediated via induced distortions of the elastic body, we approximate the inclusions as point-like. This is in line with our configurations that ensure pronounced distances between the particles. The same applies when we calculate the induced displacements on the surface of the sphere, assuming that the inclusions are sufficiently separated from the surface.

In previous investigations, events of mutual approach of individual particles up

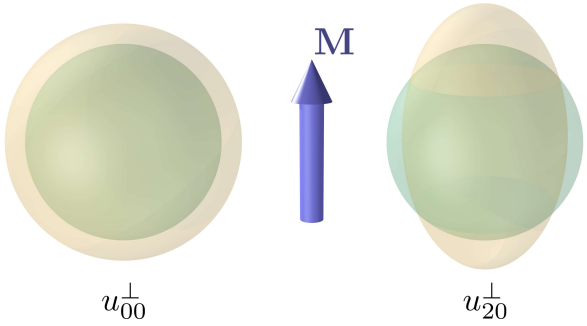

Figure 2. Illustration of the types of overall deformation of the initial spherical elastic body that are quantified by the expansion coefficients $u_{00}^{\perp}$ and $u_{20}^{\perp}$. The darker (greenish) spheres indicate the initial undeformed states, while the brighter (yellowish) ellipsoids mark the deformed states. On the one hand, the coefficient $u_{00}^{\perp}$ refers to overall isotropic expansion for $u_{00}^{\perp} > 0$, as indicated here, or isotropic contraction for $u_{00}^{\perp} < 0$. On the other hand, $u_{20}^{\perp} > 0$ represents an expansion along the axis of the magnetization $\mathbf{M}$ relative to the lateral directions, as illustrated here, while $u_{20}^{\perp} < 0$ identifies a contraction along this axis relative to the lateral dimensions. For clarity, the magnitudes of deformation are indicated in an exaggerated way.

to virtual contact under magnetic attraction were observed and analyzed [71–78]. Such a magnetomechanical collapse results when mutual magnetic attractions between individual particles surmount the elastic barrier connected to the necessary strong deformation of the elastic material between the particles. During all our investigations, we ensured that a corresponding scenario does not occur and the particles remain well separated.

On this basis, we next determine in section 3 the magnetically induced change in shape of the elastic spherical system by evaluating the resulting steady-state displacement field on the surface of the sphere [40, 41]. The components of the surface displacement field are expanded into spherical harmonics using the HEALPix package (http://healpix.sourceforge.net) [79]. We mainly concentrate on the values of two expansion coefficients as illustrated in figure 2.

First, the expansion coefficient that we denote as $u_{00}^{\perp}$ quantifies changes in the overall volume of the spherical system. For $u_{00}^{\perp} > 0$ the total volume increases, while it decreases for $u_{00}^{\perp} < 0$. Second, the expansion coefficient referred to as $u_{20}^{\perp}$ quantifies changes in the overall aspect ratio. For $u_{20}^{\perp} > 0$ the spherical system extends along the axis of magnetization relative to the lateral dimensions, while for $u_{20}^{\perp} < 0$ a relative contraction results along this axis. Thus, the coefficient $u_{20}^{\perp}$ refers to an actuation mode of relative overall axial elongation along the magnetization axis, which we are mainly interested in below. A third expansion coefficient, referred to as u_{10}^{φ}, is evaluated for particle arrangements that feature an overall twist. For nonvanishing u_{10}^{φ}, a net rotation of the upper hemisphere, as selected via the magnetization direction, relative to the lower hemisphere is observed. The sign of u_{10}^{φ} specifies the sense of this relative rotation [41]. u_{10}^{φ} represents the lowest-order coefficient to describe a magnetoelastic material in a

mode of twist/torsional actuation.

3. Results for different spatial particle arrangements and varying elastic compressibility

As detailed below, we now consider various different spatial arrangements of the discrete set of mesoscopic magnetizable particles embedded in the spherical elastic body. In each case, we evaluate the overall deformations as described in section 2 for the number fractions $x = 0$, 0.2, 0.4, 0.6, 0.8, and 1 of the smaller particles. After fixing a specific spatial particle arrangement in the form of a regular lattice structure, there is only one possible realization for $x = 0$ and $x = 1$. Conversely, many different realizations are possible for the other values of x. The smaller and larger particles can be placed in various different ways onto the given lattice sites. Except when noted otherwise, we randomly assign the particles of different sizes to these lattice sites and average our results over 50 realizations for each data point. In the case of the randomized structures, we additionally randomize the particle positions for each realization and again average over all 50 systems. In this case, averages are also necessary for $x = 0$ and $x = 1$.

Moreover, we evaluate our results for four different values of the Poisson ratio ν in each case. For $\nu = 0.5$, the elastic body is incompressible and conserving its overall volume under any type of deformation. Thus, $u_{00}^{\perp}$ should vanish. Next, $\nu = 0.3$ defines moderately compressible systems. An extreme case of compressibility is given for $\nu = 0$. For this value, stretching the elastic body along one axis does not induce any lateral elastic reaction. Finally, $\nu = -0.5$ identifies a pronounced auxetic behavior, that is, the system expands to the sides when stretched along an arbitrary axis. Such a negative Poisson ratio does not apply to the typically studied systems of magnetic gels and elastomers. However, our formalism readily allows for a corresponding evaluation for isotropic elastic materials as well, and we therefore include the associated results. Possibly, our consideration can stimulate the further future investigation of the properties of, for instance, auxetic polymeric foams containing colloidal magnetic particles [80].

In an idealized system, assuming magnetic saturation, the magnetic moment of the particles scales cubically with their radius. Therefore, our larger particles feature an eightfold magnetic moment when compared to the smaller particles. Thus, for identical configurations of larger particles, the resulting magnetic forces are 64-times as strong as for the smaller particles, see (1). In our linearly elastic description, a 64-times stronger force implies equally increased magnitudes of deformation. We therefore need to rescale our calculated quantities $u_{00}^{\perp}$, $u_{20}^{\perp}$, and u_{10}^{φ} to make our results for different values of x comparable with each other. As a divisor for rescaling, we use

$$\begin{aligned}
&\frac{1}{N^2m^2}\sum_{i=1}^{N}\sum_{j=1}^{N} m_i m_j \\
&\qquad = \frac{1}{N^2m^2}\Bigg(\sum_{i=1}^{xN}\sum_{j=1}^{xN} m_i m_j + 2\sum_{i=1}^{xN}\sum_{j=xN+1}^{N} m_i m_j + \sum_{i=xN+1}^{N}\sum_{j=xN+1}^{N} m_i m_j\Bigg) \\
&\qquad = x^2 + 2x(1-x)8 + (1-x)^2 8^2 \\
&\qquad = (8-7x)^2, \qquad (2)
\end{aligned}$$

where N denotes the total number of particles, $m_i = |\mathbf{m}_i|$, $m_j = |\mathbf{m}_j|$, m is the magnitude of the magnetic moment of the smaller particles, while i and j label all particles, starting with the smaller ones. The rescaled quantities are denoted as $\tilde{u}^{\perp}_{00}$, $\tilde{u}^{\perp}_{20}$, and $\tilde{u}^{\varphi}_{10}$. Thus, we rescale the magnitudes of deformation in terms of the overall strength of magnetic particle–particle interaction. This is important, because we intend to keep the spatial arrangements of the particle sites constant while varying x. Thus, the overall volume fraction of magnetizable particles is affected. Our rescaling allows to still quantitatively compare the resulting magnitudes of deformation for different values of x to each other, while maintaining an unchanged spatial arrangement of the particle sites.

Along these lines, we now analyze the deformational response upon magnetization for various different realizations of particle positioning within the spherical elastic body. In all cases, we take care that the deformational response remains small, as required for our theoretical description to remain quantitative. However, in experimental realizations, the amplitudes could be increased by various means, e.g., by a higher volume fraction of the magnetizable material, by a lower interparticle distance, or by using a softer elastic material to form the elastic sphere. Implicitly in our evaluation, we assume the process of magnetization to occur on a fast time scale when compared to the process of particle displacements. Each realization contains $N \approx 1000$ particles in total, unless noted otherwise. In line with realistic experimental system parameters, we set the one remaining dimensionless system parameter as $48\mu_0 m^2/\pi\mu R^6 = 5.4\times10^{-8}$. This value corresponds to, e.g., a soft elastomer of a shear modulus of 1.67 kPa containing spherical inclusions of iron oxide of radius $a = 0.01R$ [40].

As mentioned previously, assuming ideal scaling, m increases cubically with increasing linear dimension of the magnetic inclusions. Therefore, the only remaining dimensionless system parameter $48\mu_0 m^2/\pi\mu R^6$ remains unchanged when all dimensions of the system are scaled linearly by the same factor. Consequently, in this case also the material behavior controlled by $48\mu_0 m^2/\pi\mu R^6$ remains unchanged. Naturally, under experimental conditions, further effects may introduce an additional dependence on the overall system size beyond the one that we consider in our evaluation. For example, the saturation magnetization still may vary with the size of the magnetic inclusions [81].

In the introduction, we referred to studies investigating variations of the material properties and behavior as a function of varying particle size [16,17,26,50,51]. However,

while the sizes of the magnetic inclusions were altered, especially samples of identical volume fractions of these magnetic inclusions and of identical overall dimensions were compared to each other. Thus, not all linear dimensions were varied by the same factor, and thus the magnitude of the system parameter $48\mu_0 m^2/\pi\mu R^6$ was affected. As a consequence, in line with our description, modifications of the system properties were observed.

We note that most present techniques of fabricating the materials would lead to rather randomized isotropic particle positioning within the elastic body, see section 3.4. Apart from that, when samples are cured in a strong homogeneous external magnetic field during the manufacturing process, chain-like particle aggregates are formed that then are locked into the system when the surrounding elastic body is permanently established [82]. Chain-like structures are addressed in sections 3.5 and 3.6. Additionally, we devote larger parts to the evaluation of rather regular particle arrangements. In experimental model systems, such configurations can be realized by building up the elastic environment layer by layer, while during each step placing the particles by hand [68, 77, 83]. Such a procedure requires substantial effort and is predominantly possible for particles of at least a size of approximately 100 µm [68]. However, to achieve in experimental studies a similar number of particulate inclusions as in our theoretical investigation, that is, $N \approx 1000$, one may tend to switch to macroscopic experimental model systems instead [83]. Nevertheless, with the advent and further development of 3D-printing techniques also for the fabrication of magnetic gels and elastomers [84–86], we may expect that the realization of requested positional arrangements of many magnetic inclusions within elastic environments will become possible on realistic microscopic scales as well. Our consideration of clearly spatially separated magnetizable inclusions is in line with such types of technical approach [84]. In all cases, we have checked that our results for $x = 0$ are identical to those in our previous investigations [40, 41]. Thus, we here mainly focus on the dependence of the deformational effects on the binary distribution of the particle size, specifically on the fraction of smaller particles replacing the larger particles. Increase or decrease in volume, relative elongation or contraction along the axis of magnetization, and possibly induced overall twist deformation are the physical consequences of magnetization that we concentrate on.

3.1. Simple cubic lattice structure

We start by investigating systems in which the particle positioning follows regular simple cubic lattice arrangements, with magnetizations along one edge of the cubic unit cells. The fraction x of smaller particles is increased by randomly replacing larger particles by smaller ones. Our results are displayed in figure 3.

To begin, we note that, on average and for the investigated Poisson ratios $\nu < 0.5$, the overall total volume upon magnetization tends to decrease, i.e., $\tilde{u}_{00}^{\perp} < 0$, see figure 3(a). However, the rescaled reduction in volume decreases in magnitude with

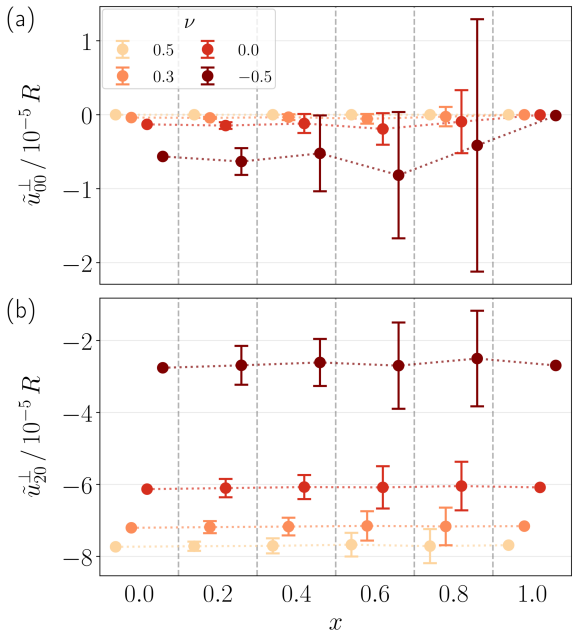

Figure 3. Deformational response of soft spherical elastic bodies containing rigid particulate inclusions arranged in a simple cubic lattice-like structure. Increasing the number fraction x of smaller particles implies that larger particles are randomly replaced by smaller ones. As illustrated in figure 2, (a) $\tilde{u}^{\perp}_{00}$ marks changes in the overall volume, while (b) $\tilde{u}^{\perp}_{20}$ is related to elongations along the magnetization axis relative to the lateral dimensions, both quantities rescaled as given by (2). Averages are taken over 50 realizations of the systems, leading to the indicated standard deviations. For fixed $\nu < 0.5$, the overall changes in volume tend to decrease in magnitude with increasing x. The elongational response remains approximately constant within the standard deviations.

increasing x. Apart from that, the systems on average show a relative contraction along their axis of magnetization, as indicated by $\tilde{u}^{\perp}_{20} < 0$ in figure 3(b). Interestingly, within the standard deviations, the values for $\tilde{u}^{\perp}_{20}$ remain approximately constant. First, this indicates that our way of rescaling according to (2) is reasonable. Second, this result suggests that very large systems of simple cubic lattice structure may be insensitive concerning the nature of their (rescaled) response against randomized positioning of differently sized particles on their lattice points. These results are in qualitative agreement with [83], where the magnetostrictive strain is approximately independent of the size of the included magnetizable particles of uniform diameter.

Yet, we do observe the existence of the noticeable standard deviations in figure 3. Evidently, the auxetic systems on average are most susceptible to the presence of differently sized magnetized particles concerning resulting variations in their overall behavior. Furthermore, they show here and also in the following the largest magnitudes of $\tilde{u}^{\perp}_{00}$. This is a direct consequence of their auxetic nature. If the magnetization induces an overall contraction along the axis of the external magnetic field, the auxetic systems

tend to contract along the lateral directions as well. In combination, this adds to the overall decrease in volume. Analogous conclusions hold for the induced elongations below.

Apparently, introducing the binary size distribution can qualitatively change the response to the external magnetic field for individual realizations of the systems. For example, as indicated by the standard deviations in figure 3(a), the binary size distribution can lead to an overall expansion ($\tilde{u}^{\perp}_{00} > 0$) instead of a contraction ($\tilde{u}^{\perp}_{00} < 0$) of the elastic sphere for some individual realizations. This observation made us look for designed individual implementations. More precisely, for a given spatial arrangement of the particle positions, e.g., a simple cubic lattice structure, we wish to use the binary size distribution to affect the overall response by selectively replacing only larger particles on specific sites by smaller ones.

Along these lines, we analyze the consequences of the following targeted approach. We split the set of all particle sites on the simple cubic lattice into two subsets. The site in the center of the sphere belongs to the first subset, all its nearest neighbors are part of the second subset. All the nearest neighbors of the latter again belong to the first subset, and so on. At the end, any two nearest neighbors always belong to the two different subsets. Each of these two subsets identifies octahedral structures with space diagonals along the axis of magnetization.

Instead of randomly replacing any of the larger particles by a smaller one, we now first only exchange those particles at random that belong to the second subset. This has profound consequences for the rescaled deformational response upon magnetization, see figure 4. Particularly, the behavior described by $\tilde{u}^{\perp}_{20}$ now is significantly affected by the binarization of the particle size distribution. The curves in figure 4(b) first monotonically rise with increasing x. At the location of the maximum at $x \approx 0.48$ all the larger particles of the second subset have been replaced by smaller ones. We find that the overall response of the systems under these circumstances can even be changed qualitatively. Namely, for Poisson ratios $\nu = -0.5$ and 0.0, the overall relative contraction along the magnetization axis is reversed into relative expansion. Beyond this point, with the further increase in x and now also randomly replacing particles belonging to the first subset, the curves monotonously drop. At $x = 0$ and $x = 1$, we find by construction the same values in figure 4 as in figure 3.

This basic example already demonstrates that a tailored assignment of different particle sizes to different lattice sites can be employed to design a requested material behavior. We continue by addressing various further types of spatial particle arrangements.

3.2. Body-centered cubic lattice structure

In contrast to simple cubic systems, body-centered cubic particle arrangements on average elongate along the magnetization axis [40]. Again, the magnetization is directed parallel to the edge of the cubic unit cell. Apart from that, we observe for random

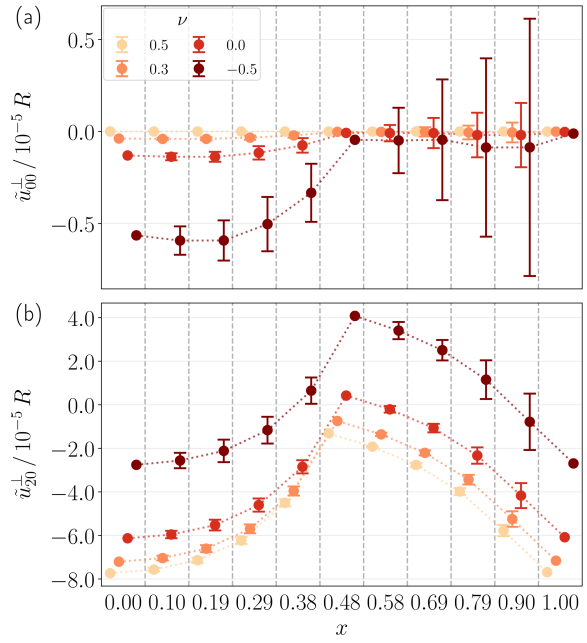

Figure 4. Same as in figure 3 for a simple cubic particle lattice. Yet, in contrast to figure 3, larger particles are not replaced by smaller ones in a completely random way. Instead, first only particles belonging to a specific subset are randomly exchanged, so that for $x \approx 0.48$ octahedral structures of larger and smaller particles remain with space diagonals along the axis of magnetization. Subsequently, also the remaining particles are exchanged at random. Obviously, this strategy has profound consequences for the rescaled overall deformational response of the systems. For Poisson ratios $\nu = -0.5$ and 0.0, we in between even observe relative contraction along the magnetization axis to be reversed into relative elongation.

particle replacements similar trends as for the simple cubic lattice structures, as seen by comparing figures 3 and 5. Thus we again turn to a more specific strategy of targeted replacement of larger by smaller particles to induce a qualitative change in behavior when modifying the particle sizes.

Instead of completely randomly picking larger particles that are replaced by smaller ones, we now first choose those particles at random that are located within the centers of the unit cells of our body-centered cubic structures. As figure 6 demonstrates, this procedure can reverse the observed behavior. Specifically, the curves for $\tilde{u}^{\perp}_{20}$ now significantly drop with increasing x, see figure 6(b). For the Poisson ratios $\nu = 0.5$, 0.3, and 0.0, they even decrease to negative values. This means that the magnetically induced relative extension along the axis of magnetization obtained for $x = 0$ is now reversed to a relative contraction.

When reaching $x \approx 0.53$, all larger particles at the centers of the cubic unit cells have been replaced by smaller ones. Then, apparently, both the spatial arrangements of the remaining larger particles and the resulting overall responses become related to those of our simple cubic lattices studied in section 3.1. Moreover, the curves in figure 6(b)

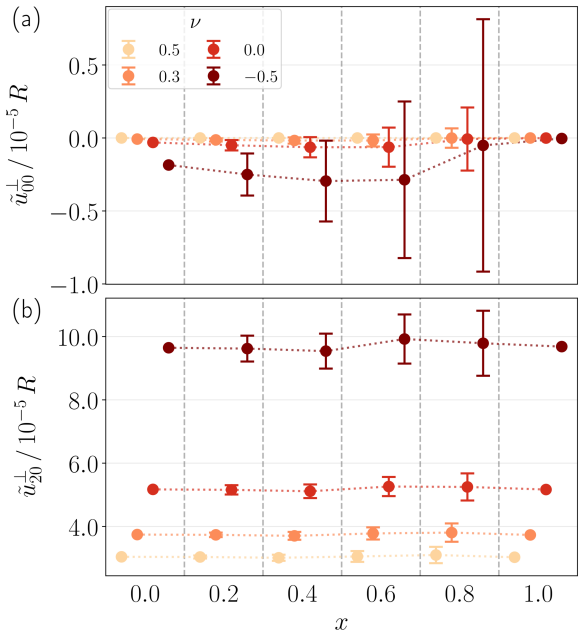

Figure 5. Same as in figure 3, here for body-centered cubic particle lattices. On average, for each value of the Poisson ratio, the spherical elastic body extends along the magnetization axis. We do not find any quantitative change in this behavior as a function of x within the standard deviations.

at $x \approx 0.53$ reach their minimum. We subsequently randomly pick the remaining larger particles for replacement, and the curves start to rise again up to $x = 1$ towards values similar to those for $x = 0$. By construction, at $x = 0$ and $x = 1$, the configurations in figure 6 are identical to those at $x = 0$ and $x = 1$ in figure 5, respectively.

3.3. Face-centered cubic lattice structure

Our results for face-centered cubic lattice structures for randomly replacing larger by smaller magnetizable particles are qualitatively similar to those for body-centered cubic lattices, as inferred by comparing figures 5 and 7. We therefore do not enlarge on specific observations, but directly turn to more specific results for targeted replacements of larger by smaller particles.

Here, instead of completely randomly replacing larger particles by smaller ones, we first only randomly exchange those particles located on the faces of the cubic unit cells. Corresponding results are displayed in figure 8. As a consequence, we find a monotonous drop of the curves of $\tilde{u}_{20}^{\perp}$ in figure 8(b) with increasing x up to $x \approx 0.76$. At this number fraction, all larger particles on the faces of the cubic unit cells have been replaced by smaller ones. Consequently, a simple cubic lattice structure of larger particles remains. For Poisson ratios $\nu = 0.3$ and 0.5, this leads to an even qualitative change in the response. The relative elongation along the axis of magnetization is reversed into a relative contraction. Beyond the number fraction of $x \approx 0.76$, the curves monotonously

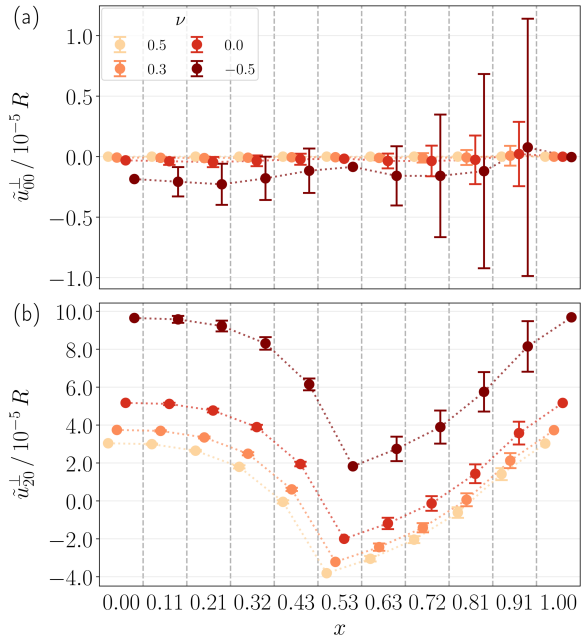

Figure 6. Same as in figure 5 for body-centered cubic particle lattices, now first selectively replacing at random those larger by smaller particles that are located in the centers of the cubic unit cells. At $x \approx 0.53$ all the center particles are replaced. This targeted approach implies an even qualitative change of overall response, with induced expansion along the magnetization axis being reversed into contraction for Poisson ratios $\nu = 0.0$, 0.3, and 0.5.

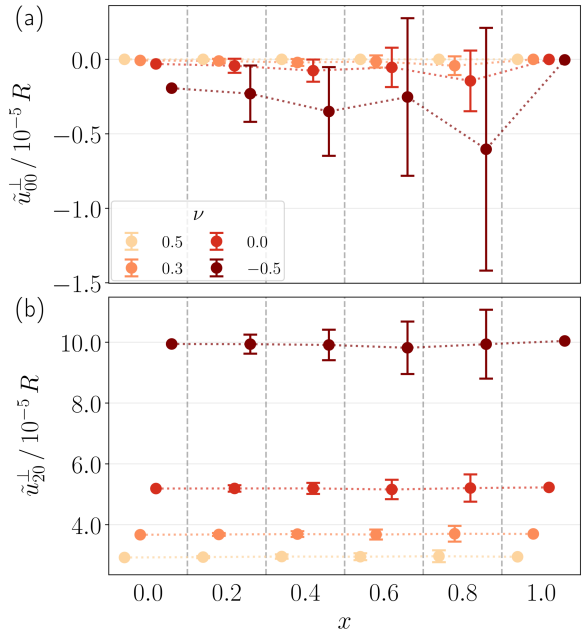

Figure 7. Same as in figure 3, here for face-centered cubic particle lattices. Similar results as for the body-centered cubic particle structures in figure 5 are obtained.

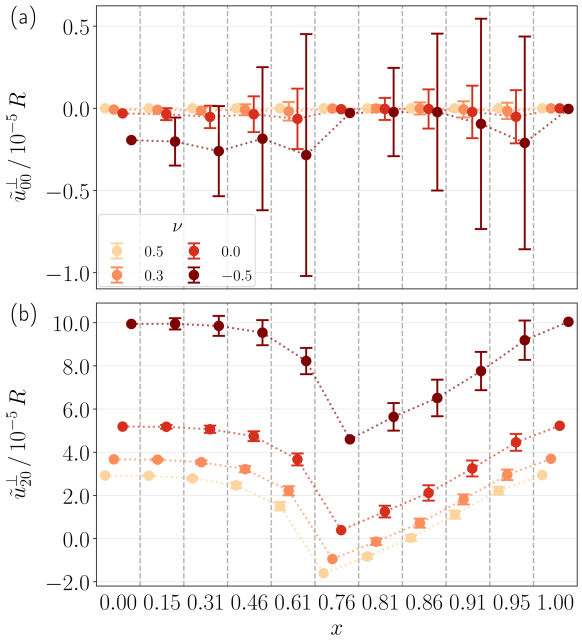

Figure 8. Same as in figure 7 for face-centered cubic particle lattices, now first selectively replacing at random those larger particles by smaller ones that are located on the faces of the cubic unit cells. At $x \approx 0.76$ all the particles on the faces have been exchanged. Again, even an qualitative change of the overall response can be observed following this targeted approach. In between, the induced overall expansion along the magnetization axis is reversed into contraction for Poisson ratios $\nu = 0.3$ and 0.5.

rise again. For $x = 0$ and $x = 1$, the same results are obtained as in figure 7.

3.4. Randomized isotropic configurations

We now turn to basically isotropic particle distributions. In this case, the particle positions are chosen at random, only confined by the conditions listed in section 2. Out of the here-studied systems, these realizations probably correspond most closely to actual samples of well-dispersed particles that are cured in the absence of an external magnetic field. Depending on x, we randomly select a fraction of the particle positions that are assigned to the smaller instead of the larger particles.

We depict corresponding results in figure 9. Again, we find that the rescaled change in volume, measured by $\tilde{u}^{\perp}_{00}$, tends to decrease in magnitude with increasing x. However, within the standard deviations, we do not observe any quantitative variation in the amount of rescaled relative elongation along the axis of magnetization indicated by $\tilde{u}^{\perp}_{20} > 0$. These values agree quantitatively with our previous results obtained for uniform particle sizes in [40]. Since the realization of randomized particle arrangements in practice most likely corresponds to fabrication methods that do not allow to control the particle positioning, we in this case also do not investigate the possibility of targeted spatial assignments of particle sizes.

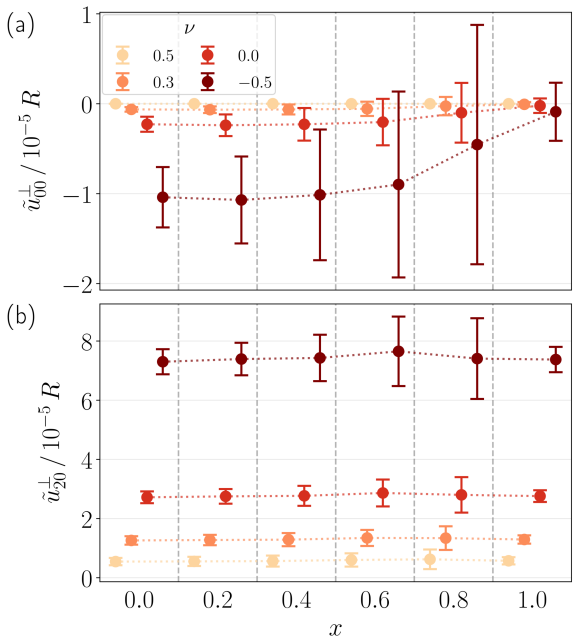

Figure 9. Same as in figure 3, here for configurations of randomized particle positions. On average, for each value of the Poisson ratio, the spherical elastic body extends along the magnetization axis. Within the standard deviations, we do not observe any quantitative change in this behavior as a function of x.

3.5. Quadratically arranged chain-like structures

In a second step, we now turn to particle structures composed of chain-like particle aggregates. Still, within each chain, our requirements of keeping the specified minimal distances between the particles are maintained, and the initial nearest-neighbor interparticle distance within all chains is constant. Every chain is aligned parallel to the axis of magnetization. Overall, the particles still form layers, oriented normal to the magnetization axis, as for the other regular lattice structures. Since our chains are arranged according to a quadratic pattern, this implies that the particles are actually organized in a primitive tetragonal lattice. The two lattice constants perpendicular to the magnetization axis are equal, the one along the magnetization axis is smaller by a factor of 0.62.

Upon magnetization, the spherical elastic body reduces its overall volume for the evaluated Poisson ratios $\nu < 0.5$, see figure 10. Generally, this effect is not influenced as much by the random replacement of larger by smaller particles as in the previous cases, as the smaller magnitudes of the standard deviations indicate. Interesting tendencies are found for the observed rescaled relative contractions along the magnetization axis, see figure 10(b). First, the rescaled magnitudes of $\tilde{u}^{\perp}_{20}$ are notably smaller for $x = 1$ than for $x = 0$. Second, focusing on the average values of $\tilde{u}^{\perp}_{20}$, the curves tend to show a minimum at intermediate values of x. This implies that randomly assigning binary

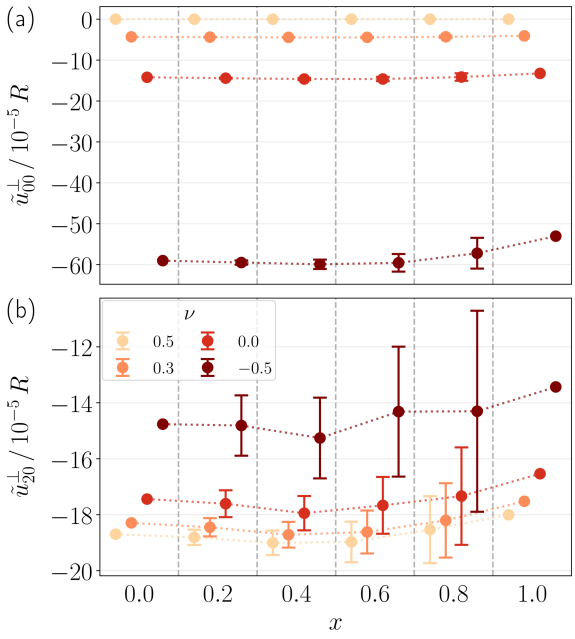

Figure 10. Same as in figure 3, but here for quadratically arranged chain-like aggregates oriented along the axis of magnetization. For Poisson ratios $\nu < 0.5$, on average, the total volume of the spherical elastic body decreases upon magnetization ($\tilde{u}^{\perp}_{00} < 0$). Moreover, for each value of the Poisson ratio, the spherical elastic body on average contracts along the magnetization axis ($\tilde{u}^{\perp}_{20} < 0$). The rescaled magnitude of this effect is slightly smaller for $x = 1$ than for $x = 0$, with weakly increased magnitudes of the averages at intermediate values of x, although not within the standard deviations.

particle sizes can in fact increase the magnitude of the rescaled contraction along the magnetization axis. The effect is not significant within our standard deviations, yet our results imply that individual systems showing such a tendency can definitely be identified.

3.6. Hexagonally arranged chain-like structures

To continue, we remain with aligned chain-like particle aggregates, now, however, arranged in a hexagonal lattice structure. In fact, this structure is related to patterns observed for real samples that are cured in the presence of a strong homogeneous external magnetic field [50]. The mutual distance between the particles required in our calculation may be realized by appropriate coating of the particles or using the particles as the actual chemical crosslinkers after surface functionalization [3, 87–89]. Initially, in our calculations, within each chain-like aggregate the particles are separated from each other by a center-to-center distance of $0.11R$, while the chains themselves show a center-to-center distance of $0.19R$.

Corresponding results for the deformation of the enclosing spherical elastic body upon magnetization along the chain-like aggregates are displayed in figure 11. They

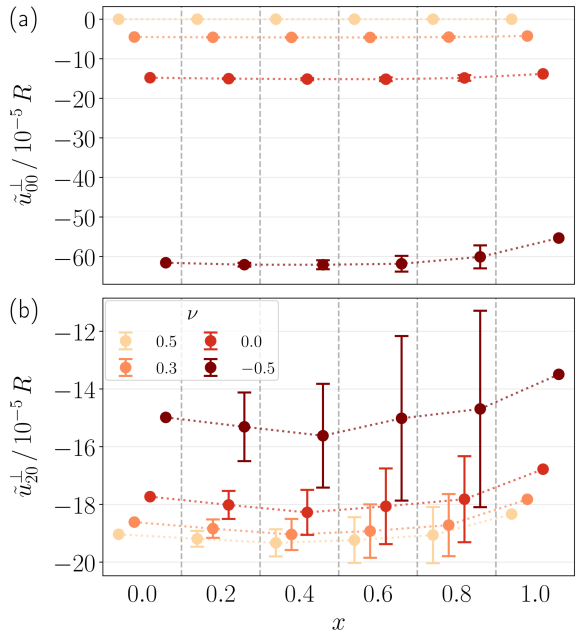

Figure 11. Same as in figure 10, here for hexagonally arranged chain-like aggregates oriented along the axis of magnetization. Similar results as for the quadratically arranged chain-like aggregates in figure 10 are obtained.

are qualitatively similar to the ones reported in section 3.5 for quadratically arranged chain-like aggregates.

3.7. Globally twisted hexagonally arranged chain-like structures

Finally, we turn to hexagonally organized chain-like structures that show an additional initial global twist. That is, an arrangement of particles similar to the one studied in section 3.6 is initially twisted around the center axis that is parallel to the untwisted chain axes. Here, we consider a total number of only $N = 623$ particles. When such a system is magnetized for not too large values of the initial twist, the structures attempt to untwist themselves. Besides the other induced types of global distortion, an overall torsional deformation results for the spherical elastic body. Therefore, corresponding systems were suggested in [41] as candidates to realize soft torsional actuators [90].

We here evaluate systems of a pitch of approximately $11.5R$, for which we observed the largest magnitude of torsional response in our previous study for a uniform particle size [41]. As can be inferred from figures 12(a) and (b), the rescaled change in overall volume and the rescaled contraction along the axis of magnetization, respectively, behave similarly to those for the untwisted structures in figures 11(a) and (b) as functions of x. We note, however, that the order of the curves for $\tilde{u}^{\perp}_{20}$ is reversed for the investigated values of the Poisson ratio.

In addition, we plot in figure 12(c) the coefficient $\tilde{u}^{\varphi}_{10}$, which quantifies the rescaled

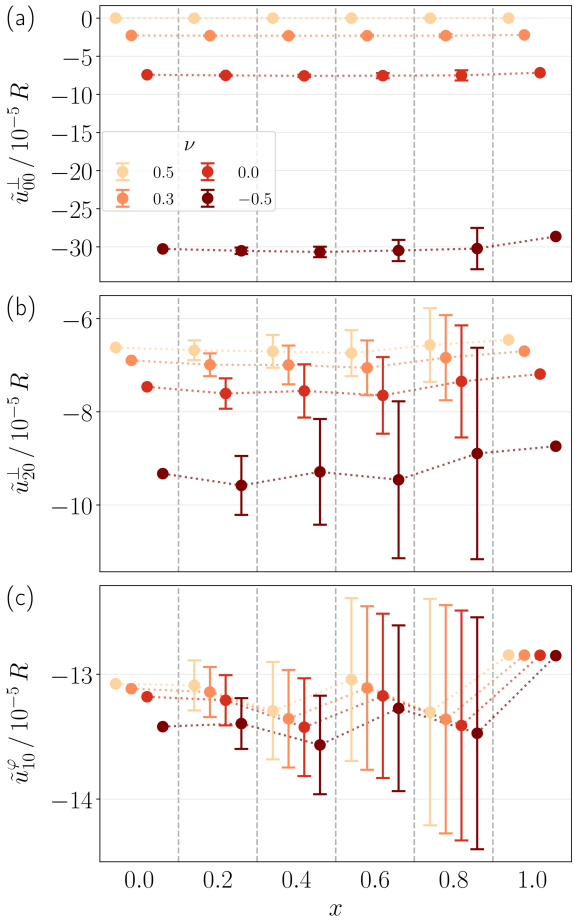

Figure 12. Same as in figure 11, here for hexagonally arranged chain-like aggregates featuring an additional initial global twist of an approximate pitch of $11.5R$. The initial twist is implemented around the center axis that is aligned with the direction of magnetization. For (a) $\tilde{u}^{\perp}_{00}$ and (b) $\tilde{u}^{\perp}_{20}$ similar results as for the untwisted structures in figure 11 are obtained, only that the magnitudes for $\tilde{u}^{\perp}_{20}$ are reversed concerning the Poisson ratios ν. Additionally, (c) $\tilde{u}^{\varphi}_{10}$ quantifies the rescaled magnitude of the torsional deformation that is induced upon magnetization when the initially twisted structures attempt to untwist themselves.

magnitude of the induced twist deformation. It describes the rotation of the upper hemisphere of our elastic body relative to the lower hemisphere, as seen from the direction of magnetization. The sign of $\tilde{u}^{\varphi}_{10}$ is related to the sense of this relative rotation and is thus connected to the sense of the initial twist that we impose. As figure 12(c) implies, the rescaled magnitudes of the effect are a bit smaller for the smaller particles at $x = 1$ than for the larger particles at $x = 0$, in line with the trends observed for $\tilde{u}^{\perp}_{00}$ and $\tilde{u}^{\perp}_{20}$ for the chain-like structures addressed in sections 3.5–3.7. Taking into account the magnitudes of the standard deviations, there is no clearly monotonic trend of the average values in figure 12(c) as a function of x.

3.8. Layered regular structures

From a practical point of view, it might be most realistic with presently available techniques to build up the systems containing regular particle arrangements layer by layer [68, 77, 83]. If these processes are automated, it may be most convenient to only use per layer one of the two particle sizes. Therefore, we add an analysis for regular particle arrangements, in which we always replace complete layers of larger particles by smaller particles in our theoretical evaluation.

In each case, we start from the center plane normal to the magnetization direction and replace all particles within this plane. Then, from there, we additionally replace all particles in the uppermost and in the lowermost layer parallel to the center plane, as seen from the direction of magnetization. These outermost layers are the n-th layers of particles as counted from the 0-th layer, the latter referring to the center plane. $n \in \mathbb{N}$ depends on the specific regular particle arrangement at hand. To further increase x, we instead replace the larger particles in each $(n-1)$-th, $(n-2)$-th, ..., third, second, and every layer by smaller particles, again counted from the center plane.

We studied the consequences of such layerwise replacement of larger by smaller particles for the simple cubic, body-centered cubic, and face-centered cubic lattice structures as well as for the quadratically and hexagonally arranged chain-like structures, see sections 3.1, 3.2, 3.3, 3.5, and 3.6, respectively. Corresponding results are depicted in figures 13–17.

Concerning all regular cubic lattice arrangements, we find that the layerwise replacement of larger by smaller particles can significantly enhance the rescaled magnetically induced increase in total volume, see figures 13(a), 14(a), and 15(a). For the investigated Poisson ratios $\nu < 0.5$, this effect is largest for the simple cubic and face-centered cubic lattices when every second layer is replaced. In contrast to that, for the body-centered cubic lattice it is most pronounced when every third layer is replaced.

Moreover, for all these three lattice types the value of $\tilde{u}_{20}^{\perp}$ shows a nonmonotonic behavior as a function of x. We observe in each case a pronounced minimum when every second layer of larger particles is replaced by smaller ones, see figures 13(b), 14(b), and 15(b). For the system containing the simple cubic lattice structure this implies that the rescaled magnitude of relative contraction along the axis of magnetization is largest in this case. Conversely, for the body-centered and face-centered cubic structures this implies a reduced rescaled magnitude of relative extension along the axis of magnetization. When every second layer of particles is replaced, we even observe a reversed behavior for the evaluated Poisson ratios $\nu > -0.5$ for the body-centered and face-centered cubic structures. That is, these systems show a relative contraction along the axis of magnetization instead of relative extension, see figures 14(b) and 15(b).

The results for the quadratically and hexagonally arranged chain-like aggregates are relatively similar to each other, see figures 16 and 17. First, the magnetically induced rescaled reduction in overall volume significantly decreases in magnitude with increasing $x < 1$ for the evaluated Poisson ratios $\nu < 0.5$. A most pronounced reduction

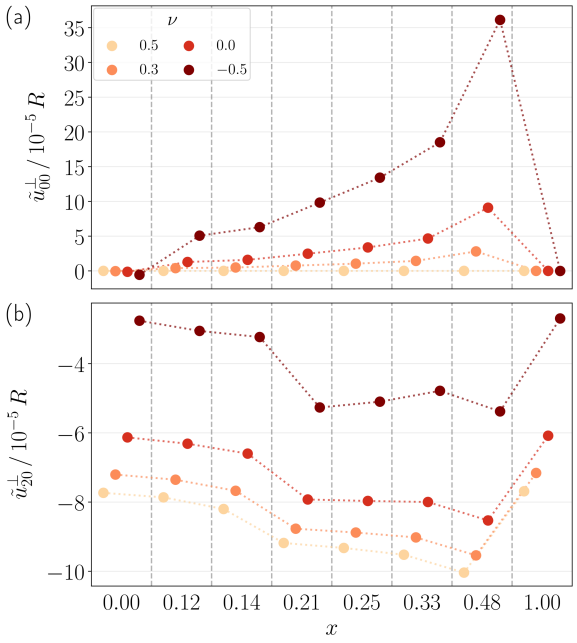

Figure 13. Same as in figure 3 for a simple cubic lattice structure, but here increasing x through a layerwise replacement of larger by smaller particles. First, all particles in the center plane normal to the axis of magnetization are replaced. Then, additionally, every n-th, $(n-1)$-th, ..., third, second, and each layer of particles is replaced, where $n \in \mathbb{N}$ refers to the outermost layers as counted from the center plane. There are pronounced effects nonmonotonic with x concerning the rescaled magnitudes of deformation. (a) A very large rescaled increase in total volume is observed for the evaluated Poisson ratios $\nu < 0.5$ when every second layer of larger particles is replaced. (b) With increasing $x < 1$, the rescaled magnitudes of contraction along the axis of magnetization are found to increase significantly and monotonically, except for $\nu = -0.5$.

in magnitude is found when every second layer of larger particles is replaced by smaller ones. Second, the rescaled relative contraction along the axis of magnetization varies nonmonotonically with x. Also this effect is most severely reduced in magnitude when the replacement of particles occurs in every second layer. Yet, remarkably, we here again observe for all evaluated Poisson ratios that the effect is increased in magnitude above the one at $x = 0$ for some intermediate values of $0 < x < 0.3$. This confirms that, indeed, the combination of different particle sizes can enhance the magnitude of magnetically induced contraction per squared employed mass of magnetizable material.

4. Conclusions

In summary, we have investigated theoretically the magnetically induced overall elastic deformation of spherical model systems of magnetic gels and elastomers containing discrete arrangements of magnetizable particles of binary size distribution. Simple

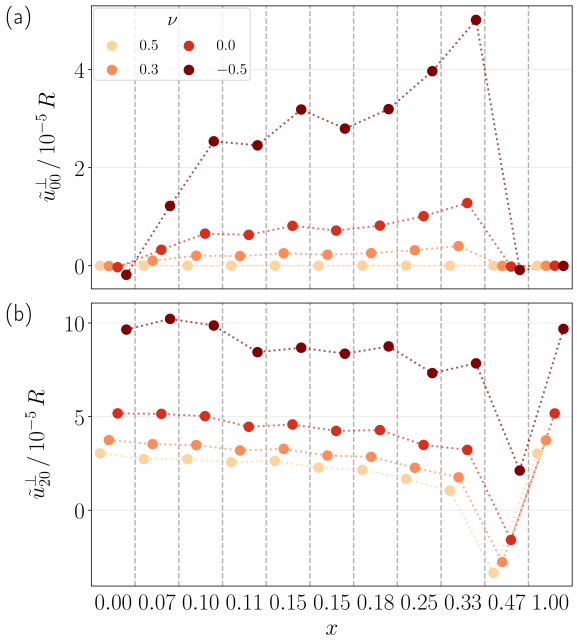

Figure 14. Same as in figure 13, but for a body-centered cubic lattice structure. (a) Similar results are obtained as for the simple cubic structures, but here with the maximum of total increase in volume observed when all particles in every third layer are replaced. (b) The rescaled magnitude of elongation along the magnetization axis mainly decreases with increasing $x < 1$, with slight nonmonotonicities. When every second layer of particles is replaced, even an inversion of the behavior into contraction along the magnetization axis is observed for the evaluated Poisson ratios $\nu > -0.5$ at $x \approx 0.47$.

cubic, body-centered cubic, face-centered cubic, and randomized isotropic particle arrangements were studied as well as systems containing quadratically or hexagonally arranged straight chain-like particle aggregates or globally twisted chain-like structures. In each case, we systematically increased the fraction of smaller particles at the cost of larger particles, keeping the total number and spatial arrangement of particles constant. Additionally, the role of the compressibility of the elastic matrix material was analyzed. We concentrate on the change of the overall volume in response to a saturating homogeneous external magnetic field as well as on the amount of relative extension or contraction along the axis of magnetization. For the systems containing the twisted chain-like structures we further evaluate the magnetically induced overall torsional deformation. To be able to compare the results for different number fractions of larger and smaller particles, we appropriately rescaled the magnitudes of the induced overall deformational response.

In the limit of uniform particle sizes, we can compare our results to corresponding previous investigations that used different approaches. For example, for a simple cubic structure we find contractional deformations along the axis of the magnetic field, in agreement with previous investigations [20, 83]. Likewise, consistency and the same type

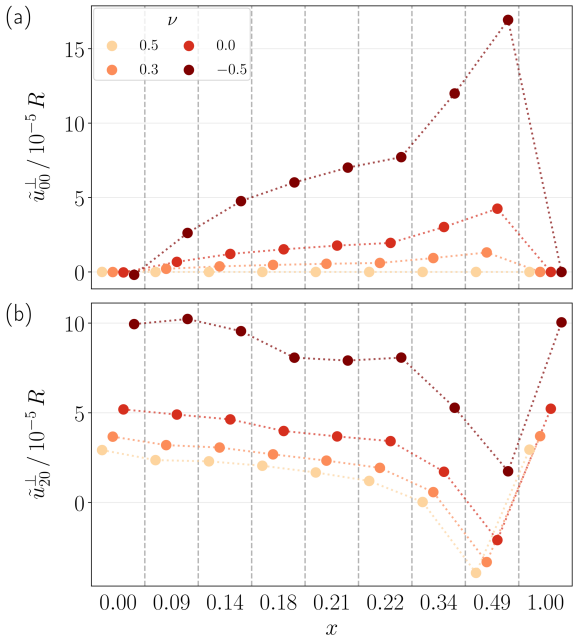

Figure 15. Same as in figure 13, but for a face-centered cubic lattice structure. The results are very similar to those for the body-centered cubic lattice structure in figure 14, only that the maximal rescaled increase in total volume in (a) is observed for the evaluated Poisson ratios $\nu > 0.5$ when every second instead of every third layer of particles is replaced.

of response is found for tetragonal structures when compared to previous studies [20,35]. Moreover, in the case of a body-centered cubic lattice structure, we observe an elongation along the axis of the magnetic field as identified in a previous analysis as well [20]. Finally, for a randomized isotropic configuration, besides a simulation result [39], we can compare to experimental observations on real samples [33, 42]. There, in all cases, an elongation along the magnetic field axis is obtained.

Our results indicate that completely random replacements of larger by smaller particles in the investigated particle arrangements do not significantly affect the averaged overall rescaled deformational response. Only for the evaluated systems containing chain-like structures, slight trends of increased averaged rescaled mechanical reaction were observed as a consequence of randomly assigned binary particle sizes. However, specific individual realizations of systems of mixed particle sizes can show remarkably different types of behavior. Therefore, selectively replacing larger by smaller particles in a targeted approach allows to design the nature of the overall rescaled deformational response. Even qualitative changes are possible, for example, relative magnetically induced contractions along the axis of magnetization can be reversed into relative expansions, and vice versa. The effect is solely tuned by selectively positioning particles of different sizes onto the particle sites. Finally, these trends were confirmed when we studied the consequences of layerwise exchange of particle sizes, which may be

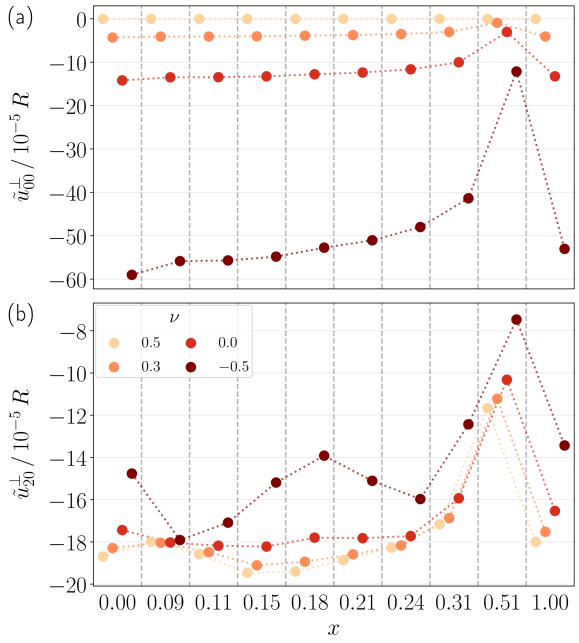

Figure 16. Same as in figure 13, but for quadratically arranged chain-like aggregates aligned along the axis of magnetization. (a) Here, the layer-by-layer replacement of larger by smaller particles with increasing $x < 1$ reduces the rescaled magnitude of the decrease in total volume for the evaluated Poisson ratios $\nu < 0.5$. The effect is markedly pronounced when every second layer is replaced at $x \approx 0.51$. (b) Similarly, the rescaled magnitude of overall relative contraction along the magnetization axis is severely reduced for $x \approx 0.51$. The behavior is nonmonotonic as a function of x. Interestingly, larger rescaled magnitudes of overall relative contraction along the axis of magnetization than those at $x = 0$ are observed at several values of $0 < x < 0.3$ for all evaluated Poisson ratios.

important for subsequent steps of practical automated realizations of corresponding systems. We expect that with the further development of 3D-printing techniques also for the fabrication of magnetic gels and elastomers [84–86], the various regular structures that we considered can be realized at some point in the future. Our investigations may then provide a basis to select requested configurations.

Although we here were presenting our results in the context of magnetically induced deformations of magnetic gels and elastomers, our discussion equally applies to electrically induced deformations of electrorheological gels and elastomers when exposed to homogeneous external electric fields [91–93]. In this case, the inclusions are electrically polarized by the external field and their mutual interactions are described by the formally identical electric dipolar interactions [67]. The analogy holds as long as dynamic effects like electrically induced leakage currents do not play a significant role.

Finally, we hope that our investigation will stimulate corresponding experimental realizations together with the further research into the controlled use of mixed particle sizes to optimize the overall material behavior [64]. Besides direct fabrication of samples

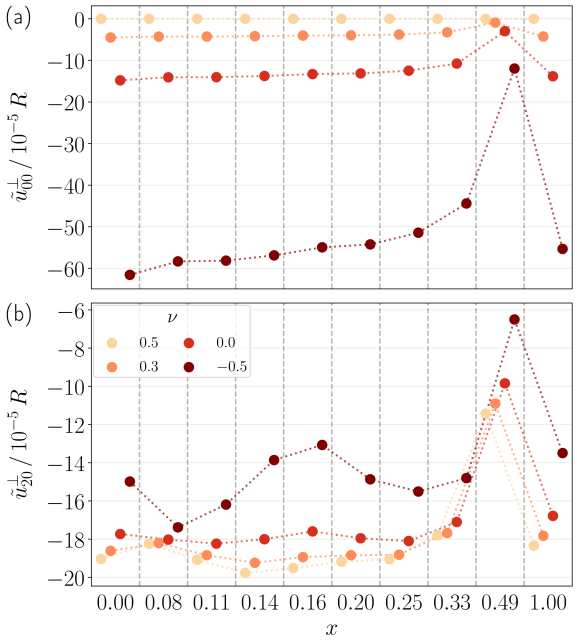

Figure 17. Same as in figure 13, but for hexagonally arranged chain-like aggregates aligned along the axis of magnetization. The observed types of behavior are similar to the ones displayed for the quadratically arranged chain-like aggregates in figure 16.

containing randomized or uniaxially structured arrangements, also positioning into requested other discrete patterns might become possible in the future when synthesizing the materials. Then the selective positioning of particles of varying sizes on specific target locations may become an additional means to optimize and adjust the resulting desired overall material behavior.

Acknowledgments

The authors thank Professor Weihua Li and his coworkers for the organization of the conference ERMR 2019 together with this associated special issue. Moreover, the authors gratefully acknowledge support by the Deutsche Forschungsgemeinschaft through the priority program SPP 1681, grant no. ME 3571/3. Some of the results in this paper were derived using the HEALPix package [79].

References

[1] Jolly M R, Carlson J D, Muñoz B C and Bullions T A 1996 *J. Intel. Mater. Syst. Struct.* **7** 613–622
[2] Filipcsei G, Csetneki I, Szilágyi A and Zrínyi M 2007 *Adv. Polym. Sci.* **206** 137–189
[3] Ilg P 2013 *Soft Matter* **9** 3465–3468
[4] Li Y, Li J, Li W and Du H 2014 *Smart Mater. Struct.* **23** 123001
[5] Odenbach S 2016 *Arch. Appl. Mech.* **86** 269–279
[6] Menzel A M 2015 *Phys. Rep.* **554** 1–45

[7] Schmauch M M, Mishra S R, Evans B A, Velev O D and Tracy J B 2017 *ACS Appl. Mater. Interfaces* **9** 11895–11901
[8] Weeber R, Hermes M, Schmidt A M and Holm C 2018 *J. Phys.: Condens. Matter* **30** 063002
[9] Weeber R, Kreissl P and Holm C 2019 *Arch. Appl. Mech.* **89** 3–16
[10] Stolbov O V and Raikher Y L 2019 *Arch. Appl. Mech.* **89** 63–76
[11] Menzel A M 2019 *Arch. Appl. Mech.* **89** 17–45
[12] Schümann M, Gundermann T and Odenbach S 2019 *Arch. Appl. Mech.* **89** 77–89
[13] Zhou Y, Huang S and Tian X 2020 *Adv. Funct. Mater.* **30** 1906507
[14] Jolly M R, Carlson J D and Muñoz B C 1996 *Smart Mater. Struct.* **5** 607–614
[15] Jarkova E, Pleiner H, Müller H W and Brand H R 2003 *Phys. Rev. E* **68** 041706
[16] Stepanov G, Abramchuk S, Grishin D, Nikitin L, Kramarenko E Y and Khokhlov A 2007 *Polymer* **48** 488–495
[17] Böse H and Röder R 2009 *J. Phys.: Conf. Ser.* **149** 012090
[18] Chertovich A V, Stepanov G V, Kramarenko E Y and Khokhlov A R 2010 *Macromolecul. Mater. Eng.* **295** 336–341
[19] Wood D S and Camp P J 2011 *Phys. Rev. E* **83** 011402
[20] Ivaneyko D, Toshchevikov V, Saphiannikova M and Heinrich G 2012 *Condens. Matter Phys.* **15** 33601
[21] Evans B A, Fiser B L, Prins W J, Rapp D J, Shields A R, Glass D R and Superfine R 2012 *J. Magn. Magn. Mater.* **324** 501–507
[22] Han Y, Hong W and Faidley L E 2013 *Int. J. Solids Struct.* **50** 2281–2288
[23] Borin D Y, Stepanov G V and Odenbach S 2013 *J. Phys.: Conf. Ser.* **412** 012040
[24] Chiba N, Yamamoto K, Hojo T, Kawai M and Mitsumata T 2013 *Chem. Lett.* **42** 253–254
[25] Pessot G, Cremer P, Borin D Y, Odenbach S, Löwen H and Menzel A M 2014 *J. Chem. Phys.* **141** 124904
[26] Sorokin V V, Stepanov G V, Shamonin M, Monkman G J, Khokhlov A R and Kramarenko E Y 2015 *Polymer* **76** 191–202
[27] Pessot G, Löwen H and Menzel A M 2016 *J. Chem. Phys.* **145** 104904
[28] Volkova T I, Böhm V, Kaufhold T, Popp J, Becker F, Borin D Y, Stepanov G V and Zimmermann K 2017 *J. Magn. Magn. Mater.* **431** 262–265
[29] Oguro T, Endo H, Kikuchi T, Kawai M and Mitsumata T 2017 *React. Funct. Polym.* **117** 25–33
[30] Pessot G, Schümann M, Gundermann T, Odenbach S, Löwen H and Menzel A M 2018 *J. Phys.: Condens. Matter* **30** 125101
[31] Watanabe M, Ikeda J, Takeda Y, Kawai M and Mitsumata T 2018 *Gels* **4** 49
[32] Zrínyi M, Barsi L and Büki A 1996 *J. Chem. Phys.* **104** 8750–8756
[33] Gollwitzer C, Turanov A, Krekhova M, Lattermann G, Rehberg I and Richter R 2008 *J. Chem. Phys.* **128** 164709
[34] Fuhrer R, Athanassiou E K, Luechinger N A and Stark W J 2009 *Small* **5** 383–388
[35] Ivaneyko D, Toshchevikov V P, Saphiannikova M and Heinrich G 2011 *Macromol. Theory Simul.* **20** 411–424
[36] Stolbov O V, Raikher Y L and Balasoiu M 2011 *Soft Matter* **7** 8484–8487
[37] Maas J and Uhlenbusch D 2016 *Smart Mater. Struct.* **25** 104002
[38] Metsch P, Kalina K A, Spieler C and Kästner M 2016 *Comp. Mater. Sci.* **124** 364–374
[39] Attaran A, Brummund J and Wallmersperger T 2017 *J. Magn. Magn. Mater.* **431** 188–191
[40] Fischer L and Menzel A M 2019 *J. Chem. Phys.* **151** 114906
[41] Fischer L and Menzel A M arXiv preprint, arXiv:2003.04402 (2020)
[42] Filipcsei G and Zrínyi M 2010 *J. Phys.: Condens. Matter* **22** 276001
[43] Rosensweig R 1985 *Ferrohydrodynamics* (Cambridge University Press, Cambridge)
[44] Huke B and Lücke M 2004 *Rep. Prog. Phys.* **67** 1731–1768
[45] Odenbach S 2004 *J. Phys.: Condens. Matter* **16** R1135–R1150
[46] Holm C and Weis J J 2005 *Curr. Opin. Colloid Interface Sci.* **10** 133–140

[47] De Vicente J, Klingenberg D J and Hidalgo-Alvarez R 2011 *Soft Matter* **7** 3701–3710
[48] Thurm S and Odenbach S 2003 *Phys. Fluids* **15** 1658–1664
[49] Kramarenko E Y, Chertovich A, Stepanov G, Semisalova A, Makarova L, Perov N and Khokhlov A 2015 *Smart Mater. Struct.* **24** 035002
[50] Borbáth T, Günther S, Borin D Y, Gundermann T and Odenbach S 2012 *Smart Mater. Struct.* **21** 105018
[51] Winger J, Schümann M, Kupka A and Odenbach S 2019 *J. Magn. Magn. Mater.* **481** 176–182
[52] Kalina K A, Metsch P and Kästner M 2016 *Int. J. Solids Struct.* **102** 286–296
[53] Becker T I, Stolbov O V, Borin D Y, Zimmermann K and Raikher Y L 2020 *Smart Mater. Struct.* in press, https://doi.org/10.1088/1361–665X/ab8fc9
[54] Bohlius S, Brand H R and Pleiner H 2004 *Phys. Rev. E* **70** 061411
[55] Gebhart P and Wallmersperger T 2019 *J. Mech. Phys. Solids* **122** 69–83
[56] Zaccarelli E, Valeriani C, Sanz E, Poon W, Cates M and Pusey P 2009 *Phys. Rev. Lett.* **103** 135704
[57] Dijkstra M, van Roij R and Evans R 1999 *Phys. Rev. Lett.* **82** 117–120
[58] Lugo-Frías R and Klapp S H 2016 *J. Phys.: Condens. Matter* **28** 244022
[59] von Lockette P R, Lofland S E, Koo J H, Kadlowec J and Dermond M 2008 *Polym. Test.* **27** 931–935
[60] Stepanov G, Borin D and Odenbach S 2009 *J. Phys.: Conf. Ser.* **149** 012098
[61] Melenev P, Raikher Y, Stepanov G, Rusakov V and Polygalova L 2011 *J. Intel. Mater. Syst. Struct.* **22** 531–538
[62] Tian T, Li W, Alici G, Du H and Deng Y 2011 *Rheol. Acta* **50** 825–836
[63] Sorokin V V, Stepanov G V, Shamonin M, Monkman G J and Kramarenko E Y 2017 *Smart Mater. Struct.* **26** 035019
[64] Li W and Zhang X 2010 *Smart Mater. Struct.* **19** 035002
[65] Landau L D and Lifshitz E M 1986 *Theory of Elasticity* (Elsevier, Oxford)
[66] Walpole L J 2002 *Proc. R. Soc. London A* **458** 705–721
[67] Jackson J D 1999 *Classical Electrodynamics* (Wiley, New York)
[68] Puljiz M, Huang S, Auernhammer G K and Menzel A M 2016 *Phys. Rev. Lett.* **117** 238003
[69] Puljiz M and Menzel A M 2017 *Phys. Rev. E* **95** 053002
[70] Puljiz M and Menzel A M 2019 *Phys. Rev. E* **99** 053002
[71] Stepanov G, Borin D Y, Raikher Y L, Melenev P and Perov N 2008 *J. Phys.: Condens. Matter* **20** 204121
[72] Annunziata M A, Menzel A M and Löwen H 2013 *J. Chem. Phys.* **138** 204906
[73] Gundermann T and Odenbach S 2014 *Smart Mater. Struct.* **23** 105013
[74] Biller A M, Stolbov O V and Raikher Y L 2014 *J. Appl. Phys.* **116** 114904
[75] Biller A M, Stolbov O V and Raikher Y L 2015 *Phys. Rev. E* **92** 023202
[76] Gundermann T, Cremer P, Löwen H, Menzel A M and Odenbach S 2017 *Smart Mater. Struct.* **26** 045012
[77] Puljiz M, Huang S, Kalina K A, Nowak J, Odenbach S, Kästner M, Auernhammer G K and Menzel A M 2018 *Soft Matter* **14** 6809–6821
[78] Goh S, Menzel A M and Löwen H 2018 *Phys. Chem. Chem. Phys.* **20** 15037–15051
[79] Górski K M, Hivon E, Banday A J, Wandelt B D, Hansen F K, Reinecke M and Bartelmann M 2005 *Astrophys. J.* **622** 759–771
[80] Scarpa F, Bullough W and Lumley P 2004 *Proc. Inst. Mech. Eng. C* **218** 241–244
[81] Li Q, Kartikowati C W, Horie S, Ogi T, Iwaki T and Okuyama K 2017 *Sci. Rep.* **7** 9894
[82] Borin D 2020 *Phil. Trans. R. Soc. A* **378** 20190256
[83] Chen W, Sun L, Li X and Wang D 2013 *Smart Mater. Struct.* **22** 105012
[84] Bastola A, Paudel M and Li L 2020 *J. Magn. Magn. Mater.* **494** 165825
[85] Kim Y, Yuk H, Zhao R, Chester S A and Zhao X 2018 *Nature* **558** 274–279
[86] Dohmen E, Saloum A and Abel J 2020 *Phil. Trans. R. Soc. A* **378** 20190257
[87] Frickel N, Messing R, Gelbrich T and Schmidt A M 2009 *Langmuir* **26** 2839–2846

[88] Frickel N, Messing R and Schmidt A M 2011 *J. Mater. Chem.* **21** 8466–8474
[89] Messing R, Frickel N, Belkoura L, Strey R, Rahn H, Odenbach S and Schmidt A M 2011 *Macromolecules* **44** 2990–2999
[90] Aziz S and Spinks G M 2020 *Mater. Horiz.* **7** 667–693
[91] An Y and Shaw M T 2003 *Smart Mater. Struct.* **12** 157–163
[92] Allahyarov E, Löwen H and Zhu L 2015 *Phys. Chem. Chem. Phys.* **17** 32479–32497
[93] Liu B and Shaw M T 2001 *J. Rheol.* **45** 641–657

P4 Magnetic elastomers as specific soft actuators – predicting particular modes of deformation from selected configurations of magnetizable inclusions

Reproduced from

L. Fischer and A. M. Menzel,
Magnetic elastomers as specific soft actuators – predicting particular modes of deformation from selected configurations of magnetizable inclusions,
J. Magn. Magn. Mater. **591**, 171695 (2024).

Digital Object Identifier (DOI): `https://doi.org/10.1016/j.jmmm.2023.171695`

Statement of contribution

Both authors contributed to this work. I performed all calculations and evaluated the results, based on ideas and discussions with AMM. Moreover, I drafted most of the first version of the manuscript (particularly section 3), including all figures, and the appendices. Finally, I also prepared the published dataset that accompanies the paper. I estimate my contribution to this work during my PhD as 85 %.
See also the "CRediT authorship contribution statement" within the publication.

Copyright and license notice

Journal of Magnetism and Magnetic Materials 591 (2024) 171695

Contents lists available at ScienceDirect

Journal of Magnetism and Magnetic Materials

journal homepage: www.elsevier.com/locate/jmmm

Research article

Magnetic elastomers as specific soft actuators – predicting particular modes of deformation from selected configurations of magnetizable inclusions

Lukas Fischer *, Andreas M. Menzel

Institut für Physik, Otto-von-Guericke-Universität Magdeburg, Universitätsplatz 2, 39106 Magdeburg, Germany

ARTICLE INFO

Dataset link: https://doi.org/10.5281/zenodo.10035624

Keywords:
Magnetic gels and elastomers
Magnetostriction
Actuation
Microstructure
Macroscopic behavior
Green's function method

ABSTRACT

Amongst the various fascinating types of material behavior featured by magnetic gels and elastomers are magnetostrictive effects. That is, deformations in shape or changes in volume are induced from outside by external magnetic fields. Application of the materials as soft actuators is therefore conceivable. Mostly, straight contraction or extension of the materials along a certain direction is discussed and investigated in this context. Here, we demonstrate that various further, different, higher modes of deformation can be excited. To this end, different spatial arrangements of the magnetizable particles enclosed by the soft elastic matrix, which constitute the materials, need to be controlled and realized. We address various different types of spatial configurations of the particles and evaluate resulting types of deformation using theoretical tools developed for this purpose. Examples are sheet-like arrangements of particles, circular or star-shaped arrangements of chain-like aggregates, or actual three-dimensional star-like particle configurations. We hope to stimulate with our work the development of experimental design and engineering methods so that selected spatial particle arrangements in magnetic gels and elastomers can be put to reality. Overall, we in this way wish to promote the transfer of these promising class of materials to real-world applications.

1. Introduction

We consider soft materials that consist of a reversibly deformable, elastic, continuous matrix containing discrete, magnetizable inclusions. Magnetic gels and elastomers [1–11] represent prime examples of this class of materials. In this case, the elastic matrix is of polymeric origin, crosslinked to an elastic network and possibly swollen by a solvent for elevated softness. The inclusions can be regarded as solid particles. For possible experimental realizations, the diameters of these particles are typically of submillimeter range, from tens to a few hundreds of micrometers.

When magnetized by external magnetic fields, the particles interact with each other magnetically. In the absence of external magnetic field gradients, the interparticle interactions are the only forces generated on the inclusions. The particles are enclosed by the surrounding elastic matrix and cannot move through it due to their size. Therefore, the forces generated on the particles are transmitted to the surrounding soft elastic matrix, leading to its deformation [12–16].

From such effects occurring on the microscopic particle scale, overall macroscopic material properties are affected. Above all, the macroscopic mechanical material behavior is modified, which is frequently referred to as the magnetorheological effect. More precisely, the induced magnetic interactions lead to changes in the static elastic moduli [2,17–24] as well as in the dynamic storage and loss moduli [1,25–36]. Since this effect works in a contactless way by external magnetic field, is tunable by the strength of the external field, and often is reversible [37], a multitude of possible applications results. Frequently, magnetically tunable vibration absorbers and damping devices are mentioned in this context [38–43].

It has been demonstrated by microcomputed x-ray tomography that the change in overall mechanical behavior is correlated to internal restructuring [44]. Specifically, chain-like aggregates of initially well separated magnetized particles can form by deformation of the surrounding elastic matrix [34,45,46]. Not only is the mechanical behavior affected by such internal restructuring. The particles usually feature electrical and thermal conductivities that are notably different from those of the surrounding elastic matrix. Thus, when the particles reversibly form anisotropic aggregates (such as chains), this causes magnetically tunable changes in transport properties, especially electric and thermal conductivity [47–52]. Only a few studies have addressed this behavior so far.

We here consider a third type of overall response of the materials to external magnetic fields. Namely, these are macroscopic magnetostrictive effects [53–66]. That is, the deformations induced by the magnetized particles in their surroundings due to the resulting magnetic interparticle interactions result in overall macroscopic distortions.

* Corresponding author.
E-mail addresses: lukas.fischer@ovgu.de (L. Fischer), a.menzel@ovgu.de (A.M. Menzel).

https://doi.org/10.1016/j.jmmm.2023.171695
Received 26 October 2023; Received in revised form 15 December 2023; Accepted 27 December 2023
Available online 9 January 2024

So far, this type of behavior has been discussed in the context of soft magnetoelastic actuators [2,7,15,58,62,67–76] that can serve, for instance, as magnetic valves.

It is a significant challenge especially for theoretical studies to link the properties on the microscopic particulate scale, especially the particle configurations and resulting magnetically induced interactions, to the macroscopic scale of overall material behavior [16,77–83]. In this way, the parameters in macroscopic continuum descriptions [28,84,85] could be substantiated by their microscopic origin. Several previous works resort to statistical approaches to handle the many microscopic degrees of freedom associated with the magnetizable particles [86,87]. These approaches by construction rely on a certain type of averaging and are justified from a coarse-grained macroscopic perspective for large samples. However, after all, each sample of an elastic composite system is of finite size. Moreover, the particle positions are fixed in this type of materials, so that each individual sample by itself does not necessarily show an averaged behavior. If we want to describe quantitatively and in detail the deformation of one specific sample, we need to calculate the overall response from the discrete arrangement of all individual inclusions in this specific realization.

Therefore, our approach is different from averaging procedures. Based on a Green's function formalism [64,88], we have developed a theoretical description that allows us to evaluate from the discrete arrangement of magnetizable inclusions and the resulting magnetic interactions when exposed to an external magnetic field the overall macroscopic deformation of the whole system. The approach is valid in the regime of linear elasticity, typically corresponding to not more than moderate elastic deformations (of, for instance, about 10% [89]), and for sufficiently separated magnetizable inclusions. We have demonstrated that, on this basis, we can determine for various regular lattice-like arrangements of magnetizable inclusions inside the elastic matrix the resulting, magnetically induced, overall deformations for sphere-like systems [64,66].

In one first study, we have shown that more specific modes of overall deformation can be excited by an appropriately chosen arrangement of the internal particle structure. More precisely, we considered globally twisted arrangements of chain-like structures and helical particle configurations [65,81]. As a result, an overall torsional mode of deformation was induced. Such systems have recently been realized experimentally as well [76].

It is our goal in the present work to extend such types of considerations. Instead of the previously addressed regular lattice-like arrangements, we now turn to more specific structures of magnetizable particles. We demonstrate that an extended spectrum of modes of overall deformation with special focus on certain specific modes of deformation can be obtained by realizing these more specific arrangements of particles. Such a perspective highlights the potential of the materials when searching for soft elastic actuators of peculiar types of induced deformation for individual tasks.

We proceed by briefly summarizing the background of the theoretical approach that we have developed for this purpose in Section 2. After that, we introduce several different types of specific arrangements of particles and evaluate their resulting overall macroscopic magnetoelastic response in the several subsections contained in Section 3. Our conclusions together with a brief perspective are provided in Section 4.

2. Theoretical description

If one wishes to calculate the actual deformation of a system as viewed from outside, it is mandatory to include the boundaries explicitly. Any sample is of finite size. When we discuss its deformation in the context of actuation, it is usually the displacement of its surfaces that determines the considered response.

Calculating by analytical theory the elastic deformations in a finite-sized system provides an extreme challenge. We have found a way by turning to spherical systems. In this case, building on previous work that considered an elastic sphere enclosed by an infinitely extended elastic matrix [88], we managed to determine the associated Green's function for the elastic deformation of a free-standing elastic sphere [64]. The Green's function quantifies the elastic displacements resulting in the elastic sphere in response to point-like force centers acting within the sphere on the elastic material. In our case, we consider the magnetizable inclusions as these point-like force centers when they are magnetized in the external magnetic field. To render such an approach quantitatively valid, the particulate inclusions need to be well separated from each other relative to their diameter.

More precisely, we consider homogeneous, isotropic, linearly elastic matrices. Their deformations are quantified by the Navier–Cauchy equations [90]

$$\mu\Delta\mathbf{u}(\mathbf{r}) + \frac{\mu}{1-2\nu}\nabla\nabla\cdot\mathbf{u}(\mathbf{r}) = -\mathbf{f}_b(\mathbf{r}). \tag{1}$$

In this equation, $\mathbf{u}(\mathbf{r})$ corresponds to the elastic displacement field at position $\mathbf{r}$, μ is the elastic shear modulus, ν represents the Poisson ratio that quantifies the compressibility of the elastic matrix, and $\mathbf{f}_b(\mathbf{r})$ sets the bulk force density acting on the elastic material. To determine the resulting displacement field, we set $\mathbf{f}_b(\mathbf{r}) = \sum_{i=1}^{N}\mathbf{F}_i\delta(\mathbf{r}-\mathbf{r}_i)$ in our case, where N provides the overall number of particulate inclusions, i labels the inclusions, while $\mathbf{F}_i$ specifies the magnetic force acting on the ith inclusion and $\mathbf{r}_i$ its position. $\delta(\mathbf{r})$ represents the Dirac delta function. An analytical expression for the Green's function associated with Eq. (1) for a spherical geometry is available [64,88], yet complex and lengthy, so we do not reproduce it here. After derivation of this Green's function for the geometry of a free-standing elastic sphere [64], we assume the inclusions as well separated from each other and thus to reasonable approximation as point-like. Then, we obtain the resulting displacement field as

$$\mathbf{u}(\mathbf{r}) = \sum_{i=1}^{N}\underline{\mathbf{G}}(\mathbf{r},\mathbf{r}_i)\cdot\mathbf{F}_i, \tag{2}$$

where $\underline{\mathbf{G}}(\mathbf{r},\mathbf{r}_i)$ denotes the corresponding Green's function, $\mathbf{r}$ the position at which we evaluate the displacement field, and $\mathbf{r}_i$ the position of the ith inclusion.

We evaluate the resulting displacement field $\mathbf{u}(\mathbf{r})$ at 49152 well distributed positions on the surface of the elastic sphere, relying on the distribution defined by the HEALPix package [91]. For our purpose, we then consider the components of radial outward, azimuthal, and polar surface displacements $u^{\perp}(\mathbf{r})$, $u^{\varphi}(\mathbf{r})$, $u^{\theta}(\mathbf{r})$, respectively. These components are directly connected to the deformation of the sphere as viewed from outside. We then expand these components of the surface displacement field into spherical harmonics. In this way, since spherical harmonics form a complete basis set of orthonormal functions on the surface of the sphere, we thus determine the resulting spectrum of normal modes of deformation. The magnitudes of the expansion coefficients are related to the strengths of the particular types of deformation associated with the specific modes.

Finally, since the inclusions are well separated from each other, we approximate their mutual magnetic interactions as dipolar. Therefore, the magnetic force $\mathbf{F}_i$ acting on the ith inclusion is specified as [92]

$$\mathbf{F}_i = -\sum_{\substack{j=1\\ j\neq i}}^{N}\frac{3\mu_0 m^2\left[5\hat{\mathbf{r}}_{ij}\left(\hat{\mathbf{m}}\cdot\hat{\mathbf{r}}_{ij}\right)^2 - \hat{\mathbf{r}}_{ij} - 2\hat{\mathbf{m}}\left(\hat{\mathbf{m}}\cdot\hat{\mathbf{r}}_{ij}\right)\right]}{4\pi r_{ij}^4}. \tag{3}$$

In this expression, μ_0 is the magnetic vacuum permeability. We consider all magnetizable inclusions to be identical in size and magnetic properties and exposed to strong homogeneous external magnetic fields, so that they are magnetized to saturation. Then, the magnetic moment $\mathbf{m}$ of magnitude m and orientation $\hat{\mathbf{m}}$ is the same for all these identical magnetic inclusions. In our coordinate frame, we set $\hat{\mathbf{z}} \parallel \hat{\mathbf{m}}$. Moreover, we introduced $\mathbf{r}_{ij} = \mathbf{r}_i - \mathbf{r}_j$, $r_{ij} = |\mathbf{r}_{ij}|$, and $\hat{\mathbf{r}}_{ij} = \mathbf{r}_{ij}/r_{ij}$. Since the deformation of the material influences the positioning of the magnetizable inclusions, which in turn affects the magnetic interactions that

cause the deformations in the first place, we use an iterative numerical scheme [64]. It leads us to the final deformed state and thus to the set of magnetic interaction forces that is utilized to calculate the surface displacements.

3. Specific discrete arrangements of particulate inclusions and overall mechanical response

In this part, we investigate the induced mechanical response of the whole system as induced by various different types of spatial configurations of discrete particulate magnetizable inclusions. To respect the requirements in Section 2, we impose a minimal center-to-center separation distance of $0.12R$ of the individual particles from each other, where R is the radius of the elastic sphere that in the following sets our unit of length. Simultaneously, a minimal distance of $0.06R$ is maintained from the surface of the sphere. We assume spherical inclusions of radius $0.02R$. To quantify the strength of the magnetic interactions relative to the elastic interactions, we rely on a nondimensional parameter $3\mu_0 m^2/4\pi\mu R^6$. In the following, its magnitude is set to 5.4×10^{-8}, in line with experimental parameter values [64]. One possible experimental set of parameters that leads to this value is given by an elastic matrix of shear modulus $\mu \approx 1.67\,\mathrm{kPa}$ [53,54,67] and saturation magnetization of $518\,\mathrm{kA\,m^{-1}}$ for the magnetizable inclusions, as would be realistic for Fe_3O_4 [93]. Besides, the inclusion radius is set to $0.02R$ as above. Along these lines, we evaluate in the following the overall magnetoelastic response of various spatial arrangements of chain-like aggregates, hexagonally structured layer-like configurations, spherical arrangements, three-dimensional star-shaped configurations, and single- and double-stranded helical arrangements. It becomes obvious that the different spatial arrangement on the particulate microscale is connected to and in parts reflected by the resulting spectrum of modes of overall deformation. Varying the microscopic structure thus generally enables modifying the relative magnitude of dominating macroscopic modes.

In each of the various cases considered in the following subsections, we address four different values of the Poisson ratio. They quantify the degree of compressibility of the elastic matrix. Specifically, $\nu = 0.5$ describes completely incompressible materials that do not allow any changes in volume under deformation. Next, $\nu = 0.3$ represents materials that are moderately compressible. $\nu = 0$ describes a strongly compressible material for which elongation along one axis does not lead to contraction along the perpendicular axes. Lastly, $\nu = -0.5$ is associated with materials that even elongate along the perpendicular axes when stretching it along an initially selected axis. Such astonishing behavior is called auxetic.

3.1. Chain-like structures

The first kind of arrangements of magnetizable inclusions inside the elastic matrix that we consider are various spatial organizations of chain-like structures. For this purpose, we specify different two-dimensional arrangements in the central plane of the elastic sphere, the normal vector to this plane coinciding with the magnetization direction. These configurations in the central plane set the spatial organization of our chain-like structures. Then, we stack magnetizable inclusions along the magnetization direction above and below these inclusions with a spacing of $0.121R$ to establish the chain-like aggregates filling the sphere.

3.1.1. Planar star-shaped arrangements

In the first case, we use a regular two-dimensional star-shaped arrangement of inclusions in the central plane, where we first select the number of arms n_{arms}. The plane is then evenly divided into n_{arms} segments, with inclusions placed on the boundaries between these segments. One inclusion is always placed at the center of the sphere. The chain-like aggregates are then grown towards the top and the bottom of the sphere from the central plane. Along one arm, we use the same distance of nearest neighbors as the distance within the chain-like aggregates ($0.121R$). Additionally, for neighboring particles in one arm, we use an alternating vertical shift of $0.121R/2$. This allows for more inclusions per arm and in total in our final configuration while respecting the imposed minimal distance of neighboring inclusions. For high $n_{arms} \geq 6$, some chains close to the center were deleted because they are too close to each other, in line with our constraints. We visualize top and tilted top views of the resulting arrangements in Fig. 1, with the missing chains visible as gaps in the regular arrangements. Additionally, we list the missing chains explicitly in Appendix A.

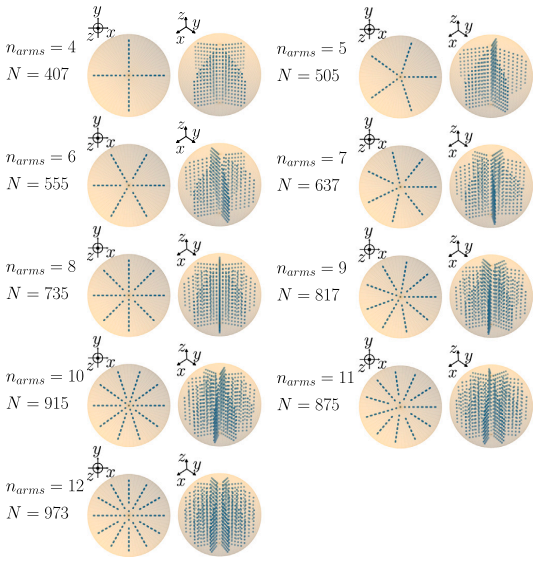

Fig. 1. Top views (left of each pair of snapshots) and tilted top views (right of each pair) of the star-shaped arrangements of chains of particles. The chains are oriented along the magnetization direction $\hat{\mathbf{z}}$. n_{arms} indicates the number of arms of each star and N sets the number of magnetizable inclusions. Gaps around the centers in the top views in the regular arrangements for $n_{arms} \geq 6$ result from our constraints, see also Appendix A.

Under magnetization, all these arrangements induce magnetostrictive deformations of the material. We here characterize and define the modes of deformation according to expansions into spherical harmonics. The most important modes, i.e. those of overall largest (absolute) magnitude, are plotted in Fig. 2 for the geometries of different values of n_{arms}. Corresponding types of deformation are illustrated on the right-hand side of Fig. 2. On the one hand, for the modes associated with the component $u^{\perp}$, the overall shape of the material is affected and we plot what the new shape looks like if only this mode of positive sign were present. On the other hand, the modes associated with u^{θ} (and also u^{φ}) describe displacements tangential to the surface. Therefore, the overall shape of a sphere is not changed by them. Instead, possibly local, tangential displacements are included by them. For modes related to the spherical harmonic $Y_{l,m}$ with $m \neq 0$, the resulting φ-dependence can manifest itself in two different ways: Either as $\cos(m\varphi)$ or as $-\sin(m\varphi)$. In the former case, we write it (using the convention of the HEALPix package [91]), as a real expansion coefficient, indicated by the letters "Re" in the plots. In the latter case, as an imaginary expansion coefficient, indicated by "Im" (with the negative sign by convention). Obviously, the resulting displacement field is real in both cases, which is a result of combining the terms with positive and negative m – we here only plot the expansion coefficient for positive m.

In our plots, we only show the nonvanishing modes, i.e. for the plots with "Re", the corresponding imaginary part is approximately zero and vice versa. For further details, we refer to Ref. [65]. The corresponding types of deformation are illustrated on the right-hand side of Fig. 2 by the black arrows. The lengths and directions of the arrows describe the displacements induced by only the corresponding mode, again for positive sign. For negative sign of the corresponding mode, all the directions are simply reversed. We illustrate the mode corresponding to either the real or to the imaginary part of the coefficient, depending on which one was found as the nonvanishing coefficient in the plots on the left-hand side.

As can be inferred from Fig. 2(a), magnetizing chain-like structures mainly leads to overall reduction in volume, i.e. $u^{\perp}_{00} < 0$ (except for incompressible materials of $\nu = 0.5$). We note here that for generic visualization on the right-hand side, we there always refer to positive values of the mode. In the present case, the illustration on the right-hand side of Fig. 2(a) is for $u^{\perp}_{00} > 0$. As we obtain negative values from our expansion, the material behavior is inverse to that, namely a reduction in volume instead of an increase in volume. Additionally, we find $u^{\perp}_{20} < 0$, see Fig. 2(b), which indicates a contraction along the magnetization direction (also referred to as oblate deformation). Again, on the right-hand side of Fig. 2(b), the visualization is for $u^{\perp}_{20} > 0$, referring to an elongation along the magnetization direction. The observed behavior is expected from the attractive interactions along the magnetization direction of each chain-like aggregate. The mode $u^{\theta}_{10} > 0$ in Fig. 2(d) indicates material displacements along the tangential direction on the surface of the sphere, within all planes containing the magnetization direction. Displacements are in opposite directions on the upper and lower hemisphere. This again contains the effect of a contraction along the magnetization direction, yet here tangentially to the surface. With lower magnitude, the values $u^{\theta}_{30} < 0$ in Fig. 2(e) modulate this behavior, indicating that displacements towards the equatorial plane are more pronounced closer to it than near the poles. Mostly, we observe an increasing trend of all these kinds of deformation with n_{arms}. This is in line with the increasing number of magnetizable inclusions. Simultaneously, the higher values of n_{arms} decrease the distance between nearby chains, therefore pronouncing the repulsive interactions between neighboring inclusions from different chains.

Additionally, we plot two modes that are strongly related to the considered configurations. Namely, these are the modes $u^{\perp}_{n_{arms},n_{arms}}$ and $u^{\varphi}_{n_{arms},n_{arms}}$, where we set both values of l and m of the corresponding spherical harmonic $Y_{l,m}$ to n_{arms}. Therefore, these modes reflect the symmetry of the underlying spatial configuration. For example, in Fig. 2(c), we observe that for $n_{arms} = 4$ the deformations characterized by $u^{\perp}_{44}$ show a four-fold symmetry as does the first configuration of $n_{arms} = 4$ in the top view in Fig. 1. In the vicinity of each chain located closer to the surface of the sphere, the contraction on the surface along the magnetization direction is more pronounced when compared to the positions that are further away from the chains. In general, this behavior is more obvious for low n_{arms}, for which the distance between different chains is larger and the deformation on the surface is therefore varying more significantly. In $u^{\varphi}_{n_{arms},n_{arms}}$, we observe a similar behavior, see Fig. 2(f). This mode shows that the surface of the elastic sphere close to the ends of the chains is displaced towards the positions of the chains. For example, the arrows in Fig. 2(f) are all positioned at $\varphi = -\pi/8$ and indicate displacements towards $\varphi = 0$, where we find one of the chain-like aggregates corresponding to the end of one arm of our planar star-shaped arrangement.

The magnitude of most of these modes increase with decreasing Poisson ratio, that is, as the elastic matrix becomes more compressible and finally auxetic, see Fig. 2. This tendency is expected because a more compressible matrix less severely restricts the deformations. However, the trend is inverted for some mode of coefficient $u^{\perp}_{20} < 0$, see Fig. 2(b) where the absolute magnitude decreases with decreasing Poisson ratio for $n_{star} \geq 8$, probably due to the more pronounced repulsive interactions as mentioned above. An inverted behavior is also observed in the modes of coefficients $u^{\theta}_{10} > 0$ and $u^{\theta}_{30} < 0$ for low values of n_{star} in Fig. 2(d) and (e), respectively.

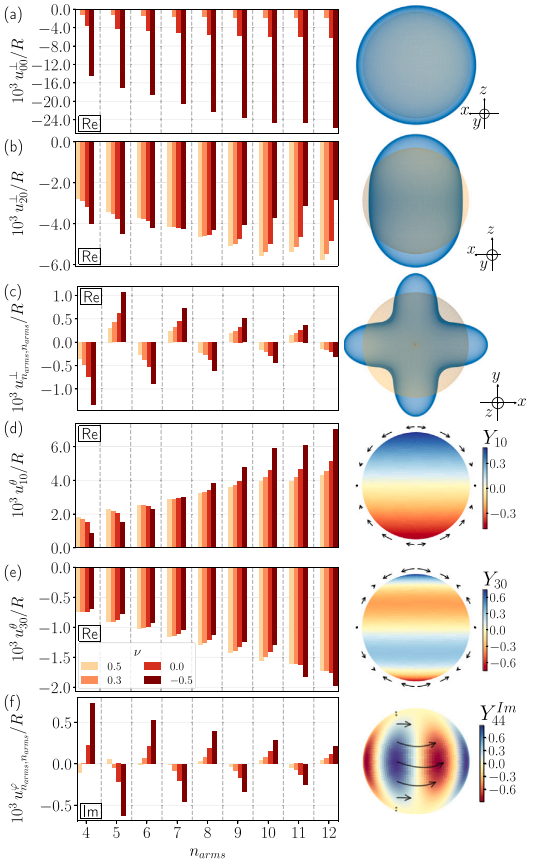

Fig. 2. For the star-shaped chain configurations in Fig. 1, we evaluate the most important deformational modes. They are characterized by an expansion into spherical harmonics of the three components of the displacement field on the surface of the elastic sphere. On the left-hand side, we plot the largest expansion coefficients depending on n_{arms} and the Poisson ratio ν of the elastic material. The second index of the respective mode m can correspond to a φ-dependence of $\cos(m\varphi)$ or $-\sin(m\varphi)$, which we label by "Re" (real) or "Im" (imaginary) in the plots by convention, respectively. From those two options, we always select the nonvanishing modes for the plots. On the right-hand side, we visualize the corresponding deformational mode (always for positive value of the coefficient, negative coefficients invert this behavior). For $u^{\perp}$ in (a)–(c), we plot the deformed shape in blue in comparison to the undeformed shape in yellow. In the first two cases, we use side views, while the third row contains a top view as in Fig. 1. For u^{θ} in (d,e), we color-code the value of the corresponding spherical harmonic in a side view of the sphere with the x-axis in the center. We illustrate the tangential polar displacements, given by u^{θ}, which the mode corresponds to using black arrows. Black dots indicate negligible displacements at this position. Similarly, we plot u^{φ} in (f), but now for corresponding tangential azimuthal displacements. As we found only an imaginary mode here, we also plot the deformations corresponding to the imaginary part of this mode (superscript Im). In (c) and (f), we plot that mode of l and m set to the value n_{arms} of the corresponding configuration. The visualizations on the right-hand side of those rows correspond to the case of $n_{arms} = 4$.

3.1.2. Planar star-shaped arrangements without vertical shift between neighboring chains

We also investigate planar star-shaped arrangements that were constructed in the same way as in the previous Section 3.1.1, but without the mutual vertical shift of neighboring chains. Instead, we increase the distance between neighboring chains to $0.121R$ so that neighboring inclusions still approximately maintain the minimal distance according

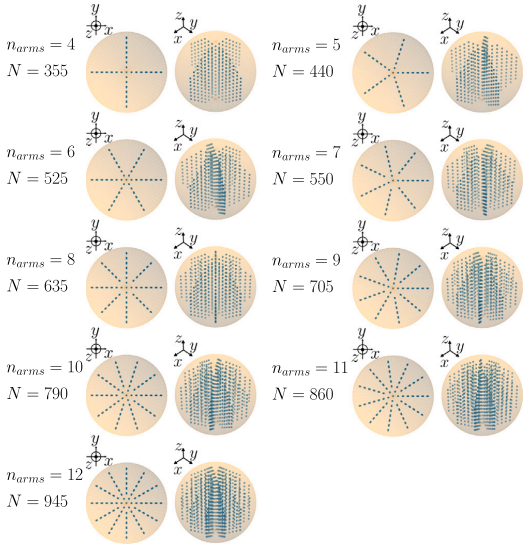

Fig. 3. Top views (left of each pair of snapshots) and tilted top views (right of each pair) of the star-shaped arrangements of chains of particles similarly to the configurations displayed in Fig. 1, but without mutual vertical shifts of neighboring chains along the magnetization direction $\hat{\mathbf{z}}$. Again, n_{arms} indicates the number of arms of each star and N sets the number of magnetizable inclusions. Appendix B contains further structural details on these configurations.

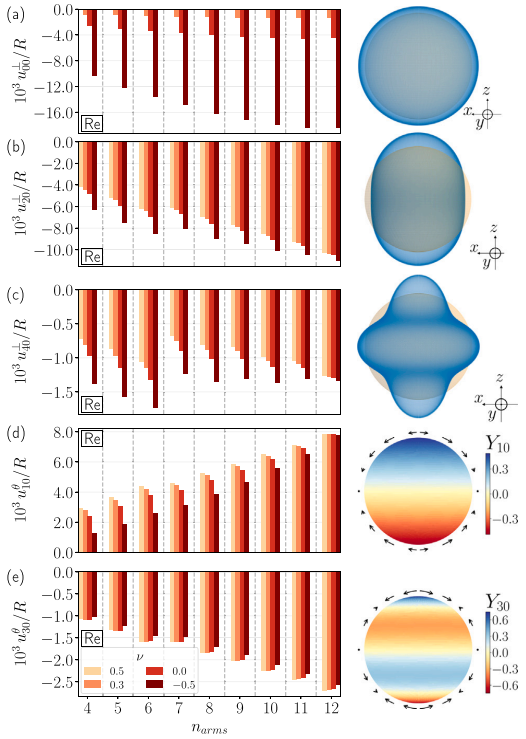

Fig. 4. For the star-shaped chain configurations without mutual vertical shift of neighboring chains along the magnetization direction in Fig. 3, we evaluate the most important deformational modes and visualize them in the same way as in Fig. 2, varying the number of arms n_{arms} of the star-shaped arrangements.

to our constraints. For $n_{arms} \geq 7$, some chains close to the center again must be deleted, see also the top views of the configurations in Fig. 3 and Appendix B.

In general, without mutual vertical shift the number of inclusions N needs to be decreased (see Figs. 1 and 3 for comparison). As may be expected, the magnetostrictive behavior is affected. We plot the most relevant modes of deformation in Fig. 4 in a similar manner as in the previous section in Fig. 2.

Fig. 4 already shows substantial differences compared to Fig. 2, while the configurations themselves in general are quite similar. We notice that the difference depends on the exact employed configuration, that is, the value of n_{arms}, and also on the Poisson ratio ν. In detail, we observe an almost uniform decrease of the dominant mode with coefficient $u^{\perp}_{00}$ that indicates changes in volume in Fig. 4(a). Associated magnitudes are reduced to approximately 70–75% of the corresponding previous values in Fig. 2(a).

In contrast to that, for the mode $u^{\perp}_{20}$ in Fig. 4(b), the amplitudes are strongly increased (up to fourfold). Such behavior is in line with the more pronounced repulsive interactions between neighboring magnetized inclusions that now occupy identical planes. Here, $u^{\perp}_{20} < 0$, so that the system contracts along the magnetization direction and extends in the planes of mutual magnetic repulsion. Besides, the auxetic systems ($\nu = -0.5$) always show the largest magnitude, while in the previous situation this was only the case for $n_{arms} \leq 7$.

In Fig. 2, the coefficient $u^{\perp}_{40}$ is not shown, but here the associated mode is a lot more significant and enters Fig. 4(c). $u^{\perp}_{40}$ is always negative for the configurations without vertical shift, while for the previous configurations with vertical shift it features both signs. This mode of negative coefficient here represents displacements that are oriented inwards at the poles and in the equatorial plane while outwards otherwise. Its increase in absolute magnitude is about or more than twofold when excluding the vertical shift.

Next, the mode of coefficient $u^{\perp}_{n_{arms},n_{arms}}$ is strongly reduced in importance and at least twofold, partially fourfold, in magnitude when compared to the configurations with vertical shift. Therefore, it does not enter Fig. 4. Also, the sign is sometimes opposite.

Concerning the mode of coefficient u^{θ}_{10} in Fig. 4(d), it shows a slight decrease in magnitude in some cases, but mainly a strong increase up to 84%, when compared to Fig. 2. When decreasing the Poisson ratio in Fig. 4(d), this mode always decreases in magnitude.

Besides, for the mode of coefficient u^{θ}_{30} in Fig. 4(e), we observe an increase that is more uniform, between approximately 26–64%, when compared to the systems with vertical shift in Section 3.1.1. In Fig. 4(e), the auxetic systems always show the lowest absolute magnitude of this mode, nonmonotonic dependence on the Poisson ratio is partly found.

Lastly, the mode $u^{\varphi}_{n_{arms},n_{arms}}$ is generally substantially decreased, at least when compared to its high magnitudes in Fig. 2(f). For certain parameters, we do observe an increase, but only at a very low level. Therefore, this mode is less prominent when compared to the modes included in Fig. 4.

3.1.3. Circular arrangements

Next, we address planar circular configurations of chains, with r_{config} denoting the radius of each circular arrangement. Each circle in the central plane of the elastic sphere is centered at the center of the sphere. Chain-like aggregates are again built starting from this central plane as described in Section 3.1. As in Section 3.1.1, a vertical shift between neighboring chains on the circle is then imposed as a further step. The procedure of filling the sphere is pursued in a way to in the end obtain that number of chains corresponding to the maximum

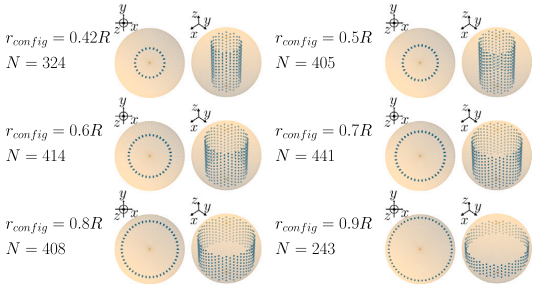

Fig. 5. Top views (left of each pair of snapshots) and tilted top views (right of each pair) of the circular configurations of chain-like aggregates of magnetizable inclusions. The chains are oriented along the magnetization direction $\hat{\mathbf{z}}$. r_{config} sets the radius of the circle and N sets the number of magnetizable inclusions.

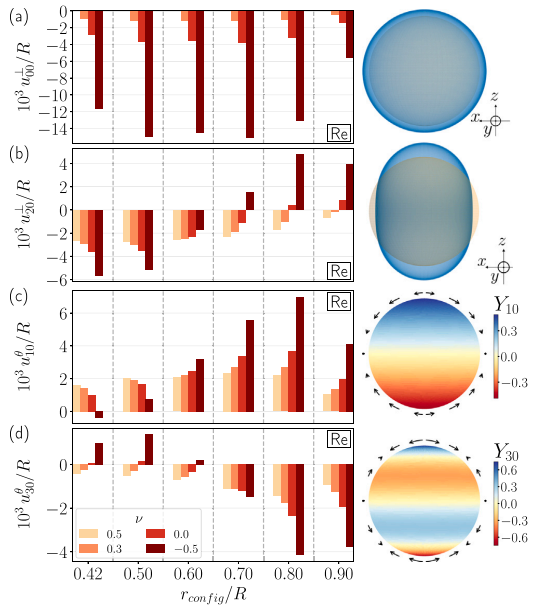

Fig. 6. Magnitudes of the most important deformational modes as in Fig. 2, but for the circular configurations of Fig. 5 with varying values of r_{config}.

number allowed under the constraints introduced before. Resulting configurations are visualized in Fig. 5.

The induced overall deformations of the sphere when magnetizing these configurations are visualized in Fig. 6, in analogy to Fig. 2. The results are similar to the results in Figs. 2 and 4. Again, we find $u_{00}^{\perp} < 0$ and $u_{10}^{\theta} > 0$, except for auxetic materials ($\nu = -0.5$) and $r_{config} = 0.42R$ where we find $u_{10}^{\theta} < 0$, see Fig. 6(c) in the first column. Here, we note that the number of inclusions N is not increasing monotonically with r_{config}, therefore, we cannot expect a monotonic increase in the magnitudes of the deformational modes. The behavior of the mode $u_{20}^{\perp}$ is even changing sign with increasing r_{config}. For low r_{config}, the behavior is as expected for individual chain-like aggregates, and we find contractions along the magnetization direction, i.e. $u_{20}^{\perp} < 0$. For larger r_{config}, the chains get shorter as the available space in the magnetization direction inside the elastic sphere decreases. Thus, repulsive interactions perpendicular to the magnetization direction between

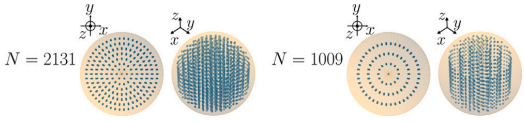

Fig. 7. Top views (left of each pair of snapshots) and tilted top views (right of each pair) of the concentric ring-like configurations of chain-like aggregates of magnetizable inclusions. The chains are oriented along the magnetization direction $\hat{\mathbf{z}}$.

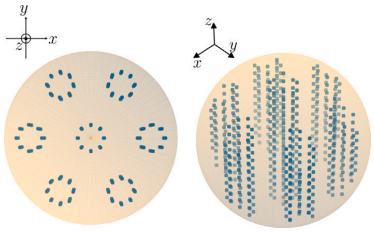

Fig. 8. Top view (left) and tilted top view (right) of the tubular configuration of chain-like aggregates of $N = 600$ magnetizable inclusions. The chains are oriented along the magnetization direction $\hat{\mathbf{z}}$.

inclusions part of different chains become more relevant. A similar change in sign can partly be observed in the mode u_{10}^{θ} for $\nu = -0.5$ and in the mode u_{30}^{θ} for $\nu \leq 0$.

3.1.4. Concentric ring-like and tubular arrangements

Building on the results in Section 3.1.3, we now combine circles of different r_{config} in one configuration. Two different variants are selected, one with a spacing of $0.121R$ in the radial direction, i.e. as a spacing between different r_{config}, and one with twice that amount. Again, we place as a many chains as permitted by our restrictions on each circle, see Fig. 7.

In tubular configurations, chains are still placed on circles. However, these circles are not concentric. Instead, 7 circles are introduced in the equatorial plane, their centers arranged in a hexagonal manner. Each circle is of a radius of $0.15R$, with a center-to-center distance between the circles of $0.7R$ for nearest neighbors. From there, we grow from each inclusion in the equatorial plane a chain-like aggregate along the magnetization direction, which results in tubular configurations, see Fig. 8. Related tubes were identified in x-ray tomographic investigations of real experimental samples of magnetic elastomers prepared under strong homogeneous external magnetic fields [94].

Probably due to the attractions along each chain-like aggregate, we find results similar to those for the star-shaped arrangements depicted in Figs. 2 and 4 for both concentric ring-like (first and second column of Fig. 9) and tubular (third column of Fig. 9) configurations. That is, volume changes are negative ($u_{00}^{\perp} < 0$), contraction along the magnetization direction prevails ($u_{20}^{\perp} < 0$), and qualitatively similar tangential response is observed ($u_{10}^{\theta} > 0$, $u_{30}^{\theta} < 0$). The notable exception to this list is $u_{20}^{\perp} < 0$ for the denser concentric ring-like arrangement. In this case, there are many chains close together, which emphasizes the repulsive interactions perpendicular to the magnetization direction. Therefore, it appears conceivable that we observe elongation ($u_{20}^{\perp} > 0$) along the magnetic field direction in this case at least for auxetic materials of $\nu = -0.5$, see the first column of Fig. 9(b).

3.1.5. Polygonal arrangements

We also constructed chain-like aggregates from regular polygonal arrangements in the equatorial plane. The center of each polygon coincides with the center of the sphere. All vertices of each polygon therefore are located at identical distance from the center, which we

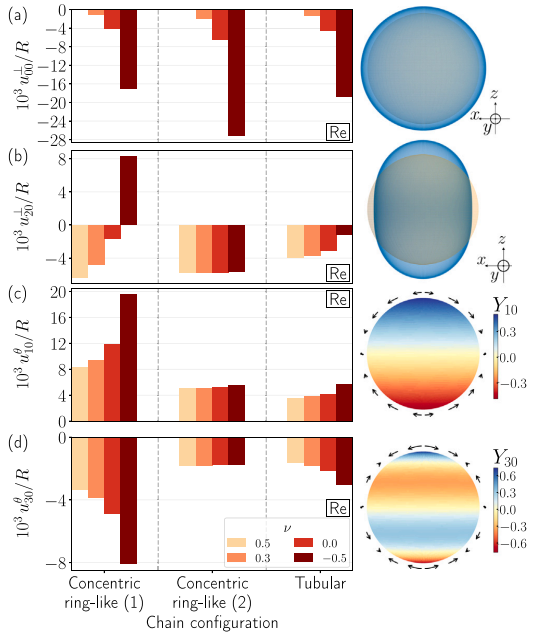

Fig. 9. Magnitudes of the most important deformational modes as in Fig. 2, but for the concentric ring-like and tubular configurations of Figs. 7 and 8, respectively.

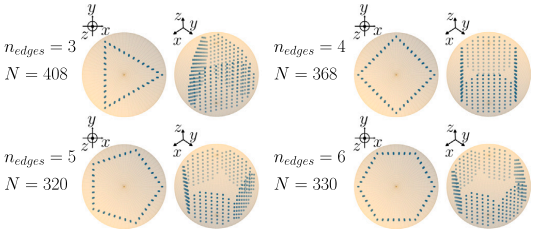

Fig. 10. Top views (left of each pair of snapshots) and tilted top views (right of each pair) of the polygonal configurations of chain-like aggregates of magnetizable inclusions. The chains are oriented along the magnetization direction $\hat{\mathbf{z}}$. n_{edges} indicates the number of edges of each polygon.

here choose as $0.9R$. We show results for different numbers of polygonal edges, denoted by n_{edges}, which equals the number of vertices, see Fig. 10.

For these arrangements, the induced modes of magnetostrictive deformation are presented in Fig. 11. Qualitatively, they are quite similar to the ones for circular arrangements in Fig. 6. As in the circular case for increasing r_{config}, increasing n_{edges} on average moves the chains further away from the center of the elastic sphere and therefore shortens the length of the chains that fits into the sphere. This most likely leads to the decrease with increasing n_{edges} in induced shrinkage of volume obvious from Fig. 11(a) and also to the decreasing contraction along the magnetization direction from Fig. 11(b). In the latter case, we even observe a change in sign for auxetic materials as in Fig. 6(b).

However, we here find $u^{\theta}_{30} < 0$ for all evaluated parameters, which implies that tangential displacements towards the equatorial plane are decreasing in magnitude with increasing distance to the equatorial plane, qualitatively similar to the results in Fig. 2(e). Additionally,

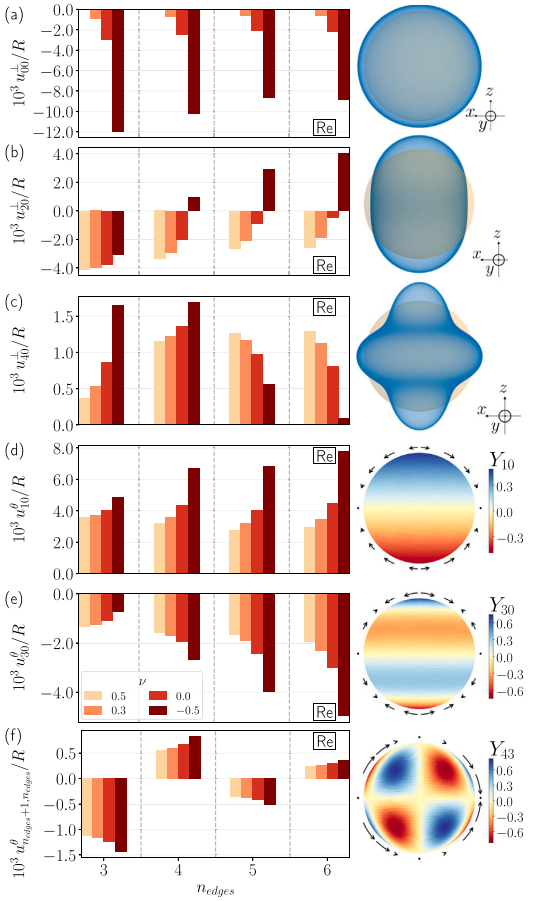

Fig. 11. Magnitudes of the most important deformational modes as in Fig. 2, but for the polygonal configurations of Fig. 10 with varying values of n_{edges}. The visualization in (f) corresponds to the case $n_{edges} = 3$.

we also present the results for $u^{\perp}_{40}$ in Fig. 11(c), where we infer that the displacements are more outwards at the poles and the equatorial plane and inwards otherwise. This modulation in the perpendicular component is analogous to the one that is represented by $u^{\theta}_{30} < 0$ for the tangential component in Fig. 11(e).

We here also plot the mode $u^{\theta}_{n_{edges}+1,n_{edges}}$ in Fig. 11(f). The mirror-symmetry of the underlying configuration with respect to the equatorial plane implies an antisymmetric mode for u^{θ}. Therefore, the parameters l and m of any nonvanishing mode corresponding to the spherical harmonic $Y_{l,m}$ have to be such that $l + m$ is odd. Consequently, the lowest-order mode for u^{θ} that reflects the n_{edges}-fold symmetry in m is the one that we plot in Fig. 11(f).

3.1.6. Hexagonal arrangements

Finally, we also consider simple hexagonal arrangements of chain-like aggregates oriented along the magnetization direction. Here, the distance of neighboring chains in the equatorial plane is set to $0.18R$. Additionally, we consider the case in which the chain-like aggregates are oriented along the x-direction instead. To this end, we apply

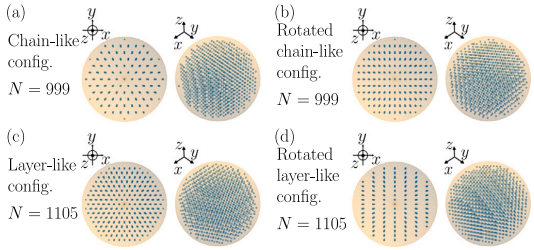

Fig. 12. Top views (left of each pair of snapshots) and tilted top views (right of each pair) of the hexagonal configurations (configs.) of chain-like aggregates of magnetizable inclusions. The chain-like aggregates are oriented along the magnetization direction $\hat{\mathbf{z}}$ in (a) and along $\hat{\mathbf{x}}$ (pointing to the right) in (b). We also investigate stacks of hexagonally structured layers instead of hexagonally arranged chain-like aggregates (smaller inner-layer spacing between nearest-neighboring inclusions when compared to the inter-inclusion distance along the chain-like aggregates). In the latter case, we investigate layer structures of normal vector along (c) $\hat{\mathbf{z}}$ and (d) $\hat{\mathbf{x}}$.

a global rotation matrix $\mathbf{R}$ to all position vectors of magnetizable inclusions, where

$$\mathbf{R} = \begin{pmatrix} 0 & 0 & 1 \\ 0 & 1 & 0 \\ -1 & 0 & 0 \end{pmatrix}. \tag{4}$$

$\mathbf{R}$ maps the x-components to negative z-components and z-components to x-components, while leaving the y-components unaffected. Moreover, we address configurations that feature an interinclusion distance of $0.25R$ along the magnetization direction (compared to $0.121R$ previously). Instead, we reduce the interinclusion spacing within the hexagonal plane to $0.121R$. Therefore, we construct a configuration of hexagonally structured layers stacked on top of each other (normal vector $\hat{\mathbf{z}}$). For these hexagonal layer structures, we also investigate the rotated configurations (normal vector $\hat{\mathbf{x}}$) after applying the same rotation matrix $\mathbf{R}$. These four configurations are visualized in Fig. 12. In all cases, $\hat{\mathbf{z}}$ still represents the magnetization direction.

For the hexagonally arranged chain-like aggregates with chains along the magnetization direction (see the first column of Fig. 13), we find a qualitatively similar magnetostrictive response as for the star-shaped arrangements of chains. A reduction in volume ($u^{\perp}_{00} < 0$) in connection with a contraction along the magnetization direction ($u^{\perp}_{20} < 0$) are observed, together with similar tangential deformations as for the aforementioned structures ($u^{\theta}_{10} > 0$, $u^{\theta}_{30} < 0$). Evidently, a rotation of the whole configuration with respect to the magnetization direction (see the second column of Fig. 13) changes the behavior even qualitatively. The overall volume is now growing under magnetization ($u^{\perp}_{00} > 0$), as we might expect from the now predominately repulsive interactions within the perpendicularly magnetized chain-like aggregates. We still find contraction along the magnetization direction ($u^{\perp}_{20} < 0$), or put differently, a sphere that expands upon magnetization across the equatorial plane, at least for $\nu \geq 0$. This also leads to the same qualitative behavior of u^{θ}_{10} and u^{θ}_{30}. Moreover, due to the chains being oriented along the x-direction, we find additional pronounced modes in this case, namely $u^{\perp}_{22} > 0$, see Fig. 13(c). This reflects the mirror-symmetry of the configuration with respect to the yz-plane. As we infer, the sphere expands in a more pronounced way along the x-axis. This is the axis along which the chains are oriented and, thus, the magnetic repulsion is strongest. Moreover, we observe $u^{\varphi}_{22} > 0$, see Fig. 13(f), which indicates azimuthal displacements towards the x-axis (middle yellow part in the visualization of the mode).

Likewise, the hexagonal layer-like structures feature repulsive internal interactions as the layer normals are oriented along the magnetization direction (third column of Fig. 13). Therefore, the qualitative

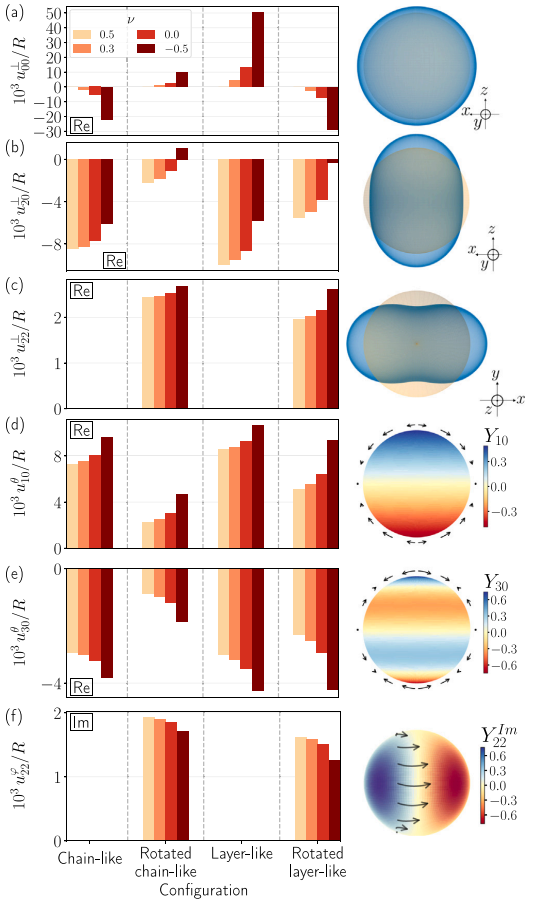

Fig. 13. Magnitudes of the most important deformational modes as in Fig. 2, but for the hexagonally arranged chain-like aggregates and hexagonally structured layer-like configurations of Fig. 12 with two different orientations for each case with the major axes along and rotated perpendicular to the magnetization direction.

response of the modes in many aspects is similar to the rotated chain-like configurations. As one exception, we find contraction ($u^{\perp}_{20} < 0$) in all cases, also in the auxetic one, see Fig. 13(b).

For the rotated configurations of hexagonal layer-like configurations, see the fourth column of Fig. 13, upon magnetization we obtain repulsive interactions between nearby inclusions along the y-direction and attractive interactions along the z-direction. Both of these interactions contribute to a contraction along the magnetization direction ($u^{\perp}_{20} < 0$), see Fig. 13(b), as discussed previously. Again, we also observe $u^{\theta}_{10} > 0$ and $u^{\theta}_{30} < 0$. $u^{\perp}_{00}$ here is found negative in Fig. 13(a), implying an overall shrinkage of the elastic sphere. We observe the same qualitative response in the modes $u^{\perp}_{22} > 0$ and $u^{\varphi}_{22} > 0$ as for the rotated chain-like aggregates, see Fig. 13(c) and (f).

To summarize the above results, for chain-like aggregates arranged in different configurations but oriented along the magnetization direction, we mostly find an overall reduction in volume ($u^{\perp}_{00} < 0$) and contraction along the magnetization direction ($u^{\perp}_{20} < 0$). We usually observe tangential displacements towards the equatorial plane ($u^{\theta}_{10} > 0$). A majority of these modes increase in magnitude with decreasing Poisson

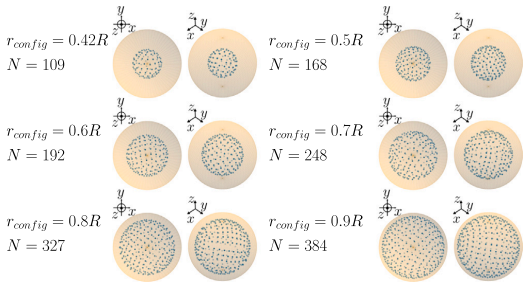

Fig. 14. Top views (left of each pair of snapshots) and tilted top views (right of each pair) of the evenly distributed spherical arrangements of magnetizable inclusions, with r_{config} as the radius of the sphere on which the inclusions are located.

ratio. Next, we concentrate on further configurations of magnetizable inclusions that do not consist of chain-like aggregates.

3.2. Spherical arrangements

We continue by placing inclusions on the surface of spheres of different radii $r_{config} < R$ with the same parameters values for r_{config} as in Section 3.1.3. The inclusions are distributed approximately evenly on the sphere of radius r_{config}, which we ensure by use of the distributions provided by the HEALPix package [91], see Fig. 14 for the resulting configurations. We further ensure that the points of evaluating the displacement field on the surface of the overall elastic sphere of radius R are not located on the same radial axis as the magnetizable inclusions underneath the surface of the sphere at distance r_{config} from the center.

As a result, we infer that the magnetostrictively induced changes in overall volume, characterized by the mode $u^{\perp}_{00}$, are not dominant when compared to the other modes. Their maximal magnitudes are below 10^{-3} with an average magnitude below 10^{-4} and thus about one magnitude below those of the other modes. As the configurations are approximately isotropic, we find both attractive and repulsive magnetic interactions. We infer from Fig. 15(a) an elongation along the magnetization direction ($u^{\perp}_{20} > 0$, prolate deformation), in contrast to the contraction that was usually observed for the chain-like arrangements in Section 3.1. This result can be illustratively explained from the configuration of the inclusions. As we get closer to the equatorial plane, the nearest neighbors are increasingly located relative to each other along the magnetization direction. Consequently, they interact in a rather attractive manner. The opposite is true closer to the poles where repulsion dominates. This supports $u^{\perp}_{20} > 0$ and $u^{\theta}_{10} > 0$, see Fig. 15(a) and (b), respectively. We also observe $u^{\theta}_{30} < 0$ in Fig. 15(c), qualitatively similar to Figs. 2(e) and 11(e). The magnitudes of deformation increase with increasing r_{config}, which again is in line with the increasing number of magnetizable inclusions N. The closer the magnetizable inclusions are located with respect to the elastic surface, that is, the larger r_{config}, the stronger the induced deformations of the surface.

3.3. 3D star-shaped arrangements

In this section, we again distribute magnetizable inclusions evenly on a spherical surface as a starting point. However, we here set a lower number ($n_{star} = 48$ or $n_{star} = 192$ compared to the number of inclusions in Section 3.2). Then, we build chain-like aggregates from the center of the elastic sphere towards these locations up to the maximal number of inclusions that is permitted by our constraints. Thus, when compared to Section 3.1.1, we now consider star-shaped configurations of chain-like aggregates arranged along the radial direction instead of the magnetization direction, see Fig. 16. The nearest-neighbor distance along the radially arranged chain-like aggregates is set to $0.121\,R$ as before.

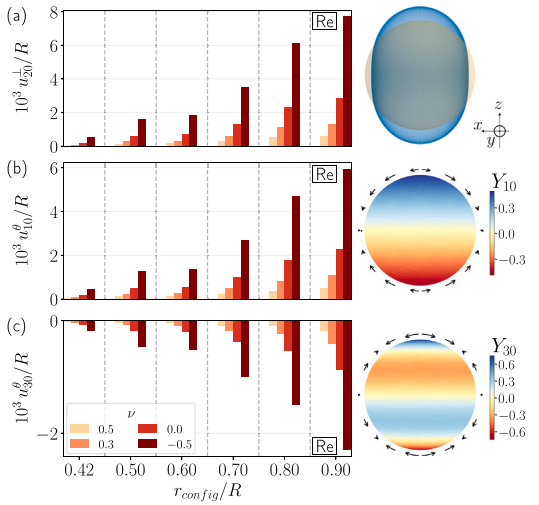

Fig. 15. Magnitudes of the most important deformational modes as in Fig. 2, but for the spherical configurations of Fig. 14.

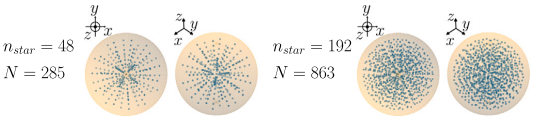

Fig. 16. Top views (left of each pair of snapshots) and tilted top views (right of each pair) of the 3D star-shaped arrangements, where we consider stars with arms/chains oriented along the radial direction. They are directed towards a set of n_{star} points that are approximately evenly distributed underneath the spherical surface.

When compared to the spherical configurations in the previous Section 3.2, we again find the same most relevant modes. Likewise, the 3D star-shaped arrangements do not lead to relevant changes in volume. In contrast to the results in Fig. 15, here all further displayed modes are of opposite sign. We observe in Fig. 17(a) a contraction along the magnetization direction ($u^{\perp}_{20} < 0$) as well as in Fig. 17(b) and (c) $u^{\theta}_{10} < 0$ and $u^{\theta}_{30} > 0$. In Fig. 17, we again observe that an increase in n_{star}, coinciding with an increase in the number of magnetizable inclusions, increases the magnitudes of deformation.

3.4. Single- and double-stranded helical arrangements

Finally, we return to helical arrangements [65]. Here, we extend the previous single-stranded [65] to double-stranded helical configurations. One motivation in this context is to generate twist-type deformations, characterized by the azimuthal deformational mode u^{φ}_{10}. From above, these configurations appear similar to the tubular configurations of Section 3.1.4, see Figs. 8 and 18.

We consider helical arrangements with center axes oriented along the magnetization direction. They are arranged on a hexagonal grid in the plane normal to the magnetization direction. The lattice constant of the hexagonal arrangement is chosen as $0.5\,R$. From each center point of the hexagonal lattice, we place one inclusion at a distance vector $\mathbf{r}^{\perp}_{helix}(z)$ in the plane perpendicular from the center axis of

$$\mathbf{r}^{\perp}_{helix}(z) = r_{helix} \begin{pmatrix} \cos \frac{\gamma z}{d_{layer}} \\ \sin \frac{\gamma z}{d_{layer}} \end{pmatrix}, \tag{5}$$

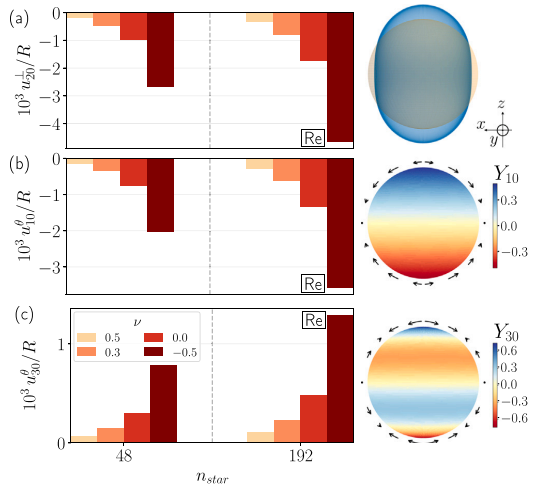

Fig. 17. Magnitudes of the most important deformational modes as in Fig. 2, but for the 3D star-shaped arrangements of Fig. 16.

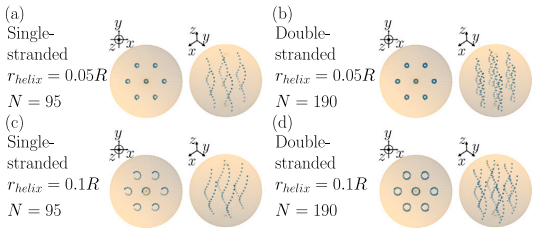

Fig. 18. Top views (left of each pair of snapshots) and tilted top views (right of each pair) of the single- and double-stranded helical configurations. (a) and (c) correspond to configurations already explored in Ref. [65]. We here choose those configurations featuring the largest twist-type deformations. The parameter r_{helix} describes the radius of each helix. For the double-stranded helical configurations in (b) and (d), we add at the height of each inclusion another inclusion on the opposite side of the helical center axis.

depending on the z-coordinate which we increase or decrease in discrete steps of $0.11R$ from the central plane to fill the elastic sphere. We here discuss two choices for r_{helix}, namely $0.05R$ and $0.1R$, the same values as in Ref. [65]. For both cases, we choose the value of γ that leads to the maximal overall twist-type response of the materials for single-stranded helices, namely $\gamma \approx 0.24\pi$ and $\gamma \approx 0.13\pi$ for $r_{helix} = 0.05R$ and $r_{helix} = 0.1R$, respectively.

To expand on Ref. [65], we now also discuss the case of double-stranded helical configurations, inspired by the structure of DNA. These configurations are generated by inserting additional inclusions at each step in the $\hat{\mathbf{z}}$-direction at $-\mathbf{r}_{helix}(z)$. We note that for $r_{helix} = 0.05R$ the distance between the two strands is $0.1R < 0.12R$ and thus slightly below our generally imposed minimal distance between any two inclusions of radius $0.02R$. Besides, the double-stranded helical configurations contain twice the amount of magnetizable inclusions, see Fig. 18 for the resulting configurations.

As we observe, the deformational response for the helical configurations (see the first two columns of Fig. 19) shows a pattern familiar from the chain-like arrangements, namely a magnetostrictive reduction in volume ($u^{\perp}_{00} < 0$, except for $\nu = 0.5$), contraction along the magnetization direction ($u^{\perp}_{20} < 0$) and mainly tangential displacements

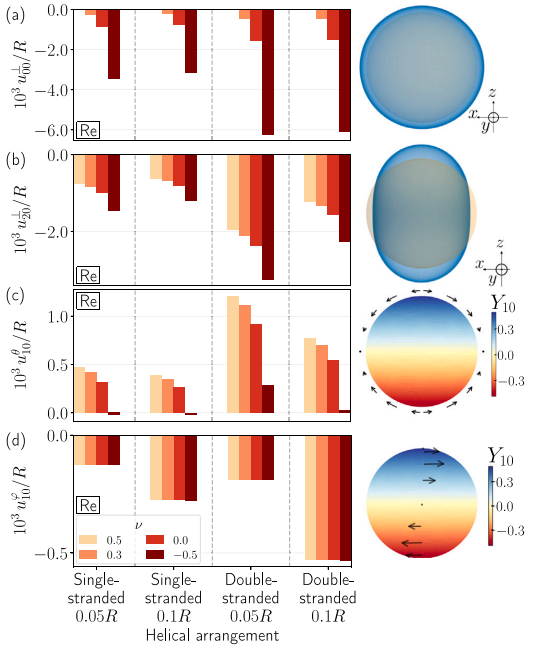

Fig. 19. Magnitudes of the most important deformational modes as in Fig. 2, but for the single- and double-stranded helical arrangements depicted in Fig. 18.

towards the equatorial plane ($u^{\theta}_{10} > 0$), see Fig. 19(a), (b), and (c), respectively. In the case of auxetic materials of $\nu = -0.5$, we find $u^{\theta}_{10} \approx 0$. Overall, these characteristics appear conceivable because from a coarser point of view, the configurations to some extent resemble chain-like arrangements. Yet, in addition, all these configurations generate an overall twist-type deformational response as quantified by u^{φ}_{10} in Fig. 19(d). The magnitude of this mode is almost independent of the Poisson ratio, as also discussed in Ref. [65].

Concerning the newly addressed double-stranded helical configurations, in general, the magnitudes of all deformational modes depicted in Fig. 19 are increased when compared to the single-stranded ones without changing the qualitative behavior. A slight exception is given by $u^{\theta}_{10} > 0$ for $\nu = -0.5$, see Fig. 19(c). In particular, concerning the resulting twist-type deformation, u^{φ}_{10} is increased in magnitude by approximately 52.7% and 92.2% for $r_{helix} = 0.05R$ and $r_{helix} = 0.1R$, respectively, see Fig. 19(d). Consequently, the double-stranded helical configurations are preferred relatively to the single-stranded ones, if a twist-type deformation of stronger extent is desired and the number of magnetizable inclusions is not restricted.

4. Conclusions

In this work, we demonstrate that specific modes of overall macroscopic deformation of magnetoelastic composite materials can be directly calculated from the specific discrete microscopic force pattern arising upon magnetization. This force pattern results from the spatial configuration and arrangement of the particulate inclusions and their mutual magnetic interactions. Our approach is based on analytical theory. It allows to effectively calculate the resulting elastic surface displacements and thus overall deformations by numerical evaluations.

Thus, we show that a broad range of different spectra of modes of deformation can be realized by implementing different types of

microscopic spatial arrangements of the particulate inclusions. For example, star-shaped arrangements of chain-like aggregates of a specific number of arms of the stars imply accordingly pronounced modes of overall deformation. Thus, if specific patterns of actuation are needed for specific purposes, for instance, filling of specifically shaped cavities by actuation of valves [70], magnetoelastic composite materials are candidates to achieve such realizations.

Experimentally, various ways of generating the different discrete particle arrangements need to be developed. For more macroscopic systems or macroscopic objects of demonstration, placement by molds or by hand is possible [12,89,95,96]. When placing the inclusions by hand, the reactive polymeric suspension would be added layer by layer between successive events of placing inclusions. The newly forming elastic matrix develops by chemical reaction and connects to the already existing elastic part of the sample [12,89]. Pouring another layer into an overall spherical cavity to generate spherical samples may be difficult for the upper hemisphere when simultaneously adding inclusions by hand. Yet, the two hemispheres could be generated separately and then in the end be linked to each other by a final reaction.

3D-printing is a promising tool to be further developed in the future [97–103] to generate samples of controlled positioning of magnetizable inclusions. Here, one way to fabricate spherical systems would be to choose three types of "inks". The first one prints the elastic material that forms the deformable elastic sphere, representing the carrier matrix. From the second one, the magnetizable inclusions are positioned. Finally, the third ink could form a block of surrounding elastic gel material that embeds the elastic sphere. It should be much softer than the printed elastic sphere so that it hardly hinders the magnetostrictive deformation of the embedded spherical sample upon magnetization. It could also be generated from a material that can be selectively dissolved in a solvent after printing the whole arrangement [104], leaving the spherical sample at the end.

Additional methods of placing the inclusions in a requested manner are conceivable. Prior to polymerization, the particle arrangement can also be controlled by external magnetic [105] or acoustic [106] fields. Once the positioning is complete as desired, polymerizing the carrier matrix fixes their locations. Generally, polymerization could be performed stepwise using processes of photopolymerization to fabricate the matrix material [107].

If the spherical samples are contained in a very soft surrounding transparent elastic box, see above, direct measurements are conceivable on such combined systems. Otherwise, free-standing elastic spheres can be maintained in a density-matched surrounding transparent fluid to then study magnetostrictive effects [53]. A strong homogeneous external magnetic field should then be applied for experimental detection. The resulting magnetostrictive deformations can be recorded by standard optical tools [53].

Overall, we establish theoretical means that allow to effectively calculate the magnetomechanical response as a function of the microscopic particulate structure. We provide a palette of different such microscopic particle arrangements together with the magnetically inducible overall deformation. From this palette, specific realizations can be selected according to a particular need. In this way, we promote the application of magnetic gels and elastomers as tailored soft actuators adjusted to given requirements that are addressed and excited reversibly in a contactless fashion from outside by external magnetic fields.

CRediT authorship contribution statement

Lukas Fischer: Data curation, Formal analysis, Investigation, Methodology, Software, Validation, Visualization, Writing – original draft. **Andreas M. Menzel:** Conceptualization, Funding acquisition, Methodology, Project administration, Resources, Supervision, Writing – original draft, Writing – review & editing.

Declaration of competing interest

The authors declare that they have no known competing financial interests or personal relationships that could have appeared to influence the work reported in this paper.

Data availability

The generated data underlying the presented figures are published on the repository Zenodo and can be found at https://doi.org/10.5281/zenodo.10035624.

Acknowledgments

The authors thank Professor Modesto T. López-López and his team for the organization of the conference ICMF 2023 in Granada together with this associated special issue. Moreover, A.M.M. thanks the German Research Foundation (Deutsche Forschungsgemeinschaft, DFG) for support through the Heisenberg Grant no. ME 3571/4-2. Some of the results in this paper have been derived using the HEALPix package [91].

Appendix A. Details on the planar star-shaped configurations considered in Section 3.1.1

Here, we list explicitly the chains that we had to exclude from the configuration in Section 3.1.1 to satisfy our constraints in detail. For $n_{arms} = 4$ and $n_{arms} = 5$, no chains have been deleted. If we number the arms of the star-shaped arrangements from 1 to n_{arms}, with 1 being the arm pointing to the right (along the x-axis) and then numbering them counter clockwise (mathematically positive sense of rotation), for $n_{arms} = 6$, the arms 2, 4, and 6 are missing the innermost chains. For $n_{arms} = 7$, the innermost chains were deleted from the arms 2, 4, 6, and 7. Similarly, for $n_{arms} = 8$, the innermost chains were deleted from the arms 2, 4, 6, and 8. Likewise, for $n_{arms} = 9$, the arms 2, 4, 6, 8, and 9 are missing the innermost chains. Again, for $n_{arms} = 10$, we deleted from the arms 2, 4, 6, 8, and 10 the innermost chains. For $n_{arms} = 11$, the arms 2, 3, 5, 6, 8, 9, 10, and 11 lack the innermost chains and the arms 2, 4, 6, 8, 10, and 11 lack the second-innermost chains. Finally, for $n_{arms} = 12$, the arms 2, 3, 5, 6, 8, 9, 11, and 12 are missing the innermost chains and the arms 2, 4, 6, 8, 10, and 12 are missing the second-innermost chains.

Appendix B. Details on the star-shaped configurations without vertical shift considered in Section 3.1.2

For the star-shaped configurations without vertical shift considered in Section 3.1.2, we likewise summarize which chains were deleted. We use the same notation as in Appendix A. For $n_{arms} = 4$ to $n_{arms} = 6$, no chains are missing. Next, for $n_{arms} = 7$ to $n_{arms} = 10$, the same chains are missing as in the case with vertical shift, see Appendix A. For $n_{arms} = 11$, the arms 2, 4, 6, 8, 10, and 11 are missing the innermost chains. Finally, for $n_{arms} = 12$, from the arms 2, 4, 6, 8, 10, and 12 we removed the innermost chains.

References

[1] M.R. Jolly, J.D. Carlson, B.C. Muñoz, T.A. Bullions, The magnetoviscoelastic response of elastomer composites consisting of ferrous particles embedded in a polymer matrix, J. Intel. Mater. Syst. Struct. 7 (1996) 613.
[2] G. Filipcsei, I. Csetneki, A. Szilágyi, M. Zrínyi, Magnetic field-responsive smart polymer composites, Adv. Polym. Sci. 206 (2007) 137.
[3] S. Odenbach, Microstructure and rheology of magnetic hybrid materials, Arch. Appl. Mech. 86 (2016) 269.
[4] R. Weeber, M. Hermes, A.M. Schmidt, C. Holm, Polymer architecture of magnetic gels: A review, J. Phys.: Condens. Matter 30 (2018) 063002.
[5] A.M. Menzel, Tuned, driven, and active soft matter, Phys. Rep. 554 (2015) 1.

[6] M.T. Lopez-Lopez, J.D.G. Durán, L.Y. Iskakova, A.Y. Zubarev, Mechanics of magnetopolymer composites: a review, J. Nanofluids 5 (2016) 479.
[7] M.M. Schmauch, S.R. Mishra, B.A. Evans, O.D. Velev, J.B. Tracy, Chained iron microparticles for directionally controlled actuation of soft robots, ACS Appl. Mater. Interfaces 9 (2017) 11895.
[8] R. Weeber, P. Kreissl, C. Holm, Studying the field-controlled change of shape and elasticity of magnetic gels using particle-based simulations, Arch. Appl. Mech. 89 (2019) 3.
[9] O.V. Stolbov, Y.L. Raikher, Magnetostriction effect in soft magnetic elastomers, Arch. Appl. Mech. 89 (2019) 63.
[10] A.M. Menzel, Mesoscopic characterization of magnetoelastic hybrid materials: Magnetic gels and elastomers, their particle-scale description, and scale-bridging links, Arch. Appl. Mech. 89 (2019) 17.
[11] M. Schümann, T. Gundermann, S. Odenbach, Microscopic investigation of the reasons for field-dependent changes in the properties of magnetic hybrid materials using x-ray microtomography, Arch. Appl. Mech. 89 (2019) 77.
[12] M. Puljiz, S. Huang, G.K. Auernhammer, A.M. Menzel, Forces on rigid inclusions in elastic media and resulting matrix-mediated interactions, Phys. Rev. Lett. 117 (2016) 238003.
[13] M. Puljiz, A.M. Menzel, Forces and torques on rigid inclusions in an elastic environment: Resulting matrix-mediated interactions, displacements, and rotations, Phys. Rev. E 95 (2017) 053002.
[14] M. Puljiz, A.M. Menzel, Displacement field around a rigid sphere in a compressible elastic environment, corresponding higher-order faxén relations, as well as higher-order displaceability and rotateability matrices, Phys. Rev. E 99 (2019) 053002.
[15] Y.L. Raikher, O.V. Stolbov, G.V. Stepanov, Shape instability of a magnetic elastomer membrane, J. Phys. D: Appl. Phys. 41 (2008) 152002.
[16] P. Metsch, K.A. Kalina, C. Spieler, M. Kästner, A numerical study on magnetostrictive phenomena in magnetorheological elastomers, Comput. Mater. Sci. 124 (2016) 364.
[17] G. Pessot, P. Cremer, D.Y. Borin, S. Odenbach, H. Löwen, A.M. Menzel, Structural control of elastic moduli in ferrogels and the importance of non-affine deformations, J. Chem. Phys. 141 (2014) 124904.
[18] D.S. Wood, P.J. Camp, Modeling the properties of ferrogels in uniform magnetic fields, Phys. Rev. E 83 (2011) 011402.
[19] D. Ivaneyko, V. Toshchevikov, M. Saphiannikova, G. Heinrich, Effects of particle distribution on mechanical properties of magneto-sensitive elastomers in a homogeneous magnetic field, Condens. Matter Phys. 15 (2012) 33601.
[20] B.A. Evans, B.L. Fiser, W.J. Prins, D.J. Rapp, A.R. Shields, D.R. Glass, R. Superfine, A highly tunable silicone-based magnetic elastomer with nanoscale homogeneity, J. Magn. Magn. Mater. 324 (2012) 501.
[21] Y. Han, W. Hong, L.E. Faidley, Field-stiffening effect of magneto-rheological elastomers, Int. J. Solids Struct. 50 (2013) 2281.
[22] D.Y. Borin, G.V. Stepanov, S. Odenbach, Tuning the tensile modulus of magnetorheological elastomers with magnetically hard powder, J. Phys.: Conf. Ser. 412 (2013) 012040.
[23] A. Zubarev, A.B. Bonhome-Espinosa, M. Alaminos, J. Duran, M.T. Lopez-Lopez, Rheological properties of magnetic biogels, Arch. Appl. Mech. 89 (2019) 91.
[24] T.I. Volkova, V. Böhm, T. Kaufhold, J. Popp, F. Becker, D.Y. Borin, G.V. Stepanov, K. Zimmermann, Motion behaviour of magneto-sensitive elastomers controlled by an external magnetic field for sensor applications, J. Magn. Magn. Mater. 431 (2017) 262.
[25] M.R. Jolly, J.D. Carlson, B.C. Muñoz, A model of the behaviour of magnetorheological materials, Smart Mater. Struct. 5 (1996) 607.
[26] G. Stepanov, S. Abramchuk, D. Grishin, L. Nikitin, E.Y. Kramarenko, A. Khokhlov, Effect of a homogeneous magnetic field on the viscoelastic behavior of magnetic elastomers, Polymer 48 (2007) 488.
[27] H. Böse, R. Röder, Magnetorheological elastomers with high variability of their mechanical properties, J. Phys.: Conf. Ser. 149 (2009) 012090.
[28] E. Jarkova, H. Pleiner, H.-W. Müller, H.R. Brand, Hydrodynamics of isotropic ferrogels, Phys. Rev. E 68 (2003) 041706.
[29] L. Chen, X.-l. Gong, W.-q. Jiang, J.-j. Yao, H.-x. Deng, W.-h. Li, Investigation on magnetorheological elastomers based on natural rubber, J. Mater. Sci. 42 (2007) 5483.
[30] A.V. Chertovich, G.V. Stepanov, E.Y. Kramarenko, A.R. Khokhlov, New composite elastomers with giant magnetic response, Macromolecul. Mater. Eng. 295 (2010) 336.
[31] N. Chiba, K. Yamamoto, T. Hojo, M. Kawai, T. Mitsumata, Wide-range modulation of dynamic modulus and loss tangent for magnetic elastomers containing submilimeter magnetic particles, Chem. Lett. 42 (2013) 253.
[32] G. Pessot, H. Löwen, A.M. Menzel, Dynamic elastic moduli in magnetic gels: Normal modes and linear response, J. Chem. Phys. 145 (2016) 104904.
[33] V.V. Sorokin, G.V. Stepanov, M. Shamonin, G.J. Monkman, A.R. Khokhlov, E.Y. Kramarenko, Hysteresis of the viscoelastic properties and the normal force in magnetically and mechanically soft magnetoactive elastomers: Effects of filler composition, strain amplitude and magnetic field, Polymer 76 (2015) 191.
[34] G. Pessot, M. Schümann, T. Gundermann, S. Odenbach, H. Löwen, A.M. Menzel, Tunable dynamic moduli of magnetic elastomers: From characterization by x-ray micro-computed tomography to mesoscopic modeling, J. Phys.: Condens. Matter 30 (2018) 125101.
[35] C. Gila-Vilchez, A.B. Bonhome-Espinosa, P. Kuzhir, A. Zubarev, J.D. Duran, M.T. Lopez-Lopez, Rheology of magnetic alginate hydrogels, J. Rheol. 62 (2018) 1083.
[36] M. Watanabe, J. Ikeda, Y. Takeda, M. Kawai, T. Mitsumata, Effect of sonication time on magnetorheological effect for monomodal magnetic elastomers, Gels 4 (2018) 49.
[37] D. Borin, M. Vaganov, S. Odenbach, Magnetic training of the soft magnetorheological elastomers, J. Magn. Magn. Mater. 589 (2024) 171499.
[38] J.D. Carlson, M.R. Jolly, Mr fluid, foam and elastomer devices, Mechatronics 10 (2000) 555.
[39] H.-X. Deng, X.-L. Gong, L.-H. Wang, Development of an adaptive tuned vibration absorber with magnetorheological elastomer, Smart Mater. Struct. 15 (2006) N111.
[40] T. Sun, X. Gong, W. Jiang, J. Li, Z. Xu, W. Li, Study on the damping properties of magnetorheological elastomers based on cis-polybutadiene rubber, Polym. Test. 27 (2008) 520.
[41] G. Liao, X. Gong, S. Xuan, C. Kang, L. Zong, Development of a real-time tunable stiffness and damping vibration isolator based on magnetorheological elastomer, J. Intel. Mater. Syst. Struct. 23 (2012) 25.
[42] V.S. Molchanov, G.V. Stepanov, V.G. Vasiliev, E.Y. Kramarenko, A.R. Khokhlov, Z.-D. Xu, Y.-Q. Guo, Viscoelastic properties of magnetorheological elastomers for damping applications, Macromolecul. Mater. Eng. 299 (2014) 1116.
[43] T.I. Becker, Y.L. Raikher, O.V. Stolbov, V. Böhm, K. Zimmermann, Magnetoactive elastomers for magnetically tunable vibrating sensor systems, Phys. Sci. Rev. 7 (2020) 1063.
[44] M. Schümann, D.Y. Borin, S. Huang, G.K. Auernhammer, R. Müller, S. Odenbach, A characterisation of the magnetically induced movement of ndfeb-particles in magnetorheological elastomers, Smart Mater. Struct. 26 (2017) 095018.
[45] T. Gundermann, S. Odenbach, Investigation of the motion of particles in magnetorheological elastomers by x-μCT, Smart Mater. Struct. 23 (2014) 105013.
[46] T. Gundermann, P. Cremer, H. Löwen, A.M. Menzel, S. Odenbach, Statistical analysis of magnetically soft particles in magnetorheological elastomers, Smart Mater. Struct. 26 (2017) 045012.
[47] N. Kchit, P. Lancon, G. Bossis, Thermoresistance and giant magnetoresistance of magnetorheological elastomers, J. Phys. D: Appl. Phys. 42 (2009) 105506.
[48] N. Kchit, G. Bossis, Electrical resistivity mechanism in magnetorheological elastomer, J. Phys. D: Appl. Phys. 42 (2009) 105505.
[49] J.L. Mietta, P.I. Tamborenea, R.M. Negri, Anisotropic magnetoresistivity in structured elastomer composites: Modelling and experiments, Soft Matter 12 (2016) 6430.
[50] D. Diaz-Bleis, C. Vales-Pinzón, Y. Freile-Pelegrín, J.J. Alvarado-Gil, Thermal characterization of magnetically aligned carbonyl iron/agar composites, Carbohyd. Polym. 99 (2014) 84.
[51] N.W. Pech-May, C. Vales-Pinzon, A. Vega-Flick, A. Oleaga, A. Salazar, J.M. Yanez-Limon, J.J. Alvarado-Gil, Heat transport in epoxy and polyester carbonyl iron microcomposites: The effect of concentration and temperature, J. Compos. Mater. 52 (2018) 1331.
[52] G.J. Jäger, L. Fischer, T. Lutz, A.M. Menzel, Variations in the thermal conductivity of magnetosensitive elastomers by magnetically induced internal restructuring, J. Phys.: Condens. Matter 34 (2022) 485101.
[53] C. Gollwitzer, A. Turanov, M. Krekhova, G. Lattermann, I. Rehberg, R. Richter, Measuring the deformation of a ferrogel sphere in a homogeneous magnetic field, J. Chem. Phys. 128 (2008) 164709.
[54] G. Filipcsei, M. Zrínyi, Magnetodeformation effects and the swelling of ferrogels in a uniform magnetic field, J. Phys.: Condens. Matter 22 (2010) 276001.
[55] O.V. Stolbov, Y.L. Raikher, M. Balasoiu, Modelling of magnetodipolar striction in soft magnetic elastomers, Soft Matter 7 (2011) 8484.
[56] A.Y. Zubarev, Effect of chain-like aggregates on ferrogel magnetodeformation, Soft Matter 9 (2013) 4985.
[57] A. Zubarev, Magnetodeformation of ferrogels and ferroelastomers. Effect of microstructure of the particles' spatial disposition, Physica A 392 (2013) 4824.
[58] J. Maas, D. Uhlenbusch, Experimental and theoretical analysis of the actuation behavior of magnetoactive elastomers, Smart Mater. Struct. 25 (2016) 104002.
[59] A. Attaran, J. Brummund, T. Wallmersperger, Modeling and finite element simulation of the magneto-mechanical behavior of ferrogels, J. Magn. Magn. Mater. 431 (2017) 188.
[60] X. Guan, X. Dong, J. Ou, Magnetostrictive effect of magnetorheological elastomer, J. Magn. Magn. Mater. 320 (2008) 158.
[61] X. Gong, G. Liao, S. Xuan, Full-field deformation of magnetorheological elastomer under uniform magnetic field, Appl. Phys. Lett. 100 (2012) 211909.
[62] F.J. Vazquez-Perez, C. Gila-Vilchez, J. Duran, A. Zubarev, L.A. de Cienfuegos, L. Rodriguez-Arco, M.T. Lopez-Lopez, Composite polymer hydrogels with high and reversible elongation under magnetic stimuli, Polymer 230 (2021) 124093.
[63] M.-A. Keip, M. Rambausek, Computational and analytical investigations of shape effects in the experimental characterization of magnetorheological elastomers, Int. J. Solids Struct. 121 (2017) 1.
[64] L. Fischer, A.M. Menzel, Magnetostriction in magnetic gels and elastomers as a function of the internal structure and particle distribution, J. Chem. Phys. 151 (2019) 114906.

[65] L. Fischer, A.M. Menzel, Towards a soft magnetoelastic twist actuator, Phys. Rev. Res. 2 (2020) 023383.
[66] L. Fischer, A.M. Menzel, Magnetically induced elastic deformations in model systems of magnetic gels and elastomers containing particles of mixed size, Smart Mater. Struct. 30 (2020) 014003.
[67] Y. An, M.T. Shaw, Actuating properties of soft gels with ordered iron particles: Basis for a shear actuator, Smart Mater. Struct. 12 (2003) 157.
[68] K. Zimmermann, V.A. Naletova, I. Zeidis, V.A. Turkov, E. Kolev, M.V. Lukashevich, G.V. Stepanov, A deformable magnetizable worm in a magnetic field — a prototype of a mobile crawling robot, J. Magn. Magn. Mater. 311 (2007) 450.
[69] R. Fuhrer, E.K. Athanassiou, N.A. Luechinger, W.J. Stark, Crosslinking metal nanoparticles into the polymer backbone of hydrogels enables preparation of soft, magnetic field-driven actuators with muscle-like flexibility, Small 5 (2009) 383.
[70] H. Böse, R. Rabindranath, J. Ehrlich, Soft magnetorheological elastomers as new actuators for valves, J. Intel. Mater. Syst. Struct. 23 (2012) 989.
[71] L. Hines, K. Petersen, G.Z. Lum, M. Sitti, Soft actuators for small-scale robotics, Adv. Mater. 29 (2017) 1603483.
[72] Y. Li, J. Li, W. Li, H. Du, A state-of-the-art review on magnetorheological elastomer devices, Smart Mater. Struct. 23 (2014) 123001.
[73] G.Z. Lum, Z. Ye, X. Dong, H. Marvi, O. Erin, W. Hu, M. Sitti, Shape-programmable magnetic soft matter, Proc. Natl. Acad. Sci. USA 113 (2016) E6007.
[74] T.I. Becker, V. Böhm, J.C. Vega, S. Odenbach, Y.L. Raikher, K. Zimmermann, Magnetic-field-controlled mechanical behavior of magneto-sensitive elastomers in applications for actuator and sensor systems, Arch. Appl. Mech. 89 (2019) 133.
[75] J. Chavez, V. Böhm, T.I. Becker, S. Gast, I. Zeidis, K. Zimmermann, Actuators based on a controlled particle-matrix interaction in magnetic hybrid materials for applications in locomotion and manipulation systems, Phys. Sci. Rev. 7 (2020) 1263.
[76] F.J. Vazquez-Perez, C. Gila-Vilchez, A. Leon-Cecilla, L. Álvarez de Cienfuegos, D. Borin, S. Odenbach, J.E. Martin, M.T. Lopez-Lopez, Fabrication and actuation of magnetic shape-memory materials, ACS Appl. Mater. Interfaces 15 (2023) 53017.
[77] R. Weeber, S. Kantorovich, C. Holm, Deformation mechanisms in 2d magnetic gels studied by computer simulations, Soft Matter 8 (2012) 9923.
[78] A.M. Menzel, Bridging from particle to macroscopic scales in uniaxial magnetic gels, J. Chem. Phys. 141 (2014) 194907.
[79] R. Weeber, S. Kantorovich, C. Holm, Ferrogels cross-linked by magnetic particles: Field-driven deformation and elasticity studied using computer simulations, J. Chem. Phys. 143 (2015) 154901.
[80] G. Pessot, R. Weeber, C. Holm, H. Löwen, A.M. Menzel, Towards a scale-bridging description of ferrogels and magnetic elastomers, J. Phys.: Condens. Matter 27 (2015) 325105.
[81] A.M. Menzel, Stimuli-responsive twist actuators made from soft elastic composite materials—linking mesoscopic and macroscopic descriptions, J. Chem. Phys. 154 (2021) 204902.
[82] M. Roghani, D. Romeis, M. Saphiannikova, Effect of microstructure evolution on the mechanical behavior of magneto-active elastomers with different matrix stiffness, Soft Matter 19 (2023) 6387.
[83] K.A. Kalina, L. Linden, J. Brummund, M. Kästner, Fe^{ANN}: an efficient data-driven multiscale approach based on physics-constrained neural networks and automated data mining, Comput. Mech. 71 (2023) 827.
[84] S. Bohlius, H.R. Brand, H. Pleiner, Macroscopic dynamics of uniaxial magnetic gels, Phys. Rev. E 70 (2004) 061411.
[85] P. Gebhart, T. Wallmersperger, A general framework for the modeling of porous ferrogels at finite strains, J. Mech. Phys. Solids 122 (2019) 69.
[86] P. Cremer, M. Heinen, A. Menzel, H. Löwen, A density functional approach to ferrogels, J. Phys.: Condens. Matter 29 (2017) 275102.
[87] D. Romeis, V. Toshchevikov, M. Saphiannikova, Elongated micro-structures in magneto-sensitive elastomers: a dipolar mean field model, Soft Matter 12 (2016) 9364.
[88] L.J. Walpole, An elastic singularity in a spherical inclusion: the Green tensor, Proc. R. Soc. London A 458 (2002) 705.
[89] M. Puljiz, S. Huang, K.A. Kalina, J. Nowak, S. Odenbach, M. Kästner, G.K. Auernhammer, A.M. Menzel, Reversible magnetomechanical collapse: Virtual touching and detachment of rigid inclusions in a soft elastic matrix, Soft Matter 14 (2018) 6809.
[90] A.-L. Cauchy, Exercices de Mathématiques, Vol. 3, Bure Frères, Paris, 1828, pp. 160–187.
[91] K.M. Górski, E. Hivon, A.J. Banday, B.D. Wandelt, F.K. Hansen, M. Reinecke, M. Bartelmann, HEALPix: a framework for high-resolution discretization and fast analysis of data distributed on the sphere, Astrophys. J. 622 (2005) 759.
[92] J.D. Jackson, Classical Electrodynamics, Wiley, New York, 1999.
[93] R. Cornell, U. Schwertmann, The Iron Oxides: Structure, Properties, Reactions, Occurrences and Uses, John Wiley & Sons, Weinheim, 2003.
[94] D. Günther, D.Y. Borin, S. Günther, S. Odenbach, X-ray micro-tomographic characterization of field-structured magnetorheological elastomers, Smart Mater. Struct. 21 (2011) 015005.
[95] X. Zhang, S. Peng, W. Wen, W. Li, Analysis and fabrication of patterned magnetorheological elastomers, Smart Mater. Struct. 17 (2008) 045001.
[96] W. Chen, L. Sun, X. Li, D. Wang, Numerical investigation on the magnetostrictive effect of magneto-sensitive elastomers based on a magneto-structural coupling algorithm, Smart Mater. Struct. 22 (2013) 105012.
[97] S. Qi, H. Guo, J. Fu, Y. Xie, M. Zhu, M. Yu, 3D printed shape-programmable magneto-active soft matter for biomimetic applications, Compos. Sci. Technol. 188 (2020) 107973.
[98] Y. Zhang, Q. Wang, S. Yi, Z. Lin, C. Wang, Z. Chen, L. Jiang, 4D printing of magnetoactive soft materials for on-demand magnetic actuation transformation, ACS Appl. Mater. Inter. 13 (2021) 4174.
[99] R. Bayaniahangar, S.B. Ahangar, Z. Zhang, B.P. Lee, J.M. Pearce, 3-D printed soft magnetic helical coil actuators of iron oxide embedded polydimethylsiloxane, Sens. Actuator B: Chem. 326 (2021) 128781.
[100] Y. Kim, H. Yuk, R. Zhao, S.A. Chester, X. Zhao, Printing ferromagnetic domains for untethered fast-transforming soft materials, Nature 558 (2018) 274.
[101] E. Dohmen, A. Saloum, J. Abel, Field-structured magnetic elastomers based on thermoplastic polyurethane for fused filament fabrication, Phil. Trans. R. Soc. A 378 (2020) 20190257.
[102] A. Bastola, M. Paudel, L. Li, Dot-patterned hybrid magnetorheological elastomer developed by 3D printing, J. Magn. Magn. Mater. 494 (2020) 165825.
[103] 3D printed magnetorheological elastomers, in: Smart Materials, Adaptive Structures and Intelligent Systems, Vol. 1: Development and Characterization of Multifunctional Materials; Mechanics and Behavior of Active Materials; Bioinspired Smart Materials and Systems; Energy Harvesting; Emerging Technologies, 2017.
[104] A. Komp, J. Rühe, H. Finkelmann, A versatile preparation route for thin free-standing liquid single crystal elastomers, Macromol. Rapid Commun. 26 (2005) 813.
[105] J.E. Martin, R.A. Anderson, D. Read, G. Gulley, Magnetostriction of field-structured magnetoelastomers, Phys. Rev. E 74 (2006) 051507.
[106] Z. Ma, A.W. Holle, K. Melde, T. Qiu, K. Poeppel, V.M. Kadiri, P. Fischer, Acoustic holographic cell patterning in a biocompatible hydrogel, Adv. Mater. 32 (2020) 1904181.
[107] J. Kim, S.E. Chung, S.-E. Choi, H. Lee, J. Kim, S. Kwon, Programming magnetic anisotropy in polymeric microactuators, Nature Mater. 10 (2011) 747.

P5 Maximized response by structural optimization of soft elastic composite systems

Reproduced from

L. Fischer and A. M. Menzel,
Maximized response by structural optimization of soft elastic composite systems,
PNAS Nexus **3**, pgae353 (2024).

Digital Object Identifier (DOI): `https://doi.org/10.1093/pnasnexus/pgae353`

Statement of contribution

Both authors contributed to the work. The idea was proposed by AMM. I developed the analytical formulae (see also **P6**), verified them and performed the numerical evaluations, including work on the numerical optimization scheme. Both authors discussed the results. AMM supervised the work and introduced the idea of comparing to the regular structures as well as initial ideas for the optimization. I drafted the manuscript, including all figures, and the supplemental material, which was then substantially revised by AMM. Finally, I also prepared the published dataset that accompanies the paper. I estimate my contribution to this work during my PhD as 90 %.
See also the section "Author Contributions" within the publication.

Copyright and license notice

PNAS Nexus, 2024, 3, pgae353
https://doi.org/10.1093/pnasnexus/pgae353
Advance access publication 21 August 2024
Research Report

Maximized response by structural optimization of soft elastic composite systems

Lukas Fischer [a,*] and Andreas M. Menzel [a]

[a]Institut für Physik, Otto-von-Guericke-Universität Magdeburg, Universitätsplatz 2, Magdeburg 39106, Germany
*To whom correspondence should be addressed: Email: lukas.fischer@ovgu.de
Edited By Horacio Espinosa

Abstract

Soft actuators triggered in a wire—and contactless way advance soft robotics, for instance, concerning microsurgical perspectives. For optimal performance in this and other contexts, maximized stimuli-responsiveness is frequently desirable. We demonstrate on the example of soft magnetoelastic systems how analytical theoretical measures in combination with computer simulations provide tools to develop optimized components. To enhance the overall macroscopic response, we adjust microstructural properties. Our strategy guides us towards ideally structured soft materials that can be fabricated using modern technologies.

Keywords: soft magnetic functional materials, composite materials, actuation, material optimization

Significance Statement

New technological developments, for example 3D printing, increasingly allow to fabricate soft elastic composite materials containing discrete sites of functionalization at prescribed positions. The full potential of such materials will only be exploited, if we manage to optimize the discrete internal positioning. Combining analytical theory and computational tools, we introduce an efficient procedure to perform such optimization on a representative example system. We demonstrate how different optimized discrete arrangements emerge depending on the requested overall mechanical response. This will substantially advance the capabilities of these soft functionalized materials. Together, our approach and results will be of interest to a community who searches to advance the properties of matter in general.

Introduction

As the backbone of soft robotics, soft actuators have attracted significant interest (1–3). They feature many advantages compared to conventional solutions, such as light weight (2, 4) and—due to their mechanical softness—improved human-robot collaboration and handling of fragile items (1–3). Also, they are relatively inexpensive (4–6) and compact (3, 5). These materials show an active deformation or stress generation in response to external stimuli. Many triggers can be used, for example heat, light, chemicals, electric, or magnetic fields (3, 6–13). Typically, magnetic fields do not interact severely with biological tissue, which is important for biological and medical applications (5–8, 14). Consequently, we focus on soft magnetoelastic systems, that is, materials consisting of a soft, often polymeric, matrix with embedded magnetic or magnetizable particles (6, 10, 15–19). When external magnetic fields are applied, induced magnetic interactions between the inclusions cause an overall, macroscopic deformation (magnetostriction) and change in macroscopic behavior. These materials are discussed as candidates for artificial muscles (11, 20) of reversible deformability (21) and adaptive dampers or vibration absorbers (22–24). The latter is due to magnetically tunable rheological properties—the so-called magnetorheological (MR) effect (15, 21, 25–29).

So far, most investigations have concentrated on corresponding materials featuring rather randomized internal particle arrangements (15, 18, 30–32). As one variation, anisotropic and chain-like structures are generated in strong uniform external magnetic fields (18, 28, 30, 33, 34). However, in general, such types of spatial arrangement will not lead to an optimized deformational response.

The advent and development of new routes of sample preparation will in the future allow for a significantly improved targeted placement of magnetizable inclusions in elastic carrier media. Accordingly, spatial arrangements tailored to the requested purpose are realized. Internal structures are optimized for maximized deformational response. Promising example techniques include 3D printing (12, 13, 29, 35–37), structuring by magnetic fields (38), sequential photopolymerization (39), acoustic holography (40), layerwise polymerization combined with particle placement by molds or by hand (41, 42), and wax-cast molding (43). We here introduce efficient means to determine the structure of optimized spatial arrangements of

Competing Interest: The authors declare no competing interest.
Received: April 22, 2024. **Accepted:** August 11, 2024

inclusions that afterward can be realized by the listed experimental methods.

Concerning the types of inclusions considered, we note that our approach does not distinguish between individual particles or agglomerates of these, for instance, in a drop of magnetic fluid. Yet, we require the condition of well-separated inclusions. Besides, due to the generic nature of our approach, the overall size of the system is not preset. Only the size of the inclusions relative to the overall size needs to be small. Therefore, as long as this condition is satisfied, even macroscopic inclusions can be described by our approach.

Results

Model for calculating the magnetostrictive effects

Our approach is based on analytical theory, which serves as an input for our computational optimization of soft magnetoelastic materials. Performing analytical calculations on finite-sized elastic systems is a challenge. We had managed to calculate explicitly the deformation of a homogeneous, isotropic, linearly elastic sphere in response to an internal force distribution (44). The shear modulus μ characterizes the elastic stiffness of the sphere and the Poisson ratio $\nu \in (-1, 1/2]$ its compressibility. Materials of $\nu = 1/2$ are incompressible, for $\nu < 1/2$ they are compressible, and for $\nu < 0$ auxetic. For small deformations, nonlinear functionals of the elastic energy can usually be expanded into a power series. There are generally only two different possible types of quadratic terms that may emerge (45). They represent linearly elastic behavior. Consequently, analyzing the behavior in terms of linear elasticity forms a reasonable and generic starting point.

We first consider spherical model systems containing N magnetic force centers. Thus, we explicitly include the boundaries of the system into our consideration. Induced changes in volume and shape, that is, magnetoelastic actuations, are quantified using the radial outward displacement field of the surface points. We expand this field into spherical harmonics (44). A first expansion coefficient $u_{00}^{\perp}$ quantifies the overall induced change in volume, see Fig. 1A. A second expansion coefficient $u_{20}^{\perp}$ quantifies elongation along a certain axis $\hat{\mathbf{z}}$ relative to lateral contraction,

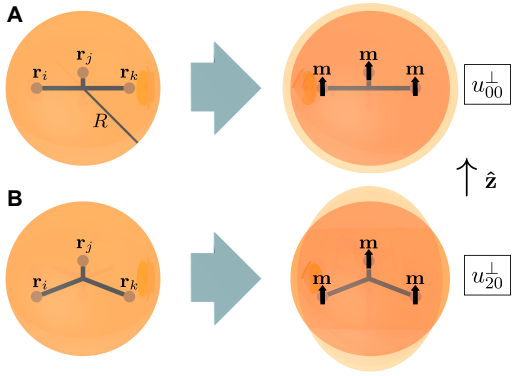

Fig. 1. Illustration of the modes of deformation $u_{00}^{\perp}$ in A) and $u_{20}^{\perp}$ in B). In the undeformed spherical ground states on the left, we here indicate three magnetizable inclusions as smaller spheres at positions $\mathbf{r}_i$, $\mathbf{r}_j$, and $\mathbf{r}_k$. Upon magnetization (right), their interacting magnetic dipole moments $\mathbf{m} \parallel \hat{\mathbf{z}}$ induce deformations of the whole sphere, implying changes in volume ($u_{00}^{\perp}$) and elongation along $\hat{\mathbf{z}}$ relative to lateral contraction ($u_{20}^{\perp}$). Deformed states are illustrated in lighter color (orange) with amplitudes not to scale.

see Fig. 1B. We here present explicit analytical expressions forming the basis of our optimization. Point-like force centers of forces $\mathbf{F}_i$ acting at positions $\mathbf{r}_i$, $i = 1, \ldots, N$, with the origin of our coordinate frame positioned at the center of the sphere of radius R, imply (46)

$$u_{00}^{\perp} = \sum_{i=1}^{N} \mathbf{F}_i \cdot \mathbf{r}_i \frac{1-2\nu}{1+\nu} \frac{1}{2\mu R^2} \sqrt{\frac{1}{4\pi}}, \tag{1}$$

$$u_{20}^{\perp} = \sum_{i=1}^{N} \frac{\sqrt{5/4\pi}}{4\mu R^2 (7+5\nu)} \Big[(-\mathbf{F}_i \cdot \underline{\boldsymbol{\delta}}^{\perp} \cdot \mathbf{r}_i + 2\mathbf{F}_i \cdot \underline{\boldsymbol{\delta}}^{\parallel} \cdot \mathbf{r}_i)(7+2\nu) + 3\frac{r_i^3}{R^2} \left(2\nu \mathbf{F}_i \cdot \underline{\boldsymbol{\delta}}^{\perp} \cdot \hat{\mathbf{r}}_i - (7-6\nu)\mathbf{F}_i \cdot \underline{\boldsymbol{\delta}}^{\parallel} \cdot \hat{\mathbf{r}}_i + \mathbf{F}_i \cdot \hat{\mathbf{r}}_i \hat{\mathbf{r}}_i \cdot \underline{\boldsymbol{\delta}}^{\parallel} \cdot \hat{\mathbf{r}}_i (7-10\nu)\right) \Big]. \tag{2}$$

Here, $\hat{\mathbf{r}}_i = \mathbf{r}_i / r_i$, $r_i = |\mathbf{r}_i|$, $\underline{\boldsymbol{\delta}}^{\parallel} = \hat{\mathbf{z}}\hat{\mathbf{z}}$, $\underline{\boldsymbol{\delta}}^{\perp} = \mathbb{1} - \underline{\boldsymbol{\delta}}^{\parallel}$, $\hat{\mathbf{z}}\hat{\mathbf{z}}$ is a dyadic product, and $\mathbb{1}$ the unit matrix.

Each point-like force center represents a magnetizable inclusion. We require a certain distance between any two force centers $|\mathbf{r}_i - \mathbf{r}_j| > 0.12R$, and a minimal distance from the boundary $r_i < 0.94R$, $i \neq j = 1, \ldots, N$. These settings (and the overall number of inclusions N) affect the resulting structures. The chosen values favor a representation using magnetic dipolar interactions and linear elasticity. Considering saturated magnetization by strong external homogeneous magnetic fields along $\hat{\mathbf{z}}$, we obtain (47)

$$\mathbf{F}_i = -\sum_{\substack{j=1 \\ j\neq i}}^{N} \frac{3\mu_0 m^2 \left[5\hat{\mathbf{r}}_{ij} \left(\hat{\mathbf{m}} \cdot \hat{\mathbf{r}}_{ij} \right)^2 - \hat{\mathbf{r}}_{ij} - 2\hat{\mathbf{m}} \left(\hat{\mathbf{m}} \cdot \hat{\mathbf{r}}_{ij} \right) \right]}{4\pi r_{ij}^4}. \tag{3}$$

Here, $\mathbf{m} = m\hat{\mathbf{m}}$ is the identical magnetic dipole moment for all inclusions, where $\hat{\mathbf{m}} = \hat{\mathbf{z}}$, $\mathbf{r}_{ij} = \mathbf{r}_i - \mathbf{r}_j$, $r_{ij} = |\mathbf{r}_{ij}|$, $\hat{\mathbf{r}}_{ij} = \mathbf{r}_{ij}/r_{ij}$, and μ_0 denotes the magnetic vacuum permeability. After rescaling, we measure lengths in units of R and the relative strength of the magnetic dipolar interaction by a nondimensional number $3\mu_0 m^2 / 4\pi\mu R^6$. The latter is set to a realistic value of 5.4×10^{-8} (44) for $\mu \approx 1.67$ kPa (48–51), inclusions of radius $r = 0.02R$, and a saturation magnetization of 518 kA m^{-1} as for Fe_3O_4 (52).

As a central benefit, we can now determine the maxima of the analytical expressions in Eqs. 1 and 2 as a function of the positions. That is, we find the largest degrees of deformation associated with the amplitudes $\pm u_{00}^{\perp}$ or $\pm u_{20}^{\perp}$. Optimization is performed as a function of the internal structural arrangements. We recall that the number of inclusions is fixed during this procedure.

Because of the many degrees of freedom $\mathbf{r}_i$, $i = 1, \ldots, N$, we resort to numerical procedures to achieve optimization. We employ simulated annealing (SA) (53–56) with modifications (57) and adjusted parameter settings, see the Supplementary Material. Typically, this method is used to minimize energies. Here, instead, we insert the right-hand sides of Eqs. 1 and 2 to maximize the deformations induced by the magnetized inclusions. The extrema are found using the locations of the N inclusions as degrees of freedom, maintaining the above-mentioned constraints. Accordingly, we transfer this well-established method to the field of material optimization.

Resulting materials of maximized actuation

Linear actuation

First, we maximize the relative contraction along the magnetic field direction, referring to linear actuators or artificial muscles. We thus minimize $u_{20}^{\perp}$ for $N = 1{,}000$ magnetizable inclusions, assuming incompressibility (48, 49, 51). The resulting optimized

structure achieves an approximately 68% higher degree of deformation $u_{20}^{\perp}$ when compared to realizations of regular lattice structures (44).

Figure 2A–C indicates that the optimal configuration closely resembles a hexagonally arranged chain-like structure. The chains are oriented along the magnetization direction and concentrated towards the center axis. Comparative tests arranging regular structures by hand confirm this picture, see the Supplementary Material. Decreasing Poisson ratios increase the magnitudes of deformation, see Fig. 2D. Simultaneously, the inclusions of the optimized structures are shifted closer to the boundary of the sphere, see the inset of Fig. 2D, and deviations from results for regular structures become significant. Increasing the inclusion density mostly enhances the deformational response, see Fig. 2E for $\nu = 1/2$. In that case, the regular hexagonal structures perform close to optimally.

Natural muscles often work in counteracting pairs (11). We therefore continue by discussing relative elongations along the magnetization direction, maximizing $u_{20}^{\perp}$. For $\nu = 1/2$ and $N = 1{,}000$, our optimization leads to an increase of approximately 129% when compared to regular structures (44).

As Fig. 3A illustrates, the optimized configuration now splits into an inner and an outer part. Both parts contain about the same number of inclusions and also contribute similarly to $u_{20}^{\perp}$. The inner part can be approximated by a regular simple cubic structure, as indicated by Steinhardt bond orientational order parameters (58), see Fig. 3B. Generating an appropriately oriented regular simple cubic configuration by hand over the whole sphere (Supplementary Material), the overall degree of deformation $u_{20}^{\perp}$ deviates by only about 0.3%.

When decreasing the Poisson ratio ν, the deformational response increases, see Fig. 3D. Simultaneously, the gap in response between optimized and regular simple cubic structure increases. The optimized locations of the inclusions are pushed closer to the spherical surface, see the inset of Fig. 3D.

Again for $\nu = 1/2$, Fig. 3E demonstrates that the deformational response mostly increases with increasing number of inclusions. Our regular simple cubic structure remains close to optimal. A disjoint inner and outer part can only be identified for $N \lesssim 1{,}400$. For $N = 2{,}000$, the simple cubic configuration is not dense enough and the deformational response decreases. Still, a regular, denser, face-centered cubic (fcc) lattice structure performs significantly worse.

Changes in volume

Next, we focus on magnetically induced overall changes in volume, quantified by $u_{00}^{\perp}$. Corresponding systems may prove useful in the design of soft magnetoelastic valves (59) or microfluidic pumps (5). Changes in volume are only possible in compressible elastic materials. For $\nu < 1/2$, Eq. 1 demonstrates that materials of different Poisson ratio ν all show qualitatively the same dependence of $u_{00}^{\perp}$ on the inclusion configuration. Thus, all of them thus lead to identical optimized structures.

We first search for a most pronounced induced shrinkage in volume, minimizing $u_{00}^{\perp}$. For $N = 1{,}000$, this optimized shrinkage increases by 24% in magnitude when compared to regular structures (44). The optimized structure mainly consists of (irregular) chain-like arrangements oriented along the magnetization direction, see Fig. 4A, B. Any two nearest-neighboring chains are shifted relative to each other along their axes by about half a vertical inclusion separation distance (Fig. S2).

With increasing N, see Fig. 4C, the arrangements remain predominantly chain-like. However, the chains tend to form square-like lattices. We compare to results for related regular structures, with neighboring chains vertically shifted (Supplementary Material). Deviations are significant, see Fig. 4C. Increasing N from about 500 to 1,500 raises the magnitude of deformational response, in contrast to the subsequent decrease, thus showing nonmonotonic behavior.

Lastly, we maximize the induced increase in volume by maximizing $u_{00}^{\perp}$. For $N = 1{,}000$, our optimized induced expansion is approximately 418% larger when compared to results for regular

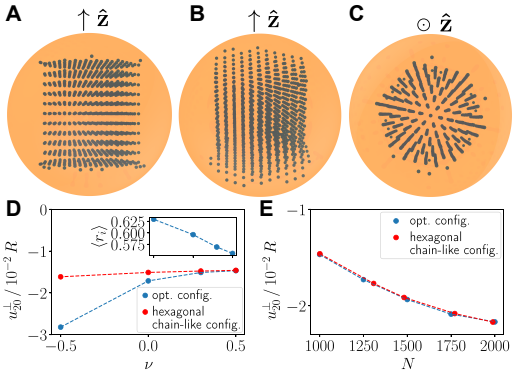

Fig. 2. Maximized relative contraction along the magnetization direction $\hat{\mathbf{z}}$, minimizing $u_{20}^{\perp}$. A–C) Resulting optimized configuration of magnetizable inclusions ("opt. config.") inside an incompressible elastic sphere of radius R (orange) for $N = 1{,}000$. A) Side view. B) Tilted top view. C) Top view. D) Degree of deformation as a function of the Poisson ratio ν. Inset: average inclusion distance from the center $\langle r_i \rangle$ vs. Poisson ratio (same scale of abscissa as in main plot). E) Variation of the degree of deformation with the inclusion number N. In D and E), we further compare deformational results for our optimized structures to those for regular hexagonal chain-like configurations, with dashed lines added as guides to the eye.

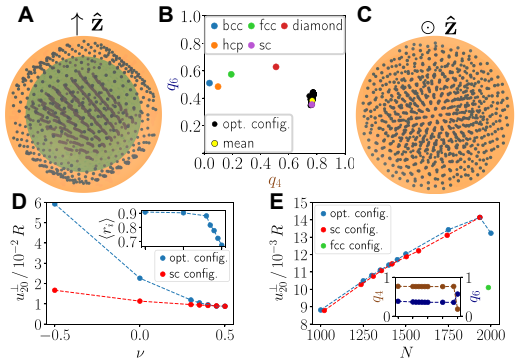

Fig. 3. Maximized relative elongation along the magnetization direction $\hat{\mathbf{z}}$, maximizing $u_{20}^{\perp}$. A, C) are analogous to Fig. 2. In A), we mark the separation between an inner and an outer part in green (slightly darker color). B) Steinhardt bond orientational order parameters q_4 and q_6 for the inner part compared to various regular lattices. D, E) are analogous to Fig. 2, now showing results for appropriately oriented regular simple cubic (sc) configurations. E) The result for a regular face-centered cubic (fcc) structure at $N = 1{,}985$ is included. Inset: variation of q_4 (brown, darker color) and q_6 (blue, lighter color) with N (same scale of abscissa as in main plot) indicate a significant change in the optimized texture at $N \approx 2{,}000$.

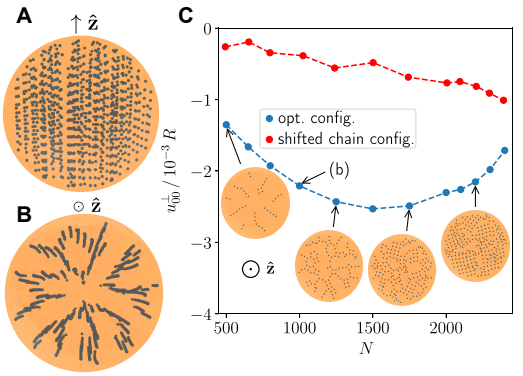

Fig. 4. Maximized decrease in total volume, minimizing $u_{00}^{\perp}$. According to Eq. 1, the resulting optimized structures are independent of the Poisson ratio ν (here $\nu = 0.3$). A) Tilted top view. B) Top view. C) It is analogous to Fig. 2E, supplemented by top views of the mean inclusion positions along each chain-like element for different inclusion numbers N.

structures (44). Figure 5A, B indicates the optimized structures to resemble hexagonal arrangements in layers stacked on top of each other. The layer-to-layer distances are much larger than the inter-inclusion distances within each layer, see Fig. 5A, B. Regular hexagonal layer structures generated by hand (Supplementary Material) performed notably worse for elevated numbers of inclusions N, see Fig. 5C.

Optimized magnetorheological effects

(Positive) magnetorheological effect

Additionally, we optimize the inclusion arrangement to maximize the magnetorheological (MR) effect of the soft magnetoelastic materials, here for prescribed affine deformations. We address cubical systems of side length a, maintaining the same conditions as before. The radius of the inclusions is set to $r = 0.03a$, which shifts the nondimensional number $3\mu_0 m^2/4\pi\mu a^6$ to approximately 6.2×10^{-7}. To this end, we define $\Delta\mu_{\text{rel}} = (\mu_{\text{magn}} - \mu)/\mu$ as the relative change in shear modulus, where μ_{magn} is the overall elastic shear modulus in the magnetized state as measured for our numerical systems.

Our cube is magnetized perpendicular to one of its facets, and we consider incompressible systems. The associated overall energy is given by

$$E = E_{\text{def}} - \sum_{\substack{i,j=1 \\ j>i}}^{N} \frac{\mu_0 m^2 \left[3\left(\hat{\mathbf{m}} \cdot \hat{\mathbf{r}}_{ij}\right)^2 - 1\right]}{4\pi r_{ij}^3}, \tag{4}$$

where E_{def} is the elastic deformation energy followed by the magnetic dipolar interaction energy (47) in the deformed state.

First, we maximize the MR effect when the system is uniaxially elongated along the magnetization direction. That is, $E_{\text{def}} = \frac{3}{2}\mu\delta^2 a^3$ in Eq. 4, where δ is the stretching ratio. To calculate $\Delta\mu_{\text{rel}}$, we evaluate the total energy, see Eq. 4, for several values of the stretching ratio δ close to the energetic minimum. Afterward, we fit the evaluated values of the total energy by a quadratic function. We determine the minimum of the resulting parabola. It identifies the new equilibrium state under magnetization. Then, the change in the quadratic coefficient of the energy around its minimum from the nonmagnetized to the magnetized state, obtained from the parabolic fit, provides $\Delta\mu_{\text{rel}}$. To fit the parabola, we always calculate the energy at five points around its minimum. We have confirmed that only minor changes (<0.01%) emerge when using 100 points.

Our optimization for $N = 200$ reveals a MR effect of $\Delta\mu_{\text{rel}} \approx 17.1\%$. In that case, the optimized structure is reminiscent of an appropriately oriented fcc lattice (Supplementary Material), see the Steinhardt bond orientational order parameters in Fig. 6A (an illustration of the imposed deformation is provided in Fig. 7A).

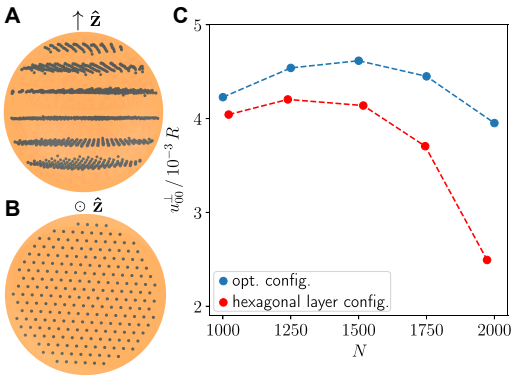

Fig. 5. Maximized total increase in volume, maximizing $u_{00}^{\perp}$ (here for $\nu = 0.3$). A) Side view. B) Top view, here only displaying the third layer from the bottom in (A). C) is analogous to Fig. 2E.

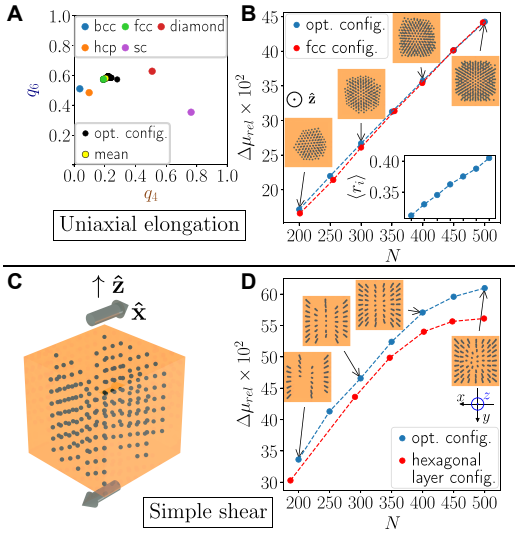

Fig. 6. Maximized relative increase in elastic modulus $\Delta\mu_{\text{rel}}$ for cubical systems by magnetization along $\hat{\mathbf{z}}$ for A, B) uniaxial elongation, here $\nu = 1/2$, and C, D) simple shear. A) Steinhardt bond order parameters for that configuration of $N = 200$ that maximizes $\Delta\mu_{\text{rel}}$. C) Tilted top view. Gray arrows indicate imposed simple shear deformations. B, D) Variation of the relative magnetorheological effect with inclusion number N, including top views of the optimized configurations. Inset in B): average distance $\langle r_i \rangle$ from the center of the cube (same scale of abscissa as in main plot).

Raising N fills the cube starting from the center outwards, see the inset of Fig. 6B, with an increasing MR effect. Here, regular structures (Supplementary Material) perform comparatively well (within >96%).

For simple shear deformations, $E_{\text{def}} = \frac{1}{2}\mu\gamma^2 a^3$ in Eq. 4, with γ as the shear ratio. Shear is imposed within the xz-plane, see Fig. 6C. Upon optimization, $\Delta\mu_{\text{rel}} \approx 33.6\%$ for $N = 200$. The optimized structures feature layers in the yz-plane of approximately hexagonal structure and of maximized mutual spacing. Increasing N, the layers approach each other, see Fig. 6D, with increasing deviations in their performance from regular structures (Supplementary Material) (remaining within 90%).

Negative magnetorheological effect

The previously considered structures show maximal hardening upon magnetization. Next, we also include results for the opposite scenario, which is significantly less frequently considered (60, 61). It is referred to as negative MR effect, that is, the materials soften upon magnetization. Thus, we now minimize $\Delta\mu_{\text{rel}}$.

Figure 7A depicts the resulting optimized structure for $N = 200$ inclusions and uniaxial elongation, featuring a negative MR effect of $\Delta\mu_{\text{rel}} \approx -22\%$. For $N \lesssim 200$, we observe that the inclusions form chains of a particular arrangement, approximately a circle with an appendage, see the leftmost inset in Fig. 7B. Neighboring chains feature a vertical shift, similar to the configurations that minimize $u_{00}^{\perp}$ from Fig. 4 (see also Fig. S2). With increasing number of inclusions N, the optimized arrangements of the chains change. More and more chains form, shifting the overall locations of chains from circular to cubic arrangements, see again the insets of Fig. 7B. Additionally, we infer from Fig. 7B that the MR effect $\Delta\mu_{\text{rel}}$ is almost perfectly proportional to the number of inclusions N. For comparison in performance, we construct regular structures by hand using quadratic and circular arrangements of the chains (Supplementary Material) with good agreement (>97%) concerning the resulting negative MR effect.

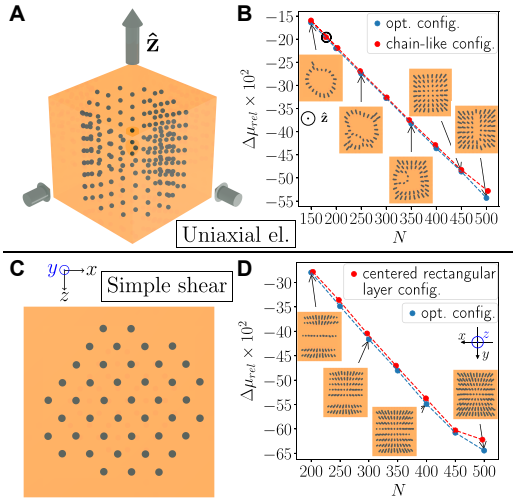

Fig. 7. Maximized magnitude of the negative MR effect, that is, strongest relative decrease in elastic modulus $\Delta\mu_{\text{rel}}$ upon magnetization. The illustration is analogous to Fig. 6 for the positive MR effect. Magnetization is imposed along $\hat{\mathbf{z}}$. A, B) Uniaxial elongation, here for $\nu = 1/2$. C, D) Simple shear. In B), we mark by a black circle the data point for $N = 180$, for which a circular texture is constructed by hand for comparison, see Section IIB of the Supplementary Material. C) Side view of the largest layer of inclusions forming when maximizing the magnitude of the negative MR effect under simple shear for $N = 200$. It corresponds to the bottommost layer in the leftmost inset (top views) in (D).

For simple shear deformations, we find a maximized negative MR effect of $\Delta\mu_{\text{rel}} \approx -27.9\%$ for $N = 200$ inclusions as displayed in Fig. 7D. See also Fig. 6C for an illustration of the imposed shear deformations. Here, we observe that our optimized textures can be divided into layers of inclusions oriented parallel to the shear plane. For $N = 200$, the largest such layer is depicted in Fig. 7C. These layers approximately feature centered rectangular structures with edge lengths along the magnetization direction and the direction of shear displacements. The larger edge length is found along the direction of shear displacements. When we increase the number of inclusions N, see Fig. 7D, we observe that the number of layers in the optimized arrangements as well as the magnitude of the negative MR effect increase. The results for regular lattice structures created by hand (Supplementary Material) show good agreement (>96%).

Conclusion

In summary, we present a route towards the design of optimized soft elastic composite materials that are structured in a way to maximize the requested overall response. To this end, we have developed and successfully applied corresponding tools. As a result, very efficient schemes of optimization are established and appropriately structured systems are presented.

As examples, we have demonstrated the optimization for soft magnetoelastic systems that respond to external magnetic fields by deformations and changes in mechanical properties. Specifically, we have maximized by adjusting the internal structure the relative elongation and contraction along the magnetization direction, the overall change in volume, and the magnetorheological effect in response to an external magnetic field. Aspects of how the deformational response and the optimized structures depend on the elastic properties of the employed material and on the total number of inclusions are addressed. We have shown that regular arrangements of inclusions do not necessarily maximize the response for finite-sized systems. Future refinements may include adjusted material models, for instance, concerning selected nonlinear elastic models, although linear elastic descriptions represent a substantial initial step of identifying most suitable arrangements (62). Including additional degrees of freedom for optimization, for instance, orientations of rod-shaped inclusions (63), may lead to further improvement.

Our results support the construction of soft components of tailored optimized response in general. Through recent technological developments, requested placement of inclusions in elastic matrices becomes possible (12, 13, 13, 29, 35–43). Applications include, but are not limited to artificial muscles, soft elastic valves and pumps, adaptive dampers, or vibration absorbers. The scheme of optimization that we present can be transferred to various other types of soft responsive composite materials. An immediate example are electrorheological gels and elastomers (50, 64, 65) or thermally actuated systems (66). More generally, whenever it is possible to link the discrete microscopic structure to the overall material behavior, a similar scheme of optimization can be employed to find the structure that maximizes the response. Overall, we support the growing field of tailored soft materials.

Acknowledgments

The authors thank Thomas Richter for a valuable discussion. Steinhardt bond orientational order parameters were calculated using pyscal (67) and pyboo (68).

Supplementary Material

Supplementary material is available at *PNAS Nexus* online.

Funding

The authors acknowledge support by the Deutsche Forschungsgemeinschaft (German Research Foundation, DFG), at an early stage of this work through the SPP 1681, grant no. ME 3571/2-3. We thank the DFG for support in the framework of the recently launched Research Unit FOR 5599, grant nos. ME 3571/10-1 and ME 3571/11-1. A.M.M. thanks the DFG for support through the Heisenberg grant ME 3571/4-1.

Author Contributions

Both authors developed the model, with conceptualization performed by A.M.M. L.F. performed the simulations, analyzed the results, and created the visualizations. Furthermore, L.F. wrote the original draft for this manuscript. A.M.M. supervised the research, helped in the investigation, administrated the project, and acquired corresponding funding. Additionally, A.M.M. performed substantial revisions of the manuscript. Both authors validated the results.

Data Availability

The generated data and numerical codes used to derive the results presented herein are published on the repository Zenodo and can be found at https://doi.org/10.5281/zenodo.13549320.

References

1 Trivedi D, Rahn CD, Kier WM, Walker ID. 2008. Soft robotics: biological inspiration, state of the art, and future research. *Appl Bionics Biomech*. 5(3):99–117.
2 Whitesides GM. 2018. Soft robotics. *Angew Chem Int Ed*. 57(16): 4258–4273.
3 Kim J, *et al*. 2019. Review of soft actuator materials. *Int J Precis Eng Man*. 20(12):2221–2241.
4 Snyder RL, Nguyen VQ, Ramanujan RV. 2010. Design parameters for magneto-elastic soft actuators. *Smart Mater Struct*. 19(5): 055017.
5 Tang S-Y, *et al*. 2018. Versatile microfluidic platforms enabled by novel magnetorheological elastomer microactuators. *Adv Funct Mater*. 28(8):1705484.
6 Weeber R, Hermes M, Schmidt AM, Holm C. 2018. Polymer architecture of magnetic gels: a review. *J Phys: Condens Matter*. 30(6): 063002.
7 Wu S, Hu W, Ze Q, Sitti M, Zhao R. 2020. Multifunctional magnetic soft composites: a review. *Multifunct Mater*. 3:042003.
8 Thévenot J, Oliveira H, Sandre O, Lecommandoux S. 2013. Magnetic responsive polymer composite materials. *Chem Soc Rev*. 42(17):7099–7116.
9 Lum GZ, *et al*. 2016. Shape-programmable magnetic soft matter. *Proc Natl Acad Sci U S A*. 113(41):E6007–E6015.
10 Sutrisno J, Purwanto A, Mazlan SA. 2015. Recent progress on magnetorheological solids: materials, fabrication, testing, and applications. *Adv Eng Mater*. 17(5):563–597.
11 Nguyen VQ, Ahmed AS, Ramanujan RV. 2012. Morphing soft magnetic composites. *Adv Mater*. 24(30):4041–4054.
12 Qi S, *et al*. 2020. 3D printed shape-programmable magneto-active soft matter for biomimetic applications. *Compos Sci Technol*. 188: 107973.
13 Bayaniahangar R, Ahangar SB, Zhang Z, Lee BP, Pearce JM. 2021. 3-D printed soft magnetic helical coil actuators of iron oxide embedded polydimethylsiloxane. *Sens Actuator B: Chem*. 326:128781.
14 Hu W, Lum GZ, Mastrangeli M, Sitti M. 2018. Small-scale soft-bodied robot with multimodal locomotion. *Nature*. 554(7690): 81–85.
15 Filipcsei G, Csetneki I, Szilágyi A, Zrínyi M. 2007. Magnetic field-responsive smart polymer composites. *Adv Polym Sci*. 206: 137–189.
16 Odenbach S. 2016. Microstructure and rheology of magnetic hybrid materials. *Arch Appl Mech*. 86(1-2):269–279.
17 Menzel AM. 2019. Mesoscopic characterization of magnetoelastic hybrid materials: magnetic gels and elastomers, their particle-scale description, and scale-bridging links. *Arch Appl Mech*. 89(1):17–45.
18 Li Y, Li J, Li W, Du H. 2014. A state-of-the-art review on magnetorheological elastomer devices. *Smart Mater Struct*. 23(12):123001.
19 Böse H, Gerlach T, Ehrlich J. 2021. Magnetorheological elastomers—an underestimated class of soft actuator materials. *J Intel Mater Syst Struct*. 32(14):1550–1564.
20 Zrínyi M, Szabó D. 2001. Muscular contraction mimicked by magnetic gels. *Int J Mod Phys B*. 15(06n07):557–563.
21 Schümann M, Odenbach S. 2017. In-situ observation of the particle microstructure of magnetorheological elastomers in presence of mechanical strain and magnetic fields. *J Magn Magn Mater*. 441:88–92.
22 Deng H-X, Gong X-L, Wang L-H. 2006. Development of an adaptive tuned vibration absorber with magnetorheological elastomer. *Smart Mater Struct*. 15(5):N111.
23 Liao GJ, Gong XL, Xuan SH, Kang CJ, Zong LH. 2012. Development of a real-time tunable stiffness and damping vibration isolator based on magnetorheological elastomer. *J Intel Mater Syst Struct*. 23(1):25–33.
24 Molchanov VS, *et al*. 2014. Viscoelastic properties of magnetorheological elastomers for damping applications. *Macromol Mater Eng*. 299(9):1116–1125.
25 Böse H, Röder R. 2009. Magnetorheological elastomers with high variability of their mechanical properties. *J Phys: Conf Ser*. 149(1): 012090.
26 Pessot G, *et al*. 2018. Tunable dynamic moduli of magnetic elastomers: from characterization by X-ray micro-computed tomography to mesoscopic modeling. *J Phys: Condens Matter*. 30(12): 125101.
27 Jolly MR, Carlson JD, Muñoz BC. 1996. A model of the behaviour of magnetorheological materials. *Smart Mater Struct*. 5(5):607–614.
28 Jolly MR, Carlson JD, Muñoz BC, Bullions TA. 1996. The magnetoviscoelastic response of elastomer composites consisting of ferrous particles embedded in a polymer matrix. *J Intel Mater Syst Struct*. 7(6):613–622.
29 Bastola AK, Paudel M, Li L. 2020. Dot-patterned hybrid magnetorheological elastomer developed by 3D printing. *J Magn Magn Mater*. 494:165825.
30 Böse H. 2007. Viscoelastic properties of silicone-based magnetorheological elastomers. *Int J Mod Phys B*. 21(28–29):4790–4797.

31 Gong X, Liao G, Xuan S. 2012. Full-field deformation of magnetorheological elastomer under uniform magnetic field. *Appl Phys Lett*. 100(21):211909.
32 Lokander M, Stenberg B. 2003. Improving the magnetorheological effect in isotropic magnetorheological rubber materials. *Polym Test*. 22(6):677–680.
33 Borbáth T, Günther S, Borin DY, Gundermann T, Odenbach S. 2012. XμCT analysis of magnetic field-induced phase transitions in magnetorheological elastomers. *Smart Mater Struct*. 21(10): 105018.
34 Danas K, Kankanala SV, Triantafyllidis N. 2012. Experiments and modeling of iron-particle-filled magnetorheological elastomers. *J Mech Phys Solids*. 60(1):120–138.
35 Zhang Y, *et al*. 2021. 4D printing of magnetoactive soft materials for on-demand magnetic actuation transformation. *ACS Appl Mater Inter*. 13(3):4174–4184.
36 Kim Y, Yuk H, Zhao R, Chester SA, Zhao X. 2018. Printing ferromagnetic domains for untethered fast-transforming soft materials. *Nature*. 558(7709):274–279.
37 Dohmen E, Saloum A, Abel J. 2020. Field-structured magnetic elastomers based on thermoplastic polyurethane for fused filament fabrication. *Phil Trans R Soc A*. 378(2171):20190257.
38 Martin JE, Anderson RA, Read D, Gulley G. 2006. Magnetostriction of field-structured magnetoelastomers. *Phys Rev E*. 74(5):051507.
39 Kim J, *et al*. 2011. Programming magnetic anisotropy in polymeric microactuators. *Nat Mater*. 10(10):747–752.
40 Ma Z, *et al*. 2020. Acoustic holographic cell patterning in a biocompatible hydrogel. *Adv Mater*. 32(4):1904181.
41 Puljiz M, Huang S, Auernhammer GK, Menzel AM. 2016. Forces on rigid inclusions in elastic media and resulting matrix-mediated interactions. *Phys Rev Lett*. 117(23):238003.
42 Zhang X, Peng S, Wen W, Li W. 2008. Analysis and fabrication of patterned magnetorheological elastomers. *Smart Mater Struct*. 17(4):045001.
43 Forster E, *et al*. 2013. Patterning of ultrasoft, agglutinative magnetorheological elastomers. *J Appl Polym Sci*. 128(4):2508–2515.
44 Fischer L, Menzel AM. 2019. Magnetostriction in magnetic gels and elastomers as a function of the internal structure and particle distribution. *J Chem Phys*. 151(11):114906.
45 Landau LD, Lifshitz EM. 1986. *Theory of elasticity*. Oxford: Elsevier.
46 Fischer L, Menzel AM. 2024. Analytical expressions for the two basic modes of surface displacement and overall deformation of a free-standing or elastically embedded sphere, arXiv, arXiv:2407.09291, https://doi.org/10.48550/arXiv.2407.09291, preprint: not peer reviewed.
47 Jackson JD. 1999. *Classical electrodynamics*. New York: Wiley.
48 Zrínyi M, Barsi L, Büki A. 1996. Deformation of ferrogels induced by nonuniform magnetic fields. *J Chem Phys*. 104(21):8750–8756.
49 Filipcsei G, Zrínyi M. 2010. Magnetodeformation effects and the swelling of ferrogels in a uniform magnetic field. *J Phys: Condens Matter*. 22(27):276001.
50 An Y, Shaw MT. 2003. Actuating properties of soft gels with ordered iron particles: basis for a shear actuator. *Smart Mater Struct*. 12(2):157–163.
51 Gollwitzer C, *et al*. 2008. Measuring the deformation of a ferrogel sphere in a homogeneous magnetic field. *J Chem Phys*. 128(16): 164709.
52 Cornell R, Schwertmann U. 2003. *The iron oxides: structure, properties, reactions, occurrences and uses*. Weinheim: John Wiley & Sons.
53 Metropolis N, Rosenbluth AW, Rosenbluth MN, Teller AH, Teller E. 1953. Equation of state calculations by fast computing machines. *J Chem Phys*. 21(6):1087–1092.
54 Kirkpatrick S, Gelatt CD, Vecchi MP. 1983. Optimization by simulated annealing. *Science*. 220(4598):671–680.
55 Vanderbilt D, Louie SG. 1984. A Monte Carlo simulated annealing approach to optimization over continuous variables. *J Comput Phys*. 56(2):259–271.
56 Matsumoto M, Nishimura T. 1998. Mersenne Twister: a 623-dimensionally equidistributed uniform pseudo-random number generator. *ACM Trans Model Comput Simul*. 8(1):3–30.
57 Karabin M, Stuart SJ. 2020. Simulated annealing with adaptive cooling rates. *J Chem Phys*. 153(11):114103.
58 Steinhardt PJ, Nelson DR, Ronchetti M. 1983. Bond-orientational order in liquids and glasses. *Phys Rev B*. 28(2):784.
59 Böse H, Rabindranath R, Ehrlich J. 2012. Soft magnetorheological elastomers as new actuators for valves. *J Intel Mater Syst Struct*. 23(9):989–994.
60 Han Y, Hong W, Faidley LE. 2013. Field-stiffening effect of magneto-rheological elastomers. *Int J Solids Struct*. 50(14): 2281–2288.
61 Yang J, *et al*. 2014. A novel magnetorheological elastomer isolator with negative changing stiffness for vibration reduction. *Smart Mater Struct*. 23(10):105023.
62 Puljiz M, *et al*. 2018. Reversible magnetomechanical collapse: virtual touching and detachment of rigid inclusions in a soft elastic matrix. *Soft Matter*. 14(33):6809–6821.
63 Abrougui MM, Lopez-Lopez MT, Duran JDG. 2019. Mechanical properties of magnetic gels containing rod-like composite particles. *Philos Trans R Soc A*. 377(2143):20180218.
64 Allahyarov E, Löwen H, Zhu L. 2015. A simulation study of the electrostriction effects in dielectric elastomer composites containing polarizable inclusions with different spatial distributions. *Phys Chem Chem Phys*. 17(48):32479–32497.
65 Liu B, Shaw MT. 2001. Electrorheology of filled silicone elastomers. *J Rheol*. 45(3):641–657.
66 Burkel B, Notbohm J. 2017. Mechanical response of collagen networks to nonuniform microscale loads. *Soft Matter*. 13:5749–5758.
67 Menon S, Leines GD, Rogal J. 2019. Pyscal: a python module for structural analysis of atomic environments. *J Open Source Softw*. 4(43):1824.
68 Leocmach M. 2017. Pyboo: a python package to compute bond orientational order parameters Pyboo: a python package to compute bond orientational order parameters. https://doi.org/10.5281/zenodo.1066568.

Supplementary material to "Maximized response by structural optimization of soft elastic composite systems"

Lukas Fischer[1] and Andreas M. Menzel[1]

[1] *Institut für Physik, Otto-von-Guericke-Universität Magdeburg, Universitätsplatz 2, 39106 Magdeburg, Germany*

(Dated: August 30, 2024)

In this supplementary material, we present technical details on the adapted algorithm of simulated annealing (SA) that we employ to adjust the internal structure to optimize a requested overall deformational or mechanical response. Particularly, we list our parameter settings for the algorithm. Furthermore, we provide more background information concerning the regular lattice structures to which we compare the performance of our optimized textures. We list corresponding lattice constants and information on how the number of inclusions N is varied.

I. TECHNICAL DETAILS ON OUR COMPUTATIONAL SCHEME

To optimize the deformational or mechanical response of our magnetoelastic actuator systems, we utilize simulated annealing (SA) with adaptive cooling rates. For this purpose, the algorithm in Ref. 1 is adapted to our situation, see also the main text.

At the beginning of each process of optimization, we initialize the positions of the inclusions at random, unless indicated otherwise. One inclusion is randomly selected at a time. To generate a new trial configuration, its position is modified by a displacement randomly chosen in the range of $[-\delta/2, \delta/2)$ for each direction. This marks one Monte Carlo (MC) step [2], where we measure lengths in units of the radius R of the elastic sphere when optimizing the magnetostrictive effect or in units of side length a of the elastic cube when addressing the magnetorheological (MR) effect. The positional constraints mentioned in the main text are obeyed, that is, minimal distances between the inclusions and from the boundary of the elastic sphere/cube are ensured. Every n_{jump} MC steps, we instead generate a completely new trial position for the selected inclusion, still maintaining the positional constraints. Individual positional changes favorable to the optimization are always accepted. Those implying an opposite trend are only accepted with a certain probability, namely $e^{-\Delta u/T}$, if $\Delta u > 0$. Here, T is a temperature-like variable and Δu marks the difference between the new trial configuration and the previous configuration, where $u = \pm u^{\perp}_{20}/R$ or $u = \pm u^{\perp}_{00}/R$ in our case, depending on the deformational mode to be minimized or maximized in the magnetostrictive case. For the optimization of the MR effect, we instead insert $u = \pm\Delta\mu_{rel}$. Since u is dimensionless by definition, T is also introduced in a dimensionless way. Afterwards, we move on to the next MC step, testing for a new trial configuration.

As our optimization is based on SA, we decrease the temperature T during the course of optimization [3]. Our "cooling schedule" starts from an initial temperature $T = T_i$. We equilibrate the system for a period of N_{eq} MC steps at the current temperature T. Afterwards, we use N_{prod} steps to sample a specific heat-like variable

$$C_V = \frac{\langle u^2 \rangle - \langle u \rangle^2}{T^2}, \tag{S1}$$

where $\langle u^2 \rangle$ and $\langle u \rangle$ mark the mean squared and mean values of u, see above. Still, the temperature remains fixed during these N_{prod} MC steps. During the next N_{cool} MC steps of our optimization, we reduce the temperature each time before generating a new trial configuration. We decrease the temperature geometrically, that is we set $T = (1-k)T_{old}$, where T_{old} denotes temperature in the previous MC step and k determines the cooling rate.

In our algorithm, the cooling rate for this period is set depending on the specific heat that was evaluated in the previous N_{prod} steps:

$$k = \begin{cases} k_s, & \text{if } C_V \geq C_V^*, \\ k_f, & \text{if } C_V < C_V^*. \end{cases} \tag{S2}$$

Here, we introduced the notations k_s and k_f for slow and fast cooling rates ($k_s \leq k_f$), respectively, and C_V^* as a characteristic threshold value of the specific heat. Consequently, our idea is to cool the system more slowly when more changes are occurring during the process of measuring the specific heat, thus allowing the system more opportunities to keep changing. Otherwise, the system is cooled faster to speed up the optimization. Together, these $N_{eq} + N_{prod} + N_{cool}$ MC steps denote one period of optimization. The same steps are repeated during the next period. Finally, our routine is stopped when no positional changes have been accepted for a number of *patience* periods (during sampling), or when the temperature has decreased to a predetermined final value of T_f.

To summarize, our scheme makes use of the parameters δ, n_{jump}, T_i, N_{eq}, N_{prod}, N_{cool}, k_s, k_f, C_V^*, *patience*, and T_f. All parameter settings that were utilized for the optimization, leading to the structures depicted in Figs. 2A–C, 3A–C of the main text for $N = 1000$ and $\nu = 0.5$, Figs. 4A,B, 5A,B of the main text for $N = 1000$ and $\nu = 0.3$, Figs. 6A,C and 7A,C of the main text for $N = 200$, are listed in Tab. I.

When turning to other values of the Poisson ratio ν or the number of inclusions N, see subfigures B, C, D,

or E of Figs. 2–7 of the main text, we usually keep most of the parameter settings as in Tab. I. It is, however, necessary to rescale the temperature-like variable in the exponents $e^{-\Delta u/T}$, because the typical magnitudes of deformation entering Δu change with ν and N. For simplicity, we rescale initial and final temperatures equally. Therefore, we define $T_i(\nu, N) = T_i\,\alpha(\nu, N)$ and $T_f(\nu, N) = T_f\,\alpha(\nu, N)$, where $\alpha(\nu, N)$ takes care of the required rescaling. We set $\alpha(0.5, 1000) = 1$ when addressing $\pm u_{20}^{\perp}$, $\alpha(0.3, 1000) = 1$ when addressing $\pm u_{00}^{\perp}$, and $\alpha(0.5, 200) = 1$ when addressing the MR effect. The employed values of α and all other adjusted parameter settings, if different from the values shown in Tab. I, when varying ν and N are listed in Tabs. II–VIII.

	δ/R	n_{jump}	T_i	N_{eq}	N_{prod}	N_{cool}	k_s	k_f	C_V^*	*patience*	T_f
$\min u_{20}^{\perp}$	0.03	200	1.5×10^{-5}	$2\,N$	$8\,N$	$30\,N$	2×10^{-9}	10^{-8}	25	10	5×10^{-8}
$\max u_{20}^{\perp}$	0.05	50	2×10^{-5}	$2\,N$	$8\,N$	$30\,N$	5×10^{-9}	10^{-8}	5	10	10^{-7}
$\min u_{00}^{\perp}$	0.02	100	3×10^{-6}	$2\,N$	$3\,N$	$25\,N$	1.6×10^{-9}	1.6×10^{-9}		100	1.5×10^{-8}
$\max u_{00}^{\perp}$	0.05	50	7×10^{-6}	$2\,N$	$8\,N$	$30\,N$	10^{-9}	2×10^{-9}	10	20	3×10^{-8}
$\max u_{00}^{\perp}$ (alt.)	0.03	100	7×10^{-6}	$2\,N$	$3\,N$	$25\,N$	1.4×10^{-9}	2×10^{-9}	2	20	3×10^{-8}
$\Delta\mu_{rel}$	0.03	100	$1.4 \times 1.5^6 \times 10^{-5}$	$2\,N$	$3\,N$	$25\,N$	2×10^{-9}	4×10^{-9}	1	20	$6 \times 1.5^6 \times 10^{-8}$

TABLE I. Parameter settings in our SA algorithm to minimize or maximize $u_{20}^{\perp}$, $u_{00}^{\perp}$, or $\Delta\mu_{rel}$, see the first column. To minimize $u_{00}^{\perp}$, the parameter C_V^* is arbitrary because we set $k_s = k_f$, see Eq. (S2). To maximize $u_{00}^{\perp}$, the parameters in the third row from the bottom are used. Yet, when varying N (see Tab. VII) we use the alternative parameter settings (alt.) of the second row from the bottom.

For elevated numbers of inclusions N, it is necessary to adjust the initial input configuration to fit all inclusions into the sphere when optimizing the magnetostrictive effect. In that case, we use a face-centered cubic (fcc) initial configuration of hexagonal layers oriented perpendicular to the magnetization direction in an ABC stacking configuration. One inclusion is positioned at the center of the elastic sphere. From there, we construct all layers. All nearest-neighbor distances in the fcc configuration approximate the minimal allowed distance. Then, we randomly delete inclusions from the full fcc configuration until the imposed number of inclusions N is reached. For optimizations of the MR effect, we also start with a simple stacking of hexagonal layers of inclusions oriented perpendicular to the magnetization direction. The bottom layer is placed at a distance of $0.061a$ from the lower boundary of the cube and one inclusion is positioned at the center of the layer, with inclusions in different layers placed above each other (denoted by hexagonal in Tab. VIII). Besides, we also utilize fcc arrangements as starting configurations (denoted by fcc in Tab. VIII), similarly to the simple stacking of hexagonal layers, however, with fcc featuring an ABC stacking. (As a remark we add that we never observed a decrease in performance after applying our scheme of optimization when compared to the performance of the initial configuration.)

Furthermore, all optimizations are performed starting from 8 different initializations of the employed random number generator Mersenne Twister [4], leading to comparable results. Deviations in the results are at most of the order of the symbol sizes in the presented figures. Among these, we always selected those configurations of most competitive performance when plotting Figs. 2–7 of the main text.

ν	α
0.5	1
0.3	1.03
0	1.17
−0.5	1.94

TABLE II. Parameter settings in our SA algorithm when minimizing $u_{20}^{\perp}$ for different values of the Poisson ratio ν, leading to the results in Fig. 2D of the main text.

N	α	initialization
1000	1	random
1250	1.25	random
1500	1.5	random
1750	1.5	fcc
2000	1.5	fcc

TABLE III. Parameter settings in our SA algorithm when minimizing $u_{20}^{\perp}$ for different inclusion numbers N, leading to the results in Fig. 2E of the main text.

ν	α	C_V^*
0.5	1	5
0.45	1.01	5
0.4	1.08	5
0.35	1.19	5
0.3	4/3	5
0	2.57	5
−0.5	6.77	2

TABLE IV. Parameter settings in our SA algorithm when maximizing $u_{20}^{\perp}$ for different values of the Poisson ratio ν, leading to the results in Fig. 3D of the main text.

N	α	initialization
1000	1	random
1250	1.25	random
1300	1.3	random
1350	1.35	random
1400	1.4	random
1450	1.45	random
1500	1.5	random
1750	1.5	fcc
2000	1.5	fcc

TABLE V. Parameter settings in our SA algorithm when maximizing $u_{20}^{\perp}$ for different inclusion numbers N, leading to the results in Fig. 3E of the main text.

N	α	initialization
500	0.5	random
650	0.65	random
800	0.8	random
1000	1	random
1250	1.25	random
1500	1.5	random
1750	1.75	fcc
2000	2	fcc
2100	0.995	fcc
2200	0.936	fcc
2300	0.867	fcc
2400	0.788	fcc

TABLE VI. Parameter settings in our SA algorithm when minimizing $u_{00}^{\perp}$ for different inclusion numbers N, leading to the results in Fig. 4C of the main text.

N	α	initialization
1000	1	random
1250	1.25	random
1500	1.5	random
1750	1.75	fcc
2000	2	fcc

TABLE VII. Parameter settings in our SA algorithm when maximizing $u_{00}^{\perp}$ for different inclusion numbers N, leading to the results in Fig. 5C of the main text.

N	α	initialization
150	0.75	random
200	1	random
250	1.25	random
300	1.5	random
350	1.75	random
400	2	hexagonal
450	2.25	hexagonal/fcc (uniaxial elongation, max.)
500	2.5	hexagonal/fcc (uniaxial elongation, max.)

TABLE VIII. Parameter settings in our SA algorithm when maximizing the magnitude of the MR effect $\Delta\mu_{rel}$ for different inclusion numbers N, leading to the results in Figs. 6B,D and Figs. 7B,D of the main text.

II. DETAILS ON THE REGULAR LATTICES TO WHICH WE COMPARE OUR OPTIMIZED STRUCTURES

In the main text, we compared the performance of our optimized configurations to those resulting from more regular arrangements. The latter were constructed artificially, guided by the optimized textures. In the following, we include details on the employed regular structures, first for the studies on magnetostrictive effects, then for the studies on magnetorheological (MR) effects.

A. Regular lattice structures for comparison with optimized magnetostrictive effects

We begin by minimizing $u_{20}^{\perp}$. The performance of our optimized structures in Figs. 2D,E of the main text is compared to results obtained for more regular textures. Specifically, these were regular structures consisting of hexagonally arranged chain-like aggregates. To construct them, we start from layers of hexagonally positioned inclusions. Their normal vectors coincide with the magnetization direction (z-direction). To maximize the magnetic repulsion within each hexagonal layer, we approach the minimal allowed inclusion distance by setting the lattice constant to $0.121R$. The distance between neighboring layers is set to an identical value of $0.121R$. Inclusions within nearest-neighboring layers are located above and below each other, so that they form chains. For simplicity, we anchor the lattices by placing one first inclusion at the center of the sphere and by building up the lattice from there. For a regular arrangement of $N = 1001$ inclusions (to be compared to the optimized structure for $N = 1000$), we confine ourselves to the 11 innermost layers. Moreover, we only consider inclusions that are located within a distance of $\rho = 0.62R$ from that center axis of the sphere oriented parallel to the magnetization direction. The resulting deformations characterized by $u_{20}^{\perp}$ for this configuration and for different values of the Poisson ratio ν are displayed in Fig. 2D of the main text.

To accommodate increasing numbers of inclusions N

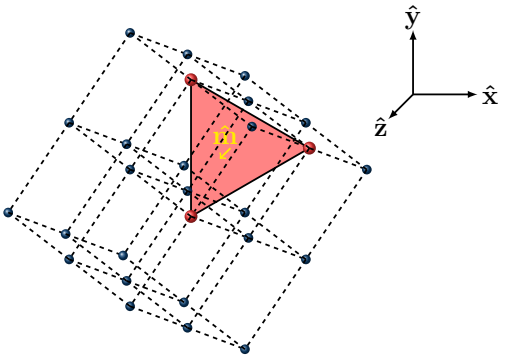

FIG. S1. To best approximate the deformational response of the optimized structure for maximal relative elongation $u_{20}^{\perp}$, we identified a simple cubic lattice. Here, we illustrate its orientation. The normal vector of the plane indicated in red coincides with the magnetization direction $\hat{\mathbf{m}}$ (by construction).

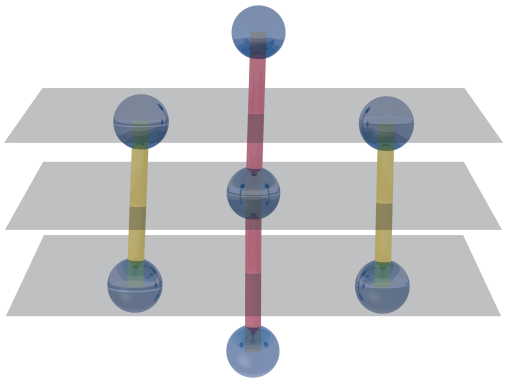

FIG. S2. Configurations that maximize the decrease in volume, minimizing $u_{00}^{\perp}$, see Fig. 4A of the main text, contain chain-like elements along the magnetization direction. Here, we illustrate the typical nearest-neighbor structure of these chains, where inclusions in neighboring chains are vertically shifted relative to each other by about one half (vertical) nearest-neighbor distance.

we increase ρ. Moreover, we slightly shift the regular arrangements of inclusions homogeneously along the magnetization direction by a distance Δz. We observe that the optimized structures do not feature a layer exactly in the middle of the sphere. Indeed, through numerical trials with different values of Δz the performance was increased further. Appropriate numbers n_+ and n_- of layers above and below the center of the sphere, respectively, are determined by numerical trials as well to further optimize the deformational response. For $N = 1001$, 1308, 1482, 1771, 1988, we use values of $\rho/R = 0.62$, 0.65, 0.73, 0.78, 0.84, $\Delta z/R = 0$, 0.043, 0.019, 0.005, 0.019, $n_+ = 5$, 6, 6, 7, 7, and $n_- = 5$, 6, 6, 6, 7, respectively. Corresponding results for $u_{20}^{\perp}$ are shown in Figs. 2D,E of the main text.

Next, when maximizing $u_{20}^{\perp}$ (see Fig. 3 of the main text), we identified a simple cubic (sc) lattice to best approximate the optimized structures. As in the previous case, a lattice constant of $0.121R$ is employed. The orientation of this regular structure provides additional degrees of freedom to improve its performance. We start from an sc lattice for which the lattice vectors coincide with the coordinate axes of our Cartesian coordinate system, the z-direction again indicating the magnetization direction. Then, a global rotation is applied to this lattice. We found a rotation by a rotation matrix

$$\underline{\mathbf{R}} = \begin{pmatrix} \sqrt{\frac{2}{3}} & -\sqrt{\frac{1}{6}} & -\sqrt{\frac{1}{6}} \\ 0 & \sqrt{\frac{1}{2}} & -\sqrt{\frac{1}{2}} \\ \sqrt{\frac{1}{3}} & \sqrt{\frac{1}{3}} & \sqrt{\frac{1}{3}} \end{pmatrix} \tag{S3}$$

to approximately lead to best performance. It sets a rotation by a rotation angle of about 56.6° around the axis $\left((\sqrt{3}-1)(\sqrt{2}-1)+1,\ -1,\ \sqrt{2}-1\right)$. The resulting orientation is illustrated in Fig. S1.

We again place the first inclusion at the center of the sphere. Furthermore, to set the number of inclusions, we only include lattice positions within a distance r from the center. We use $r/R = 0.747$, 0.81, 0.82, 0.83, 0.85, 0.86, 0.88, 0.9, 0.94 to obtain $N = 1021$, 1237, 1309, 1357, 1419, 1503, 1575, 1743, 1935, respectively. The resulting performance for $u_{20}^{\perp}$ is depicted in Figs. 3D,E of the main text. In the latter figure, we also display results for a face-centered cubic (fcc) configuration of $r/R = 0.84$. There, the edges of the cubic unit cells are oriented along the axes of our Cartesian coordinate system, leading to $N = 1985$. In that case, we likewise use a nearest-neighbor distance of $0.121R$.

Third, we optimize $u_{00}^{\perp}$, starting with its minimization, see Fig. 4C of the main text. In that case, we use regular chain-like structures with a vertical shift of neighboring chains by half the inter-inclusion distance along each chain, as was similarly observed for the optimized structures, see Fig. S2. The lateral arrangement of these chains in the optimized structure is mostly irregular. For our regular structures, we arrange the chains in a square lattice. The corresponding lattice constant is set to approximately $0.108R$. We construct the configuration starting from a chain that runs through the center of the sphere. The center is located symmetrically between the two innermost inclusions on that chain. As in the previous case, we use a radial cut-off distance r from the center of the sphere to adjust the number of inclusions N. We set $r/R = 0.55$, 0.6, 0.65, 0.7, 0.75, 0.8, 0.84, 0.878, 0.89, 0.907, 0.92, 0.932 to obtain $N = 494$, 654, 798, 1024, 1240, 1502, 1742, 2006, 2094, 2206, 2296,

2392, respectively.

Next, we compare the results for textures of maximized $u_{00}^{\perp}$, see Fig. 5C of the main text, to the performance of regular configurations of inclusions. To this end, we arrange the inclusions in 11 layers of orientation normal to the magnetization direction. Within each layer, the inclusions are hexagonally organized, with a distance between nearest neighbors of $0.121R$. The textures are constructed starting from one inclusion at the center of the sphere. In this case, however, the inter-layer spacing l is always chosen larger than $0.121R$. Thus, nearest neighbors are found within the layers, not along the magnetization direction. By adjusting l and only keeping inclusions that are located within our constraints inside the sphere, we change the number of inclusions N. Setting $l/R = 0.27$, 0.22, 0.18, 0.155, 0.126 leads to $N = 1021$, 1239, 1517, 1745, 1973, respectively.

B. Regular lattice structures for comparison with optimized magnetorheological effects

Similarly, we construct by hand regular lattice structures, the performance of which we compare to our optimized ones that maximize the MR effect as described in the main text for an elastic cubical system. In general, the optimized structures guide us to the particular parameters used for our constructed regular lattice structures. In this way, the latter are adapted to the former.

For the positive MR effect, maximizing $\Delta\mu_{rel}$ for uniaxial elongation, see Figs. 6A,B of the main text, we utilize an fcc arrangement (ABC stacking of hexagonal layers) with a lattice constant of $0.121a$, where a is the side length of the elastic cube. The bottommost hexagonal layer when viewed along the magnetization direction is always inserted at $0.1a$ from the bottom surface of the cube. The lattice is anchored by placing an inclusion at the center of the cube. A cut-off value ρ for the lateral distance of an inclusion from the center axis of the cube oriented parallel to the magnetization direction is set to tune the number of inclusions. Here, the value of ρ is chosen per layer, adapted from the optimized structures, generally decreasing the numbers of inclusions in the topmost and bottommost layers when compared to the other layers. For example, for $N = 201$ inclusions (for comparison to the optimized structures of $N = 200$), we use $\rho = 0.2a$ for the topmost and bottommost layers and $\rho = 0.35a$ for another 6 layers in between, resulting in a total of 8 layers. We also generate fcc configurations of 255, 300, 354, 399, 449, 497 inclusions, here always using 9 layers of varying ρ. The layer distance is chosen such that an fcc lattice of lattice constant $0.121a$ results.

When instead maximizing the positive MR effect for simple shear deformations, see Figs. 6C,D of the main text, textures consisting of hexagonally structured layers with their normals oriented along the direction of the shear displacements are introduced. The same lattice constant as above is used. This time, for each layer an inclusion is placed on that center axis of the cube that is oriented along the direction of shear displacements. The number of layers and locations of layers are adapted from the optimized configurations. We alternately select opposite sides from one layer to the next with respect to the central shear plane. Approximately, our procedure consists of cutting inclusions from these sides, starting from maximal distance from the central shear plane. We observe such asymmetric features in the optimized structures, see Fig. 6D of the main text. This procedure leads to $N = 187$, 291, 347, 402, 448, 499 inclusions organized in 4, 5, 6, 6, 7, 8 layers, respectively. In the last two cases, we use an alternating AB stacking of the layers to fit all inclusions into the cube.

Turning to the less frequently considered negative MR effect, we first consider the case of uniaxial elongation of the cube in the main text, see Figs. 7A,B. Neighboring chains forming when optimizing the structures are vertically shifted with respect to each other, similarly to what is displayed in Fig. S2. We generally use a square lattice arrangement of these chains for simplicity, as its performance shows good agreement in the resulting negative MR effect. For comparison, for $N = 180$ we also arrange 24 chains on a circle of radius $0.42a$, showing a magnitude of the negative MR effect in line with the trend of corresponding square lattice arrangements of the chains. We shift the inclusions in neighboring chains vertically by half of the nearest-neighbor distance in a single chain ($0.121a$). Their lateral distance is chosen such that neighboring inclusions from different chains have the same total distance from each other of $0.121a$. Therefore, each inner inclusion on a chain has two nearest neighbors on the same chain and two more per neighboring chain, for a total of up to 10 nearest neighbors. To tune the inclusion numbers of the square lattice arrangements of the chains, we selectively delete chains, leading to arrangements of $N = 150$, 203, 248, 301, 346, 398, 450, 503 with 20, 27, 33, 40, 46, 53, 60, 67 chains, respectively. The chains for deletion are selected by comparison to the optimized structures, which are displayed as the insets in Fig. 7B of the main text, approximately such that the square lattice of chains has a gap in the middle. Results for these square lattice arrangements as well as the one circular arrangement of the chains mentioned above for $N = 180$ are presented in Fig. 7B of the main text (chain-like config.). The data point for $N = 180$ of circular arrangement of the chains is highlighted by the black circular mark.

Lastly, we turn to the negative MR effect under simple shear deformations, see Figs. 7C,D of the main text. The resulting optimized structures in that case are similar to the ones for the positive MR effect under simple shear. However, the layers here are oriented parallel to the plane of simple shear. Furthermore, as can be inferred from Fig. 7C of the main text, the layers do not consist of regular hexagons anymore. Instead, they resemble a centered rectangular lattice, with the longer edge along the magnetization direction. We choose $0.146a$ for the edge length along the direction of shear displacements and

$0.194a$ for the edge length along the magnetization direction. Again, we set the numbers and locations of the layers as inferred from the optimized structures. To restrict the number of inclusions in each layer, we use a cut-off value ρ for the lateral distances of the inclusions from that center axis that is oriented perpendicular to the shear plane, similar to the maximization of $\Delta\mu_{rel}$ for uniaxial elongation (in contrast to the rather diagonal reduction in Fig. 7C of the main text). Here, ρ is chosen for each layer again by comparison to the optimized structures. For example, we observe that the optimized structures for $N = 200$ inclusions feature a center layer (see the leftmost inset of Fig. 7D of the main text) with fewer inclusions compared to the other layers. Therefore, we choose a smaller value for ρ for that layer. In this way, we obtain $N = 203$, 248, 297, 347, 399, 450, 497 with 5, 6, 7, 7, 7, 8, 9 layers, respectively. For $N = 497$, we use an alternating AB stacking of the layers.

[1] M. Karabin and S. J. Stuart, Simulated annealing with adaptive cooling rates, J. Chem. Phys. **153**, 114103 (2020).
[2] N. Metropolis, A. W. Rosenbluth, M. N. Rosenbluth, A. H. Teller, and E. Teller, Equation of state calculations by fast computing machines, J. Chem. Phys. **21**, 1087 (1953).
[3] S. Kirkpatrick, C. D. Gelatt, and M. P. Vecchi, Optimization by simulated annealing, Science **220**, 671 (1983).
[4] M. Matsumoto and T. Nishimura, Mersenne Twister: a 623-dimensionally equidistributed uniform pseudo-random number generator, ACM T. Model. Comput. S. **8**, 3 (1998).

P6 Analytical expressions for the two basic modes of surface displacement and overall deformation of a free-standing or elastically embedded sphere

Reproduced from

L. Fischer and A. M. Menzel,
Analytical expressions for the two basic modes of surface displacement and overall deformation of a free-standing or elastically embedded sphere,
arXiv:2407.09291 (2024).

Digital Object Identifier (DOI): `https://doi.org/10.48550/arXiv.2407.09291`

Statement of contribution

Both authors contributed to this work. I performed all calculations and wrote the initial draft for sections II–VIII. AMM wrote the initial draft for abstract, introduction, and conclusions. Both authors revised the manuscript. I estimate my contribution to this work during my PhD as 95 %.

Copyright and license notice

P7 Variations in the thermal conductivity of magnetosensitive elastomers by magnetically induced internal restructuring

Reproduced from

G. J. L. Jäger, L. Fischer, T. Lutz, and A. M. Menzel,
Variations in the thermal conductivity of magnetosensitive elastomers by magnetically induced internal restructuring,
J. Phys.: Condens. Matter **34**, 485101 (2022).

Digital Object Identifier (DOI): `https://doi.org/10.1088/1361-648X/ac98e8`

Statement of contribution

All authors contributed to this work. The initial idea was proposed by AMM and discussed by GJLJ, LF, and AMM. GJLJ performed the numerical evaluations, collected the data and prepared all figures. I helped with and thoroughly checked the numerical implementation. All authors discussed the results. I was involved in editing the final version of the manuscript. I also supervised the project jointly with AMM. I estimate my contribution to this work during my PhD as 10 %.

Copyright and license notice

OPEN ACCESS
IOP Publishing
Journal of Physics: Condensed Matter
J. Phys.: Condens. Matter **34** (2022) 485101 (14pp)
https://doi.org/10.1088/1361-648X/ac98e8

Variations in the thermal conductivity of magnetosensitive elastomers by magnetically induced internal restructuring

Gustav J L Jäger, Lukas Fischer, Tyler Lutz and Andreas M Menzel*

Institut für Physik, Otto-von-Guericke-Universität Magdeburg, Universitätsplatz 2, 39106 Magdeburg, Germany

E-mail: a.menzel@ovgu.de

Received 12 August 2022, revised 29 September 2022
Accepted for publication 10 October 2022
Published 20 October 2022

Abstract

Magnetosensitive elastomers respond to external magnetic fields by changing their stiffness and shape. These effects result from interactions among magnetized inclusions that are embedded within an elastic matrix. Strong external magnetic fields induce internal restructuring, for example the formation of chain-like aggregates. However, such reconfigurations affect not only the overall mechanical properties of the elastomers but also the transport through such systems. We concentrate here on the transport of heat, that is thermal conductivity. For flat, thin model systems representing thin films or membranes and modeled by bead-spring discretizations, we evaluate the internal restructuring in response to magnetization of the particles. For each resulting configuration, we evaluate the associated thermal conductivity. We analyze the changes in heat transport as a function of the strength of magnetization, particle number, density of magnetizable particles (at fixed overall particle number), and aspect ratio of the system. We observe that varying any one of these parameters can induce pronounced changes in the bulk thermal conductivity. Our results motivate future experimental and theoretical studies of systems with magnetically tunable thermal but also electric conductivity—both of which have only rarely been addressed so far.

Keywords: magnetosensitive elastomers, thermal conductivity, magnetically induced restructuring

(Some figures may appear in colour only in the online journal)

* Author to whom any correspondence should be addressed.

1. Introduction

Magnetosensitive elastomers are materials comprised of magnetizable inclusions embedded in an elastic carrier matrix [1–6]. The latter is usually a rubber or gel. Applying homogeneous external magnetic fields, the materials respond by changes in their overall properties. Most prominently, their stiffness and damping behavior, quantified in terms of static and dynamic mechanical moduli are affected [1, 6–12]. Similarly, shape changes occur in general, which is termed magnetostriction [13–17]. Both types of reaction illustrate how the materials sense magnetic variations in their environment. Possible applications therefore comprise tunable damping devices [18–20] and soft actuators [21–23], which are capable of a wider range of motion, such as jumping, walking, and rolling. Highly elastic magnetosensitive elastomers therefore are promising materials in soft robotics [20].

On a more microscopic level, an external magnetic field induces interactions between the magnetized inclusions. These interactions cause the inclusions to exert forces on and thus deform their elastic environment. Under sufficiently strong magnetic forces, the inclusions can substantially reorganize and rearrange themselves by deforming the elastic carrier matrix. For example, for two nearby particles, mutual attraction leading to their collapse towards virtual contact has been analyzed both theoretically [24–27] and experimentally [27]. Magnetically induced deformations and buckling of initially straight, chain-like aggregates were observed [28]. Specifically important for our considerations is internal restructuring leading to the formation of chains, which, likewise, have been reported in theoretical [11, 29, 30] and experimental [10, 31] studies. This effect has been correlated with changes in the elastic Young modulus of the materials of nearly an order of magnitude [10].

In the present work, we focus on the tunability of transport properties of such materials by external magnetic fields. Specifically, we concentrate on variations of heat transport through the system, as quantified by thermal conductivity.

Ferromagnetic fluids, a related class of materials composed of colloidal suspensions of magnetic particles in a carrier liquid, have been shown to exhibit increased thermal conductivity along the direction of an externally applied magnetic field and no changes in the conductivity in the direction perpendicular to the applied field [32, 33]. The change in thermal conductivity is reversible and decreases quickly once the magnetic field is turned off. Magnetic elastomers or gels designed to behave similarly in response to external fields could find medical application as a potentially biocompatible elastic carrier matrix. Compared to ferromagnetic fluids, soft elastic solids are generally more convenient to handle—requiring no container to hold them in place—and may be less susceptible to evaporation.

While there has been some research into the electrical conductivity of magnetosensitive elastomers, investigations focusing on thermal conductivity are still rarer. When homogeneous external magnetic fields are applied already during the curing process, chain-like aggregates form and are permanently imprinted in the materials [1, 34, 35]. The stronger the magnetic field during fabrication, the lower in general is the electric resistance [36–38]. Moreover, the chains can be separated or reconnected by stretching or compressing the material, which alters the electrical conductivity.

Thermal conductivity has been measured for a composite of carbonyl iron and agar [39]. There, again, the inclusions were aligned by an external magnetic field during curing, while stronger magnetic field amplitudes lead to larger thermal conductivity. The largest increase of thermal conductivity due to alignment was around 30% measured for a mass fraction of 10% carbonyl iron particles. Increasing the mass fraction of carbonyl iron increases thermal conductivity.

While there is some research on the electrical conductivity the main focus has been on materials with an already imprinted chain structure. However, in highly elastic elastomers and especially gels, these chains can also form when applying an external magnetic field after the curing process [29]. Here, the aim is studying the effect of this internal restructuring on the thermal conductivity.

In contrast to these works on prestructured materials, we here focus on systems that initially contain rather random arrangements of the magnetizable particles. We consider internal restructuring into anisotropic, mainly chain-like aggregates when external magnetic fields are applied. To this end, a coarse-grained bead-spring model is evaluated in two dimensions [11, 30]. We thus focus on the behavior of thin elastic films and membranes of magnetosensitive elastomers. In the restructured state under the influence of the external magnetic field, the change in thermal conductivity is evaluated as a function of the achieved magnetization of the magnetizable particles, their average distance, the overall particle number, and the aspect ratio of the rectangular system. Substantial tunability of the thermal conductivity is revealed.

We proceed as follows. In section 2, we present our theoretical model equations. Appropriate parameter values are selected in section 3. We describe how we evaluate the thermal conductivity in section 4. Our results for the variation of thermal conductivity as a function of the parameters mentioned above are provided in section 5. We conclude in section 6.

2. Bead-spring model for magnetosensitive elastomers

Our coarse-grained minimal model describes a mesh of springs with magnetizable beads connected to some of its nodes. The spherical beads represent the magnetizable inclusions and include the magnetic interactions [29], while the springs represent the elastic material behavior [40].

We start from a hexagonal network. During initialization, the position of each node is shifted by a random value chosen from a normal distribution of standard deviation of 10% of the lattice parameter $2d_c$. Then, N_m nodes are selected to associate to them the N_m magnetizable beads. We place springs between any two nodes that are closer than 1.5 times the lattice parameter. An example system is depicted in figure 1. The top and bottom layers are not counted to the total amount of nodes, as

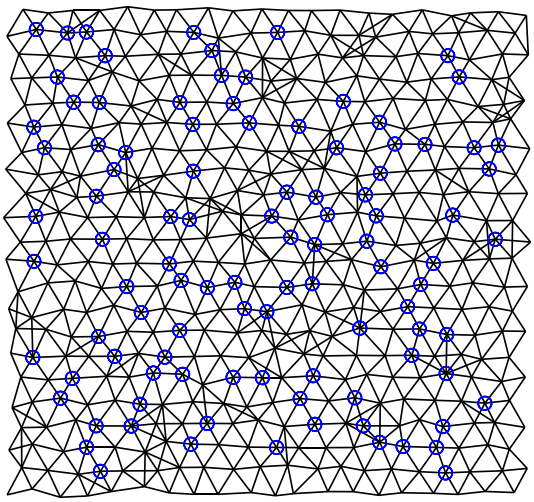

Figure 1. Example of a randomized hexagonal spring network with initial shifts of the nodes by a normal distribution of standard deviation of $0.2d_c$, a lattice parameter $2d_c$, and a maximum spring length of $3d_c$. Springs (black lines) connect the nodes and magnetizable beads (blue circles) are randomly associated to the nodes. This example system features 20×20 nodes and 100 magnetizable beads.

they are not used in the calculation of the thermal conductivity (see below).

Between any two nodes i and j of positions $\boldsymbol{r}_i$ and $\boldsymbol{r}_j$, respectively, the distance vector is defined via $\boldsymbol{r}_{ij} = \boldsymbol{r}_i - \boldsymbol{r}_j$. Out of a total amount of nodes N, there are a number of N_m magnetizable particles, all of diameter d_c. With the spring constant k, the elastic interaction potential is given by

$$U_{el} = \frac{1}{2}\sum_{\langle i,j\rangle} k\left(|\boldsymbol{r}_{ij}| - |\boldsymbol{r}_{ij,0}|\right)^2. \tag{1}$$

In this expression, $\langle i,j\rangle$ includes only pairs of nodes that are connected by springs, while $\boldsymbol{r}_{ij,0}$ sets the spring length in the undeformed state.

In the magnetized state, we always assume the external magnetic fields strong enough to approximately induce the saturation magnetization of magnitude M_S in the magnetizable particles. In homogeneous external magnetic fields and for monodisperse particles, an identical magnetic dipole moment $\boldsymbol{m}$ arises for each particle, so that

$$|\boldsymbol{m}| = m = M_S\frac{\pi}{6}d_c^3. \tag{2}$$

As a result, we obtain the magnetic interaction potential [41]

$$U_m = \frac{\mu_0}{4\pi}\frac{1}{2}m^2\sum_{\substack{i,j=1\\ i\neq j}}^{N_m}\frac{r_{ij}^2 - 3(\hat{\boldsymbol{m}}\cdot\boldsymbol{r}_{ij})^2}{r_{ij}^5}, \tag{3}$$

where $\hat{\boldsymbol{m}} = \boldsymbol{m}/m$, $r_{ij} = |\boldsymbol{r}_{ij}|$, and μ_0 is the magnetic vacuum permeability.

Finally, the steric interaction potential between the beads is assumed as a modified version of the Weeks–Chandler–Andersen potential [11, 42]

$$U_s = \sum_{\substack{i,j=1\\ i\neq j}}^{N_m}\Theta(d_c - r_{ij})\varepsilon_s\left[\left(\frac{r_{ij}}{\sigma^s}\right)^{-12} - \left(\frac{r_{ij}}{\sigma^s}\right)^{-6}\right. \tag{4}$$

$$\left. - \left(\frac{d_c}{\sigma^s}\right)^{-12} + \left(\frac{d_c}{\sigma^s}\right)^{-6} - \frac{c(r_{ij}-d_c)^2}{2}\right]. \tag{4}$$

Here, Θ denotes the Heaviside step function, while $\sigma^s = 2^{-1/6}d_c$ and $c = 18/d_c^2$ depend on the exponents of U_s, in this case -6 and -12. Since U_s is always 0 if $|\boldsymbol{r}_{ij}| > d_c$, it is necessary to ensure a smooth transition and subsequent differentiability at $|\boldsymbol{r}_{ij}| = d_c$. That means σ^s and c are chosen so that $dU_s/dr_{ij}|_{r_{ij}=d_c} = 0$ and $d^2U_s/dr_{ij}^2|_{r_{ij}=d_c} = 0$ are satisfied. ε_s sets the magnitude of the steric interaction.

To determine the new restructured states when magnetized, we assume overdamped dynamics of the nodes. For the equation of motion, combining $U = U_{\mathrm{el}} + U_m + U_s$, we then obtain

$$\frac{d\boldsymbol{r}_i}{dt} = -\frac{1}{\zeta}\boldsymbol{\nabla}_i U, \tag{5}$$

with a damping coefficient ζ set equal for all nodes. $\boldsymbol{\nabla}_i$ refers to the derivative with respect to the position of node i and t denotes time. As indicated above, we confine ourselves to two-dimensional evaluations representing thin sheets or membranes of magnetosensitive elastomers.

3. Rescaling of the basic equations and setting the system parameters

For the outlined description to represent real systems, it is necessary to choose appropriate values for the parameters. To find the actual number of independent parameters, we first rescale the equations in section 2 and then set realistic parameter values.

First, measure lengths in units of the diameter d_c of the magnetizable particles. Thus, distances become $r'_{ij} = r_{ij}/d_c$. Energies are rescaled by kd_c^2, so that equations (1), (3) and (4) become

$$U'_{\mathrm{el}} = \frac{1}{2}\sum_{\langle i,j\rangle}^{N}\left(\boldsymbol{r}'_{ij} - \boldsymbol{r}'_{ij,0}\right)^2, \tag{6}$$

$$U'_m = \frac{1}{2}\frac{\mu_0 m^2}{4\pi k d_c^5}\sum_{\substack{i,j=1\\ i\neq j}}^{N_m}\frac{r_{ij}'^2 - 3(\hat{\boldsymbol{m}}\cdot\boldsymbol{r}'_{ij})^2}{r_{ij}'^5}, \tag{7}$$

and

$$U'_s = \frac{\varepsilon_s}{kd_c^2}\sum_{\substack{i,j=1\\ i\neq j}}^{N_m}\Theta(1-r'_{ij})\left[\left(\frac{r'}{\sigma^{s\prime}}\right)^{-12} - \left(\frac{r'}{\sigma^{s\prime}}\right)^{-6}\right. \tag{8}$$

$$\left. - \left(\frac{1}{\sigma^{s\prime}}\right)^{-12} + \left(\frac{1}{\sigma^{s\prime}}\right)^{-6} - \frac{c'(r'_{ij}-1)^2}{2}\right]. \tag{8}$$

Here, $\sigma^{s'} = 2^{-1/6}$ and $c' = 18$. Moreover, time is rescaled by ζ/k, so that equation (5) reads

$$\frac{d\boldsymbol{r}_i'}{dt'} = -\boldsymbol{\nabla}_i' U'. \tag{9}$$

Thus, time becomes $t' = tk/\zeta$ with an incremental time step $\tau' = \tau k/\zeta$ that we use to discretize equation (9) when we iterate it forward in time.

Now, there are only two dimensionless parameters remaining in equations (7) and (8) that control the system behavior. However, the role of the coefficient $\varepsilon_s' = \varepsilon_s/kd_c^2$ in equation (8) for our purposes is simply to ensure sufficient volume exclusion of the particles. It is chosen large enough so that magnetized beads are generally not overlapping and low enough so that numerical stability is maintained. This leaves us with only one actual remaining system parameter, namely

$$\Gamma = \frac{\mu_0 m^2}{4\pi k d_c^5} = \frac{\pi \mu_0 M_s^2}{36\sqrt{3} b E_{3D}}. \tag{10}$$

in equation (7), where E_{3D} is the Young modulus for three-dimensional systems. This scaled squared magnetic moment describes the relative strength of the magnetic versus the elastic interactions. To provide realistic results, this coefficient is approximated in the following on the basis of typical experimental data.

First, the saturation magnetization of carbonyl iron particles is around $M_s = 2 \times 10^6\,\mathrm{Am}^{-1}$ [11, 43]. Average diameters for volume equivalent spheres of these particles reported in the literature are, for example, $d_c = 34\ \mu$m for 15 wt % and 28 μm for 40 wt % samples [11].

The magnitude of the spring constant k for the spring network should reflect the magnitude of the elastic modulus of the underlying elastic material. In two dimensions (2D) it was shown that the Young modulus satisfies [44]

$$E_{2D} = \frac{4\mu(\lambda+\mu)}{\lambda+2\mu}, \tag{11}$$

with λ and μ being the Lamé constants [44, 45]. The corresponding calculations were performed for uniaxial strain and stress. For a triangular lattice, the relation to the spring constant was found to be [44, 46]

$$\mu = \lambda = \frac{3}{4\sqrt{3}}k. \tag{12}$$

Equations (11) and (12) are based on the hexagonal unit cell, see figure 2, of edge length b (in units of the bead diameter d_c) equal to the undeformed spring length. In the corresponding calculations these cells were assumed to have a thickness of $b/2$ [46]. It follows with the respective units of E_{3D} and E_{2D} as Nm^{-2} and Nm^{-1} that the relation between the three dimensional Young modulus E_{3D} and E_{2D} is

$$E_{2D} = \frac{b}{2} d_c E_{3D}. \tag{13}$$

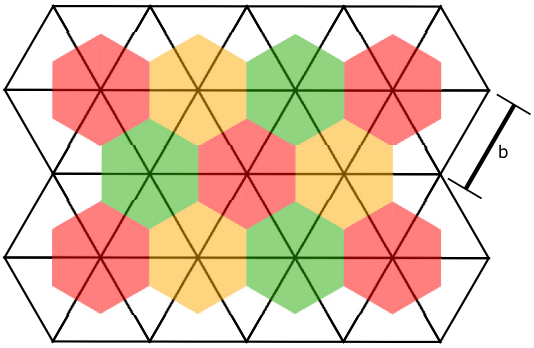

Figure 2. Regular hexagonal unit cells underlying the spring network to extract the relation between the spring constant k and the Young modulus E_{3D} [46]. b denotes the length of the springs in units of the bead diameter d_c.

Combining equations (11)–(13), we find

$$\frac{b}{2} d_c E_{3D} = \frac{2}{\sqrt{3}} k. \tag{14}$$

This relation, together with equation (2), justifies the second equality in equation (10). The typical Young modulus is of the order of magnitude 10 kPa for a magnetic elastomer [10] and 1 Pa for a soft magnetic gel [28].

The Poisson ratio for elastic materials that are quantitatively described by the spring network is 1/3 [44, 46]. This means that our spring network represents a compressible medium. Different Poisson ratios can be achieved if angular interactions are added at the nodes connecting the springs [44, 46].

As we can see, the spring length b (in units of d_c) enters the expression for the remaining parameter Γ in equation (10). We will therefore include it into our considerations below. We approach b from the mass fraction φ of magnetizable particles in the medium, which we select as silicone rubber to set the associated parameter values [44].

We choose, for instance in figure 2, a unit cell with a node at the center that carries a magnetizable bead. As above, we assume the thickness of the sheet to be of size $bd_c/2$. Thus, we obtain the following expression for the mass fraction using the volume $\pi d_c^3/6$ of the magnetizable bead and the volume $\sqrt{3}b^3 d_c^3/4$ of the unit cell,

$$\begin{aligned}\varphi &= \frac{m_m}{m_{\mathrm{total}}} \\ &= \frac{N_m \rho_m \pi/6}{Nb^3\,\rho_{\mathrm{silicone}}\sqrt{3}/4 + N_m(\rho_m - \rho_{\mathrm{silicone}})\pi/6}.\end{aligned} \tag{15}$$

From there, we find together with $\rho_{\mathrm{silicone}} = 970\,\mathrm{kg\,m}^{-3}$ [47] and $\rho_m = 7800\,\mathrm{kg\,m}^{-3}$ [48],

$$b \approx \left[\frac{N_m}{N}\left(\frac{9.72}{\varphi} - 8.51\right)\right]^{1/3}. \tag{16}$$

A sufficiently large number of magnetizable particles N_m is necessary to facilitate chain formation upon magnetization. We therefore set the overall number ratio of beads and nodes $\frac{N_m}{N}$ within the range of 25% and 50%. An approximate mass fraction φ from around 10% to 25% then implies a range of b from around 2 to 3.5.

4. Evaluation of the thermal conductivity

For each configuration and parameter setting, we iterate equation (9) forward in time using an Euler forward integration scheme until a steady state is reached. We then evaluate the thermal conductivity of the resulting configuration.

From the heat flux

$$\boldsymbol{q} = -\lambda_{\mathrm{loc}} \boldsymbol{\nabla} T, \tag{17}$$

where T is the local temperature and λ_{loc} denotes thermal conductivity [49], together with the conservation equation of thermal energy

$$\rho c \frac{dT}{dt} = -\boldsymbol{\nabla} \cdot \boldsymbol{q}, \tag{18}$$

where ρ is the (mass) density and c the specific heat capacity [50], we obtain the thermal diffusion equation

$$\frac{dT}{dt} = \frac{\lambda_{\mathrm{loc}}}{\rho c} \nabla^2 T = a \nabla^2 T, \tag{19}$$

with $a = \lambda_{\mathrm{loc}}/\rho c$ representing the thermal diffusivity [50].

The thermal conductivity of silicone can be found in the literature as $\lambda_{\mathrm{silicone}} = 0.2\,\mathrm{W\ m^{-1}K^{-1}}$ [51], its density as $\rho_{\mathrm{silicone}} = 970\,\mathrm{kg\ m^{-3}}$ [47], and its specific heat capacity as $c_{\mathrm{silicone}} = 1250\,\mathrm{J kg^{-1}K^{-1}}$ [52]. The values for the magnetizable beads are chosen for iron carbonyl powder. We assume a density of $\rho_m = 7800\,\mathrm{kg\,m^{-3}}$ [48], a thermal conductivity of $\lambda_m = 80.4\,\mathrm{W\ m^{-1}K^{-1}}$ [53], and a specific heat capacity of $c_m = 460\,\mathrm{J kg^{-1}K^{-1}}$ [39]. This leads to thermal diffusivities of $a_{\mathrm{silicone}} = 1.6495 \times 10^{-7}\,\mathrm{m^2\ s^{-1}}$ and $a_m = 2.2408 \times 10^{-5}\,\mathrm{m^2\ s^{-1}}$, respectively.

To evaluate equation (19) in our situation, we employ an appropriate discretization of our system. We start from the nodes of our spring network and obtain discrete cells around them using a Voronoi tessellation [54]. We identify the temperature of each Voronoi cell with the temperature at the node that it contains. On this basis, we evaluate the heat flux between neighboring cells as described in the following. Corresponding quantities are introduced in figure 3.

Using Gauß' theorem, we obtain from equation (19) for the ith cell of 'volume' V_i

$$\int_{V_i} \frac{dT}{dt} d^3 r = \int_{\partial V_i} a \hat{\boldsymbol{n}} \cdot \boldsymbol{\nabla} T d^2 f, \tag{20}$$

where $\hat{\boldsymbol{n}}$ denotes the outward normal unit vector. Next, we assume constant temperature T_i within the ith cell. According to equations (19) and (20), heat exchange with all cells $\langle i \rangle$ neighboring the ith cell can then be discretized as

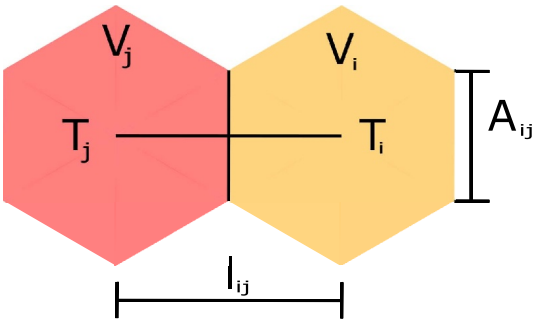

Figure 3. Quantities used for the discretization to calculate the heat conduction between neighboring cells i and j are their 'volumes' V_i and V_j, respectively, absolute temperatures T_i and T_j, respectively, absolute contact 'area' A_{ij} of the unit cells, and absolute distance l_{ij} between the central nodes.

$$\frac{dT_i}{dt} = \frac{1}{V_i} \sum_{\langle i \rangle} A_{ij} a_{ij} \frac{T_j - T_i}{l_{ij}}. \tag{21}$$

Here, a_{ij} is the thermal diffusivity between cells i and j, A_{ij} is their contact 'area', and l_{ij} is their distance, see figure 3. Thus, we find

$$\frac{dT_i}{dt} = \frac{1}{V_i \rho_i c_i} \sum_{\langle i \rangle} A_{ij} \lambda_{ij} \frac{T_j - T_i}{l_{ij}}. \tag{22}$$

Since this equation represents a discretized version of the heat equation, we expect conservation of heat, which we have confirmed in our numerical evaluations as described below.

To calculate the overall thermal conductivity, we induce an overall heat flux through the system. For this purpose, the temperatures of the boundary nodes on the left- and right-hand sides are fixed at T_{left} and T_{right}, respectively. Under these boundary conditions, the temperatures of all other nodes, here identified with the temperatures of the corresponding Voronoi cells, can then be found by iterating equation (22) forward in time. When a steady state is reached, the temperatures of all cells are constant in time, $dT_i/dt = 0$. This leaves us with

$$0 = \sum_{\langle i \rangle} A_{ij} \lambda_{ij} \frac{T_i - T_j}{l_{ij}}. \tag{23}$$

Equation (23) can be rewritten as a vector equation for all Voronoi cells as

$$\boldsymbol{0} = \boldsymbol{A}_{vc} \cdot \boldsymbol{T}_c + \boldsymbol{A}_{vv} \cdot \boldsymbol{T}_v, \tag{24}$$

where $\boldsymbol{T}_c$ is the vector of all temperatures of the boundary cells that are kept constant. The vector $\boldsymbol{T}_v$ contains all temperatures of the inner cells. The entries of the matrices $\boldsymbol{A}_{vv}$ and $\boldsymbol{A}_{vc}$ are extracted from the coefficients in equation (23). In fact, they constitute the negative discretized Laplacian operator for a graph with weighted edges [55]. We then calculate the temperature of each cell by solving equation (24) for $\boldsymbol{T}_v$,

$$\boldsymbol{T}_v = -\boldsymbol{A}_{vv}^{-1} \cdot \boldsymbol{A}_{vc} \cdot \boldsymbol{T}_c. \tag{25}$$

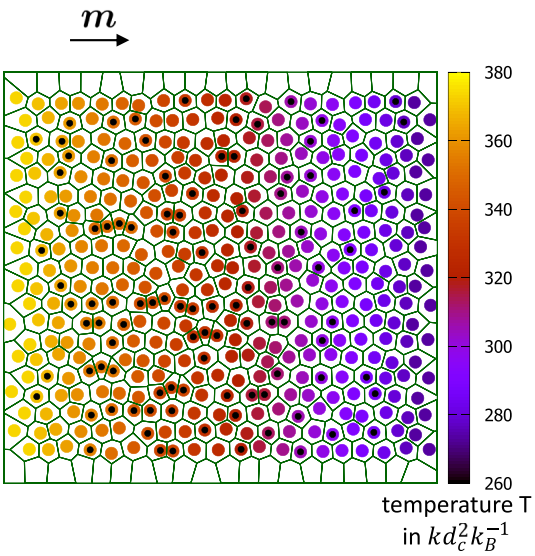

Figure 4. Heat conduction through a magnetized example bead-spring system of 20×20 nodes. Those nodes carrying magnetic beads are marked by black dots. Only little chain formation of magnetized beads has occurred in this case through the induced magnetic moments $\boldsymbol{m}$ oriented as indicated. Cell boundaries around the nodes as obtained from Voronoi tessellation are depicted by the dark lines. The temperature of each cell is indicated by the color scheme according to the scale on the right-hand side. (k_B denotes the Boltzmann constant.)

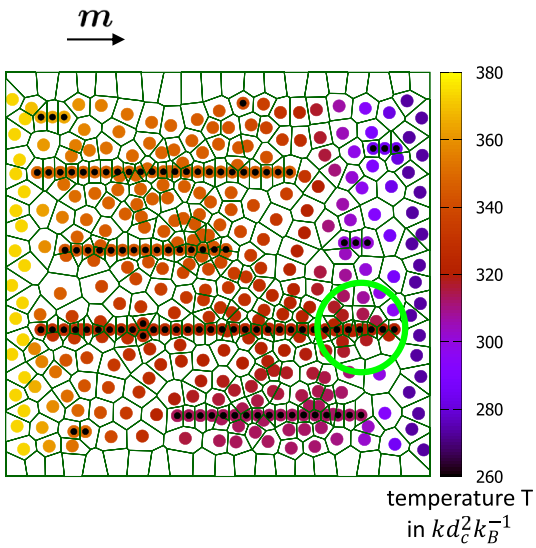

Figure 5. Same as in figure 4, but for a system of substantial chain formation. The bright green circle outlines a region where the Voronoi cells around several nodes not carrying magnetizable beads are wedged between cells containing magnetizable beads. Still the surrounding beads are considered as being in contact due to their proximity.

In equation (23), the thermal conductivity λ_{ij} is set to $\lambda_{\text{silicone}}$ by default. It is only altered to λ_m, when both cells i and j hold magnetized beads that are virtually in contact. Two beads are considered as being in contact when they are at most a center-to-center distance of $1.04\,d_c$ apart from each other. This corresponds to additional 4% of the effective steric radius and approximately corresponds to the magnitude of the numerical fluctuations observed for touching particles under strong magnetization. For illustration two examples for a system of 20×20 nodes are displayed in figures 4 and 5. Here and in the following, we induce the magnetic dipole moments $\boldsymbol{m}$ along the negative overall temperature gradient.

A special situation occurs when two magnetized beads are in contact but their Voronoi cells are not neighbors. Then, thermal conductivities involving the Voronoi cells $\langle o \rangle$ obstructing the connection will also be set to $\lambda_{\langle o \rangle i} = \lambda_{\langle o \rangle j} = \lambda_m$. This situation can occur when a cell not containing any magnetizable bead is wedged between two magnetized particles, see the configuration marked by a bright green circle on the right-hand side of the longest chain in figure 5.

The upper and lower rows of Voronoi cells in these figures do not contribute to the total amount of nodes N. They are excluded from the calculation of the thermal conductivity. Rather, they serve as purely auxiliary nodes to construct all Voronoi cells.

To now calculate the overall thermal conductivity of the entire system, we determine the total heat transported per time through a cross section A cutting through the whole sample perpendicular to the overall temperature gradient. We check that this transferred heat is identical through any cross section. The latter is required by conservation of thermal energy. Denoting by $\langle A; i,j \rangle$ all pairs of cells whose contact 'areas' A_{ij} together form the cross sectional 'areas' A, the total heat flux is calculated via

$$q_{\text{total}} = \frac{1}{A} \left| \sum_{\langle A; i,j \rangle} A_{ij} \lambda_{ij} \frac{T_i - T_j}{l_{ij}} \right|. \tag{26}$$

At the same time, the overall thermal conductivity λ is defined via

$$q_{\text{total}} = \lambda \frac{|T_{\text{left}} - T_{\text{right}}|}{l}, \tag{27}$$

where l is the averaged distance between the left and right boundary nodes. Combining equations (26) and (27), the overall thermal conductivity can be calculated as

$$\lambda = \frac{l \left| \sum_{\langle A; i,j \rangle} A_{ij} \lambda_{ij} \frac{T_i - T_j}{l_{ij}} \right|}{A \, |T_{\text{left}} - T_{\text{right}}|}. \tag{28}$$

The cross section A is averaged as well. q_{total} is calculated for as many cross sections as possible to verify conservation of heat.

Calculating l and A, averaging l and A, assuming a roughly rectangular shape of the system, and initially randomizing the placement of the nodes [56] all contribute to the error when determining λ. In our tests, we observed errors up to 6.1%, which is tolerable within the framework of our discussion.

We measure all thermal conductivities in units of $\lambda_{\text{silicone}}$ in order to highlight the relative change in conductivity due to magnetization, which in the initial system approximately equals $\lambda_{\text{silicone}}$ by construction. Moreover, along these lines we eliminate the unit of thermal conductivity $k_B k/d_c\zeta$, which contains the unknown damping coefficient ζ.

5. Results

Using the implementation as described above, we evaluate the magnetically induced changes in overall thermal conductivity when we vary the scaled squared magnetic moment Γ, see equation (10), the average spring length b, the total number of magnetizable particles N_m, and the aspect ratio of the considered rectangular systems. In all cases, we magnetize the system from the initial, nonmagnetized state upon each change in the mentioned parameters. The internally restructured state is identified and the thermal conductivity is evaluated for each parameter setting separately. Additionally, we correlate the observed changes in overall thermal conductivity with the size of the generated chain-like clusters. We also briefly address the dynamics when the magnetization is turned on and off again.

5.1. Dependence on the relative strength of magnetic interactions Γ

We begin by considering the dependence of the overall thermal conductivity λ on the scaled squared magnetic moment Γ, see equation (10). For systems of $N_m = 150$ magnetizable beads randomly associated to the $N = 400$ nodes, we display in figure 6 results averaged over 50 realizations of the system (blue). A substantial increase of the overall thermal conductivity by a factor of approximately 4 is observed in a range of Γ that still corresponds to realistic parameter values. The averaged curve shows a nearly monotonic increase with Γ.

For one selected example system, we additionally show in figure 6 the dependence of the overall thermal conductivity as a function of the strength of magnetic interactions Γ (red). Associated snapshots illustrate the formation of the aggregates with increasing Γ for this specific example. It demonstrates the tendency of increasing integration of magnetizable beads into chain-like structures when Γ rises. Naturally, the increasing magnetic interactions facilitate this reorganization against the restoring elastic spring forces. For sufficiently large values of Γ almost all magnetized beads are parts of large clusters and thus the thermal conductivity basically reaches saturation.

The sample system we depict in red is typical in that its thermal conductivity does not increase monotonically in Γ. This nonmonotonicity is the result of two distinct effects. First, with increasing Γ, beads that are in virtual contact increasingly overlap. The employed steric interaction potential is not perfectly hard and the steric interaction parameter $\varepsilon_s' = 100$ is finite. This overlap leads to an effective decrease in chain length when further increasing Γ. In reality, such effects may be observed if still some remaining soft material remains between the mechanically hard particles, for instance, for coated particles and/or absorbed polymer chains on their surfaces. Specific examples are provided by particles that serve as crosslinkers of the systems [57, 58]. A slight decrease in thermal conductivity may be associated with these effects, to which we attribute the gradual tapering off of λ in the high-Γ regime.

Second, the more pronounced steps of decrease on the red curve for the individual system in figure 6 can be of dynamic origin. We illustrate a corresponding scenario on a small example system of only $N_m = 12$ particles in figure 7.

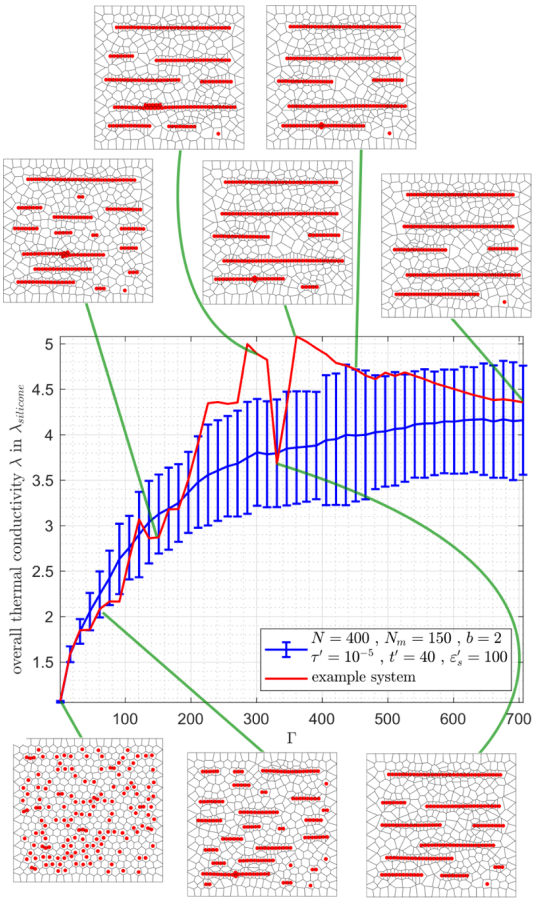

Figure 6. Overall thermal conductivity λ as a function of the scaled squared magnetic moment Γ averaged over 50 different realizations (blue line) of the system for 20×20 nodes, $N = 400$, $N_m = 150$, $b = 2$, $\tau' = 10^{-5}$, and $\varepsilon_s' = 100$, at $t' = 40$. Standard deviations are marked by bars. Snapshots with the magnetizable particles in red and the Voronoi cells depicted in black are taken from one randomly selected example of the 50 systems. For that specific realization, we show the corresponding evolution of λ with increasing Γ as the red line.

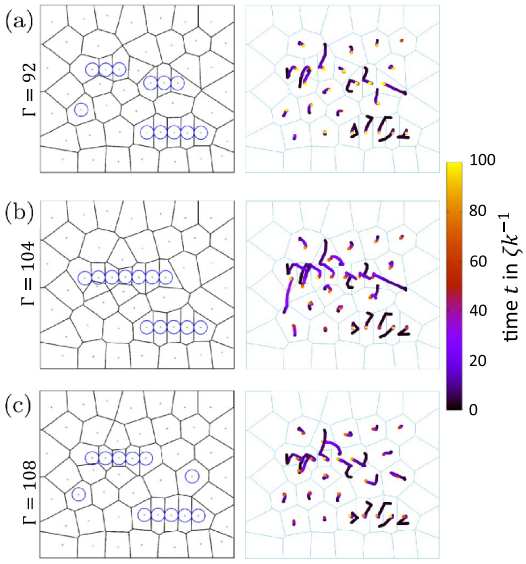

Figure 7. For illustration, we consider a small example system of $N_m = 12$ magnetizable beads. The panels on the left-hand side show the final states upon chain formation for different strengths of magnetic interaction (a) $\Gamma = 92$, (b) $\Gamma = 104$, and (c) $\Gamma = 108$. In these snapshots, blue spheres represent the magnetized beads and the black mesh corresponds to the boundaries of the Voronoi cells. Associated panels on the right-hand side depict the trajectories of the individual nodes, where brightening colors represent progression in time.

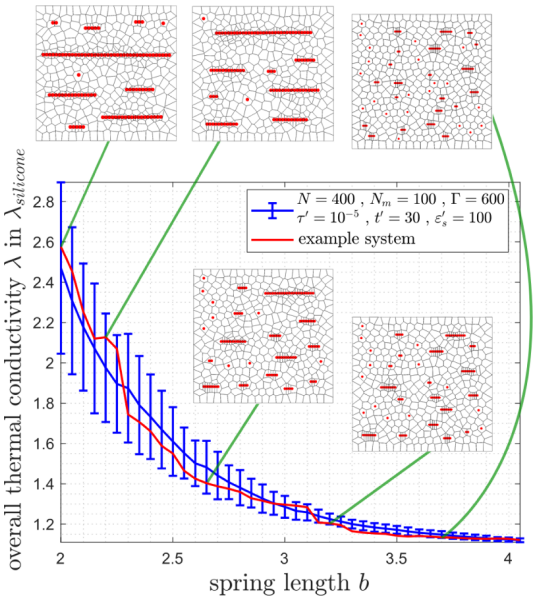

Figure 8. Overall thermal conductivity λ as a function of the relative spring length b (measured in units of the bead diameter d_c) averaged over 50 realizations of the system of 20×20 nodes for $N = 400$, $N_m = 100$, $\Gamma = 600$, $\tau' = 10^{-5}$, and $\varepsilon_s' = 100$, at $t' = 30$. Snapshots for one randomly selected realization with the magnetizable beads indicated in red and the Voronoi cells depicted in black are included as insets.

In figure 7(a), for $\Gamma = 92$, smaller chains of 3 magnetized beads form, besides one remaining separate bead and another chain of 5 beads, leading to an overall thermal conductivity of $\lambda = 1.62\lambda_{\text{silicone}}$. Further aggregation is prevented as the necessary magnetic interactions cannot overcome the prevailing elastic interactions. These elastic interactions are partially overcome when the magnetic interactions are increased to $\Gamma = 104$, see figure 7(b), when significantly longer chains of 5 and 7 beads form. As a consequence, the thermal conductivity increases to $\lambda = 2.07\lambda_{\text{silicone}}$. However, at still larger $\Gamma = 108$ in figure 7(c), the overall thermal conductivity again drops to a lower value of $\lambda = 1.71\lambda_{\text{silicone}}$. This lower value is correlated with on average two shorter chains of only 5 beads and two remaining separated beads.

To understand this behavior, we recall that, for each value of Γ, the system is initiated in a nonmagnetized state. Then the beads are magnetized. The speed of the subsequent dynamics increases with Γ. For $\Gamma = 108$, quicker contraction implies that the outer beads cannot follow the quick displacement of the inner beads when the upper chain in figure 7(c) is formed. This is different for the slower dynamics in figure 7(b) for lower Γ. The more separated structures in figure 7(c) correlate with a reduced overall thermal conductivity for $\Gamma = 108$ when compared to $\Gamma = 104$. The two separate particles remain separated because the distances to the other particles are too large and thus the magnetic attractions are too weak to overcome the elastic counterforces. Thus, on the side, we conjecture that the protocol of introducing the magnetization can influence the resulting internal structure. It may thus represent another means of tailoring the resulting thermal conductivity.

As can be inferred from the right panel for $\Gamma = 108$ in figure 7(c), the separated magnetizable bead on the right-hand side even turns around while the aggregation dynamics is in progress. This happens at the time when the upper and lower chains form quickly and the particles within the quickly formed chains are already too far apart to induce significant attraction.

In contrast to that, the averaged curve for a larger system size in figure 6 does not exhibit any sharp elevations in thermal conductivity any more. While there are some nonmonotonic intervals, there are not any significant spikes outside the given standard deviation.

5.2. *Impact of the average scaled spring length* b

First, we recall that the initial spring network corresponds to a randomized hexagonal arrangement. Therefore, we refer to the averaged spring length b in this system. Second, b is measured in units of d_c and thus represents a relative, dimensionless parameter. The relation between b and the mass fraction φ was given in equation (16).

Figure 8 displays the overall thermal conductivity as a function of the spring length b when averaged over 50 different realizations of the system at an elevated magnitude of magnetization. All other parameters, including the total number of magnetizable particles and aspect ratio of the systems are kept fixed. The decrease in thermal conductivity for increasing relative spring length b is apparent.

The reason for this decrease is inferred from the snapshots added as insets in figure 8 for one specific example realization. For lower values of b, corresponding to increased densities of the magnetizable particles, the system is able to form elongated chain-like clusters. Due to the small initial distances between the magnetized beads, mutual magnetic interactions are strong and the elastic counterforces are easily overcome. We recall that the strength of magnetic dipole interaction scales as the inverse cubic interparticle distance, see equation (3). With increasing relative spring length b, the average initial distance between nearest neighboring beads is larger and the same magnetic moment may not be sufficient any longer to induce cluster formation. This effect is clearly visible from the insets in figure 8 corresponding to an elevated spring length b.

5.3. Dependence on the number of magnetizable particles N_m

Along analogous lines as above, figure 9 displays the overall thermal conductivity λ as a function of the number of magnetizable particles N_m, while all other parameters remain fixed. The curve displays some nonmonotonic steps, see also the discussion in section 5.1, yet well within the range of the standard deviations. Thus, as a general trend, the thermal conductivity rises with increasing numbers of magnetizable particles as expected. The snapshots in figure 9 taken for one specific example realization illustrate that generally the lengths of the formed chain-like aggregates increases with increasing N_m, which supports overall heat transport through the system.

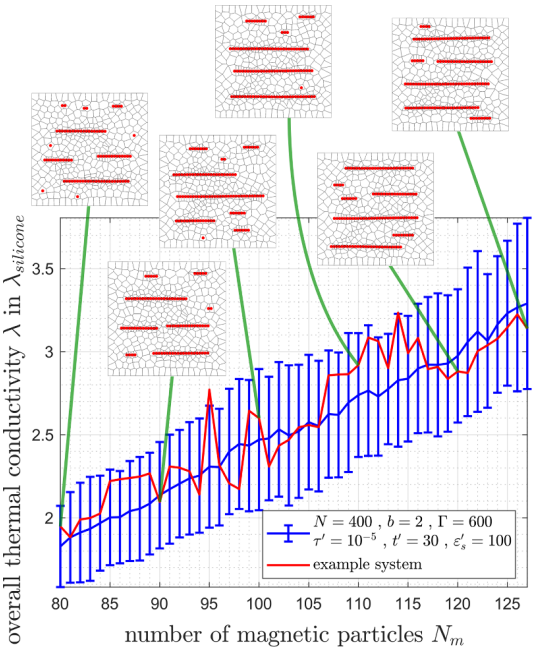

Figure 9. Overall thermal conductivity λ as a function of the number N_m of magnetizable particles averaged over 50 realizations of systems of 20×20 nodes for $N = 400$, $b = 2$, $\Gamma = 600$, $\tau' = 10^{-5}$, and $\varepsilon_s' = 100$, at $t' = 30$. As insets, we include snapshots for one randomly chosen system, where we indicate the magnetizable beads in red and the boundaries of the Voronoi cells in black.

5.4. Effect of the aspect ratio

All the data in sections 5.1–5.3 were obtained for initially square-like systems of 20×20 nodes. To get an impression of the relevance of this shape, we vary the aspect ratio to other rectangular contours. Figure 10 depicts selected example systems of (a) 40×10 nodes (longest system), (b) 25×16 nodes (long system), (c) 20×20 nodes (square system), (d) 16×25 nodes (wide system), and (e) 10×40 nodes (widest system). The remaining parameter values were all kept identical in the different situations.

The overall thermal conductivities for systems elongated along the overall thermal gradient are displayed in figure 11, where for each aspect ratio we again average over 50 different realizations. There, the values of the overall thermal conductivity are virtually the same as in the square system. However, their standard deviation substantially increases with elongated systems. Since the systems are slimmer perpendicular to the direction of magnetization, in some individual systems an exceptionally long chain-like aggregate forms. Such individual occurrences significantly increase the thermal conductivity and thus the standard deviation.

In contrast to that, figure 12 shows results for systems that are initially wider perpendicular to the magnetization direction. For wider aspect ratios, the averaged overall thermal conductivity decreases, but remains within the standard deviation. Since the systems are shorter along the magnetization direction, the maximum length of the chain-like aggregates is reduced.

5.5. Correlation with the average cluster size

In addition, we correlate the magnetically induced changes in the overall thermal conductivity λ with the average size of the formed chain-like clusters. To this end, we reconsidered the above examples of square-shaped systems and the averages over 50 realizations as displayed in figures 6, 8, and 9, that is, for increasing strength of magnetic interaction Γ, relative spring length b, and total number of magnetizable beads N_m, respectively. The size of a cluster is defined as the total number of beads that are in virtual contact with each other. The average cluster sizes were obtained by first averaging

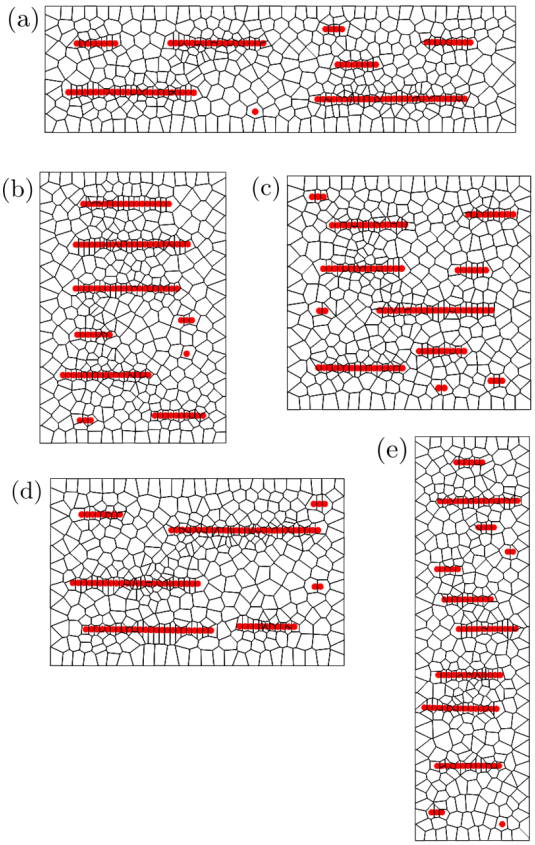

Figure 10. Example systems of different aspect ratios but otherwise identical parameter settings. Specifically, we address systems of (a) 40×10 nodes (longest system), (b) 25×16 nodes (long system), (c) 20×20 nodes (square system, see sections 5.1–5.3), (d) 16×25 nodes (wide system), and (e) 10×40 nodes. The snapshots show the systems in the magnetized state for scaled squared magnetic moment $\Gamma = 600$, relative spring length $b = 2$, number of magnetizable particles $N_m = 100$, strength of steric interactions $\varepsilon_s' = 100$, and incremental timestep $\tau' = 10^{-5}$ at $t' = 30$.

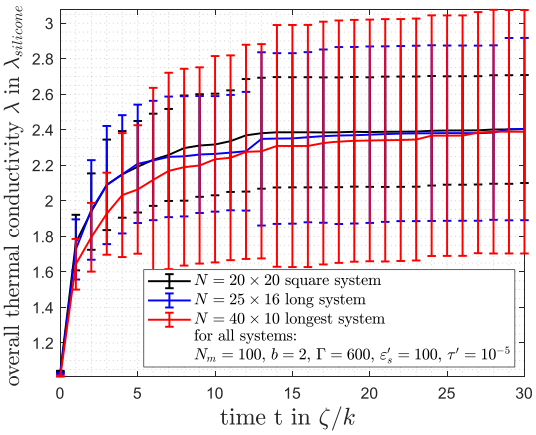

Figure 11. Overall thermal conductivity λ as a function of time for initially square-shaped systems and systems initially elongated along the magnetization direction. Again, we average over 50 different realizations for each aspect ratio.

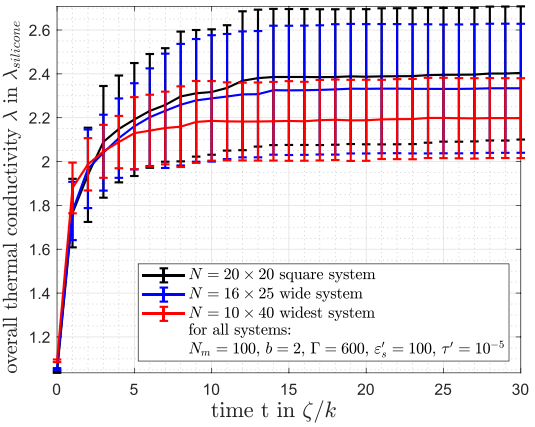

Figure 12. Overall thermal conductivity λ as a function of time for initially square-shaped systems and systems initially shorter along the magnetization direction, averaged over 50 different realizations for each aspect ratio.

the sizes of all clusters in each realization and subsequently over the 50 different realizations. Associated standard deviations depicted below are associated with the second averaging step.

Our results are summarized by figure 13. In all cases, an increase in average cluster size is related to an increase in thermal conductivity. The average cluster size and thus the thermal conductivity increases with increasing scaled squared magnetic moment Γ, see figure 13(a), decreasing relative spring length b, see figure 13(b), and increasing total number of magnetizable particles N_m, figure 13(c).

We add a remark concerning the leveling slope of the curve in figure 13(a) at elevated strengths of magnetic interactions Γ. This effect is partially linked to imperfections that arise during the magnetically induced aggregation. The clusters do not necessarily feature a perfect chain-like structure, as illustrated on the example in figure 14. First, when a shorter chain approaches a longer chain obliquely from the side, the shorter chain may laterally dock and attach to the longer one. Due to the magnetic attraction within the longer chain, the smaller chain is prevented from being absorbed into the longer chain. Examples are displayed in figure 14 as marked by the green circles. Second, two longer chain-like clusters may connect while partially overlapping side by side. A corresponding resulting structure is depicted in figure 14 as marked by the blueish circle.

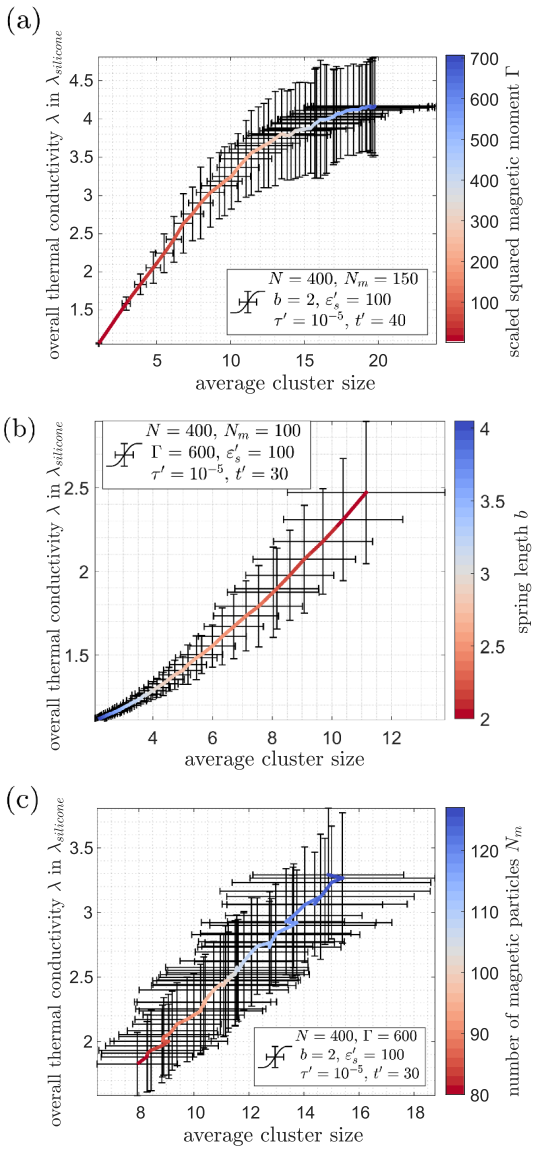

Figure 13. Correlation between the average size of the formed chain-like clusters and the magnetically induced change in overall thermal conductivity λ. Results are shown for increasing (a) scaled squared magnetic moment Γ, (b) relative spring length b, and (c) total number of magnetizable particles N_m, see the color codes on the right-hand sides. Again, we average over 50 realizations of each system. The data correspond to our results in figures 6, 8, and 9, respectively.

5.6. Dynamical aspects when switching on and off the magnetization

Our basic dynamic equations equation (5) in our investigation serve to find the final static state upon magnetization. In this simplified form, they are not suited to quantitatively extract details of the underlying dynamic processes themselves. Nevertheless, a simple qualitative insight is provided.

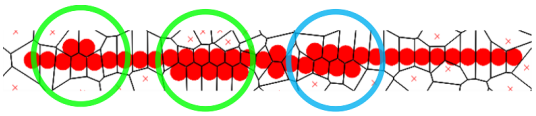

Figure 14. Snapshot of a chain-like cluster formed upon magnetization. It contains two types of imperfections. One type refers to smaller chain-like aggregates attached to the side, as marked by the left two (greenish) circles. The other type implies imperfectly joined chains that partially overlap, as marked by the right (blueish) circle. (Parameter settings: 20×20 nodes, $\Gamma = 600$, $b = 1.7$, $N_m = 200$, $\varepsilon_s' = 100$, $\tau' = 10^{-5}$, $t' = 30$.)

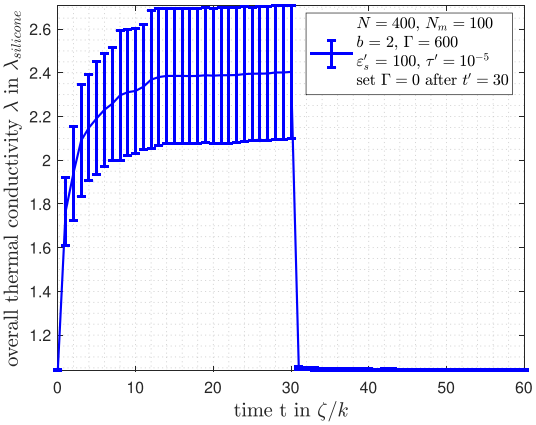

Figure 15. Overall thermal conductivity λ as a function of time when averaged over 50 realizations of a system of 20×20 nodes. Magnetization is induced at $t = 0$, while it is switched off again at $t = 30\zeta/k$.

Figure 15 displays the time evolution of the overall thermal conductivity when at $t = 0$ the beads are magnetized to $\Gamma = 600$, while at $t = 30\zeta/k$ their magnetization is switched off again.

Interestingly, it takes a while until the saturation value of the thermal conductivity is reached, while it quickly drops towards zero when magnetization is switched off. The longer initial procedure can be explained by the coarsening process when the large chain-like clusters form upon magnetization. Initially formed smaller clusters need to migrate collectively as larger objects to assemble into larger chain-like structures over time. In contrast to that, when the magnetization drops to zero, each particle individually is driven by the restoring elastic forces to find back into a separated arrangement.

6. Conclusions

In this work, we analyzed the magnetically induced changes of thermal conductivity in thin films or membranes of magneto-sensitive elastomers. To this end, we employed a simple yet

effective bead-spring model. Magnetizable inclusions are represented by spherical beads randomly placed on the nodes of a randomized hexagonal spring network. The latter represents the underlying elastic interactions in the material.

Upon magnetization, depending on the strength of the induced magnetic interactions relative to the mechanical stiffness, internal restructuring occurs. Particularly, chain-like particle aggregates form. We determine the changes in overall thermal conductivity resulting from the internal restructuring. The rearrangement of the magnetizable particles can lead to a substantial increase of thermal conductivity along the magnetic field direction.

Along these lines, we studied the consequences of varying the scaled squared induced magnetic moments of the beads, the lengths of the springs forming the elastic network, the number of magnetizable particles, and the aspect ratio of the rectangular network structure. Individual systems may display nonmonotonic behavior when altering one of the aforementioned quantities. Yet, the behavior generally smoothens out on average.

Increasing the scaled squared magnetic moment, which relates the strength of the magnetic interactions to the elastic stiffness, causes an increase in thermal conductivity associated with increasing lengths of the chain-like aggregates, until a saturation level is reached. Conversely, an increasing spring length, which is related to the volume fraction of magnetizable particles, causes the thermal conductivity to drop, while the overall system size increases. For a low spring length, large clusters form, with an increased amount of imperfections in the chain-like structure. In that case, the distances between the magnetizable particles are so small that the resulting modified dynamics counteracts proper alignment in perfect particle chains. Generally, an increase in the volume fraction of magnetizable particles causes an increase in thermal conductivity, while we have not observed a substantial effect of the aspect ratio. We further supported our results by relating the variations of thermal conductivity as induced by changes in the mentioned parameters to changes in the averaged cluster size. A qualitative consideration of the dynamics of the system indicates that cluster formation and the associated increase in thermal conductivity upon magnetization occur significantly slower than cluster dissociation and decrease of thermal conductivity when the particles are demagnetized.

In future investigations, the discretization into a spring network and the associated Voronoi tessellation into discrete cells could be refined. Specifically, individual particles could be represented by multiple Voronoi cells of higher thermal conductivity. Additionally, the bead diameters could be varied to represent conditions of polydisperse particle distributions. The influence of the magnetization protocol on the resulting structures and thermal conductivity should be analyzed. Besides, in nonuniform magnetic fields, additional translational forces emerge. Finally, the description so far has only addressed thin flat systems, representing thin films and membranes of magnetosensitive elastomers. Extensions to three-dimensional systems appear desirable.

Overall, we hope that our study will further motivate investigations on the promising magnetically tunable transport properties of magnetosensitive elastomers. So far, some studies on the electric conductivity [36–38] and a few on the thermal conductivity [39, 59] have been reported for these materials. Both on the experimental and on the theoretical side, a lot of future work is still in order to fully understand the resulting types of behavior. This includes microscopic aspects of thermal coupling between individual polymer chains and the particle surfaces. The results will be important both from a fundamental and applied perspective.

Data availability statement

The data that support the findings of this study are presented as data points in the figures and are available upon reasonable request from the authors. The data that support the findings of this study are available upon reasonable request from the authors.

Acknowledgments

The authors thank the German Research Foundation (Deutsche Forschungsgemeinschaft, DFG) for support of this work through the SPP 1681 via Project No. ME 3571/3-3 (G J L J, L F) and through the Research Grant No. ME 3571/5-1 (T L). A M M acknowledges support by the DFG through the Heisenberg Grant No. ME 3571/4-1.

ORCID iDs

Gustav J L Jäger https://orcid.org/0000-0002-4002-5259
Lukas Fischer https://orcid.org/0000-0002-8462-3517
Tyler Lutz https://orcid.org/0000-0001-9811-007X
Andreas M Menzel https://orcid.org/0000-0003-0713-4979

References

[1] Filipcsei G, Csetneki I, Szilágyi A and Zrínyi M 2007 Magnetic field-responsive smart polymer composites *Adv. Polym. Sci.* **206** 137–89
[2] Odenbach S 2016 Microstructure and rheology of magnetic hybrid materials *Arch. Appl. Mech.* **86** 269–79
[3] Weeber R, Hermes M, Schmidt A M and Holm C 2018 Polymer architecture of magnetic gels: a review *J. Phys.: Condens. Matter* **30** 063002
[4] Auernhammer G K 2019 Magnetorheological gels in two and three dimensions: understanding the interplay between single particle motion, internal deformations and matrix properties *Arch. Appl. Mech.* **89** 153–65
[5] Menzel A M 2019 Mesoscopic characterization of magnetoelastic hybrid materials: magnetic gels and elastomers, their particle-scale description and scale-bridging links *Arch. Appl. Mech.* **89** 17–45
[6] Bastola A K, Paudel M, Li L and Li W 2020 Recent progress of magnetorheological elastomers: a review *Smart Mater. Struct.* **29** 123002
[7] Jolly M R, Carlson J D and Munoz B C 1996 A model of the behaviour of magnetorheological materials *Smart Mater. Struct.* **5** 607

[8] Jolly M R, Carlson J D, Muñoz B C and Bullions T A 1996 The magnetoviscoelastic response of elastomer composites consisting of ferrous particles embedded in a polymer matrix *J. Intell. Mater. Syst. Struct.* **7** 613–22
[9] Böse H and Röder R 2009 Magnetorheological elastomers with high variability of their mechanical properties *J. Phys.: Conf. Ser.* **149** 012090
[10] Schümann M and Odenbach S 2017 *In-situ* observation of the particle microstructure of magnetorheological elastomers in presence of mechanical strain and magnetic fields *J. Magn. Magn. Mater.* **441** 88–92
[11] Pessot G, Schümann M, Gundermann T, Odenbach S, Löwen H and Menzel A M 2018 Tunable dynamic moduli of magnetic elastomers: from characterization by x-ray micro-computed tomography to mesoscopic modeling *J. Phys.: Condens. Matter* **30** 125101
[12] Morillas J R and de Vicente J 2020 Magnetorheology: a review *Soft Matter* **16** 9614–42
[13] Metsch P, Kalina K A, Spieler C and Kästner M 2016 A numerical study on magnetostrictive phenomena in magnetorheological elastomers *Comput. Mater. Sci.* **124** 364–74
[14] Attaran A, Brummund J and Wallmersperger T 2017 Modeling and finite element simulation of the magneto-mechanical behavior of ferrogels *J. Magn. Magn. Mater.* **431** 188–91
[15] Stolbov O V and Raikher Y L 2019 Magnetostriction effect in soft magnetic elastomers *Arch. Appl. Mech.* **89** 63–76
[16] Fischer L and Menzel A M 2019 Magnetostriction in magnetic gels and elastomers as a function of the internal structure and particle distribution *J. Chem. Phys.* **151** 114906
[17] Fischer L and Menzel A M 2020 Magnetically induced elastic deformations in model systems of magnetic gels and elastomers containing particles of mixed size *Smart Mater. Struct.* **30** 014003
[18] Sun T L, Gong X L, Jiang W Q, Li J F, Xu Z B and Li W H 2008 Study on the damping properties of magnetorheological elastomers based on *cis*-polybutadiene rubber *Polym. Test.* **27** 520–6
[19] Hu G, Guo M, Li W, Du H and Alici G 2011 Experimental investigation of the vibration characteristics of a magnetorheological elastomer sandwich beam under non-homogeneous small magnetic fields *Smart Mater. Struct.* **20** 127001
[20] Bira N, Dhagat P and Davidson J R 2020 A review of magnetic elastomers and their role in soft robotics *Front. Robot. AI* **7** 588391
[21] Hu W, Lum G Z, Mastrangeli M and Sitti M 2018 Small-scale soft-bodied robot with multimodal locomotion *Nature* **554** 81–85
[22] Fischer L and Menzel A M 2020 Towards a soft magnetoelastic twist actuator *Phys. Rev. Res.* **2** 023383
[23] Birster K, Schweitzer R, Schopphoven C and Tschöpe A 2022 Field-induced deformation of ferromagnetic soft nanocomposites *J. Phys. D: Appl. Phys.* **55** 075003
[24] Annunziata M A, Menzel A M and Löwen H 2013 Hardening transition in a one-dimensional model for ferrogels *J. Chem. Phys.* **138** 204906
[25] Biller A M, Stolbov O V and Raikher Y L 2014 Modeling of particle interactions in magnetorheological elastomers *J. Appl. Phys.* **116** 114904
[26] Biller A M, Stolbov O V and Raikher Y L 2015 Mesoscopic magnetomechanical hysteresis in a magnetorheological elastomer *Phys. Rev.* E **92** 023202
[27] Puljiz M, Huang S, Kalina K A, Nowak J, Odenbach S, Kästner M, Auernhammer G K and Menzel A M 2018 Reversible magnetomechanical collapse: virtual touching and detachment of rigid inclusions in a soft elastic matrix *Soft Matter* **14** 6809–21
[28] Huang S, Pessot G, Cremer P, Weeber R, Holm C, Nowak J, Odenbach S, Menzel A M and Auernhammer G K 2016 Buckling of paramagnetic chains in soft gels *Soft Matter* **12** 228–37
[29] Stepanov G V, Borin D Y, Raikher Y L, Melenev P V and Perov N S 2008 Motion of ferroparticles inside the polymeric matrix in magnetoactive elastomers *J. Phys.: Condens. Matter* **20** 204121
[30] Pessot G, Löwen H and Menzel A M 2016 Dynamic elastic moduli in magnetic gels: normal modes and linear response *J. Chem. Phys.* **145** 104904
[31] Gundermann T and Odenbach S 2014 Investigation of the motion of particles in magnetorheological elastomers by X-μCT *Smart Mater. Struct.* **23** 105013
[32] Gavili A, Zabihi F, Isfahani T D and Sabbaghzadeh J 2012 The thermal conductivity of water base ferrofluids under magnetic field *Exp. Therm. Fluid Sci.* **41** 94–98
[33] Shima P D and Philip J 2011 Tuning of thermal conductivity and rheology of nanofluids using an external stimulus *J. Phys. Chem.* C **115** 20097–104
[34] Collin D, Auernhammer G K, Gavat O, Martinoty P and Brand H R 2003 Frozen-in magnetic order in uniaxial magnetic gels: preparation and physical properties *Macromol. Rapid Commun.* **24** 737–41
[35] Günther D, Borin D Y, Günther S and Odenbach S 2011 X-ray micro-tomographic characterization of field-structured magnetorheological elastomers *Smart Mater. Struct.* **21** 015005
[36] Kchit N, Lancon P and Bossis G 2009 Thermoresistance and giant magnetoresistance of magnetorheological elastomers *J. Phys. D: Appl. Phys.* **42** 105506
[37] Kchit N and Bossis G 2009 Electrical resistivity mechanism in magnetorheological elastomer *J. Phys. D: Appl. Phys.* **42** 105505
[38] Mietta J L, Tamborenea P I and Negri R M 2016 Anisotropic magnetoresistivity in structured elastomer composites: modelling and experiments *Soft Matter* **12** 6430–41
[39] Diaz-Bleis D, Vales-Pinzón C, Freile-Pelegrín Y and Alvarado-Gil J J 2014 Thermal characterization of magnetically aligned carbonyl iron/agar composites *Carbohydrate Polym.* **99** 84–90
[40] Garishin O C and Moshev V V 2002 Damage model of elastic rubber particulate composites *Theor. Appl. Fract. Mech.* **38** 63–69
[41] Jackson J D 1999 *Classical Electrodynamics* (New York: Wiley)
[42] Weeks J D, Chandler D and Andersen H C 1971 Role of repulsive forces in determining the equilibrium structure of simple liquids *J. Chem. Phys.* **54** 5237–47
[43] Bombard A J F, Joekes I, Alcantara M R and Knobel M 2001 Magnetic susceptibility and magnetic hysteresis loop of some carbonyl iron powders used in magnetorheological fluids *Mater. Sci. Forum* **416–418** 753–8
[44] Kot M, Nagahashi H and Szymczak P 2015 Elastic moduli of simple mass spring models *Vis. Comput.* **31** 1339–50
[45] Landau D and Lifshitz E M 1970 Theory of elasticity 2nd edn (Oxford: Pergamon)
[46] Ostoja-Starzewski M 2002 Lattice models in micromechanics *Appl. Mech. Rev.* **55** 35–59
[47] Wacker Chemie AG 2022 ELASTOSIL RT 745 A/B, thermally curing silicone rubber (RTV-2) (available at: www.wacker.com/h/en-us/medias/ELASTOSIL-RT-745-AB-en-2022.02.02.pdf)
[48] BASF 2007 Safety data sheet carbonyl iron powder cm (available at: https://ehslegacy.unr.edu/msdsfiles/21298.pdf)
[49] Baehr H D and Stephan K 2010 *Wärme- und Stoffübertragung* 7th edn (Berlin: Springer)

[50] Hahn D W and Özisik M N 2002 *Heat Conduction* 3rd edn (Hoboken, NJ: Wiley)
[51] Wacker Chemie AG 2022 Flyer industriesilikone gb final (available at: www.hellermanntyton.com/binaries/content/assets/downloads/si/tehni%C4%8Dni-listi/ostali-izdelki/090615_flyer_industriesilikone_gb.pdf)
[52] Wacker Chemie AG 2022 Solid and liquid silicone rubber—material and processing guidelines (available at: www.wacker.com/h/en-iq/medias/6709-EN.pdf)
[53] Rahim M S A, Ismail I and Aqida S N 2017 Effects of nano copper additive on thermal conductivity of magnetorheological fluid at different environment temperature *Mater. Sci. Forum* **890** 108–11
[54] Rycroft C H 2009 VORO++: a three-dimensional Voronoi cell library in C++ *Chaos* **19** 041111
[55] Bıyıkoglu T, Leyodold J and Stadler P F 1915 *Laplacian Eigenvectors of Graphs, Perron-Frobenius and Faber-Krahn Type Theorems* (Berlin: Springer)
[56] Sattari A S, Rizvi Z H, Motra H B and Wuttke F 2017 Meso-scale modeling of heat transport in a heterogeneous cemented geomaterial by lattice element method *Granular Matter* **19** 66
[57] Messing R, Frickel N, Belkoura L, Strey R, Rahn H, Odenbach S and Schmidt A M 2011 Cobalt ferrite nanoparticles as multifunctional cross-linkers in PAAm ferrohydrogels *Macromolecules* **44** 2990–9
[58] Ilg P 2013 Stimuli-responsive hydrogels cross-linked by magnetic nanoparticles *Soft Matter* **9** 3465–8
[59] Pech-May N W, Vales-Pinzon C, Vega-Flick A, Oleaga A, Salazar A, Yanez-Limon J M and Alvarado-Gil J J 2018 Heat transport in epoxy and polyester carbonyl iron microcomposites: the effect of concentration and temperature *J. Compos. Mater.* **52** 1331–8

P8 Elastic deformations of loaded core-shell systems

Reproduced from

J. Kolker, L. Fischer, A. M. Menzel, and H. Löwen,
Elastic deformations of loaded core-shell systems,
J. Elasticity **150**, 77 (2022).

Digital Object Identifier (DOI): `https://doi.org/10.1007/s10659-022-09897-1`

Statement of contribution

All authors contributed to this work. The first version of the main text was drafted by JK (except for the introduction and parts of the conclusion, which were drafted by HL and AMM), who also performed most of the calculations and prepared all figures. I thoroughly checked all calculations and discussed the calculations as well as the underlying theory. All authors discussed the results and edited the manuscript. I estimate my contribution to this work during my PhD as 35 %.

Copyright and license notice

Journal of Elasticity
https://doi.org/10.1007/s10659-022-09897-1

Elastic Deformations of Spherical Core-Shell Systems Under an Equatorial Load

Jannis Kolker[1] · **Lukas Fischer**[2] · **Andreas M. Menzel**[2] · **Hartmut Löwen**[1]

Received: 7 January 2022 / Accepted: 4 May 2022

Abstract
Macroscopic elastic core-shell systems can be generated as toy models to be deformed and haptically studied by hand. On the mesoscale, colloidal core-shell particles and microgels are fabricated and investigated by different types of microscopy. We analyse, using linear elasticity theory, the response of spherical core-shell systems under the influence of a line density of force that is oriented radially and acts along the equator of the outer surface. Interestingly, deformational coupling of the shell to the core can determine the resulting overall appearance in response to the forces. We address various combinations of radii, stiffness, and Poisson ratio of core and shell and illustrate the resulting deformations. Macroscopically, the situation could be realized by wrapping a cord around the equator of a macroscopic model system and pulling it tight. On the mesoscale, colloidal microgel particles symmetrically confined to the interface between two immiscible fluids are pulled radially outward by surface tension.

Keywords Linear elasticity theory · Core-shell system · Deformation under external load · Continuum theory

Mathematics Subject Classification 74B10 · 74A10 · 74A30

1 Introduction

Solid sphere-like core-shell systems containing an inner part, the core, of elastic properties different from a surrounding outer part, the shell, are encountered in various contexts on different length scales. On large macroscopic scales, many stars, planets and moons can be approximated by a core and a shell of different elasticity [1]. Jelly sweets covered by a solid layer represent a popular example of not only mechanical or haptic but also culinary experience. Conversely, on the mesoscopic colloidal scale and even down to the nanoscale,

✉ J. Kolker

✉ L. Fischer

[1] Institut für Theoretische Physik II, Heinrich-Heine-Universität Düsseldorf, Universitätsstraße 1, 40225 Düsseldorf, Germany

[2] Institut für Physik, Otto-von-Guericke-Universität Magdeburg, Universitätsplatz 2, 39106 Magdeburg, Germany

Published online: 26 May 2022

there are numerous soft matter systems involving core-shell particles. These can be prepared in various ways [2, 3] as spherical colloidal particles with a polymer coating [4–6], as micelles [7] or as polymer networks with different crosslinking degrees in the inner and outer part [8–10]. Their controlled fabrication is not only pivotal for applications (such as microreactors [11, 12], targeted drug delivery [13, 14] or smart elastic materials [15, 16]). They also serve as model systems to tailor effective repulsive square-shoulder potentials [17–27] and to understand fundamental questions of statistical mechanics such as freezing and glass formation [4, 28–30].

Our focus in this work is laid on the coupled elastic deformation of inner and outer part, that is core and shell, respectively. We address spherical elastic systems when exposed to a radially oriented force line density along the equatorial circumference of the shell. This setup is motivated by the elasticity problem underlying colloidal core-shell microgel particles that are adsorbed to the interface between two immiscible fluids. At their common contact line, the two fluids pull on the shell of the microgel particle approximately in a radially outward direction in a symmetric setup [31–33]. In many of such interfacial situations, the wetting properties of the surface of a material are crucial for adsorption. A core-shell system provides an appropriate opportunity to adjust by a shell these surface wetting properties to the current need. At the same time, the elastic properties of the core under the influence of an interface are explored. Moreover, the particles may be density matched or functionalized, for example integrating magnetic behaviour, by the selected core material [34–36]. On macroscopic toy model systems, the force densities can be applied by hand, while on even larger, global scales atmospheric effects may lead to equatorially located line-like force densities on planets. An example is the thin area of low atmospheric pressure located around the equator of the earth in the inter-tropical convergence zone. In view of these different systems and situations, the imposed equatorial line force density can either be oriented radially inward (compressive) or radially outward (tensile). In the mathematical treatment this difference is represented by an inversion of the sign of the load.

In this paper, we study the underlying elasticity problem. We present a general continuum theory to compute and predict the shape change of an elastic core-shell system when loaded by an equatorial ring of line force density. Importantly not only the shell deforms, but also the inner core, and the two deformations are coupled to each other by the overall architecture. Through this coupling, the core can influence or even determine the type of deformation of the shell, although the load is applied from outside to the shell, not to the core. We analyse the resulting change of shape in detail, as a function of the relative size of core and shell, different mechanical stiffness of core and shell, as well as their compressibility. In particular, we include the possibility of an elastic *auxetic* response [37–42]. The latter is characterized by a negative Poisson ratio, i.e. when stretched along one axis the system expands along the perpendicular axes. Materials exhibiting corresponding elastic properties have been identified, constructed and analysed [43–46]. In particular it is interesting to consider core and shell materials with different Poisson ratios, as their competition can result in qualitatively different modes of deformation. Our study links to previously investigated geometries, particularly spherical one-component systems [47] or hollow capsules [48] as special cases. Moreover, our additional predictions can be verified by experiments on different scales.

2 Theory and Geometry

Within linear elasticity theory, small deformations of elastic materials are described. The position $\mathbf{r}$ of a material element can be mapped to its position $\mathbf{r}'$ in the deformed state

by adding the displacement vector $\mathbf{u}$. The displacement field $\mathbf{u}(\mathbf{r})$ in the bulk satisfies the homogeneous Navier-Cauchy equations [49]

$$(1-2\nu)\nabla^2\mathbf{u}(\mathbf{r}) + \nabla(\nabla\cdot\mathbf{u}(\mathbf{r})) = \mathbf{0} \tag{1}$$

with $-1 < \nu \leq 1/2$ denoting the Poisson ratio of the elastic substance in three-dimensional situations [50]. Materials with $\nu = 1/2$ are incompressible, while those with negative Poisson ratio are referred to as *auxetic* materials [50]. The latter, when stretched along a certain axis, expand along the lateral directions (instead of undergoing lateral contraction). We ignore any force acting on the bulk, for example gravity. Consequently, in the bulk, the right-hand side of Eq. (1) is set equal to zero.

Furthermore, linear elasticity theory for homogeneous isotropic materials dictates the stress-strain relation [50]

$$\frac{E}{1+\nu}\left(\underline{\boldsymbol{\varepsilon}}(\mathbf{r}) + \frac{\nu}{1-2\nu}\mathrm{Tr}\left(\underline{\boldsymbol{\varepsilon}}(\mathbf{r})\right)\underline{\mathbf{I}}\right) = \underline{\boldsymbol{\sigma}}(\mathbf{r}). \tag{2}$$

Equation (2) describes the relationship between the strain tensor $\underline{\boldsymbol{\varepsilon}}(\mathbf{r}) = \left(\nabla\mathbf{u}(\mathbf{r}) + (\nabla\mathbf{u}(\mathbf{r}))^{\mathrm{T}}\right)/2$ as the symmetrized gradient of the displacement field $\mathbf{u}(\mathbf{r})$ and the symmetric Cauchy stress tensor $\underline{\boldsymbol{\sigma}}$ (we mark second-rank tensors and matrices by an underscore). E is the Young modulus of the elastic material and $\underline{\mathbf{I}}$ is the unit matrix. The Young modulus E and the Poisson ratio ν are sufficient to quantify the properties of a homogeneous isotropic elastic material.

The boundary conditions at the surface of the elastic shell are

$$\underline{\boldsymbol{\sigma}}(\mathbf{r})\cdot\mathbf{n} = \frac{\lambda}{R_\mathrm{s}}\delta\left(\theta - \frac{\pi}{2}\right)\mathbf{n}. \tag{3}$$

Here, $\mathbf{n}$ describes the outward normal unit vector of the surface and $\delta\left(\theta - \frac{\pi}{2}\right)/R_\mathrm{s}$, with δ the Dirac delta function, sets the location of the line at which the loading force line density of amplitude λ is acting on the core-shell system. We use spherical coordinates so that $\theta = \frac{\pi}{2}$ specifies the equator.

Since we are describing a core-shell material, different elastic properties and radii are attributed to the core and to the shell, see Fig. 1. The core (green) is assigned the radius R_c, the Young modulus E_c, and the Poisson ratio ν_c. The shell (red) is defined by the outer radius R_s, the Young modulus E_s, and the Poisson ratio ν_s. According to Eq. (3), $\lambda > 0$ marks the amplitude of a line density of force pointing radially outward along the equator of the outer surface of the shell.

The system is characterized by the following five dimensionless parameters. First, the ratio $\lambda/E_\mathrm{s}R_\mathrm{s}$ of the loading force line density on the surface to the Young modulus of the shell describes the relative strength of the load magnitude and is proportional to the amplitude of deformation. The second parameter is the ratio of Young moduli $E_\mathrm{c}/E_\mathrm{s}$ of the core to the shell and in addition, the two dimensionless Poisson ratios ν_c and ν_s of core and shell, respectively, enter the elasticity theory. The fifth parameter is the size ratio $R_\mathrm{c}/R_\mathrm{s}$ of the core to the shell.

In spherical coordinates, the position vector $\mathbf{r}$ transforms from the unloaded configuration to the loaded configuration as $\mathbf{r}' = \mathbf{r} + u_r\mathbf{e}_r + u_\theta\mathbf{e}_\theta$, with u_r the radial and u_θ the polar component of the displacement field. $\mathbf{e}_r$ and $\mathbf{e}_\theta$ denote the radial and polar unit vector, respectively. Due to the special axial symmetry of the problem, the azimuthal component of the displacement field, u_ϕ, is zero. Concerning the homogeneous Navier-Cauchy equations

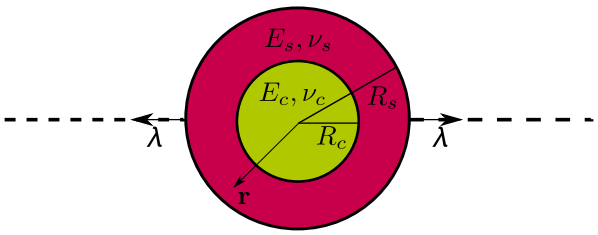

Fig. 1 Schematic visualisation of the core-shell system, here still in its initial spherical shape for illustration. The core (green) is assigned the radius R_c, the Young modulus E_c, and the Poisson ratio ν_c. The shell (red) is described by the outer radius R_s, the Young modulus E_s, and the Poisson ratio ν_s. The system is loaded by exposition to a ring of force line density around the equator of the outer sphere of magnitude λ.

Eq. (1) and the stress-strain relation Eq. (2) recast in spherical coordinates, where in our case the azimuthal dependence vanishes, see the Supporting Information (SI).

For both core and shell we solve Eq. (1) by separation into a series expansion of the polar dependence in terms of Legendre polynomials $P_n(\cos\theta)$ and associated r-dependent prefactors ($r = |\mathbf{r}|$) [51]. We distinguish by superscripts c and s the solutions for core and shell, respectively. More precisely, the solutions [47, 52, 53] of the Navier-Cauchy equations (1) split into a radial component $u_r^{(c)}(\mathbf{r})$ and a polar component $u_\theta^{(c)}(\mathbf{r})$ for the core and take the form

$$u_r^{(c)}(\mathbf{r}) = \sum_{n=0}^{\infty} \left(a_n^{(c)} (n+1)(-2+n+4\nu_c) r^{n+1} + b_n^{(c)} n r^{n-1} \right) P_n(\cos\theta), \tag{4}$$

$$u_\theta^{\mathrm{c}}(\mathbf{r}) = \sum_{n=1}^{\infty} \left(a_n^{(c)} (5+n-4\nu_c) r^{n+1} + b_n^{(c)} r^{n-1} \right) \frac{d}{d\theta} P_n(\cos\theta). \tag{5}$$

The solutions for the shell additionally contain terms inverse in the radial distance from the origin

$$\begin{aligned} u_r^{(s)}(\mathbf{r}) = \sum_{n=0}^{\infty} \Big(& a_n^{(s)} (n+1)(-2+n+4\nu_s) r^{n+1} + b_n^{(s)} n r^{n-1} \\ & + n(3+n-4\nu_s) c_n^{(s)} r^{-n} - (n+1) d_n^{(s)} r^{-(n+2)} \Big) P_n(\cos\theta), \end{aligned} \tag{6}$$

$$\begin{aligned} u_\theta^{(s)}(\mathbf{r}) = \sum_{n=1}^{\infty} \Big(& a_n^{(s)} (5+n-4\nu_s) r^{n+1} + b_n^{(s)} r^{n-1} \\ & - (-4+n+4\nu_s) c_n^{(s)} r^{-n} + d_n^{(s)} r^{-(n+2)} \Big) \frac{d}{d\theta} P_n(\cos\theta). \end{aligned} \tag{7}$$

As boundary conditions, we use that the traction vectors at the interface of core and shell (at radius R_c) must be equal

$$\underline{\boldsymbol{\sigma}}^{(c)}(R_c \mathbf{e}_r) \cdot \mathbf{n} = \underline{\boldsymbol{\sigma}}^{(s)}(R_c \mathbf{e}_r) \cdot \mathbf{n}. \tag{8}$$

Requiring strict elastic no-slip coupling, also the deformations at the interface must be equal

$$\mathbf{u}^{(c)}(R_c \mathbf{e}_r) = \mathbf{u}^{(s)}(R_c \mathbf{e}_r). \tag{9}$$

Since the Legendre polynomials form a complete orthogonal set, the Dirac delta function in Eq. (3) can be expanded in Legendre polynomials

$$\delta\left(\theta-\frac{\pi}{2}\right)=\sum_{n=0}^{\infty}\frac{2n+1}{2}P_n\left(\cos\left(\frac{\pi}{2}\right)\right)P_n\left(\cos\theta\right). \tag{10}$$

Due to the assumed mirror symmetry with respect to the equatorial plane, all odd series expansion components in the core and shell solution in Eqs. (4)-(7) vanish. Therefore we can write for the radial displacement

$$u_r^{(i)}\left(\mathbf{r}\right)=u_{r,0}^{(i)}\left(r\right)+u_{r,2}^{(i)}\left(r\right)P_2\left(\cos(\theta)\right)+\cdots \tag{11}$$

with $i=c$ for the core and $i=s$ for the shell, respectively. Here, the first component $u_{r,0}^{(i)}(r)$ describes the overall volume change. We note that this term will vanish for $\nu_i\to 1/2$ and remains as the only component for $\nu_i\to -1$. The second component gives the first correction to a spherical shape. A positive prefactor $u_{r,2}^{(i)}(r)$ describes a relative prolate deformation while $u_{r,2}^{(i)}(r)<0$ implies a relative oblate deformation. It is in fact the latter case of an oblate deformation which we expect when the core-shell particle is pulled outwards at the equator ($\lambda>0$).

The solutions for the displacements of the core and the shell diverge in response to the Dirac delta function at the equator on the surface of the shell, see the boundary condition Eq. (3). Yet, each mode of deformation is only excited to a finite degree by the Dirac delta function, see Eq. (10). Therefore, the second components $u_{r,2}^{(c)}(r)$ and $u_{r,2}^{(s)}(r)$ for the core and the shell remain finite and $u_{r,2}^{(s)}(r)$ is even finite at the surface of the shell. We shall use them as parameters to characterise the relative oblate or prolate deformation of the core and the shell shape.

For convenience, we evaluate these second components at the core and shell radii and normalize them with the corresponding unloaded radii of the core and the shell, respectively. Hence, we use subsequently $u_{r,2}^{(c)}/R_c\equiv u_{r,2}^{(c)}(R_c)/R_c$ and $u_{r,2}^{(s)}/R_s\equiv u_{r,2}^{(s)}(R_s)/R_s$ as dimensionless measures for the shape of the core and the shell.

3 Results and Discussion

3.1 General Solution and Limiting Behaviour

We first present the solutions for the displacements under the prescribed boundary conditions by providing the core coefficients of the expansions (4) and (5)

$$a_n^{(c)}=\frac{\lambda}{E_{\mathrm{s}}R_{\mathrm{s}}}\frac{2n+1}{2}P_n\left(0\right)\left(\frac{R_{\mathrm{c}}}{R_{\mathrm{s}}}\right)^{-2}R_{\mathrm{s}}^{-n}\left[\left(\frac{E_{\mathrm{c}}}{E_{\mathrm{s}}}\right)\tilde{c}_{01,n}+\tilde{c}_{02,n}\right]\frac{1}{D}, \tag{12}$$

$$b_n^{(c)}=-\frac{\lambda}{E_{\mathrm{s}}R_{\mathrm{s}}}\frac{2n+1}{2}P_n\left(0\right)R_{\mathrm{s}}^{-(n-2)}\left[\left(\frac{E_{\mathrm{c}}}{E_{\mathrm{s}}}\right)\tilde{c}_{03,n}+\tilde{c}_{04,n}\right]\frac{1}{D}, \tag{13}$$

and the shell coefficients of the expansions (6) and (7)

$$a_n^{(s)}=\frac{\lambda}{E_{\mathrm{s}}R_{\mathrm{s}}}\frac{2n+1}{2}P_n\left(0\right)R_{\mathrm{s}}^{-n}$$

$$\times \left[\left(\frac{E_c}{E_s} \right)^2 \tilde{c}_{05,n} + \left(\frac{E_c}{E_s} \right) \tilde{c}_{06,n} + \tilde{c}_{07,n} \right] \frac{1}{D}, \tag{14}$$

$$b_n^{(s)} = -\frac{\lambda}{E_s R_s} \frac{2n+1}{2} P_n(0) R_s^{-(n-2)} \times \left[\left(\frac{E_c}{E_s} \right)^2 \tilde{c}_{08,n} + \left(\frac{E_c}{E_s} \right) \tilde{c}_{09,n} + \tilde{c}_{10,n} \right] \frac{1}{D}, \tag{15}$$

$$c_n^{(s)} = \frac{\lambda}{E_s R_s} \frac{2n+1}{2} P_n(0) \left(\frac{R_c}{R_s} \right)^{n-1} R_c^n R_s \times \left[\left(\frac{E_c}{E_s} \right)^2 \tilde{c}_{11,n} + \left(\frac{E_c}{E_s} \right) \tilde{c}_{12,n} + \tilde{c}_{13,n} \right] \frac{1}{D}, \tag{16}$$

$$d_n^{(s)} = -\frac{\lambda}{E_s R_s} \frac{2n+1}{2} P_n(0) \left(\frac{R_c}{R_s} \right)^{n-1} R_c^{n+2} R_s \times \left[\left(\frac{E_c}{E_s} \right)^2 \tilde{c}_{14,n} + \left(\frac{E_c}{E_s} \right) \tilde{c}_{15,n} + \tilde{c}_{16,n} \right] \frac{1}{D}, \tag{17}$$

with

$$D = \left(\frac{E_c}{E_s} \right)^2 \tilde{c}_{17,n} + \frac{E_c}{E_s} \tilde{c}_{18,n} + \tilde{c}_{19,n}. \tag{18}$$

The constants $\tilde{c}_{01,n}$ to $\tilde{c}_{19,n}$ are listed in the SI. In the absence of a core, i.e. $R_c \to 0$, or in the absence of the shell, i.e. $R_c \to R_s$, we recover the previous solution for a one-component system as given in Ref. [47]. Also for the special case of $E_c = E_s$ and $\nu_c = \nu_s$ of identical core and shell elasticities, our solution reduces to that of a one-component system.

3.2 Relative Deformation of the Shell and the Core

In the following, the degrees of deformation of the core and the shell are investigated for volume conserving conditions ($\nu_c = \nu_s = 1/2$) for both tensile ($\lambda > 0$) and compressive ($\lambda < 0$) situations. Figure 2 shows the relative deformation $u_{r,2}^{(i)}/R_i$ for a tensile (left column) and a compressive (right column) line force density. The relative deformation is plotted for the shell ($i = s$) in a) and b) and for the core ($i = c$) in c) and d) as a function of the ratios of Young moduli E_c/E_s. Data are provided for several size ratios R_c/R_s ranging from 0.3 to 1.

The first observation is that the coefficient $u_{r,2}^{(i)}/R_i$ is negative for the tensile case and positive for a compressive situation, corresponding to a relative oblate and prolate deformation. This is a simple consequence of the force load pulling or pushing the equator to the outward or inward direction, respectively.

Second, the absolute magnitude of deformation decreases in both cases with increasing E_c/E_s which is the expected trend if the core is getting harder than the shell (at fixed shell elasticity). For $E_c/E_s \to 0$ we obtain the special case of a hollow sphere. In this limit, the relative deformation of the core and the shell reaches a finite saturation (note the logarithmic scale in Fig. 2). In the opposite limit $E_c/E_s \to \infty$ the core gets rigid, which implies that the displacement of the shell stays finite but the displacement of the core tends to zero. We find a common finite slope of ± 1 for the curves associated with the core for $E_c/E_s \to \infty$ in Fig. 2.

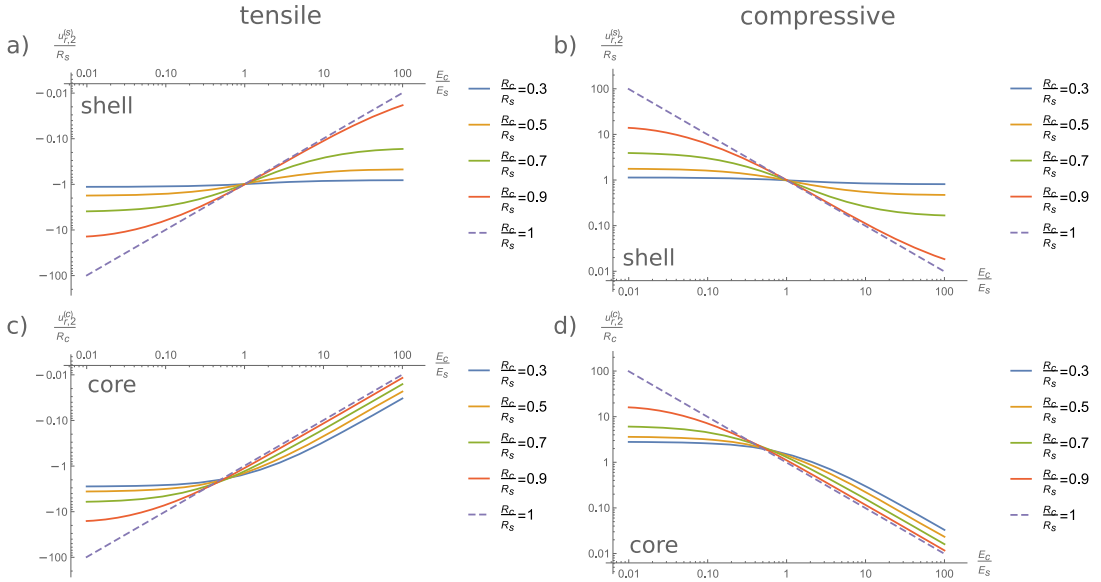

Fig. 2 Relative deformation $u_{r,2}^{(i)}/R_i$ as a function of the ratio of Young moduli E_c/E_s at different size ratios R_c/R_s. Two cases are considered, namely **a**,**c**) tensile (oriented radially outward, $\lambda/(E_s R_s) = 1$) and **b**,**d**) compressive (oriented radially inward, $\lambda/(E_s R_s) = -1$) line force densities. For both cases the relative deformation of the shell ($i = s$) in **a**) and **b**) and the core ($i = c$) in **c**) and **d**) is shown on a double logarithmic scale. Further parameters are $\nu_c = \nu_s = 1/2$. The blue dashed line corresponds to the limit of a one-component system (for $R_c/R_s = 1$).

Moreover, in Fig. 2a all curves intersect in the same point at $E_c = E_s$. At this point the two materials are identical and the size ratio becomes irrelevant for the deformation at the shell surface. The curves of Fig. 2b do not exhibit a common intersection point due to our normalization of the relative deformation with R_c and the fact that the radial deformation is in general not homogeneous along the radius. For increasing R_c/R_s, the influence of the core grows and the curves exhibit more sensitivity as a function of E_c for fixed E_s.

To complement the picture, Fig. 3 shows the same quantity as in Fig. 2 for the tensile case, namely the relative oblate deformation $u_{r,2}^{(i)}/R_i$, but now as a function of the size ratio R_c/R_s for a) the shell ($i = s$) and b) the core ($i = c$). Curves for several ratios of Young moduli E_c/E_s are displayed. For $E_c = E_s$ (dashed red curves), the resulting effective one-component system features a shell displacement that does not depend on the size ratio of core to shell. Conversely, the plotted core displacement does depend on the size ratio for $E_c = E_s$ because it is normalized by the size of the core. The deformation scaled by R_c in the limit of small core size $R_c \to 0$ (see Fig. 3b) reaches different limits for different ratios of Young moduli although the core becomes vanishingly small. Furthermore, the limit of a hollow sphere system $E_c/E_s \to 0$, is also shown in Fig. 3a) and b).

3.3 Deformational Behaviour for Different Poisson Ratios of Core and Shell

We now study the different deformation behaviour for the core and the shell with respect to their Poisson ratios. In particular we explore the elastic response for an auxetic core combined with a regular elastic shell, and vice versa. Such combinations can, at least, be realized in macroscopic elastic model systems, when appropriate materials are chosen. Thus their behaviour is investigated systematically for varying compressibility and auxetic properties. Figure 4 shows the deformational behaviour of the core and the shell as a function of their (in general different) Poisson ratios ν_c and ν_s. For simplicity we here consider the same

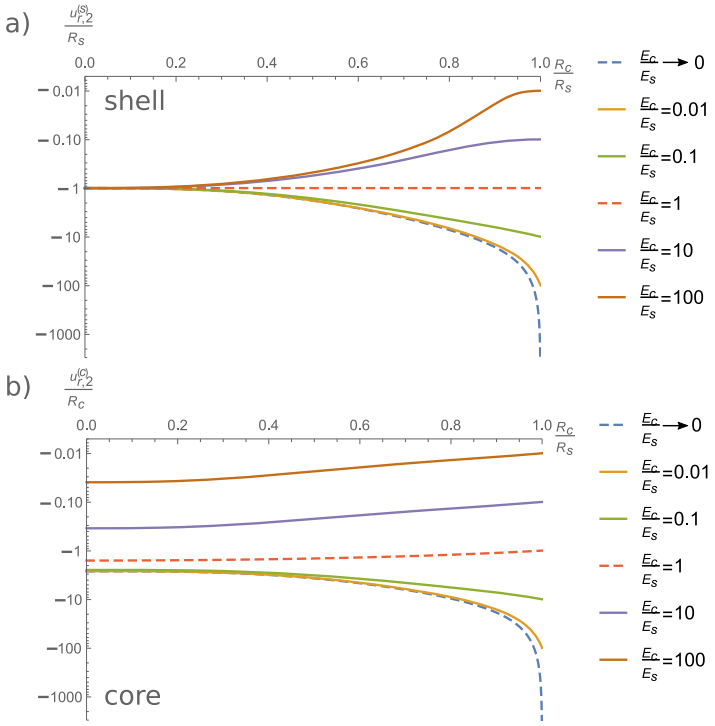

Fig. 3 Relative oblate deformation $u^{(i)}_{r,2}/R_i$ as a function of the size ratio R_c/R_s for different ratios of Young moduli E_c/E_s for a) the shell ($i = s$) and b) the core ($i = c$) on semi-logarithmic scale. Further parameters are $\nu_c = \nu_s = 1/2$ and $\lambda/(E_s R_s) = 1$. The red ($E_c/E_s = 1$) and blue ($E_c/E_s \to 0$) dashed curves correspond to one-component and hollow sphere systems, respectively.

stiffness of the core and the shell, $E_c = E_s$. Moreover we fix the core size to $R_c = 0.5R_s$ and the load amplitude to $\lambda/(E_s R_s) = 0.1$.

We distinguish between two different states of the displacement: I) the shell is more oblate than the core and II) the core is more oblate than the shell. In order to do so, we use the absolute value of the (here always negative) second coefficient of relative deformation of the shell $\left|u^{(s)}_{r,2}/R_s\right|$ and the core $\left|u^{(c)}_{r,2}/R_c\right|$. For state I) (reddish and greenish in Fig. 4) we have $\left|u^{(s)}_{r,2}/R_s\right| > \left|u^{(c)}_{r,2}/R_c\right|$, while for state II) (greyish in Fig. 4) we have $\left|u^{(s)}_{r,2}/R_s\right| < \left|u^{(c)}_{r,2}/R_c\right|$. See also the two schematic sketches on the top right-hand side of Fig. 4. The transition from I) to II), given by the same relative degree of oblate deformation $\left|u^{(s)}_{r,2}/R_s\right| = \left|u^{(c)}_{r,2}/R_c\right|$, is shown in Fig. 4 by the yellow line separating the two regions. There is a non-monotonic behaviour of this line as a function of ν_c for an auxetic shell ($\nu_s \approx -0.6$) and a nearly incompressible core.

The different colour codes on the right hand side in Fig. 4 represent the magnitude of the relative oblate deformation of the shell for state I) and of the core for state II). For nine selected points indicated in the $\nu_c\nu_s$-plane we illustrate the corresponding shapes of the core and the shell as given by the components $u^{(c)}_{r,0}$, $u^{(c)}_{r,2}$, $u^{(s)}_{r,0}$ and $u^{(s)}_{r,2}$, respectively, describing the change in volume and relative oblate deformation.

At the origin in the state diagram, where $\nu_c = \nu_s = 0$, the relative oblate deformation of the core and the shell are equal so that the yellow line passes through the origin in Fig. 4. Strictly speaking, this point [and all others on the diagonal from (a) to (d)] describes a one-component system, because there the elastic properties of the core and the shell are identical. We note that in general the yellow line of $\left|u^{(s)}_{r,2}/R_s\right| = \left|u^{(c)}_{r,2}/R_c\right|$ does not coincide with the diagonal of $\nu_c = \nu_s$ in Fig. 4, although we find a one-component material in the latter case. One aspect that contributes to this result is the inhomogeneous stress and strain distribution in the system, resulting from the force density that is concentrated at the equator. Further remarks on these stress and strain distributions are given in Sect. 3.4.

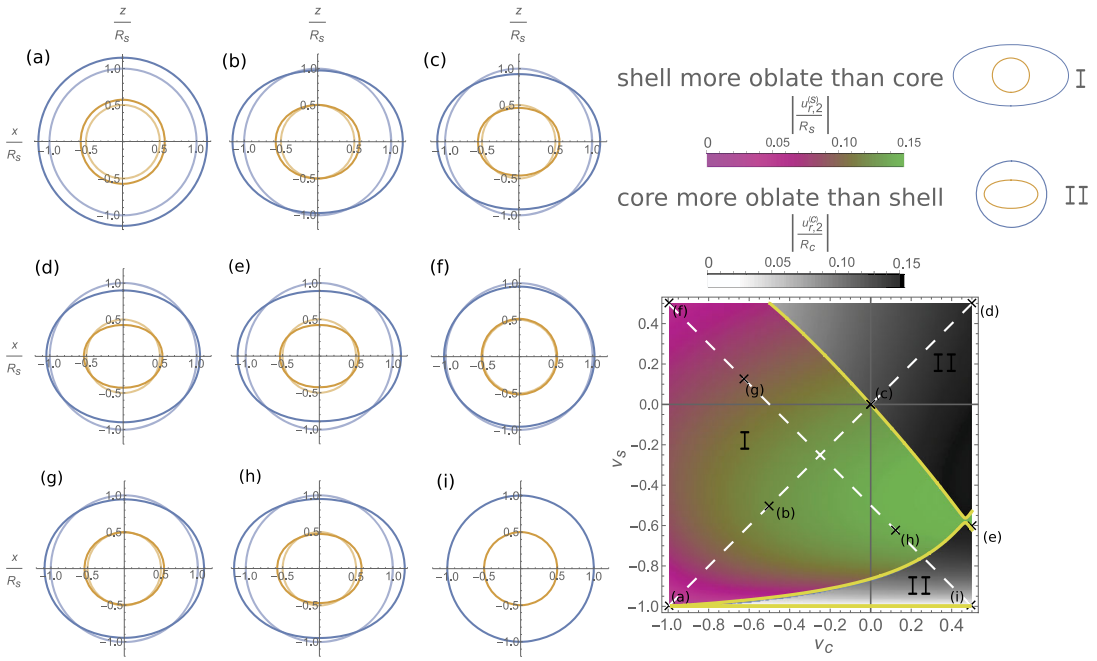

Fig. 4 Bottom right: State diagram exhibiting two situations I) and II) in the plane spanned by the two Poisson ratios of the core ν_c and the shell ν_s at fixed $E_c = E_s$, $R_c = 0.5R_s$ and $\lambda/(E_s R_s) = 0.1$. In I), corresponding to the reddish and greenish region, the relative oblate deformation of the shell is larger in magnitude than that of the core, see schematic representation on the top right. Here we plot in region I of the state diagram $\left|u_{r,2}^{(s)}/R_s\right|$ as colour-coded on the top right. Conversely, in II), corresponding to the greyish region in the state diagram, the relative oblate deformation of the core is larger in magnitude than that of the shell. Here we plot in region II of the state diagram $\left|u_{r,2}^{(c)}/R_c\right|$ as colour-coded on the top right. The two states I) and II) are separated by yellow lines, which represent the same relative degree of oblate deformation. Effectively, a one-component system is given by the (white dashed) diagonal from (**a**) to (**d**). Furthermore, for nine parameter combinations indicated for various points (**a**)-(**i**) in the state diagram, the corresponding elliptical shapes of core and shell are shown on the left with the light curves as a reference to the undeformed system.

Clearly, for the parameter combinations on the yellow line separating regions I) and II), the relative oblate deformations of core and shell are equal, as seen in Fig. 4 (a), (c), and (i) $\left(\left|u_{r,2}^{(s)}/R_s\right| = \left|u_{r,2}^{(c)}/R_c\right|\right)$. In the special cases of (a) and (i) we recover spherical shapes of core and shell, even if the volume has changed $\left(\left|u_{r,2}^{(c)}/R_c\right| = \left|u_{r,2}^{(s)}/R_s\right| = 0\right)$. We observe that $\left|u_{r,2}^{(c)}/R_c\right|$ and $\left|u_{r,2}^{(s)}/R_s\right|$ in the state diagram are continuous when varying the Poisson ratios, even in the vicinity of (e). For $\nu_s = -1$, we found that the shell determines the considered modes $u_{r,2}^{(c)}$ and $u_{r,2}^{(s)}$, forcing them to vanish. In conclusion, different Poisson ratios can largely tune the behaviour of the core-shell structure under external loading.

3.4 Internal Stress Field

We now provide explicit data for the internal stress field. For quasi volume conserving conditions ($\nu_c = \nu_s = 0.4999$), a size ratio of $R_c/R_s = 0.5$, and an amplitude of $\lambda/(E_s R_s) = 0.1$ of the force line density, loaded configurations of the core-shell system for three different ratios of Young moduli E_c/E_s are shown in Fig. 5.

The loaded configurations are colour coded for the components of the (symmetric) stress tensor, defined by $\underline{\sigma}^{(\mathrm{i})} = \sigma_{rr}^{(\mathrm{i})}\mathbf{e}_r \otimes \mathbf{e}_r + \sigma_{r\theta}^{(\mathrm{i})}(\mathbf{e}_\theta \otimes \mathbf{e}_r + \mathbf{e}_r \otimes \mathbf{e}_\theta) + \sigma_{\theta\theta}^{(\mathrm{i})}\mathbf{e}_\theta \otimes \mathbf{e}_\theta$, for the core

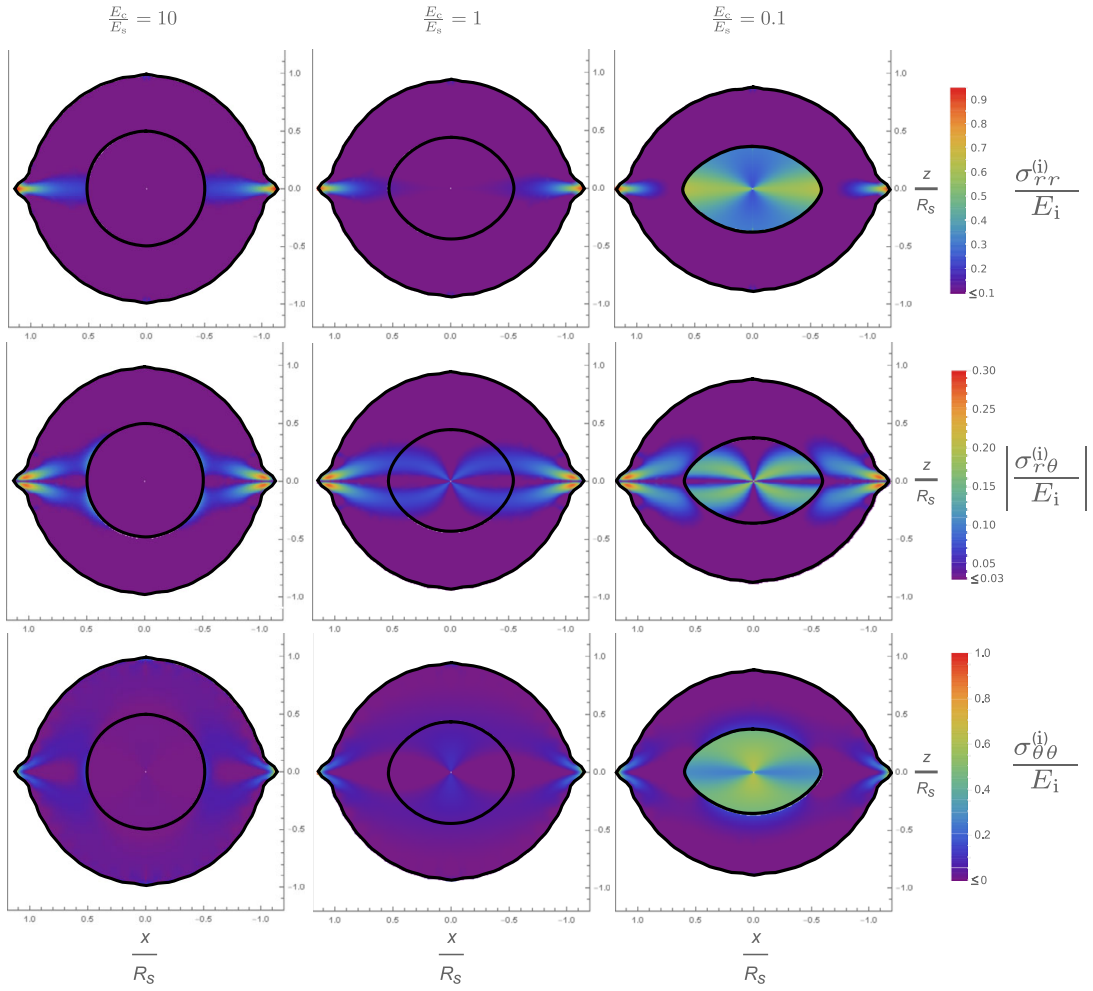

Fig. 5 Loaded configurations of the core-shell system at fixed $\nu_c = \nu_s = 0.4999$, $R_c = 0.5R_s$, and $\lambda/(E_s R_s) = 0.1$. The colour code reflects the three scaled components of the symmetric stress tensor $\sigma^{(i)}_{rr}/E_i$, $|\sigma^{(i)}_{r\theta}|/E_i$ and $\sigma^{(i)}_{\theta\theta}/E_i$ for the core ($i = c$) and the shell ($i = s$). Three different ratios of Young moduli E_c/E_s each are shown for the three components. The core and shell boundaries are indicated by black lines. To achieve a better resolution, only the absolute value of $\sigma^{(\mathrm{i})}_{r\theta}/E_{\mathrm{i}}$ is shown. By symmetry, this tensor component changes sign in the different quadrants of the xz-plane.

($i = c$) and the shell ($i = s$). The components of the stress tensor are scaled by the respective E_i in the core ($i = c$) and in the shell ($i = s$). Results for the deformations and associated components of stress are calculated from Eqs. (2) and (4)-(7), where the infinite series are truncated at $n = 32$.

For all configurations, all components of the stress tensor are of the greatest extent around the equatorial line of loading along the shell surface. Clearly, the system there experiences a displacement in positive radial (outward) direction. Due to the quasi-incompressibility of both shell and core, a strong degree of inverted displacement results at the poles.

For $E_c \ll E_s$, the soft core deforms more easily than the surrounding harder shell and experiences a higher amount of scaled stress. The scaled stress of the quasi-incompressible shell is transferred from the equator towards the inside by the bulk elasticity of the shell (see the right column in Fig. 5). Conversely, for $E_c \gg E_s$, there is hardly any influence of the deformation of the shell on the core for the scaled stresses (see the left column in Fig. 5).

For comparison, the center column in Fig. 5 shows a loaded one-component system $E_c = E_s$ and the corresponding scaled components of stress.

4 Conclusions

We have analysed in detail the deformational response of an elastic core-shell system to a radially oriented force line density acting along the outside equatorial line. Natural extensions of our considerations include the following.

First, the axially symmetric situation that we addressed could be generalized to systems exposed to line densities that are modulated along the circumference. Moreover, the effect of surface force densities applied in patches or distributed over the whole surface area could be analysed, instead of pure force line densities. In a further step, the imposed distortions may not only be imposed from outside, but could additionally result from internal active or actuation centers. Obvious candidates for corresponding actuatable cores are given by magnetic gels [54, 55]. For these types of systems, magnetically induced deformations have already been analysed by linear elasticity theory in the case of one-component elastic spheres [56–58].

The considered geometry of loading can effectively be realised in experiments on the mesoscale by exposing core-shell microgel particles to the interface between two immiscible fluids acting on the elastic system [32, 33]. There, interfacial tension radially pulls on the equatorial circumference along the common contact line in a symmetric setup. Yet, our description can be applied to any system on any scale that can be characterized by continuum elasticity theory. For example, macroscopic elastic core-shell spheres could be generated as toy models using soft transparent elastic shells on an elastic core. The line of loading force could then simply be imposed by tying a cord around the equator of these macroscopic core-shell spheres and tightening it. In this setup, the direction of the force is inverted as well. However, this in our evaluation simply means that all directions of displacement are inverted. Such macroscopic approaches may support the involvement of auxetic components [37–42]. Depending on the materials at hand, this strategy may facilitate the experimental confirmation of our results, possibly by direct visual inspection.

Supplementary Information The online version contains supplementary material available at https://doi.org/10.1007/s10659-022-09897-1.

Acknowledgements L.F. and A.M.M. thank the Deutsche Forschungsgemeinschaft (DFG) for support through the SPP 1681 on magnetic hybrid materials, grant no. ME 3571/2-3, and for support through the Heisenberg Grant ME 3571/4-1 (A.M.M.). H.L. acknowledges funding from the Deutsche Forschungsgemeinschaft (DFG) under grant number LO 418/22-1.

Funding Note Open Access funding enabled and organized by Projekt DEAL.

References

1. Jacobs, J.: The Earth's Core. Int. Geophys. **20**, 213–237 (1975)
2. Caruso, F.: Adv. Mater. **13**, 11–22 (2001)
3. Schärtl, W.: Nanoscale **2**, 829–843 (2010)
4. Pusey, P.N.: In: Hansen, J.P., Levesque, D., Zinn-Justin, J. (eds.) Liquids, Freezing and the Glass Transition. North-Holland, Amsterdam (1991)
5. Lekkerkerker, H.N., Tuinier, R.: In: Colloids and the Depletion Interaction, pp. 57–108. Springer, Dordrecht (2011)
6. Royall, C.P., Poon, W.C., Weeks, E.R.: Soft Matter **9**, 17–27 (2013)
7. Förster, S., Abetz, V., Müller, A.H.: In: Polyelectrolytes with Defined Molecular Architecture II. Advances in Polymer Science, vol. 166, pp. 173–210. Springer, Berlin (2004)
8. Rey, M., Fernandez-Rodriguez, M.A., Karg, M., Isa, L., Vogel, N.: Acc. Chem. Res. **53**, 414–424 (2020)
9. Rey, M., Hou, X., Tang, J.S.J., Vogel, N.: Soft Matter **13**, 8717–8727 (2017)
10. Plamper, F.A., Richtering, W.: Acc. Chem. Res. **50**, 131–140 (2017)
11. Yang, Z., Yang, L., Zhang, Z., Wu, N., Xie, J., Cao, W.: Colloids Surf. A, Physicochem. Eng. Asp. **312**, 113–117 (2008)
12. Liu, N., Zhao, S., Yang, Z., Liu, B.: ACS Appl. Mater. Interfaces **11**, 47008–47014 (2019)
13. Kataoka, K., Harada, A., Nagasaki, Y.: Adv. Drug Deliv. Rev. **47**, 113–131 (2001)
14. Bonacucina, G., Cespi, M., Misici-Falzi, M., Palmieri, G.F.: J. Pharm. Sci. **98**, 1–42 (2009)
15. Motornov, M., Roiter, Y., Tokarev, I., Minko, S.: Prog. Polym. Sci. **35**, 174–211 (2010)
16. Förster, S., Plantenberg, T.: Angew. Chem., Int. Ed. **41**, 688–714 (2002)
17. Heyes, D., Aston, P.: J. Chem. Phys. **97**, 5738–5748 (1992)
18. Bolhuis, P., Frenkel, D.: J. Phys. Condens. Matter **9**, 381–387 (1997)
19. Denton, A., Löwen, H.: J. Phys. Condens. Matter **9**, L1 (1997)
20. Jagla, E.: Phys. Rev. E **58**, 1478–1486 (1998)
21. Malescio, G., Pellicane, G.: Nat. Mater. **2**, 97–100 (2003)
22. Pauschenwein, G.J., Kahl, G.: J. Chem. Phys. **129**, 174107 (2008)
23. Yuste, S.B., Santos, A., López de Haro, M.: Mol. Phys. **109**, 987–995 (2011)
24. Norizoe, Y., Kawakatsu, T.: J. Chem. Phys. **137**, 024904 (2012)
25. Pattabhiraman, H., Gantapara, A.P., Dijkstra, M.: J. Chem. Phys. **143**, 164905 (2015)
26. Gabriëlse, A., Löwen, H., Smallenburg, F.: Materials **10**, 1280 (2017)
27. Somerville, W.R., Law, A.D., Rey, M., Vogel, N., Archer, A.J., Buzza, D.M.A.: Soft Matter **16**, 3564–3573 (2020)
28. Ivlev, A., Morfill, G., Löwen, H., Royall, C.P.: Complex Plasmas and Colloidal Dispersions: Particle-resolved Studies of Classical Liquids and Solids, vol. 5. World Scientific, Singapore (2012)
29. Gasser, U.: J. Phys. Condens. Matter **21**, 203101 (2009)
30. Karg, M., Pich, A., Hellweg, T., Hoare, T., Lyon, L.A., Crassous, J., Suzuki, D., Gumerov, R.A., Schneider, S., Potemkin, I.I., Richtering, W.: Langmuir **35**, 6231–6255 (2019)
31. Bresme, F., Oettel, M.: J. Phys. Condens. Matter **19**, 413101 (2007)
32. Harrer, J., Rey, M., Ciarella, S., Löwen, H., Janssen, L.M.C., Vogel, N.: Langmuir **35**, 10512–10521 (2019)
33. Kolker, J., Harrer, J., Ciarella, S., Rey, M., Ickler, M., Janssen, L.M.C., Vogel, N., Löwen, H.: Soft Matter **17**, 5581–5589 (2021)
34. Rauh, A., Rey, M., Barbera, L., Zanini, M., Karg, M., Isa, L.: Soft Matter **13**, 158–169 (2017)
35. Vasudevan, S.A., Rauh, A., Kroger, M., Karg, M., Isa, L.: Langmuir **34**, 15370–15382 (2018)
36. Huang, S., Gawlitza, K., von Klitzing, R., Gilson, L., Nowak, J., Odenbach, S., Steffen, W., Auernhammer, G.K.: Langmuir **32**, 712–722 (2016)
37. Huang, C., Chen, L.: Adv. Mater. **28**, 8079–8096 (2016)
38. Ren, X., Das, R., Tran, P., Ngo, T.D., Xie, Y.M.: Smart Mater. Struct. **27**, 023001 (2018)
39. Scarpa, F., Bullough, W., Lumley, P.: Proc. Inst. Mech. Eng., Part C, J. Mech. Eng. Sci. **218**, 241–244 (2004)
40. Lakes, R.: Science **235**, 1038–1041 (1987)
41. Chan, N., Evans, K.: J. Mater. Sci. **32**, 5945–5953 (1997)
42. Caddock, B., Evans, K.: J. Phys. D, Appl. Phys. **22**, 1877–1882 (1989)
43. Babaee, S., Shim, J., Weaver, J.C., Chen, E.R., Patel, N., Bertoldi, K.: Adv. Mater. **25**, 5044–5049 (2013)
44. Jiang, Y., Li, Y.: Sci. Rep. **8**, 2397 (2018)
45. Kim, Y., Yuk, H., Zhao, R., Chester, S.A., Zhao, X.: Nature **558**, 274–279 (2018)
46. Evans, K.E.: Endeavour **15**, 170–174 (1991)
47. Style, R.W., Isa, L., Dufresne, E.R.: Soft Matter **11**, 7412–7419 (2015)
48. Hegemann, J., Boltz, H.-H., Kierfeld, J.: Soft Matter **14**, 5665–5685 (2018)

49. Cauchy, A.L.B.: Exercices de mathématiques. De Bure Frères, vol. 3. (1828)
50. Landau, L., Lifshitz, E.: Theory of Elasticity, 3rd edn. Butterworth-Heinemann, Oxford (1986)
51. Love, A.E.H.: A Treatise on the Mathematical Theory of Elasticity. Cambridge University Press, Cambridge (1927)
52. Duan, H.L., Wang, J., Huang, Z.P., Karihaloo, B.L.: Proc. R. Soc. A, Math. Phys. Eng. Sci. **461**, 3335–3353 (2005)
53. Yi, X., Duan, H.L., Karihaloo, B.L., Wang, J.: Arch. Mech. **59**, 259–281 (2007)
54. Weeber, R., Hermes, M., Schmidt, A.M., Holm, C.: J. Phys. Condens. Matter **30**, 063002 (2018)
55. Odenbach, S.: Arch. Appl. Mech. **86**, 269–279 (2016)
56. Fischer, L., Menzel, A.M.: J. Chem. Phys. **151**, 114906 (2019)
57. Fischer, L., Menzel, A.M.: Phys. Rev. Res. **2**, 023383 (2020)
58. Fischer, L., Menzel, A.M.: Smart Mater. Struct. **30**, 014003 (2021)

Supporting Information:

Elastic deformations of loaded core-shell systems

Jannis Kolker,[*,†] Lukas Fischer,[*,‡] Andreas M. Menzel,[‡] and Hartmut Löwen[†]

†*Institut für Theoretische Physik II: Weiche Materie, Heinrich-Heine-Universität Düsseldorf, D-40225 Düsseldorf, Germany*

‡*Institut für Physik, Otto-von-Guericke-Universität Magdeburg, Universitätsplatz 2, D-39106 Magdeburg, Germany*

E-mail: jannis.kolker@hhu.de; lukas.fischer@ovgu.de

In this supporting information, the Navier-Cauchy equations and stress-strain relations Eqs. (1) and (2) in the main text, respectively, are presented in spherical coordinates for the problem under investigation. The further dependences of the coefficients $a_n^{(c)}$, $b_n^{(c)}$, $a_n^{(s)}$, $b_n^{(s)}$, $c_n^{(s)}$, $d_n^{(s)}$ on the dimensionless parameters $\frac{\lambda}{E_\mathrm{s}R_\mathrm{s}}$, $\frac{E_\mathrm{c}}{E_\mathrm{s}}$, $\frac{R_\mathrm{c}}{R_\mathrm{s}}$, ν_c, ν_s and on the index n are listed in a two-step order. First, the dependence of the coefficients on the amplitude of the deformation $\frac{\lambda}{E_\mathrm{s}R_\mathrm{s}}$, the ratio of the Young moduli $\frac{E_\mathrm{c}}{E_\mathrm{s}}$ and the ratio of the radii $\frac{R_\mathrm{c}}{R_\mathrm{s}}$ is shown and in the second step the dependence on the index n as well as on the Poisson ratios for core ν_c and shell ν_s is emphasised. At last the asymptotic behaviour for $n \to \infty$ is analysed for the Legendre polynomials and the general rescaled solutions for the radial component of the displacement field for the core and the shell.

Navier-Cauchy equations and stress-strain relations in spherical coordinates

Due to the special axial symmetry of the problem, the azimuthal component u_ϕ of the displacement field $\mathbf{u}(\mathbf{r})$ is zero and any ϕ-dependence vanishes. Therefore, the displacement field can be written as $\mathbf{u}(\mathbf{r}) = u_r(r,\theta)\mathbf{e}_r + u_\theta(r,\theta)\mathbf{e}_\theta$, where $\mathbf{e}_r$ and $\mathbf{e}_\theta$ denote the radial and polar unit vectors, respectively. Then the homogeneous Navier-Cauchy equations, Eq. (1) in the main text, in spherical coordinates for the problem under investigation become

$$\begin{aligned} 2(1-\nu)\left(\frac{\partial}{\partial r}\left(\frac{1}{r^2}\frac{\partial}{\partial r}\left(r^2 u_r(r,\theta)\right)\right) + \frac{1}{\sin\theta}\frac{\partial}{\partial r}\left(\frac{1}{r}\frac{\partial}{\partial\theta}\left(\sin\theta u_\theta(r,\theta)\right)\right)\right) \\ -(1-2\nu)\left(\frac{1}{r^2\sin\theta}\frac{\partial}{\partial\theta}\left(\sin\theta\left(\frac{\partial}{\partial r}\left(r u_\theta(r,\theta)\right) - \frac{\partial}{\partial\theta}u_r(r,\theta)\right)\right)\right) = 0 \end{aligned} \tag{1}$$

for the radial direction and

$$2(1-\nu)\left(\frac{1}{r^3}\frac{\partial}{\partial\theta}\frac{\partial}{\partial r}\left(r^2u_r\left(r,\theta\right)\right)+\frac{1}{r^2}\frac{\partial}{\partial\theta}\left(\frac{1}{\sin\theta}\frac{\partial}{\partial\theta}\left(\sin\theta u_\theta\left(r,\theta\right)\right)\right)\right)$$
$$-(1-2\nu)\left(-\frac{1}{r}\frac{\partial}{\partial r}\left(\frac{\partial}{\partial r}\left(ru_\theta\left(r,\theta\right)\right)-\frac{\partial}{\partial\theta}u_r\left(r,\theta\right)\right)\right)=0 \tag{2}$$

for the polar direction. The nontrivial components of the stress-strain relation, Eq. (2) in the main text, in spherical coordinates for the underlying problem read

$$\sigma_{rr}(r,\theta)=\frac{E}{1+\nu}\left(\varepsilon_{rr}(r,\theta)+\frac{\nu}{1-2\nu}\left(\varepsilon_{rr}(r,\theta)+\varepsilon_{\theta\theta}(r,\theta)\right)\right), \tag{3}$$
$$\sigma_{r\theta}(r,\theta)=\frac{E}{1+\nu}\varepsilon_{r\theta}(r,\theta), \tag{4}$$
$$\sigma_{\theta\theta}(r,\theta)=\frac{E}{1+\nu}\left(\varepsilon_{\theta\theta}(r,\theta)+\frac{\nu}{1-2\nu}\left(\varepsilon_{rr}(r,\theta)+\varepsilon_{\theta\theta}(r,\theta)\right)\right). \tag{5}$$

Here, in spherical coordinates, we inserted for the symmetric Cauchy stress tensor $\underline{\sigma}\left(\mathbf{r}\right)=\sigma_{rr}(r,\theta)\mathbf{e}_r\otimes\mathbf{e}_r+\sigma_{r\theta}(r,\theta)\left(\mathbf{e}_\theta\otimes\mathbf{e}_r+\mathbf{e}_r\otimes\mathbf{e}_\theta\right)+\sigma_{\theta\theta}(r,\theta)\mathbf{e}_\theta\otimes\mathbf{e}_\theta$ and for the strain tensor $\underline{\varepsilon}\left(\mathbf{r}\right)=\varepsilon_{rr}(r,\theta)\mathbf{e}_r\otimes\mathbf{e}_r+\varepsilon_{r\theta}(r,\theta)\left(\mathbf{e}_\theta\otimes\mathbf{e}_r+\mathbf{e}_r\otimes\mathbf{e}_\theta\right)+\varepsilon_{\theta\theta}(r,\theta)\mathbf{e}_\theta\otimes\mathbf{e}_\theta$, where $\otimes$ denotes the dyadic product.

Dependence of the coefficients $a_n^{(c)}, b_n^{(c)}, a_n^{(s)}, b_n^{(s)}, c_n^{(s)}, d_n^{(s)}$ on the amplitude of deformation $\frac{\lambda}{E_\mathbf{s}R_\mathbf{s}}$, the ratio of Young moduli $\frac{E_\mathbf{c}}{E_\mathbf{s}}$ and the ratio of radii $\frac{R_\mathbf{c}}{R_\mathbf{s}}$

The coefficients $a_n^{(c)}, b_n^{(c)}, a_n^{(s)}, b_n^{(s)}, c_n^{(s)}, d_n^{(s)}$ with $n\geq 0$ are listed and their dependence on the amplitude of deformation $\frac{\lambda}{E_\mathrm{s}R_\mathrm{s}}$, the ratio of Young moduli $\frac{E_\mathrm{c}}{E_\mathrm{s}}$ and the ratio of radii $\frac{R_\mathrm{c}}{R_\mathrm{s}}$ is highlighted. The expressions are found from the solutions of the relative deformation

$\frac{\mathbf{u}^{(c)}(R_c\mathbf{e}_r)}{R_c}$ and $\frac{\mathbf{u}^{(s)}(R_s\mathbf{e}_r)}{R_s}$, respectively:

$$\frac{a_n^{(c)}}{R_c}R_c^{n+1} = \frac{\lambda}{E_s R_s}\frac{2n+1}{2}P_n(0)\left(\frac{R_c}{R_s}\right)^{(n-2)}\left[\left(\frac{E_c}{E_s}\right)\tilde{c}_{01,n}+\tilde{c}_{02,n}\right]\frac{1}{D},$$

$$\frac{b_n^{(c)}}{R_c}R_c^{n-1} = -\frac{\lambda}{E_s R_s}\frac{2n+1}{2}P_n(0)\left(\frac{R_c}{R_s}\right)^{(n-2)}\left[\left(\frac{E_c}{E_s}\right)\tilde{c}_{03,n}+\tilde{c}_{04,n}\right]\frac{1}{D},$$

$$\begin{aligned}
\frac{a_n^{(s)}}{R_s}R_s^{n+1} &= \frac{\lambda}{E_s R_s}\frac{2n+1}{2}P_n(0)\left[\left(\frac{E_c}{E_s}\right)^2\tilde{c}_{05,n}+\left(\frac{E_c}{E_s}\right)\tilde{c}_{06,n}+\tilde{c}_{07,n}\right]\frac{1}{D},\\
\frac{b_n^{(s)}}{R_s}R_s^{n-1} &= -\frac{\lambda}{E_s R_s}\frac{2n+1}{2}P_n(0)\left[\left(\frac{E_c}{E_s}\right)^2\tilde{c}_{08,n}+\left(\frac{E_c}{E_s}\right)\tilde{c}_{09,n}+\tilde{c}_{10,n}\right]\frac{1}{D},\\
\frac{c_n^{(s)}}{R_s}R_s^{-n} &= \frac{\lambda}{E_s R_s}\frac{2n+1}{2}P_n(0)\left(\frac{R_c}{R_s}\right)^{(2n-1)}\left[\left(\frac{E_c}{E_s}\right)^2\tilde{c}_{11,n}+\left(\frac{E_c}{E_s}\right)\tilde{c}_{12,n}+\tilde{c}_{13,n}\right]\frac{1}{D},\\
\frac{d_n^{(s)}}{R_s}R_s^{-(n+2)} &= -\frac{\lambda}{E_s R_s}\frac{2n+1}{2}P_n(0)\left(\frac{R_c}{R_s}\right)^{(2n+1)}\left[\left(\frac{E_c}{E_s}\right)^2\tilde{c}_{14,n}+\left(\frac{E_c}{E_s}\right)\tilde{c}_{15,n}+\tilde{c}_{16,n}\right]\frac{1}{D},
\end{aligned}$$

where

$$D = \left(\frac{E_c}{E_s}\right)^2\tilde{c}_{17,n}+\frac{E_c}{E_s}\tilde{c}_{18,n}+\tilde{c}_{19,n}. \tag{6}$$

The constants $\tilde{c}_{01,n}$ to $\tilde{c}_{19,n}$ are given below with their dependence on the ratio of radii $\frac{R_c}{R_s}$:

$$
\begin{aligned}
\tilde{c}_{01,n} =& c_{01,n} + c_{02,n}\left(\frac{R_c}{R_s}\right)^2 + c_{03,n}\left(\frac{R_c}{R_s}\right)^{(2n+1)} + c_{04,n}\left(\frac{R_c}{R_s}\right)^{(2n+3)},\\
\tilde{c}_{02,n} =& c_{05,n} + c_{06,n}\left(\frac{R_c}{R_s}\right)^2 + c_{07,n}\left(\frac{R_c}{R_s}\right)^{(2n+1)} + c_{08,n}\left(\frac{R_c}{R_s}\right)^{(2n+3)},\\
\tilde{c}_{03,n} =& c_{09,n} + c_{10,n}\left(\frac{R_c}{R_s}\right)^2 + c_{11,n}\left(\frac{R_c}{R_c}\right)^{(2n+1)} + c_{12,n}\left(\frac{R_c}{R_s}\right)^{(2n+3)},\\
\tilde{c}_{04,n} =& c_{13,n} + c_{14,n}\left(\frac{R_c}{R_s}\right)^2 + c_{15,n}\left(\frac{R_c}{R_s}\right)^{(2n+1)} + c_{16,n}\left(\frac{R_c}{R_s}\right)^{(2n+3)},\\
\tilde{c}_{05,n} =& c_{17,n} + c_{18,n}\left(\frac{R_c}{R_s}\right)^{(2n-1)} + c_{19,n}\left(\frac{R_c}{R_s}\right)^{(2n+1)},\\
\tilde{c}_{06,n} =& c_{20,n} + c_{21,n}\left(\frac{R_c}{R_s}\right)^{(2n-1)} + c_{22,n}\left(\frac{R_c}{R_s}\right)^{(2n+1)},\\
\tilde{c}_{07,n} =& c_{23,n} + c_{24,n}\left(\frac{R_c}{R_s}\right)^{(2n-1)} + c_{25,n}\left(\frac{R_c}{R_s}\right)^{(2n+1)},\\
\tilde{c}_{08,n} =& c_{26,n} + c_{27,n}\left(\frac{R_c}{R_s}\right)^{(2n+1)} + c_{28,n}\left(\frac{R_c}{R_s}\right)^{(2n+3)},\\
\tilde{c}_{09,n} =& c_{29,n} + c_{30,n}\left(\frac{R_c}{R_s}\right)^{(2n+1)} + c_{31,n}\left(\frac{R_c}{R_s}\right)^{(2n+3)},\\
\tilde{c}_{10,n} =& c_{32,n} + c_{33,n}\left(\frac{R_c}{R_s}\right)^{(2n+1)} + c_{34,n}\left(\frac{R_c}{R_s}\right)^{(2n+3)},
\end{aligned}
$$

$$
\begin{aligned}
\tilde{c}_{11,n} =& c_{35,n} + c_{36,n}\left(\frac{R_\mathrm{c}}{R_\mathrm{s}}\right)^2 + c_{37,n}\left(\frac{R_\mathrm{c}}{R_\mathrm{s}}\right)^{(2n+3)},\\
\tilde{c}_{12,n} =& c_{38,n} + c_{39,n}\left(\frac{R_\mathrm{c}}{R_\mathrm{s}}\right)^2 + c_{40,n}\left(\frac{R_\mathrm{c}}{R_\mathrm{s}}\right)^{(2n+3)},\\
\tilde{c}_{13,n} =& c_{41,n} + c_{42,n}\left(\frac{R_\mathrm{c}}{R_\mathrm{s}}\right)^2 + c_{43,n}\left(\frac{R_\mathrm{c}}{R_\mathrm{s}}\right)^{(2n+3)},\\
\tilde{c}_{14,n} =& c_{44,n} + c_{45,n}\left(\frac{R_\mathrm{c}}{R_\mathrm{s}}\right)^2 + c_{46,n}\left(\frac{R_\mathrm{c}}{R_\mathrm{s}}\right)^{(2n+1)},\\
\tilde{c}_{15,n} =& c_{47,n} + c_{48,n}\left(\frac{R_\mathrm{c}}{R_\mathrm{s}}\right)^2 + c_{49,n}\left(\frac{R_\mathrm{c}}{R_\mathrm{s}}\right)^{(2n+1)},\\
\tilde{c}_{16,n} =& c_{50,n} + c_{51,n}\left(\frac{R_\mathrm{c}}{R_\mathrm{s}}\right)^2 + c_{52,n}\left(\frac{R_\mathrm{c}}{R_\mathrm{s}}\right)^{(2n+1)},\\
\tilde{c}_{17,n} =& c_{53,n} + c_{54,n}\left(\frac{R_\mathrm{c}}{R_\mathrm{s}}\right)^{(2n-1)} + c_{55,n}\left(\frac{R_\mathrm{c}}{R_\mathrm{s}}\right)^{(2n+1)} + c_{56,n}\left(\frac{R_\mathrm{c}}{R_\mathrm{s}}\right)^{(2n+3)} + c_{57,n}\left(\frac{R_\mathrm{c}}{R_\mathrm{s}}\right)^{(4n+2)},\\
\tilde{c}_{18,n} =& c_{58,n} + c_{59,n}\left(\frac{R_\mathrm{c}}{R_\mathrm{s}}\right)^{(2n-1)} + c_{60,n}\left(\frac{R_\mathrm{c}}{R_\mathrm{s}}\right)^{(2n+1)} + c_{61,n}\left(\frac{R_\mathrm{c}}{R_\mathrm{s}}\right)^{(2n+3)} + c_{62,n}\left(\frac{R_\mathrm{c}}{R_\mathrm{s}}\right)^{(4n+2)},\\
\tilde{c}_{19,n} =& c_{63,n} + c_{64,n}\left(\frac{R_\mathrm{c}}{R_\mathrm{s}}\right)^{(2n-1)} + c_{65,n}\left(\frac{R_\mathrm{c}}{R_\mathrm{s}}\right)^{(2n+1)} + c_{66,n}\left(\frac{R_\mathrm{c}}{R_\mathrm{s}}\right)^{(2n+3)} + c_{67,n}\left(\frac{R_\mathrm{c}}{R_\mathrm{s}}\right)^{(4n+2)}.
\end{aligned}
$$

Dependence of the constants $c_{01,n}$ to $c_{67,n}$ on the index n, the Poisson ratio of the core ν_c and of the shell ν_s

The constants $c_{01,n}$ to $c_{67,n}$ only depend on the index n, the Poisson ratio of the core ν_c and of the shell ν_s. They are listed below:

$$
\begin{aligned}
c_{01,n} &= 0,\\
c_{02,n} &= -\frac{4(-1+n)^2(3+8n+4n^2)(-1+\nu_\mathrm{s})(-2-3n+2\nu_\mathrm{s}+4n\nu_\mathrm{s})}{(1+\nu_\mathrm{c})(1+\nu_\mathrm{s})^2},\\
c_{03,n} &= -\frac{2(1+2n)^2(-3+n+2n^2)(-1+\nu_\mathrm{s})(-2+n^2+2\nu_\mathrm{s})}{(1+\nu_\mathrm{c})(1+\nu_\mathrm{s})^2},\\
c_{04,n} &= \frac{2n(2+n)(3-n-14n^2+4n^3+8n^4)(-1+\nu_\mathrm{s})}{(1+\nu_\mathrm{c})(1+\nu_\mathrm{s})^2},\\
c_{05,n} &= 0,\\
c_{06,n} &= \frac{4(-1+n)(3+8n+4n^2)(-1+\nu_\mathrm{s})(1+n+n^2-\nu_\mathrm{s}-2n\nu_\mathrm{s})}{(1+\nu_\mathrm{s})^3},
\end{aligned}
$$

$$c_{07,n} = \frac{2(1+2n)^2(-3+n+2n^2)(-1+\nu_s)(-2+n^2+2\nu_s)}{(1+\nu_s)^3},$$

$$c_{08,n} = -\frac{2n(2+n)(3-n-14n^2+4n^3+8n^4)(-1+\nu_s)}{(1+\nu_s)^3},$$

$$c_{09,n} = \frac{4(-1+4n^2)(1+n+n^2+\nu_c+2n\nu_c)(-1+\nu_s)(-1+2n+n^2+2\nu_s)}{(1+\nu_c)(1+\nu_s)^2},$$

$$c_{10,n} = -\frac{4(-1+n)(3+11n+12n^2+4n^3)(-1+\nu_s)(5-\nu_c-6\nu_s+2n(-1+\nu_c+\nu_s)+n^2(-2+4\nu_s))}{(1+\nu_c)(1+\nu_s)^2},$$

$$c_{11,n} = -\frac{2(3+2n)^2(-1-2n+n^2+2n^3)(-1+\nu_s)(-2+n^2+2\nu_s)}{(1+\nu_c)(1+\nu_s)^2},$$

$$c_{12,n} = 2(2+n)(-1+4n^2)(-1+\nu_s)\left[\frac{5n^3+2n^4+n^2(6-8\nu_s)}{(1+\nu_c)(1+\nu_s)^2}\right.$$
$$\left. + \frac{-4(1+\nu_c)(-1+2\nu_s)-n(1+8\nu_s+4\nu_c(-3+4\nu_s))}{(1+\nu_c)(1+\nu_s)^2}\right],$$

$$c_{13,n} = -\frac{4(-2-n+8n^2+4n^3)(-1+2\nu_c+n(-3+4\nu_c))(-1+\nu_s)(-1+2n+n^2+2\nu_s)}{(1+\nu_s)^3},$$

$$c_{14,n} = \frac{4(-1+n)(3+11n+12n^2+4n^3)(-1+\nu_s)(5-4\nu_c+n^2(-2+4\nu_c)-3\nu_s+n(6\nu_c-2(1+\nu_s)))}{(1+\nu_s)^3},$$

$$c_{15,n} = \frac{2(3+2n)^2(-1-2n+n^2+2n^3)(-1+\nu_s)(-2+n^2+2\nu_s)}{(1+\nu_s)^3},$$

$$c_{16,n} = -2(2+n)(-1+4n^2)(-1+\nu_s)\left[\frac{5n^3+2n^4+n^2(6-8\nu_c)}{(1+\nu_s)^3}\right.$$
$$\left. + \frac{-4(-1+2\nu_c)(1+\nu_s)-n(1-12\nu_s+8\nu_c(1+2\nu_s))}{(1+\nu_s)^3}\right],$$

$$c_{17,n} = \frac{4(-1+n)^2(1+n+n^2+\nu_c+2n\nu_c)(-2-3n+2\nu_s+4n\nu_s)}{(1+\nu_c)^2(1+\nu_s)},$$

$$c_{18,n} = \frac{2(-1+n)(1+2n)(1+n+n^2+\nu_c+2n\nu_c)(-2+n^2+2\nu_s)}{(1+\nu_c)^2(1+\nu_s)},$$

$$c_{19,n} = -\frac{2(-1+n)n(2+n)(-1+2n)(1+n+n^2+\nu_c+2n\nu_c)}{(1+\nu_c)^2(1+\nu_s)},$$

$$c_{20,n} = -4(-1+n)\left[\frac{-3(-1+3\nu_c)(-1+\nu_s)+n^2(-4+\nu_c(9-16\nu_s)+9\nu_s)}{(1+\nu_c)(1+\nu_s)^2}\right.$$
$$\left. + \frac{n(-14+\nu_c(27-32\nu_s)+15\nu_s)+4n^3(5-6\nu_s+\nu_c(-6+8\nu_s))+2n^4(5-6\nu_s+\nu_c(-6+8\nu_s))}{(1+\nu_c)(1+\nu_s)^2}\right],$$

$$c_{21,n} = -\frac{2(-1-n+2n^2)(-1+5\nu_c+6n(-1+2\nu_c)+n^2(-2+4\nu_c))(-2+n^2+2\nu_s)}{(1+\nu_c)(1+\nu_s)^2},$$

$$c_{22,n} = \frac{2n(2+n)(1-3n+2n^2)(-1+5\nu_c+6n(-1+2\nu_c)+n^2(-2+4\nu_c))}{(1+\nu_c)(1+\nu_s)^2},$$

$$c_{23,n} = \frac{4(-1+n)(2+n)(-1+2\nu_c+n(-3+4\nu_c))(1+n+n^2-\nu_s-2n\nu_s)}{(1+\nu_s)^3},$$

$$c_{24,n} = \frac{2(-2-3n+3n^2+2n^3)(-1+2\nu_c+n(-3+4\nu_c))(-2+n^2+2\nu_s)}{(1+\nu_s)^3},$$

$$c_{25,n} = -\frac{2n(2+n)^2(1-3n+2n^2)(-1+2\nu_c+n(-3+4\nu_c))}{(1+\nu_s)^3},$$

$$c_{26,n} = \frac{4(-1+n)(1+n+n^2+\nu_c+2n\nu_c)(-2-3n+2\nu_s+4n\nu_s)(-1+2n+n^2+2\nu_s)}{(1+\nu_s)(1+\nu_c)^2},$$

$$c_{27,n} = \frac{2(-1+n)(3+5n+2n^2)(1+n+n^2+\nu_c+2n\nu_c)(-2+n^2+2\nu_s)}{(1+\nu_c)^2(1+\nu_s)},$$

$$c_{28,n} = -\frac{2(-1+n)(2+n)(1+2n)(1+n+n^2+\nu_c+2n\nu_c)(8+n+n^2-24\nu_s+16\nu_s^2)}{(1+\nu_c)^2(1+\nu_s)},$$

$$c_{29,n} = -4(-1+2n+n^2+2\nu_s)\left[\frac{-3(-1+3\nu_c)(-1+\nu_s)+n^2(-4+\nu_c(9-16\nu_s)+9\nu_s)}{(1+\nu_c)(1+\nu_s)^2}\right.$$
$$\left. + \frac{n(-14+\nu_c(27-32\nu_s)+15\nu_s)+4n^3(5-6\nu_s+\nu_c(-6+8\nu_s))+2n^4(5-6\nu_s+\nu_c(-6+8\nu_s))}{(1+\nu_c)(1+\nu_s)^2}\right],$$

$$c_{30,n} = -\frac{2(-3-2n+3n^2+2n^3)(-1+5\nu_c+6n(-1+2\nu_c)+n^2(-2+4\nu_c))(-2+n^2+2\nu_s)}{(1+\nu_c)(1+\nu_s)^2},$$

$$c_{31,n} = 2(2+n)(1+2n)\left[\frac{(6n^4(-1+2\nu_c)+n^5(-2+4\nu_c)-12(-1+\nu_s)(-1+\nu_c+2\nu_c\nu_s)-n(11+\nu_c-4\nu_s-28\nu_c\nu_s-8\nu_s^2+32\nu_c\nu_s^2)}{(1+\nu_c)(1+\nu_s)^2}\right.$$
$$\left.+\frac{n^3(9-8\nu_s+\nu_c(-15+16\nu_s))+2n^2(3+16\nu_s-16\nu_s^2+2\nu_c(-7-4\nu_s+8\nu_s^2)))}{(1+\nu_c)(1+\nu_s)^2}\right],$$

$$c_{32,n} = \frac{4(2+n)(-1+2\nu_c+n(-3+4\nu_c))(-1+2n+n^2+2\nu_s)(1+n+n^2-\nu_s-2n\nu_s)}{(1+\nu_s)^3},$$

$$c_{33,n} = \frac{2(2+n)(-3-2n+3n^2+2n^3)(-1+2\nu_c+n(-3+4\nu_c))(-2+n^2+2\nu_s)}{(1+\nu_s)^3},$$

$$c_{34,n} = -\frac{2(2+n)(1+2n)(-1+2\nu_c+n(-3+4\nu_c))(4-2n-n^2+2n^3+n^4-4\nu_s^2)}{(1+\nu_s)^3},$$

$$c_{35,n} = -\frac{2(-1+n)(1+2n)(1+n+n^2+\nu_c+2n\nu_c)(-1+2n+n^2+2\nu_s)}{(1+\nu_s)(1+\nu_c)^2},$$

$$c_{36,n} = \frac{2(-1+n)^2(3+5n+2n^2)(1+n+n^2+\nu_c+2n\nu_c)}{(1+\nu_c)^2(1+\nu_s)},$$

$$c_{37,n} = \frac{4(-1+n)(2+n)(1+n+n^2+\nu_c+2n\nu_c)(-1+2\nu_s+n(-3+4\nu_s))}{(1+\nu_c)^2(1+\nu_s)},$$

$$c_{38,n} = \frac{2(-1-n+2n^2)(-1+5\nu_c+6n(-1+2\nu_c)+n^2(-2+4\nu_c))(-1+2n+n^2+2\nu_s)}{(1+\nu_c)(1+\nu_s)^2},$$

$$c_{39,n} = -\frac{2(-1+n)^2(3+5n+2n^2)(-1+5\nu_c+6n(-1+2\nu_c)+n^2(-2+4\nu_c))}{(1+\nu_c)(1+\nu_s)^2},$$

$$c_{40,n} = -\frac{4(-1+n)(2+n)(-2+\nu_c+\nu_s+4\nu_c\nu_s+n^3(-6+4\nu_c+4\nu_s)+8n^2(-1+2\nu_c\nu_s)+n(-8+\nu_c+\nu_s+16\nu_c\nu_s))}{(1+\nu_c)(1+\nu_s)^2},$$

$$c_{41,n} = -\frac{2(-2-3n+3n^2+2n^3)(-1+2\nu_c+n(-3+4\nu_c))(-1+2n+n^2+2\nu_s)}{(1+\nu_s)^3},$$

$$c_{42,n} = \frac{2(-1+n)^2(2+n)(3+5n+2n^2)(-1+2\nu_c+n(-3+4\nu_c))}{(1+\nu_s)^3},$$

$$c_{43,n} = \frac{4(-1+n)(2+n)(-1+2\nu_c+n(-3+4\nu_c))(1+n+n^2+\nu_s+2n\nu_s)}{(1+\nu_s)^3},$$

$$c_{44,n} = \frac{2(-1+n)n(-1+2n)(1+n+n^2+\nu_c+2n\nu_c)(-1+2n+n^2+2\nu_s)}{(1+\nu_s)(1+\nu_c)^2},$$

$$c_{45,n} = -\frac{2(-1+n)^2(1+2n)(1+n+n^2+\nu_c+2n\nu_c)(8+n+n^2-24\nu_s+16\nu_s^2)}{(1+\nu_c)^2(1+\nu_s)},$$

$$c_{46,n} = -\frac{4(-1+n)(1+n+n^2+\nu_c+2n\nu_c)(-2+n^2+2\nu_s)(-1+2\nu_s+n(-3+4\nu_s))}{(1+\nu_c)^2(1+\nu_s)},$$

$$c_{47,n} = -\frac{2n(1-3n+2n^2)(-1+5\nu_c+6n(-1+2\nu_c)+n^2(-2+4\nu_c))(-1+2n+n^2+2\nu_s)}{(1+\nu_c)(1+\nu_s)^2},$$

$$c_{48,n} = 2(-1+n)(1+2n)\left[\frac{(6n^4(-1+2\nu_c)+n^5(-2+4\nu_c)-12(-1+\nu_s)(-1+\nu_c+2\nu_c\nu_s)-n(11+\nu_c-4\nu_s-28\nu_c\nu_s-8\nu_s^2+32\nu_c\nu_s^2)}{(1+\nu_c)(1+\nu_s)^2}\right.$$
$$\left.+\frac{n^3(9-8\nu_s+\nu_c(-15+16\nu_s))+2n^2(3+16\nu_s-16\nu_s^2+2\nu_c(-7-4\nu_s+8\nu_s^2))}{(1+\nu_c)(1+\nu_s)^2}\right],$$

$$c_{49,n} = \frac{4(-1+n)(-2+n^2+2\nu_s)(-2+\nu_c+\nu_s+4\nu_c\nu_s+n^3(-6+4\nu_c+4\nu_s)+8n^2(-1+2\nu_c\nu_s)+n(-8+\nu_c+\nu_s+16\nu_c\nu_s))}{(1+\nu_c)(1+\nu_s)^2},$$

$$c_{50,n} = \frac{2n(2-5n+n^2+2n^3)(-1+2\nu_c+n(-3+4\nu_c))(-1+2n+n^2+2\nu_s)}{(1+\nu_s)^3},$$

$$c_{51,n} = -\frac{2(-1+n)(1+2n)(-1+2\nu_c+n(-3+4\nu_c))(4-2n-n^2+2n^3+n^4-4\nu_s^2)}{(1+\nu_s)^3},$$

$$c_{52,n} = -\frac{4(-1+n)(-1+2\nu_c+n(-3+4\nu_c))(-2+n^2+2\nu_s)(1+n+n^2+\nu_s+2n\nu_s)}{(1+\nu_s)^3},$$

$$c_{53,n} = -\frac{8(-1+n)^2(1+n+n^2+\nu_c+2n\nu_c)(1+n+n^2+\nu_s+2n\nu_s)(-2-3n+2\nu_s+4n\nu_s)}{(1+\nu_c)^2(1+\nu_s)^2},$$

$$c_{54,n} = \frac{2(-1+n)(1+2n)^2(1+n+n^2+\nu_c+2n\nu_c)(4-2n-n^2+2n^3+n^4-4\nu_s^2)}{(1+\nu_c)^2(1+\nu_s)^2},$$

$$c_{55,n} = -\frac{4(-1+n)^2n(-6-n+17n^2+16n^3+4n^4)(1+n+n^2+\nu_c+2n\nu_c)}{(1+\nu_c)^2(1+\nu_s)^2},$$

$$c_{56,n} = \frac{2(-1+n)^2(2+n)(1+2n)^2(1+n+n^2+\nu_c+2n\nu_c)(8+n+n^2-24\nu_s+16\nu_s^2)}{(1+\nu_c)^2(1+\nu_s)^2},$$

$$c_{57,n} = -\frac{8(-1+n)(2+n)(1+n+n^2+\nu_c+2n\nu_c)(1+n+n^2-\nu_s-2n\nu_s)(-1+2\nu_s+n(-3+4\nu_s))}{(1+\nu_c)^2(1+\nu_s)^2},$$

$$c_{58,n} = 8(-1+n)(1+n+n^2+\nu_s+2n\nu_s)\left[\frac{-3(-1+3\nu_c)(-1+\nu_s)+n^2(-4+\nu_c(9-16\nu_s)+9\nu_s)}{(1+\nu_c)(1+\nu_s)^3}\right.$$
$$\left.+\frac{n(-14+\nu_c(27-32\nu_s)+15\nu_s)+4n^3(5-6\nu_s+\nu_c(-6+8\nu_s))+2n^4(5-6\nu_s+\nu_c(-6+8\nu_s))}{(1+\nu_c)(1+\nu_s)^3}\right],$$

$$c_{59,n} = -\frac{2(-1+n)(1+2n)^2(-1+5\nu_c+6n(-1+2\nu_c)+n^2(-2+4\nu_c))(4-2n-n^2+2n^3+n^4-4\nu_s^2)}{(1+\nu_c)(1+\nu_s)^3},$$

$$c_{60,n} = \frac{4(-1+n)^2n(-6-n+17n^2+16n^3+4n^4)(-1+5\nu_c+6n(-1+2\nu_c)+n^2(-2+4\nu_c))}{(1+\nu_c)(1+\nu_s)^3},$$

$$c_{61,n} = -2(1+2n)^2(-2+n+n^2)\left[\frac{6n^4(-1+2\nu_c)+n^5(-2+4\nu_c)-12(-1+\nu_s)(-1+\nu_c+2\nu_c\nu_s)}{(1+\nu_c)(1+\nu_s)^3}\right.$$
$$\left.+\frac{-n(11+\nu_c-4\nu_s-28\nu_c\nu_s-8\nu_s^2+32\nu_c\nu_s^2)+n^3(9-8\nu_s+\nu_c(-15+16\nu_s))+2n^2(3+16\nu_s-16\nu_s^2+2\nu_c(-7-4\nu_s+8\nu_s^2))}{(1+\nu_c)(1+\nu_s)^3}\right],$$

$$c_{62,n} = 8(-1+n)(2+n)(1+n+n^2-\nu_s-2n\nu_s)\left[\frac{-2+\nu_c+\nu_s+4\nu_c\nu_s+n^3(-6+4\nu_c+4\nu_s)+8n^2(-1+2\nu_c\nu_s)}{(1+\nu_c)(1+\nu_s)^3}\right.$$
$$\left.+\frac{n(-8+\nu_c+\nu_s+16\nu_c\nu_s)}{(1+\nu_c)(1+\nu_s)^3}\right],$$

$$c_{63,n} = -\frac{8(-1+n)(2+n)(-1+2\nu_c+n(-3+4\nu_c))(1+n+n^2-\nu_s-2n\nu_s)(1+n+n^2+\nu_s+2n\nu_s)}{(1+\nu_s)^4},$$

$$c_{64,n} = \frac{2(1+2n)^2(-2+n+n^2)(-1+2\nu_c+n(-3+4\nu_c))(4-2n-n^2+2n^3+n^4-4\nu_s^2)}{(1+\nu_s)^4},$$

$$c_{65,n} = -\frac{4n(-2+n+n^2)^2(-3+n+8n^2+4n^3)(-1+2\nu_c+n(-3+4\nu_c))}{(1+\nu_s)^4},$$

$$c_{66,n} = \frac{2(-1+n)(2+n)(1+2n)^2(-1+2\nu_c+n(-3+4\nu_c))(4-2n-n^2+2n^3+n^4-4\nu_s^2)}{(1+\nu_s)^4},$$

$$c_{67,n} = -\frac{8(-1+n)(2+n)(-1+2\nu_c+n(-3+4\nu_c))(1+n+n^2-\nu_s-2n\nu_s)(1+n+n^2+\nu_s+2n\nu_s)}{(1+\nu_s)^4}.$$

Asymptotic behaviour of the Legendre polynomials P_n and the general rescaled solutions for the radial component of the displacement field for the core $u_r^{(\mathbf{c})}/R_c$ and for the shell $u_r^{(\mathbf{s})}/R_s$

For the Legendre polynomials $P_n(\cos\theta)$ with $\theta = \pi/2$, the dependence on the index n is as follows[1]

$$P_n(0) = \begin{cases} \frac{(-1)^m}{2^{2m}} \frac{(2m)!}{(m!)^2} & \text{for } \; n = 2m, \\ 0 & \text{for } \; n = 2m+1. \end{cases} \tag{7}$$

Let $a_m = \frac{1}{2^{2m}} \frac{(2m)!}{(m!)^2}$. To calculate the asymptotic behaviour of this coefficient for $m \to \infty$, Stirling's formula can be used:

$$N! = \sqrt{2\pi N} \left(\frac{N}{e}\right)^N \left(1 + \mathcal{O}\left(\frac{1}{N}\right)\right), \tag{8}$$

where e denotes Euler's number. Applying this formula to a_m leads (for large m) to:

$$\begin{aligned} a_m &\approx \frac{1}{2^{2m}} \frac{\sqrt{2\pi 2m}}{2\pi m} \left(\frac{2m}{e}\right)^{2m} \left(\frac{e}{m}\right)^{2m} \\ &= \frac{2^{2m}}{2^{2m}} \frac{\sqrt{2\pi 2m}}{2\pi m} \\ &= \frac{1}{\sqrt{\pi m}}. \end{aligned} \tag{9}$$

Thus, the following asymptotic behaviour for $P_n(0)$ results:

$$P_n(0) \approx \begin{cases} \sqrt{\frac{2}{\pi n}} & \text{for } \; n \,\text{even}, \\ 0 & \text{for } \; n \,\text{odd}. \end{cases} \tag{10}$$

Furthermore, the dependence on the index n for the angles $\theta = 0, \pi$ gives[1]

$$P_n(1) = 1, \tag{11}$$

$$P_n(-1) = \begin{cases} 1 & \text{for } n \text{ even}, \\ -1 & \text{for } n \text{ odd}. \end{cases} \tag{12}$$

The case of n being odd is, due to the assumed mirror symmetry, irrelevant for the investigated problem, therefore $P_n(\cos 0) = P_n(\cos \pi) = 1$ holds true.

The general rescaled solution for the radial component of the displacement field for the core $u_r^{(c)}/R_c$ is obtained at the core radius R_c as follows

$$\frac{u_r^{(c)}(R_c \mathbf{e}_r)}{R_c} = \sum_{n=0}^{\infty} G_{r,n}^{(c)} \left(\frac{\lambda}{E_s R_s}, \frac{E_c}{E_s}, \frac{R_c}{R_s}, \nu_c, \nu_s \right) \frac{2n+1}{2} P_n(0) P_n(\cos\theta) \tag{13}$$

where $G_{r,n}^{(c)}(\lambda/(E_s R_s), E_c/E_s, R_c/R_s, \nu_c, \nu_s)$ is the corresponding kernel function of the core and the remaining factors in the sum result from the expansion of the Dirac delta function in Legendre polynomials. In terms of the coefficients $a_n^{(c)}$ and $b_n^{(c)}$, (13) can also be written as

$$\begin{aligned} \frac{u_r^{(c)}(R_c \mathbf{e}_r)}{R_c} &= \sum_{n=0}^{\infty} \left(\frac{a_n^{(c)}}{R_c} R_c^{n+1} (n+1)(-2+n+4\nu_c) + \frac{b_n^{(c)}}{R_c} R_c^{n-1} n \right) P_n(\cos\theta) \\ &= \sum_{n=0}^{\infty} \frac{2n+1}{2} P_n(0) P_n(\cos\theta) \left(\frac{R_c}{R_s} \right)^{(n-2)} \frac{\lambda}{E_s R_s} \\ &\quad \times \frac{1}{D} \left(\underbrace{\left[\left(\frac{E_c}{E_s} \right) \tilde{c}_{01,n} + \tilde{c}_{02,n} \right] (n+1)(-2+n+4\nu_c)}_{I} - \underbrace{\left[\left(\frac{E_c}{E_s} \right) \tilde{c}_{03,n} + \tilde{c}_{04,n} \right] n}_{II} \right). \end{aligned} \tag{14}$$

Comparing the solution for $u_r^{(c)}/R_c$ here with that in (13), it can be concluded that the kernel function of the core $G_{r,n}^{(c)}$ is the product of the factors $(R_c/R_s)^{(n-2)}$, $\lambda/(E_s R_s)$, $1/D$

(see Eq. (6)) and the sum of 14I + 14II. By multiplying the sum 14I + 14II by $1/D$, an order in index n of $\mathcal{O}(1)$ can be proved in the asymptotic behaviour of the limit $n \to \infty$ for $R_c/R_s < 1$. Therefore, the factor $(R_c/R_s)^{(n-2)}$ is the dominant factor in the asymptotic behaviour for the limit $n \to \infty$ of the kernel function of the core $G^{(\mathrm{c})}_{r,n}$. Combined with the n-dependence of the Legendre polynomials $P_n(\cos\theta)$ the general rescaled radial solution of the core $u^{(\mathrm{c})}_r/R_c$ at the core radius R_c gives a convergent series at the poles and at the equator, due to the $(R_c/R_s)^n$-dependence ($R_c/R_s < 1$, exponential decrease).

The general rescaled solution for the radial component of the displacement field for the shell $u^{(\mathrm{s})}_r/R_s$ is obtained at the outer shell radius R_s as

$$\frac{u^{(\mathrm{s})}_r(R_s\mathbf{e}_r)}{R_s} = \sum_{n=0}^{\infty} G^{(\mathrm{s})}_{r,n}\left(\frac{\lambda}{E_s R_s}, \frac{E_c}{E_s}, \frac{R_c}{R_s}, \nu_c, \nu_s\right) \frac{2n+1}{2} P_n(0)\, P_n(\cos\theta) \tag{15}$$

where $G^{(\mathrm{s})}_{r,n}(\lambda/(E_s R_s), E_c/E_s, R_c/R_s, \nu_c, \nu_s)$ is the corresponding kernel function of the shell and the remaining factors are the same as for the core solution. In terms of the coefficients

$a_n^{(s)}$, $b_n^{(s)}$, $c_n^{(c)}$ and $d_n^{(c)}$, (15) can also be written as

$$\begin{aligned}
\frac{u_r^{(s)}\left(R_s\mathbf{e}_r\right)}{R_s} &= \sum_{n=0}^{\infty}\left(\frac{a_n^{(s)}}{R_s}R_s^{n+1}(n+1)(-2+n+4\nu_s)+\frac{b_n^{(s)}}{R_s}R_s^{n-1}n\right.\\
&\qquad\left.+\frac{c_n^{(s)}}{R_s}R_s^{-n}n(3+n-4\nu_s)-\frac{d_n^{(s)}}{R_s}R_2^{-(n+2)}(n+1)\right)P_n\left(\cos\theta\right)\\
&= \sum_{n=0}^{\infty}\frac{2n+1}{2}P_n(0)P_n\left(\cos\theta\right)\frac{\lambda}{E_sR_s}\\
&\qquad\times\frac{1}{D}\left(\underbrace{\left[\left(\frac{E_c}{E_s}\right)^2\tilde{c}_{05,n}+\left(\frac{E_c}{E_s}\right)\tilde{c}_{06,n}+\tilde{c}_{07,n}\right](n+1)(-2+n+4\nu_s)}_{I}\right.\\
&\qquad\underbrace{-\left[\left(\frac{E_c}{E_s}\right)^2\tilde{c}_{08,n}+\left(\frac{E_c}{E_s}\right)\tilde{c}_{09,n}+\tilde{c}_{10,n}\right]n}_{II}\\
&\qquad\underbrace{+\left(\frac{R_c}{R_s}\right)^{(2n-1)}\left[\left(\frac{E_c}{E_s}\right)^2\tilde{c}_{11,n}+\left(\frac{E_c}{E_s}\right)\tilde{c}_{12,n}+\tilde{c}_{13,n}\right]n(3+n-4\nu_s)}_{III}\\
&\qquad\left.\underbrace{+\left(\frac{R_c}{R_s}\right)^{(2n+1)}\left[\left(\frac{E_c}{E_s}\right)^2\tilde{c}_{14,n}+\left(\frac{E_c}{E_s}\right)\tilde{c}_{15,n}+\tilde{c}_{16,n}\right](n+1)}_{IV}\right)
\end{aligned}\tag{16}$$

By comparing the solution for $u_r^{(s)}/R_s$ with that in (15), it can be concluded that the kernel function of the shell $G_{r,n}^{(s)}$ is the product of the factors $\lambda/(E_sR_s)$, $1/D$ and the sum of 16I + 16II + 16III + 16IV. By multiplying the sum 16I + 16II by $1/D$, an order in index n of $\mathcal{O}(1/n)$ can be proved in the asymptotic behaviour of the limit $n\to\infty$ for $R_c/R_s<1$. Multiplying the sum 16III + 16IV by $1/D$ leads to a dominant factor of $(R_c/R_s)^{2n}$ under the same conditions. Therefore, the asymptotic behaviour for $n\to\infty$ is proportional to $1/n$ for the kernel function of the shell $G_{r,n}^{(s)}$. Combined with the n-dependence of the Legendre polynomials $P_n\left(\cos\theta\right)$ the general rescaled radial solution for the shell $u_r^{(s)}/R_s$ at the outer

shell radius R_s results in a divergent series at the equator ($\theta = \pi/2$), due to the $1/n$-dependence of $G^{(s)}_{r,n}$ (harmonic series) and a convergent series at the poles ($\theta = 0, \pi$), due to the property of the Legendre polynomials at the poles (alternating series and a monotonic decrease to zero of the absolute value of the summands).

References

(1) Arfken, G., Weber H.; *Mathematical Methods for Physicists*; Elsevier Academic Press, United Kingdom, 2005.

Chapter 3

Concluding remarks

3.1 Summary

In this dissertation, a comprehensive evaluation of effects that can be observed by varying the arrangement of magnetizable inclusions in magnetic gels and elastomers is presented. We mainly focus on magnetostriction, i.e. deformations induced by homogeneous external magnetic fields, and magnetorheological effects, here particularly implying changes in elastic moduli. For this purpose, we have developed a scale-bridging approach in **P1** to calculate the overall magnetostrictive effects from the arrangement of magnetizable inclusions. Afterward, it was used to evaluate these effects for a selection of regular as well as randomized arrangements, identifying even qualitative differences. The employed elastic matrix material, particularly its compressibility, also influences the magnetostrictive behavior qualitatively. This description was subsequently expanded and applied to twist-type deformations in **P2**, polydisperse configurations of magnetizable inclusions in **P3**, and higher-order modes of deformation in **P4**.

When substantiated with additional analytical calculations as presented in **P6**, we managed to optimize configurations for maximized magnetostrictive as well as magnetorheological effects in **P5**. Naturally, which configurations are optimal depends on several parameters, such as the desired mode of deformation or type of magnetorheological effect, the number of magnetizable inclusions, as well as the employed elastic matrix material. With modern fabrication techniques, the targeted placement of magnetizable inclusions that is necessary for practical realization of our predicted optimized configurations is within reach. In our investigations, we identify the ones that are the most promising to be fabricated to substantially improve the performance of the materials.

As a more rarely investigated effect, we study magnetically induced changes in the thermal conductivity of magnetic gels and elastomers in **P7**. Finally, we investigate linearly elastic deformations of spherical core-shell systems as another example of elastic composite systems when subject to an applied equatorial force line density in **P8**.

The results in **P1**–**P7** can to a large extent be directly applied to electrorheological

gels and elastomers [49–51], simply replacing the magnetic by electric moments as induced by external electrical fields. For our approach to remain accurate, dynamical effects should be small, such as electrical currents.

Lastly, I would like to point to prior dissertations in this research area that provide further reading and were helpful in preparing the present work. Namely, these are the dissertations by Mate Puljiz [233], Giorgio Pessot [234], Peet Cremer [235], Karl Kalina (in German) [236], and Philipp Gebhart (in German) [93].

3.2 Outlook

In the future, I hope that a targeted placement of magnetizable inclusions in elastic matrices develops as promising as it appears at the moment for practical realization of the strategies outlined in this work. Potentially, also using explicitly the polydispersity of the particle sizes is promising. Experimental tools to realize corresponding systems are primarily 3D printing [22–24, 24–27], but other options exist, namely structuring by magnetic fields [28], sequential photopolymerization [29], acoustic holography [30], layerwise polymerization combined with particle placement by molds or by hand [31, 32], and wax-cast molding [33]. In this way, the results presented in **P1**–**P5** can be set into practice. One very promising direction in the future would be to fully automate the overall process, so that that these experimental results could directly be connected to an optimization pipeline [237].

On the theoretical side, an immediate extension consists of identifying optimized arrangements for other modes of deformation as well, besides those listed in **P5**. However, this necessitates new analytical derivations in analogy to **P6** to link between the discrete positioning of the inclusions and macroscopic modes of deformation. Furthermore, introducing nonlinear elasticity into our scheme of evaluation represents an important aspect. It would increase quantitative accuracy in the limit of large deformations. As a major difficulty, the superposition principle, as detailed in Sec. 1.2, would then be no longer applicable. Therefore, further developments are needed in that case to mitigate the huge increase in resulting computational requirements.

Additionally, the description of the magnetic effects could likewise be expanded. It might be worthwhile to study magnetizable inclusions that are not magnetized to saturation, leading to mutual magnetization effects [69] or to also include moments beyond the dipole approximation [84]. Still, these approaches are more computationally demanding, which limits their use to lower numbers of magnetizable inclusions. Another new avenue is provided by magnetically hard inclusions, which cause hysteretic behavior of magnetic gels and elastomers [44, 111, 112]. Therefore, they allow these materials to perform history-dependent functions, opening another means of customization and potential optimization. Finally, studying dynamical effects in the magnetostrictive behavior, possibly using a viscoelastic description, is

another open direction.

Generally, theoretical descriptions of these materials remain challenging, as important features are associated with different scales. Therefore, scale-bridging links [37, 193, 238] need to be developed further in the future to compliment each other and lead to a more unified understanding of the effects of interest, such as the magnetostrictive and magnetorheological effects. For these descriptions, ideally, the analysis starts at the microscale of the polymeric network, is then connected to the mesoscale of the configuration of magnetic or magnetizable inclusions, and is finally bridged to the macroscale where the global effects of interest can be observed.

Magnetic gels and elastomers are a promising class of materials. Applications are already discussed and outlined in a wide range of areas, but still, they can become much more common and much more effective at the tasks that they are to perform. Additionally applications might open for them in the future, particularly when combining them intelligently with other "smart" adaptable materials. One example could be to connect their change in the thermal conductivity, see **P7**, with other thermoresponsive materials. In this way, new functionalities can be realized and more possibilities open up to control these systems. Generally, for magnetic gels and elastomers to reach their full potential, it is important to characterize their behavior theoretically and experimentally in detail across the scales. It was my intention with this work to contribute to this endeavor, to facilitate and to stimulate further progress.

References

[1] A. M. Menzel, *Tuned, driven, and active soft matter*, Phys. Rep. **554**, 1 (2015).

[2] G. Filipcsei, I. Csetneki, A. Szilágyi, and M. Zrínyi, *Magnetic field-responsive smart polymer composites*, Adv. Polym. Sci. **206**, 137 (2007).

[3] S. Odenbach, *Microstructure and rheology of magnetic hybrid materials*, Arch. Appl. Mech. **86**, 269 (2016).

[4] R. Weeber, M. Hermes, A. M. Schmidt, and C. Holm, *Polymer architecture of magnetic gels: A review*, J. Phys.: Condens. Matter **30**, 063002 (2018).

[5] A. M. Menzel, *Mesoscopic characterization of magnetoelastic hybrid materials: Magnetic gels and elastomers, their particle-scale description, and scale-bridging links*, Arch. Appl. Mech. **89**, 17 (2019).

[6] Y. Li, J. Li, W. Li, and H. Du, *A state-of-the-art review on magnetorheological elastomer devices*, Smart Mater. Struct. **23**, 123001 (2014).

[7] H. Böse, T. Gerlach, and J. Ehrlich, *Magnetorheological elastomers — an underestimated class of soft actuator materials*, J. Intel. Mater. Syst. Struct. **32**, 1550 (2021).

[8] J. Sutrisno, A. Purwanto, and S. A. Mazlan, *Recent progress on magnetorheological solids: Materials, fabrication, testing, and applications*, Adv. Eng. Mater. **17**, 563 (2015).

[9] S. Bednarek, *The giant magnetostriction in ferromagnetic composites within an elastomer matrix*, Appl. Phys. A **68**, 63 (1999).

[10] J. M. Ginder, S. M. Clark, W. F. Schlotter, and M. E. Nichols, *Magnetostrictive phenomena in magnetorheological elastomers*, Int. J. Mod. Phys. B **16**, 2412 (2002).

[11] X. Guan, X. Dong, and J. Ou, *Magnetostrictive effect of magnetorheological elastomer*, J. Magn. Magn. Mater. **320**, 158 (2008).

[12] G. Diguet, E. Beaugnon, and J.-Y. Cavaillé, *From dipolar interactions of a random distribution of ferromagnetic particles to magnetostriction*, J. Magn. Magn. Mater. **321**, 396 (2009).

[13] G. Diguet, E. Beaugnon, and J. Y. Cavaillé, *Shape effect in the magnetostriction of ferromagnetic composite*, J. Magn. Magn. Mater. **322**, 3337 (2010).

[14] J. Maas and D. Uhlenbusch, *Experimental and theoretical analysis of the actuation behavior of magnetoactive elastomers*, Smart Mater. Struct. **25**, 104002 (2016).

[15] Y. Han, A. Mohla, X. Huang, W. Hong, and L. E. Faidley, *Magnetostriction and field stiffening of magneto-active elastomers*, Int. J. Appl. Mech. **7**, 1550001 (2015).

[16] D. Y. Borin, S. Odenbach, and G. V. Stepanov, *Stress induced by the striction of hybrid magnetoactive elastic composites*, J. Magn. Magn. Mater. **470**, 85 (2019).

[17] X. Gong, G. Liao, and S. Xuan, *Full-field deformation of magnetorheological elastomer under uniform magnetic field*, Appl. Phys. Lett. **100**, 211909 (2012).

[18] S. Abramchuk, E. Kramarenko, G. Stepanov, L. Nikitin, G. Filipcsei, A. Khokhlov, and M. Zrinyi, *Novel highly elastic magnetic materials for dampers and seals: Part I. Preparation and characterization of the elastic materials*, Polym. Adv. Technol. **18**, 883 (2007).

[19] D. V. Saveliev, I. A. Belyaeva, D. V. Chashin, L. Y. Fetisov, D. Romeis, W. Kettl, E. Y. Kramarenko, M. Saphiannikova, G. V. Stepanov, and M. Shamonin, *Giant extensional strain of magnetoactive elastomeric cylinders in uniform magnetic fields*, Materials **13**, 3297 (2020).

[20] C. Gollwitzer, A. Turanov, M. Krekhova, G. Lattermann, I. Rehberg, and R. Richter, *Measuring the deformation of a ferrogel sphere in a homogeneous magnetic field*, J. Chem. Phys. **128**, 164709 (2008).

[21] G. Filipcsei and M. Zrínyi, *Magnetodeformation effects and the swelling of ferrogels in a uniform magnetic field*, J. Phys.: Condens. Matter **22**, 276001 (2010).

[22] S. Qi, H. Guo, J. Fu, Y. Xie, M. Zhu, and M. Yu, *3D printed shape-programmable magneto-active soft matter for biomimetic applications*, Compos. Sci. Technol. **188**, 107973 (2020).

[23] Y. Zhang, Q. Wang, S. Yi, Z. Lin, C. Wang, Z. Chen, and L. Jiang, *4D printing of magnetoactive soft materials for on-demand magnetic actuation transformation*, ACS Appl. Mater. Inter. **13**, 4174 (2021).

[24] R. Bayaniahangar, S. B. Ahangar, Z. Zhang, B. P. Lee, and J. M. Pearce, *3-D printed soft magnetic helical coil actuators of iron oxide embedded polydimethylsiloxane*, Sens. Actuator B: Chem. **326**, 128781 (2021).

[25] Y. Kim, H. Yuk, R. Zhao, S. A. Chester, and X. Zhao, *Printing ferromagnetic domains for untethered fast-transforming soft materials*, Nature **558**, 274 (2018).

[26] E. Dohmen, A. Saloum, and J. Abel, *Field-structured magnetic elastomers based on thermoplastic polyurethane for fused filament fabrication*, Phil. Trans. R. Soc. A **378**, 20190257 (2020).

[27] A. Bastola, M. Paudel, and L. Li, *Dot-patterned hybrid magnetorheological elastomer developed by 3D printing*, J. Magn. Magn. Mater. **494**, 165825 (2020).

[28] J. E. Martin, R. A. Anderson, D. Read, and G. Gulley, *Magnetostriction of field-structured magnetoelastomers*, Phys. Rev. E **74**, 051507 (2006).

[29] J. Kim, S. E. Chung, S.-E. Choi, H. Lee, J. Kim, and S. Kwon, *Programming magnetic anisotropy in polymeric microactuators*, Nature Mater. **10**, 747 (2011).

[30] Z. Ma, A. W. Holle, K. Melde, T. Qiu, K. Poeppel, V. M. Kadiri, and P. Fischer, *Acoustic holographic cell patterning in a biocompatible hydrogel*, Adv. Mater. **32**, 1904181 (2020).

[31] M. Puljiz, S. Huang, G. K. Auernhammer, and A. M. Menzel, *Forces on rigid inclusions in elastic media and resulting matrix-mediated interactions*, Phys. Rev. Lett. **117**, 238003 (2016).

[32] X. Zhang, S. Peng, W. Wen, and W. Li, *Analysis and fabrication of patterned magnetorheological elastomers*, Smart Mater. Struct. **17**, 045001 (2008).

[33] E. Forster, M. Mayer, R. Rabindranath, H. Böse, G. Schlunck, G. J. Monkman, and M. Shamonin, *Patterning of ultrasoft, agglutinative magnetorheological elastomers*, J. Appl. Polym. Sci. **128**, 2508 (2013).

[34] L. J. Walpole, *An elastic singularity in a spherical inclusion: the Green tensor*, Proc. R. Soc. London A **458**, 705 (2002).

[35] L. Fischer, Coupling between magnetism and deformation in the case of magnetic elastomers, Master thesis, Düsseldorf, Heinrich-Heine-Universität, 2019.

[36] F. J. Vazquez-Perez, C. Gila-Vilchez, A. Leon-Cecilla, L. Álvarez de Cienfuegos, D. Borin, S. Odenbach, J. E. Martin, and M. T. Lopez-Lopez, *Fabrication and actuation of magnetic shape-memory materials*, ACS Appl. Mater. Interfaces **15**, 53017 (2023).

[37] A. M. Menzel, *Stimuli-responsive twist actuators made from soft elastic composite materials—linking mesoscopic and macroscopic descriptions*, J. Chem. Phys. **154**, 204902 (2021).

[38] N. Metropolis, A. W. Rosenbluth, M. N. Rosenbluth, A. H. Teller, and E. Teller, *Equation of state calculations by fast computing machines*, J. Chem. Phys. **21**, 1087 (1953).

[39] S. Kirkpatrick, C. D. Gelatt, and M. P. Vecchi, *Optimization by simulated annealing*, Science **220**, 671 (1983).

[40] D. Vanderbilt and S. G. Louie, *A Monte Carlo simulated annealing approach to optimization over continuous variables*, J. Comput. Phys. **56**, 259 (1984).

[41] M. Karabin and S. J. Stuart, *Simulated annealing with adaptive cooling rates*, J. Chem. Phys. **153**, 114103 (2020).

[42] G. Pessot, P. Cremer, D. Y. Borin, S. Odenbach, H. Löwen, and A. M. Menzel, *Structural control of elastic moduli in ferrogels and the importance of non-affine deformations*, J. Chem. Phys. **141**, 124904 (2014).

[43] B. A. Evans, B. L. Fiser, W. J. Prins, D. J. Rapp, A. R. Shields, D. R. Glass, and R. Superfine, *A highly tunable silicone-based magnetic elastomer with nanoscale homogeneity*, J. Magn. Magn. Mater. **324**, 501 (2012).

[44] D. Y. Borin, G. V. Stepanov, and S. Odenbach, *Tuning the tensile modulus of magnetorheological elastomers with magnetically hard powder*, J. Phys.: Conf. Ser. **412**, 012040 (2013).

[45] A. Zubarev, A. B. Bonhome-Espinosa, M. Alaminos, J. Duran, and M. T. Lopez-Lopez, *Rheological properties of magnetic biogels*, Arch. Appl. Mech. **89**, 91 (2019).

[46] T. I. Volkova, V. Böhm, T. Kaufhold, J. Popp, F. Becker, D. Y. Borin, G. V. Stepanov, and K. Zimmermann, *Motion behaviour of magneto-sensitive elastomers controlled by an external magnetic field for sensor applications*, J. Magn. Magn. Mater. **431**, 262 (2017).

[47] Y. Han, W. Hong, and L. E. Faidley, *Field-stiffening effect of magneto-rheological elastomers*, Int. J. Solids Struct. **50**, 2281 (2013).

[48] J. Yang, S. Sun, H. Du, W. Li, G. Alici, and H. Deng, *A novel magnetorheological elastomer isolator with negative changing stiffness for vibration reduction*, Smart Mater. Struct. **23**, 105023 (2014).

[49] Y. An and M. T. Shaw, *Actuating properties of soft gels with ordered iron particles: Basis for a shear actuator*, Smart Mater. Struct. **12**, 157 (2003).

[50] E. Allahyarov, H. Löwen, and L. Zhu, *A simulation study of the electrostriction effects in dielectric elastomer composites containing polarizable inclusions with different spatial distributions*, Phys. Chem. Chem. Phys. **17**, 32479 (2015).

[51] B. Liu and M. T. Shaw, *Electrorheology of filled silicone elastomers*, J. Rheol. **45**, 641 (2001).

[52] B. Burkel and J. Notbohm, *Mechanical response of collagen networks to nonuniform microscale loads*, Soft Matter **13**, 5749 (2017).

[53] Z. M. Sherman, M. P. Howard, B. A. Lindquist, R. B. Jadrich, and T. M. Truskett, *Inverse methods for design of soft materials*, J. Chem. Phys. **152**, (2020).

[54] L. D. Landau and E. M. Lifshitz, *Theory of Elasticity* (Elsevier, Oxford, 1986).

[55] M. Puljiz and A. M. Menzel, *Memory-based mediated interactions between rigid particulate inclusions in viscoelastic environments*, Phys. Rev. E **99**, 012601 (2019).

[56] D. Tabor, *The bulk modulus of rubber*, Polymer **35**, 2759 (1994).

[57] M. Doi, *Gel dynamics*, J. Phys. Soc. Jpn. **78**, 052001 (2009).

[58] U. Chippada, N. Langrana, and B. Yurke, *Complete mechanical characterization of soft media using nonspherical rods*, J. Appl. Phys. **106**, 063528 (2009).

[59] C. Huang and L. Chen, *Negative Poisson's ratio in modern functional materials*, Advanced Materials **28**, 8079 (2016).

[60] X. Ren, R. Das, P. Tran, T. D. Ngo, and Y. M. Xie, *Auxetic metamaterials and structures: A review*, Smart Materials and Structures **27**, 023001 (2018).

[61] F. Scarpa, W. Bullough, and P. Lumley, *Trends in acoustic properties of iron particle seeded auxetic polyurethane foam*, Proc. Inst. Mech. Eng. C **218**, 241 (2004).

[62] R. Lakes, *Foam structures with a negative Poisson's ratio*, Science **235**, 1038 (1987).

[63] N. Chan and K. Evans, *Fabrication methods for auxetic foams*, Journal of Materials Science **32**, 5945 (1997).

[64] B. Caddock and K. Evans, *Microporous materials with negative Poisson's ratios. I. microstructure and mechanical properties*, Journal of Physics D: Applied Physics **22**, 1877 (1989).

[65] A.-L. Cauchy, *Exercices de Mathématiques* (Bure Frères, Paris, 1828).

[66] L. Kelvin, *Note on the integration of the equations of equilibrium of an elastic solid*, Cambridge and Dublin Mathematical Journal **3**, 87 (1848).

[67] M. Puljiz and A. M. Menzel, *Forces and torques on rigid inclusions in an elastic environment: Resulting matrix-mediated interactions, displacements, and rotations*, Phys. Rev. E **95**, 053002 (2017).

[68] S. Kim and S. Karrila, *Microhydrodynamics: Principles and Selected Applications* (Butterworth-Heinemann, Boston, 1991).

[69] M. Puljiz, S. Huang, K. A. Kalina, J. Nowak, S. Odenbach, M. Kästner, G. K. Auernhammer, and A. M. Menzel, *Reversible magnetomechanical collapse: Virtual touching and detachment of rigid inclusions in a soft elastic matrix*, Soft Matter **14**, 6809 (2018).

[70] L. Fischer and A. M. Menzel, *Magnetostriction in magnetic gels and elastomers as a function of the internal structure and particle distribution*, J. Chem. Phys. **151**, 114906 (2019).

[71] A. M. Menzel, *Force-induced elastic matrix-mediated interactions in the presence of a rigid wall*, Soft Matter **13**, 3373 (2017).

[72] M. C. Wapler, J. Leupold, I. Dragonu, D. von Elverfeld, M. Zaitsev, and U. Wallrabe, *Magnetic properties of materials for MR engineering, micro-MR and beyond*, J. Magn. Reson. **242**, 233 (2014).

[73] M. Widdrat, Formation and alteration of magnetite nanoparticles, PhD dissertation, Universität Potsdam, 2014.

[74] T. Saragi, B. Permana, A. Therigan, H. D. Sinaga, T. Maulana, and R. Risdiana, *Study of magnetic properties and relaxation time of nanoparticle Fe3O4-SiO2*, Materials **15**, 1573 (2022).

[75] J.-L. Dormann, D. Fiorani, and E. Tronc, *Magnetic relaxation in fine-particle systems*, Adv. Chem. Phys. **98**, 283 (1997).

[76] M. I. Shliomis, *Magnetic fluids*, Sov. Phys. Usp. **17**, 153 (1974).

[77] M. Kole and S. Khandekar, *Engineering applications of ferrofluids: A review*, J. Magn. Magn. Mater. **537**, 168222 (2021).

[78] J. D. Jackson, *Classical Electrodynamics* (Wiley, New York, 1999).

[79] R. Weeber, F. Nestler, F. Weik, M. Pippig, D. Potts, and C. Holm, *Accelerating the calculation of dipolar interactions in particle based simulations with open boundary conditions by means of the P2NFFT method*, J. Comput. Phys. **391**, 243 (2019).

[80] S. J. Erickson, R. Prost, and M. Timins, *The "magic angle" effect: background physics and clinical relevance.*, Radiology **188**, 23 (1993).

[81] E. T. Whittaker and G. N. Watson, *A Course of Modern Analysis: an Introduction to the General Theory of Infinite Processes and of Analytic Functions; with an Account of the Principal Transcendental Functions* (Cambridge University Press, Cambridge, 1920).

[82] R. Cornell and U. Schwertmann, *The Iron Oxides: Structure, Properties, Reactions, Occurrences and Uses* (John Wiley & Sons, Weinheim, 2003).

[83] J. L. Kirschvink, A. Kobayashi-Kirschvink, and B. J. Woodford, *Magnetite biomineralization in the human brain.*, Proc. Natl. Acad. Sci. U.S.A. **89**, 7683 (1992).

[84] A. M. Biller, O. V. Stolbov, and Y. L. Raikher, *Modeling of particle interactions in magnetorheological elastomers*, J. Appl. Phys. **116**, 114904 (2014).

[85] P. Metsch, D. Romeis, K. A. Kalina, A. Raßloff, M. Saphiannikova, and M. Kästner, *Magneto-mechanical coupling in magneto-active elastomers*, Materials **14**, 434 (2021).

[86] A. M. Biller, O. V. Stolbov, and Y. L. Raikher, *Mesoscopic magnetomechanical hysteresis in a magnetorheological elastomer*, Phys. Rev. E **92**, 023202 (2015).

[87] M. Zrínyi, L. Barsi, and A. Büki, *Deformation of ferrogels induced by nonuniform magnetic fields*, J. Chem. Phys. **104**, 8750 (1996).

[88] P. Metsch, K. Kalina, J. Brummund, and M. Kästner, *Two-and three-dimensional modeling approaches in magneto-mechanics: A quantitative comparison*, Arch. Appl. Mech. **89**, 47 (2019).

[89] M. Roghani, D. Romeis, and M. Saphiannikova, *Effect of microstructure evolution on the mechanical behavior of magneto-active elastomers with different matrix stiffness*, Soft Matter **19**, 6387 (2023).

[90] H. Schmidt, B. B. Straub, D. Sindersberger, U. Bröckel, G. J. Monkman, and G. K. Auernhammer, *Collision and separation of nickel particles embedded in a polydimethylsiloxan matrix under a rotating magnetic field: A strong magneto active function*, Colloid Polym. Sci. **299**, 955 (2021).

[91] H. Schmidt, Mesoscale modeling of magnetic elastomers and gels – theory and simulations, PhD dissertation, Darmstadt, Technische Universität, 2021.

[92] K. A. Kalina, J. Brummund, P. Metsch, M. Kästner, D. Y. Borin, J. M. Linke, and S. Odenbach, *Modeling of magnetic hystereses in soft MREs filled with NdFeB particles*, Smart Mater. Struct. **26**, 105019 (2017).

[93] P. Gebhart, Skalenübergreifende Modellierung magneto-aktiver Polymere auf Grundlage energie-basierter Variationsprinzipien, PhD dissertation, Dresden, Technische Universität, 2024.

[94] D. Mukherjee and K. Danas, *An evolving switching surface model for ferromagnetic hysteresis*, J. Appl. Phys. **125**, (2019).

[95] A. K. Bastola, M. Paudel, L. Li, and W. Li, *Recent progress of magnetorheological elastomers: A review*, Smart Materials and Structures **29**, 123002 (2020).

[96] R. Ahamed, S.-B. Choi, and M. M. Ferdaus, *A state of art on magneto-rheological materials and their potential applications*, J. Intel. Mater. Syst. Struct. **29**, 2051 (2018).

[97] J. Rabinow, *The magnetic fluid clutch*, Electr. Eng. **67**, 1167 (1948).

[98] J. R. Morillas and J. de Vicente, *Magnetorheology: A review*, Soft Matter **16**, 9614 (2020).

[99] S. Wahid, I. Ismail, S. Aid, and M. Rahim, *Magneto-rheological defects and failures: A review*, IOP Conf. Ser.: Mat. Sci. Eng. **114**, 012101 (2016).

[100] C. Scherer and A. M. Figueiredo Neto, *Ferrofluids: Properties and applications*, Braz. J. Phys. **35**, 718 (2005).

[101] K. Raj and R. Moskowitz, *Commercial applications of ferrofluids*, J. Magn. Magn. Mater. **85**, 233 (1990).

[102] L. J. Felicia, S. Vinod, and J. Philip, *Recent advances in magnetorheology of ferrofluids (magnetic nanofluids) — a critical review*, J. Nanofluids **5**, 1 (2016).

[103] M. Cowley and R. E. Rosensweig, *The interfacial stability of a ferromagnetic fluid*, J. Fluid Mech. **30**, 671 (1967).

[104] S. S. Papell. *Low viscosity magnetic fluid obtained by the colloidal suspension of magnetic particles*, (U.S. Patent 3 215 572, filed Oct. 1963). Available online: https://ntrs.nasa.gov/api/citations/19700030808/downloads/19700030808.pdf.

[105] M. T. Lopez-Lopez, J. D. G. Durán, L. Y. Iskakova, and A. Y. Zubarev, *Mechanics of magnetopolymer composites: A review*, J. Nanofluids **5**, 479 (2016).

[106] P. Ilg, *Stimuli-responsive hydrogels cross-linked by magnetic nanoparticles*, Soft Matter **9**, 3465 (2013).

[107] M. R. Jolly, J. D. Carlson, B. C. Muñoz, and T. A. Bullions, *The magnetoviscoelastic response of elastomer composites consisting of ferrous particles embedded in a polymer matrix*, J. Intel. Mater. Syst. Struct. **7**, 613 (1996).

[108] A. V. Chertovich, G. V. Stepanov, E. Y. Kramarenko, and A. R. Khokhlov, *New composite elastomers with giant magnetic response*, Macromolecul. Mater. Eng. **295**, 336 (2010).

[109] J.-H. Koo, A. Dawson, and H.-J. Jung, *Characterization of actuation properties of magnetorheological elastomers with embedded hard magnetic particles*, J. Intel. Mater. Syst. Struct. **23**, 1049 (2012).

[110] M. Schümann, D. Y. Borin, S. Huang, G. K. Auernhammer, R. Müller, and S. Odenbach, *A characterisation of the magnetically induced movement of NdFeB-particles in magnetorheological elastomers*, Smart Mater. Struct. **26**, 095018 (2017).

[111] G. Stepanov, D. Y. Borin, A. Bakhtiiarov, and P. Storozhenko, *Magnetic properties of hybrid elastomers with magnetically hard fillers: rotation of particles*, Smart Mater. Struct. **26**, 035060 (2017).

[112] G. Stepanov, D. Y. Borin, A. Bakhtiiarov, and P. Storozhenko, *Influence of the size of magnetic filler particles on the properties of hybrid magnetic elastomer with magnetically hard filler*, J. Magn. Magn. Mater. **498**, 166071 (2020).

[113] D. Y. Borin, G. Stepanov, et al., *Oscillation measurements on magnetoactive elastomers with complex composition*, J. Optoelectron. Adv. Mater. **15**, 249 (2013).

[114] J. M. Linke, D. Y. Borin, and S. Odenbach, *First-order reversal curve analysis of magnetoactive elastomers*, RSC Adv. **6**, 100407 (2016).

[115] D. Borin, G. Stepanov, and E. Dohmen, *Hybrid magnetoactive elastomer with a soft matrix and mixed powder*, Arch. Appl. Mech. **89**, 105 (2019).

[116] Y. Alapan, A. C. Karacakol, S. N. Guzelhan, I. Isik, and M. Sitti, *Reprogrammable shape morphing of magnetic soft machines*, Sci. Adv. **6**, eabc6414 (2020).

[117] H. Böse, *Viscoelastic properties of silicone-based magnetorheological elastomers*, Int. J. Mod. Phys. B **21**, 4790 (2007).

[118] M. Lokander and B. Stenberg, *Improving the magnetorheological effect in isotropic magnetorheological rubber materials*, Polym. Test. **22**, 677 (2003).

[119] T. Borbáth, S. Günther, D. Y. Borin, T. Gundermann, and S. Odenbach, *XμCT analysis of magnetic field-induced phase transitions in magnetorheological elastomers*, Smart Mater. Struct. **21**, 105018 (2012).

[120] K. Danas, S. Kankanala, and N. Triantafyllidis, *Experiments and modeling of iron-particle-filled magnetorheological elastomers*, J. Mech. Phys. Solids **60**, 120 (2012).

[121] D. Borin, *Targeted patterning of magnetic microparticles in a polymer composite*, Phil. Trans. R. Soc. A **378**, 20190256 (2020).

[122] D. Günther, D. Y. Borin, S. Günther, and S. Odenbach, *X-ray micro-tomographic characterization of field-structured magnetorheological elastomers*, Smart Mater. Struct. **21**, 015005 (2011).

[123] M. Schümann and S. Odenbach, *In-situ observation of the particle microstructure of magnetorheological elastomers in presence of mechanical strain and magnetic fields*, J. Magn. Magn. Mater. **441**, 88 (2017).

[124] T. Gundermann, P. Cremer, H. Löwen, A. M. Menzel, and S. Odenbach, *Statistical analysis of magnetically soft particles in magnetorheological elastomers*, Smart Mater. Struct. **26**, 045012 (2017).

[125] M. Schümann, J. Morich, S. Günther, and S. Odenbach, *The evaluation of anisotropic particle structures of magnetorheological elastomers by means of pair correlation function*, J. Magn. Magn. Mater. **502**, 166537 (2020).

[126] M. Schümann and S. Odenbach, *The microstructure of magnetorheological materials characterized by means of computed X-ray microtomography*, Phys. Sci. Rev **8**, 1487 (2023).

[127] R. Messing, N. Frickel, L. Belkoura, R. Strey, H. Rahn, S. Odenbach, and A. M. Schmidt, *Cobalt ferrite nanoparticles as multifunctional cross-linkers in PAAm ferrohydrogels*, Macromolecules **44**, 2990 (2011).

[128] L. Roeder, M. Reckenthaler, L. Belkoura, S. Roitsch, R. Strey, and A. Schmidt, *Covalent ferrohydrogels based on elongated particulate cross-linkers*, Macromolecules **47**, 7200 (2014).

[129] N. Frickel, R. Messing, T. Gelbrich, and A. M. Schmidt, *Functional silanes as surface modifying primers for the preparation of highly stable and well-defined magnetic polymer hybrids*, Langmuir **26**, 2839 (2009).

[130] N. Frickel, R. Messing, and A. M. Schmidt, *Magneto-mechanical coupling in $CoFe_2O_4$-linked PAAm ferrohydrogels*, J. Mater. Chem. **21**, 8466 (2011).

[131] J. Seifert, K. Koch, M. Hess, and A. M. Schmidt, *Magneto-mechanical coupling of single domain particles in soft matter systems*, Phys. Sci. Rev. **7**, 1237 (2022).

[132] Z. Rigbi and L. Jilken, *The response of an elastomer filled with soft ferrite to mechanical and magnetic influences*, J. Magn. Magn. Mater. **37**, 267 (1983).

[133] M. R. Jolly, J. D. Carlson, and B. C. Muñoz, *A model of the behaviour of magnetorheological materials*, Smart Mater. Struct. **5**, 607 (1996).

[134] G. Stepanov, S. Abramchuk, D. Grishin, L. Nikitin, E. Y. Kramarenko, and A. Khokhlov, *Effect of a homogeneous magnetic field on the viscoelastic behavior of magnetic elastomers*, Polymer **48**, 488 (2007).

[135] H. Böse and R. Röder, *Magnetorheological elastomers with high variability of their mechanical properties*, J. Phys.: Conf. Ser. **149**, 012090 (2009).

[136] L. Chen, X.-l. Gong, W.-q. Jiang, J.-j. Yao, H.-x. Deng, and W.-h. Li, *Investigation on magnetorheological elastomers based on natural rubber*, J. Mater. Sci. **42**, 5483 (2007).

[137] N. Chiba, K. Yamamoto, T. Hojo, M. Kawai, and T. Mitsumata, *Wide-range modulation of dynamic modulus and loss tangent for magnetic elastomers containing submilimeter magnetic particles*, Chem. Lett. **42**, 253 (2013).

[138] V. V. Sorokin, G. V. Stepanov, M. Shamonin, G. J. Monkman, A. R. Khokhlov, and E. Y. Kramarenko, *Hysteresis of the viscoelastic properties and the normal force in magnetically and mechanically soft magnetoactive elastomers: Effects of filler composition, strain amplitude and magnetic field*, Polymer **76**, 191 (2015).

[139] G. Pessot, M. Schümann, T. Gundermann, S. Odenbach, H. Löwen, and A. M. Menzel, *Tunable dynamic moduli of magnetic elastomers: From characterization by X-ray micro-computed tomography to mesoscopic modeling*, J. Phys.: Condens. Matter **30**, 125101 (2018).

[140] C. Gila-Vilchez, A. B. Bonhome-Espinosa, P. Kuzhir, A. Zubarev, J. D. Duran, and M. T. Lopez-Lopez, *Rheology of magnetic alginate hydrogels*, J. Rheol. **62**, 1083 (2018).

[141] M. Watanabe, J. Ikeda, Y. Takeda, M. Kawai, and T. Mitsumata, *Effect of sonication time on magnetorheological effect for monomodal magnetic elastomers*, Gels **4**, 49 (2018).

[142] T. A. Nadzharyan, M. Shamonin, and E. Y. Kramarenko, *Theoretical modeling of magnetoactive elastomers on different scales: a state-of-the-art review*, Polymers **14**, 4096 (2022).

[143] Y. L. Raikher and O. Stolbov, *Magnetodeformational effect in ferrogel samples*, J. Magn. Magn. Mater. **258**, 477 (2003).

[144] R. Weeber, P. Kreissl, and C. Holm, *Magnetic field controlled behavior of magnetic gels studied using particle-based simulations*, Phys. Sci. Rev. **8**, 1465 (2023).

[145] J. Joule, in *The Annals of Electricity, Magnetism, and Chemistry; and Guardian of Experimental Science* (Sherwood, Gilbert and Piper, Manchester, 1842).

[146] A. Clark, H. Savage, and M. Spano, *Effect of stress on the magnetostriction and magnetization of single crystal* $Tb_{.27}Dy_{.73}Fe_2$, IEEE T. Magn. **20**, 1443 (1984).

[147] M. Puljiz and A. M. Menzel, *Displacement field around a rigid sphere in a compressible elastic environment, corresponding higher-order Faxén relations, as well as higher-order displaceability and rotateability matrices*, Phys. Rev. E **99**, 053002 (2019).

[148] P. Metsch, K. A. Kalina, C. Spieler, and M. Kästner, *A numerical study on magnetostrictive phenomena in magnetorheological elastomers*, Comp. Mater. Sci. **124**, 364 (2016).

[149] G. Zhou and Z. Jiang, *Deformation in magnetorheological elastomer and elastomer–ferromagnet composite driven by a magnetic field*, Smart Mater. Struct. **13**, 309 (2004).

[150] T. Gundermann and S. Odenbach, *Investigation of the motion of particles in magnetorheological elastomers by X-*μ*CT*, Smart Mater. Struct. **23**, 105013 (2014).

[151] N. Kchit, P. Lancon, and G. Bossis, *Thermoresistance and giant magnetoresistance of magnetorheological elastomers*, J. Phys. D: Appl. Phys. **42**, 105506 (2009).

[152] N. Kchit and G. Bossis, *Electrical resistivity mechanism in magnetorheological elastomer*, J. Phys. D: Appl. Phys. **42**, 105505 (2009).

[153] J. L. Mietta, P. I. Tamborenea, and R. M. Negri, *Anisotropic magnetoresistivity in structured elastomer composites: Modelling and experiments*, Soft Matter **12**, 6430 (2016).

[154] D. Diaz-Bleis, C. Vales-Pinzón, Y. Freile-Pelegrín, and J. J. Alvarado-Gil, *Thermal characterization of magnetically aligned carbonyl iron/agar composites*, Carbohyd. Polym. **99**, 84 (2014).

[155] N. W. Pech-May, C. Vales-Pinzon, A. Vega-Flick, A. Oleaga, A. Salazar, J. M. Yanez-Limon, and J. J. Alvarado-Gil, *Heat transport in epoxy and polyester carbonyl iron microcomposites: The effect of concentration and temperature*, J. Compos. Mater. **52**, 1331 (2018).

[156] G. Cha, Y. S. Ju, L. A. Ahuré, and N. M. Wereley, *Experimental characterization of thermal conductance switching in magnetorheological fluids*, J. Appl. Phys. **107**, (2010).

[157] I. Forero-Sandoval, A. Vega-Flick, J. Alvarado-Gil, and R. Medina-Esquivel, *Study of thermal conductivity of magnetorheological fluids using the thermal-wave resonant cavity and its relationship with the viscosity*, Smart Mater. Struct. **26**, 025010 (2016).

[158] T. I. Becker, V. Böhm, J. C. Vega, S. Odenbach, Y. L. Raikher, and K. Zimmermann, *Magnetic-field-controlled mechanical behavior of magneto-sensitive elastomers in applications for actuator and sensor systems*, Arch. Appl. Mech. **89**, 133 (2019).

[159] R. Snyder, V. Nguyen, and R. Ramanujan, *Design parameters for magneto-elastic soft actuators*, Smart Mater. Struct. **19**, 055017 (2010).

[160] S.-Y. Tang, X. Zhang, S. Sun, D. Yuan, Q. Zhao, S. Yan, L. Deng, G. Yun, J. Zhang, S. Zhang, and W. Li, *Versatile microfluidic platforms enabled by novel magnetorheological elastomer microactuators*, Adv. Funct. Mater. **28**, 1705484 (2018).

[161] S. Wu, W. Hu, Q. Ze, M. Sitti, and R. Zhao, *Multifunctional magnetic soft composites: A review*, Multifunct. Mater. **3**, 042003 (2020).

[162] W. Hu, G. Z. Lum, M. Mastrangeli, and M. Sitti, *Small-scale soft-bodied robot with multimodal locomotion*, Nature **554**, 81 (2018).

[163] J. Thévenot, H. Oliveira, O. Sandre, and S. Lecommandoux, *Magnetic responsive polymer composite materials*, Chem. Soc. Rev. **42**, 7099 (2013).

[164] P. Jauch, A. Weidner, S. Riedel, N. Wilharm, S. Dutz, and S. G. Mayr, *Collagen–iron oxide nanoparticle based ferrogel: Large reversible magnetostrains with potential for bioactuation*, Multifunct. Mater. **3**, 035001 (2020).

[165] J. Spangenberg, D. Kilian, C. Czichy, T. Ahlfeld, A. Lode, S. Günther, S. Odenbach, and M. Gelinsky, *Bioprinting of magnetically deformable scaffolds*, ACS Biomater. Sci. Eng. **7**, 648 (2021).

[166] Y. Kim and X. Zhao, *Magnetic soft materials and robots*, Chem. Rev. **122**, 5317 (2022).

[167] H.-X. Deng, X.-L. Gong, and L.-H. Wang, *Development of an adaptive tuned vibration absorber with magnetorheological elastomer*, Smart Mater. Struct. **15**, N111 (2006).

[168] G. Liao, X. Gong, S. Xuan, C. Kang, and L. Zong, *Development of a real-time tunable stiffness and damping vibration isolator based on magnetorheological elastomer*, J. Intel. Mater. Syst. Struct. **23**, 25 (2012).

[169] V. S. Molchanov, G. V. Stepanov, V. G. Vasiliev, E. Y. Kramarenko, A. R. Khokhlov, Z.-D. Xu, and Y.-Q. Guo, *Viscoelastic properties of magnetorheological elastomers for damping applications*, Macromolecul. Mater. Eng. **299**, 1116 (2014).

[170] T. Sun, X. Gong, W. Jiang, J. Li, Z. Xu, and W. Li, *Study on the damping properties of magnetorheological elastomers based on cis-polybutadiene rubber*, Polym. Test. **27**, 520 (2008).

[171] Y. Li, J. Li, T. Tian, and W. Li, *A highly adjustable magnetorheological elastomer base isolator for applications of real-time adaptive control*, Smart Mater. Struct. **22**, 095020 (2013).

[172] V. Q. Nguyen, A. S. Ahmed, and R. V. Ramanujan, *Morphing soft magnetic composites*, Adv. Mater. **24**, 4041 (2012).

[173] M. Zrínyi and D. Szabó, *Muscular contraction mimicked by magnetic gels*, Int. J. Mod. Phys. B **15**, 557 (2001).

[174] H. Böse, R. Rabindranath, and J. Ehrlich, *Soft magnetorheological elastomers as new actuators for valves*, J. Intel. Mater. Syst. Struct. **23**, 989 (2012).

[175] J.-H. Yoo and N. M. Wereley, *Design of a high-efficiency magnetorheological valve*, J. Intel. Mater. Syst. Struct. **13**, 679 (2002).

[176] M. Behrooz and F. Gordaninejad, *A flexible micro fluid transport system featuring magnetorheological elastomer*, Smart Mater. Struct. **25**, 025011 (2016).

[177] D. Collin, G. K. Auernhammer, O. Gavat, P. Martinoty, and H. R. Brand, *Frozen-in magnetic order in uniaxial magnetic gels: Preparation and physical properties*, Macromol. Rapid Commun. **24**, 737 (2003).

[178] Y. L. Raikher, O. V. Stolbov, and G. V. Stepanov, *Shape instability of a magnetic elastomer membrane*, J. Phys. D: Appl. Phys. **41**, 152002 (2008).

[179] R. Fuhrer, E. K. Athanassiou, N. A. Luechinger, and W. J. Stark, *Crosslinking metal nanoparticles into the polymer backbone of hydrogels enables preparation of soft, magnetic field-driven actuators with muscle-like flexibility*, Small **5**, 383 (2009).

[180] M. M. Schmauch, S. R. Mishra, B. A. Evans, O. D. Velev, and J. B. Tracy, *Chained iron microparticles for directionally controlled actuation of soft robots*, ACS Appl. Mater. Interfaces **9**, 11895 (2017).

[181] L. Hines, K. Petersen, G. Z. Lum, and M. Sitti, *Soft actuators for small-scale robotics*, Adv. Mater. **29**, 1603483 (2017).

[182] K. Zimmermann, V. A. Naletova, I. Zeidis, V. A. Turkov, E. Kolev, M. V. Lukashevich, and G. V. Stepanov, *A deformable magnetizable worm in a magnetic field — a prototype of a mobile crawling robot*, J. Magn. Magn. Mater. **311**, 450 (2007).

[183] J. Chavez, V. Böhm, T. I. Becker, S. Gast, I. Zeidis, and K. Zimmermann, *Actuators based on a controlled particle-matrix interaction in magnetic hybrid materials for applications in locomotion and manipulation systems*, Phys. Sci. Rev. **7**, 1263 (2020).

[184] T. Kimura, Y. Umehara, and F. Kimura, *Magnetic field responsive silicone elastomer loaded with short steel wires having orientation distribution*, Soft Matter **8**, 6206 (2012).

[185] T. I. Becker, Y. L. Raikher, O. V. Stolbov, V. Böhm, and K. Zimmermann, *Magnetoactive elastomers for magnetically tunable vibrating sensor systems*, Phys. Sci. Rev. **7**, 1063 (2020).

[186] T.-Y. Liu, S.-H. Hu, T.-Y. Liu, D.-M. Liu, and S.-Y. Chen, *Magnetic-sensitive behavior of intelligent ferrogels for controlled release of drug*, Langmuir **22**, 5974 (2006).

[187] C. S. Brazel, *Magnetothermally-responsive nanomaterials: Combining magnetic nanostructures and thermally-sensitive polymers for triggered drug release*, Pharm. Res. **26**, 644 (2009).

[188] J. K. Oh and J. M. Park, *Iron oxide-based superparamagnetic polymeric nanomaterials: Design, preparation, and biomedical application*, Prog. Poly. Sci. **36**, 168 (2011).

[189] R. Weeber, S. Kantorovich, and C. Holm, *Deformation mechanisms in 2D magnetic gels studied by computer simulations*, Soft Matter **8**, 9923 (2012).

[190] R. Weeber, S. Kantorovich, and C. Holm, *Ferrogels cross-linked by magnetic nanoparticles – deformation mechanisms in two and three dimensions studied by means of computer simulations*, J. Magn. Magn. Mater. **383**, 262 (2015).

[191] R. Weeber, P. Kreissl, and C. Holm, *Studying the field-controlled change of shape and elasticity of magnetic gels using particle-based simulations*, Arch. Appl. Mech. **89**, 3 (2019).

[192] R. Weeber, S. Kantorovich, and C. Holm, *Ferrogels cross-linked by magnetic particles: Field-driven deformation and elasticity studied using computer simulations*, J. Chem. Phys. **143**, 154901 (2015).

[193] G. Pessot, R. Weeber, C. Holm, H. Löwen, and A. M. Menzel, *Towards a scale-bridging description of ferrogels and magnetic elastomers*, J. Phys.: Condens. Matter **27**, 325105 (2015).

[194] E. Jarkova, H. Pleiner, H.-W. Müller, and H. R. Brand, *Hydrodynamics of isotropic ferrogels*, Phys. Rev. E **68**, 041706 (2003).

[195] S. Bohlius, H. R. Brand, and H. Pleiner, *Macroscopic dynamics of uniaxial magnetic gels*, Phys. Rev. E **70**, 061411 (2004).

[196] T. Potisk, H. Pleiner, and H. R. Brand, *Influence of tetrahedral order on ferromagnetic gel phases*, Eur. Phys. J. E **42**, 35 (2019).

[197] A. Attaran, J. Brummund, and T. Wallmersperger, *Modeling and finite element simulation of the magneto-mechanical behavior of ferrogels*, J. Magn. Magn. Mater. **431**, 188 (2017).

[198] P. Gebhart and T. Wallmersperger, *A general framework for the modeling of porous ferrogels at finite strains*, J. Mech. Phys. Solids **122**, 69 (2019).

[199] Y. L. Raikher and O. Stolbov, *Magnetodeformational effect in ferrogel objects*, J. Magn. Magn. Mater. **289**, 62 (2005).

[200] Y. L. Raikher and O. Stolbov, *Deformation of an ellipsoidal ferrogel sample in a uniform magnetic field*, J. Appl. Mech. Tech. Phys. **46**, 434 (2005).

[201] K. Morozov, M. Shliomis, and H. Yamaguchi, *Magnetic deformation of ferrogel bodies: Procrustes effect*, Phys. Rev. E **79**, 040801 (2009).

[202] K. A. Kalina, P. Metsch, and M. Kästner, *Microscale modeling and simulation of magnetorheological elastomers at finite strains: A study on the influence of mechanical preloads*, Int. J. Solids Struct. **102**, 286 (2016).

[203] M. A. Annunziata, A. M. Menzel, and H. Löwen, *Hardening transition in a one-dimensional model for ferrogels*, J. Chem. Phys. **138**, 204906 (2013).

[204] G. Pessot, H. Löwen, and A. M. Menzel, *Dynamic elastic moduli in magnetic gels: Normal modes and linear response*, J. Chem. Phys. **145**, 104904 (2016).

[205] R. Weeber and C. Holm. arXiv preprint, arXiv:1704.06578 (2017).

[206] D. Ivaneyko, V. Toshchevikov, and M. Saphiannikova, *Dynamic-mechanical behaviour of anisotropic magneto-sensitive elastomers*, Polymer **147**, 95 (2018).

[207] S. Goh, A. M. Menzel, and H. Löwen, *Dynamics in a one-dimensional ferrogel model: Relaxation, pairing, shock-wave propagation*, Phys. Chem. Chem. Phys. **20**, 15037 (2018).

[208] I. S. Novikau, P. A. Sánchez, and S. S. Kantorovich, *The influence of an applied magnetic field on the self-assembly of magnetic nanogels*, J. Mol. Liq. **307**, 112902 (2020).

[209] A. B. Dobroserdova, E. V. Novak, and S. S. Kantorovich, *Switching-field and first-order-reversal-curve distribution measurements in magnetic elastomers by molecular dynamics simulations: Accounting for polydispersity*, Phys. Rev. E **107**, 044606 (2023).

[210] M. Kot, H. Nagahashi, and P. Szymczak, *Elastic moduli of simple mass spring models*, Vis. Comp. **31**, 1339 (2015).

[211] M. Ostoja-Starzewski, *Lattice models in micromechanics*, Appl. Mech. Rev. **55**, 35 (2002).

[212] D. S. Wood and P. J. Camp, *Modeling the properties of ferrogels in uniform magnetic fields*, Phys. Rev. E **83**, 011402 (2011).

[213] D. Ivaneyko, V. P. Toshchevikov, M. Saphiannikova, and G. Heinrich, *Magneto-sensitive elastomers in a homogeneous magnetic field: A regular rectangular lattice model*, Macromol. Theory Simul. **20**, 411 (2011).

[214] D. Ivaneyko, V. Toshchevikov, M. Saphiannikova, and G. Heinrich, *Effects of particle distribution on mechanical properties of magneto-sensitive elastomers in a homogeneous magnetic field*, Condens. Matter Phys. **15**, 33601 (2012).

[215] D. Yaremchuk, D. Ivaneyko, and J. Ilnytskyi, *Magnetostriction in the magneto-sensitive elastomers with inhomogeneously magnetized particles: Pairwise interaction approximation*, J. Magn. Magn. Mater. **589**, 171554 (2024).

[216] P. Cremer, M. Heinen, A. Menzel, and H. Löwen, *A density functional approach to ferrogels*, J. Phys.: Condens. Matter **29**, 275102 (2017).

[217] S. Goh, R. Wittmann, A. M. Menzel, and H. Löwen, *Classical density functional theory for a two-dimensional isotropic ferrogel model with labeled particles*, Phys. Rev. E **100**, 012605 (2019).

[218] S. Goh, A. M. Menzel, R. Wittmann, and H. Löwen, *Density functional approach to elastic properties of three-dimensional dipole-spring models for magnetic gels*, J. Chem. Phys. **158**, 054909 (2023).

[219] S. Richter, C. Deters, and A. Menzel, *Rotating spherical particle in a continuous viscoelastic medium—a microrheological example situation*, Europhys. Lett. **134**, 68002 (2021).

[220] S. K. Richter and A. M. Menzel, *Mediated interactions between rigid inclusions in two-dimensional elastic or fluid films*, Phys. Rev. E **105**, 014609 (2022).

[221] T. Lutz, A. M. Menzel, and A. Daddi-Moussa-Ider, *Internal sites of actuation and activation in thin elastic films and membranes of finite thickness*, Phys. Rev. E **109**, 054802 (2024).

[222] T. Lutz, S. K. Richter, and A. M. Menzel, *Effect of boundaries on displacements and motion in two-dimensional fluid or elastic films and membranes*, Phys. Rev. E **106**, 054609 (2022).

[223] O. Stolbov and Y. Raikher, *Large-scale shape transformations of a sphere made of a magnetoactive elastomer*, Polymers **12**, 2933 (2020).

[224] K. A. Kalina, A. Raßloff, M. Wollner, P. Metsch, J. Brummund, and M. Kästner, *Multiscale modeling and simulation of magneto-active elastomers based on experimental data*, Phys. Sci. Rev. **8**, 1 (2023).

[225] K. A. Kalina, P. Metsch, J. Brummund, and M. Kästner, *A macroscopic model for magnetorheological elastomers based on microscopic simulations*, Int. J. Solids Struct. **193**, 200 (2020).

[226] P. Gebhart, A. Attaran, and T. Wallmersperger, *Multiphysics modeling of porous ferrogels at finite strains*, Phys. Sci. Rev. **7**, 1209 (2022).

[227] P. Gebhart and T. Wallmersperger, *A constitutive macroscale model for compressible magneto-active polymers based on computational homogenization data: Part I — magnetic linear regime*, Int. J. Solids Struct. **236**, 111294 (2022).

[228] P. Gebhart and T. Wallmersperger, *A constitutive macroscale model for compressible magneto-active polymers based on computational homogenization data: Part II — magnetic nonlinear regime*, Int. J. Solids Struct. **258**, 111984 (2022).

[229] D. Romeis, P. Metsch, M. Kästner, and M. Saphiannikova, *Theoretical models for magneto-sensitive elastomers: A comparison between continuum and dipole approaches*, Phys. Rev. E **95**, 042501 (2017).

[230] K. A. Kalina, P. Gebhart, J. Brummund, L. Linden, W. Sun, and M. Kästner, *Neural network-based multiscale modeling of finite strain magneto-elasticity with relaxed convexity criteria*, Comput. Meth. Appl. Mech. Eng. **421**, 116739 (2024).

[231] P. Metsch, H. Schmidt, D. Sindersberger, K. A. Kalina, J. Brummund, G. K. Auernhammer, G. J. Monkman, and M. Kästner, *Field-induced interactions in magneto-active elastomers - a comparison of experiments and simulations*, Smart Mater. Struct. **29**, 085026 (2020).

[232] M. Tarama, P. Cremer, D. Y. Borin, S. Odenbach, H. Löwen, and A. M. Menzel, *Tunable dynamic response of magnetic gels: impact of structural properties and magnetic fields*, Phys. Rev. E **90**, 042311 (2014).

[233] M. Puljiz, Matrix-Mediated Interactions between Particulate Inclusions in Linearly Elastic and Viscoelastic Environments, PhD dissertation, Düsseldorf, Heinrich-Heine-Universität, 2019.

[234] G. Pessot, Coarse-Grained Discretized Description of Magneto-Responsive Elastomers: Mesoscopic Modeling as a Bridge Pillar between Microscopic Simulations and Macroscopic Behavior, PhD dissertation, Düsseldorf, Heinrich-Heine-Universität, 2017.

[235] P. Cremer, Mesoscale modeling of magnetic elastomers and gels – theory and simulations, PhD dissertation, Düsseldorf, Heinrich-Heine-Universität, 2017.

[236] K. A. Kalina, Mehrskalige Modellierung und Finite-Elemente-Simulation magnetorheologischer Elastomere, PhD dissertation, Dresden, Technische Universität, 2021.

[237] A. E. Gongora, B. Xu, W. Perry, C. Okoye, P. Riley, K. G. Reyes, E. F. Morgan, and K. A. Brown, *A Bayesian experimental autonomous researcher for mechanical design*, Sci. Adv. **6**, eaaz1708 (2020).

[238] A. M. Menzel, *Bridging from particle to macroscopic scales in uniaxial magnetic gels*, J. Chem. Phys. **141**, 194907 (2014).

Declaration of Honor

I hereby declare that I prepared this thesis without the impermissible help of third parties and that none other than the aids indicated have been used; all sources of information are clearly marked, including my own publications.

In particular I have not consciously:

- fabricated data or rejected undesirable results,
- misused statistical methods with the aim of drawing other conclusions than those warranted by the available data,
- plagiarized external data or publications,
- presented the results of other researchers in a distorted way.

I am aware that violations of copyright may lead to injunction and damage claims by the author and also to prosecution by the law enforcement authorities. I hereby agree that the thesis may be electronically reviewed with the aim of identifying plagiarism.
I hereby agree that the thesis may be electronically reviewed with the aim of identifying plagiarism.

This work has not yet been submitted as a doctoral thesis in the same or a similar form in Germany, nor in any other country. It has not yet been published as a whole.

Magdeburg, _____

_____